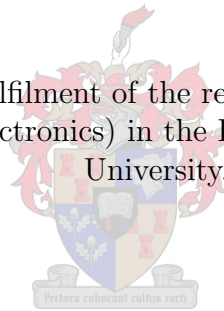


Investigating PV module failure mechanisms caused by indirect lightning strikes

Thesis presented in partial fulfilment of the requirements for the degree Master of
Engineering (Electrical and Electronics) in the Faculty of Engineering at Stellenbosch
University.



Supervisors: Dr. A.J. Rix & Dr. P.G. Wiid

Kurt Michael Coetzer

April 2019

Declaration

I have read and understand the Stellenbosch University Policy on Plagiarism and the definitions of plagiarism and self-plagiarism contained in the Policy [Plagiarism: The use of the ideas or material of others without acknowledgement, or the re-use of one's own previously evaluated or published material without acknowledgement or indication thereof (self-plagiarism or textrecycling)].

I also understand that direct translations are plagiarism, unless accompanied by an appropriate acknowledgement of the source. I also know that verbatim copy that has not been explicitly indicated as such, is plagiarism.

I know that plagiarism is a punishable offence and may be referred to the University's Central Disciplinary Committee (CDC) who has the authority to expel me for such an offence.

I know that plagiarism is harmful for the academic environment and that it has a negative impact on any profession.

Accordingly all quotations and contributions from any source whatsoever (including the internet) have been cited fully (acknowledged); further, all verbatim copies have been expressly indicated as such (e.g. through quotation marks) and the sources are cited fully.

I declare that, except where a source has been cited, the work contained in this assignment is my own work and that I have not previously (in its entirety or in part) submitted it for grading in this module/assignment or another module/assignment.

Signature
Kurt Michael Coetzer

April 2019
Date

Abstract

Investigating PV module failure mechanisms caused by indirect lightning strikes

K.M. Coetzer

*Department of Electrical and Electronic Engineering,
University of Stellenbosch
Private Bag X1, Matieland 7602, South Africa*

Thesis: M.Eng (Electrical)
April 2019

There is an ever increasing global adoption of solar photovoltaic (PV) technologies as sources of renewable energy due to an increasing worldwide energy demand, the depletion of fossil fuel reserves, the shift towards environmentally friendly sources of energy, and an increasing supply, coupled with a decreasing cost, of solar PV technologies. Lightning poses a significant risk to person and property, with some experts estimating a global increase of up to 100 % in the level of lightning activity for every 1 °C rise in average global temperatures. An increasing implementation of solar PV technologies and an estimated increase in global lightning activity create cause for concern for solar PV plant owners.

Repair log data from three utility-scale solar PV power plants was examined, and occurrences of the failure of bypass diodes were noted. An impulse generator was designed and constructed in order to ascertain the failure modes of a bypass diode. Once this understanding was gathered, metal-oxide varistors (MOVs) were investigated as a suitable bypass diode protection measure. An appropriately chosen MOV was found to protect a bypass diode to a level at least double that of the level at which the bypass diode would normally fail.

Computational electromagnetic simulations were performed in order to investigate how the geometry of a PV module, and module interconnections, may influence the extent to which currents may be induced within a PV installation. From simulations, it was found that the presence of the continuously conductive frame of a PV module greatly reduced the net magnetic flux passing through the module, reducing the magnitudes of the induced currents. A reduction of 40 % in the magnitudes of the currents induced within the inter-module wiring was observed in a simulation with multiple series-connected PV modules. Neater inter-module wiring, with a smaller loop area, reduced the magnitude of the currents induced within the inter-module wiring by between 93 % and 98 %.

Testing was performed in a high-voltage laboratory in order to establish the extent to which currents may be induced within an actual PV module. The testing concluded that although a current may be induced within the internal traces of a PV module, it is loop areas within the inter-module wiring which are most likely to result in the induction of currents within the PV installation. Good wiring practice should therefore be applied during the installation of PV systems in order to reduce the formation of loop areas which magnetic fields may couple into.

Uittreksel

Onderzoek van FV-module faalingsmeganismes veroorzaak deur indirekte weerligstaking

(“Investigating PV module failure mechanisms caused by indirect lightning strikes”)

K.M. Coetzer

*Departement van Elektriese en Elektroniese Ingenieurswese,
Universiteit van Stellenbosch
Privaatsak X1, Matieland 7602, Suid Afrika*

Tesis: M.Ing (Elektries)
April 2019

Daar is 'n globale toename in die gebruik van fotovoltaiëse (FV) sonkrag as 'n bron van hernubare energie weens die toenemende wêreldwye aanvraag na energie, die uitputting van fossielbrandstofreserwes, die oorgang na omgewingsvriendelike energiebronne en 'n toenemende beskikbaarheid, tesame met dalende kostes, van sonkrag FV tegnologieë. Weerlig is 'n beduidende risiko vir mense en eiendom, met sommige kenners wat 'n globale toename van tot 100% voorspel rakende die vlak van weerligaktiwiteit vir elke 1°C styging in gemiddelde globale temperature. 'n Toenemende implementering van sonkrag-tegnologieë en 'n beraamde toename in globale weerligaktiwiteit veroorsaak rede vir kommer vir FV-aanleg eienaars.

Historiese instandhoudingsdata van drie grootskaalse FV-sonkragstasies is bestudeer en voorvalle van omloop-diode falings is waargeneem. 'n Impulsgenerator is ontwerp en geïmplementeer om die faalings-modusse van 'n omloop-diode te bepaal. Met die verstaan van die begrip, is metaaloksied-varistors (MOVs) se geskiktheid as 'n omloop-diode beskermingsmaatreël ondersoek. 'n Geskikte MOV kan 'n omloop-diode beskerm tot 'n maksimum van tweemaal die vlak waarby die omloop-diode normaalweg sou faal.

Elektromagentiese-simulasies is uitgevoer om te ondersoek hoe die dimensies van 'n FV-module, asook die tussenverbindings, moontlik die vlak waarmee strome in die FV installasie geïnduseer kan word beïnvloed. Vanaf hierdie simulasies is daar gevind dat die teenwoordigheid van die kontinue en geleidende raam van 'n FV-module grootliks die resulterende netto magnetiese-vloed verminder het, wat gevolglik ook die grootte van die geïnduseerde strome verminder het. Verder is 'n afname van 40% waargeneem vir die strome wat geïnduseer word tussen die kabelverbindings van verskeie serie-gekonnekteerde FV-modules. Daar is ook bepaal dat 'n sorgvuldige benadering tot kabelverbindings tussen FV-modules, met 'n kleiner lus-area, die geïnduseerde stroomgroottes verminder met tussen 93% en 98%.

Toetse was uitgevoer in 'n hoë-spannings-laboratorium, sodat die omvang van geïnduseerde strome binne in 'n FV-module vasgestel kon word. Daar is vasgestel met hierdie toetse dat, alhoewel 'n stroom waarskynlik geïnduseer kan word in die interne FV-sel konneksies van 'n module, die lus-areas van die kabelkonneksies 'n groter effek het op die geïnduseerde

strome van 'n FV-installasie. 'n Sorgsame benadering tot die bedrading van FV-stelsel installasies moet dus toegepas word, sodat die vorming van lus-areas, waarmee magnetiese velde kan koppel, verminder kan word.

Acknowledgements

I would firstly like to thank my supervisors, Dr Arnold Rix and Dr Gideon Wiid, for their guidance, patience, and support throughout the duration of the project.

I would like to thank my parents, Michael and Christine Coetzer, my brother, Brandon Coetzer, and my girlfriend, Claire Potgieter, for their unending support throughout this research - it meant the world to me.

I would like to thank Ms Gail Linnow, from the South African Weather Service, for the supply of the requested lightning flash data.

I would like to thank Scatec Solar for funding this research. Particular gratitude is expressed to the engineering manager, Mr Ivan Hobbs, for the gathering of the repair log data from the three plants considered.

I would like to thank Mr Kevin Rossouw and Mr Armand du Plessis, for their assistance in translating the abstract into Afrikaans.

I would also like to express my sincere gratitude to the following technical, administrative, and academic staff members of the Electrical and Electronic Engineering faculty for their assistance:

Dr Danie Ludick, for his assistance with the use of the computing clusters used for the computational electromagnetic simulations, and his patience and willingness to submit multiple successive jobs whenever small adjustments were necessary.

Prof Matthys Botha, for his assistance in accessing the computational electromagnetic simulation package used, and for his initial guidance in setting up the model used in these simulations.

Mr Nelius Bekker, for his assistance with the configuration and supervision of the high-voltage experiments conducted, and for his patience and willingness to help with the many small changes required to obtain the desired waveform timing parameters.

Dr Johann Straus, for the brainstorming session which produced many ideas for the design of the modular impulse generator.

Mr Wynand van Eeden and Mr Wessel Croukamp, for their assistance with PCB manufacturing, 3D-printing, and any necessary machining.

Mrs Jenny Martin, for the swift handling of many component orders.

Mr Pietro Petzer, Mr Andre Swart, and Mr Brent Gideons, for their willingness to help at the drop of a hat whenever test equipment was required, or whenever manufacturing of a part was necessary.

Mr Hilton Johnson and Mr Ashley Cupido, for the steady supply of last-minute components.

List of Publications

National conferences:

- KM Coetzer, AJ Rix, and PG Wiid, "*Impulse generator design to investigate indirect lightning strike effects on utility-scale photovoltaic installations*", 26th South African Universities Power Engineering Conference (SAUPEC 2018), Johannesburg, South Africa, 24-26 January, 2018.
- KM Coetzer, PG Wiid, and AJ Rix, "*An investigation into the failure mechanisms of Schottky barrier diodes, as commonly implemented as bypass diodes in photovoltaic modules*", 5th South African Solar Energy Conference (SASEC 2018), Durban, South Africa, 25-27 June, 2018.

Dedication

*To my parents and grandparents.
Without their encouragement and support, none of this would have been possible.*

Contents

List of Figures	XVII
List of Tables	XVIII
Nomenclature	XIX
1 Introduction	1
1.1 Chapter Overview	3
1.2 Lightning Activity Near PV Power Plants	3
1.3 Bypass Diode Failures at PV Power Plants	7
1.4 Problem Statement	9
1.5 Research Goals	9
1.6 Research Objectives and Thesis Outline	9
1.6.1 Literature Review	9
1.6.2 Bypass Diode Failure Mechanisms	10
1.6.3 Electromagnetic Modelling of a PV Module and String of Modules	10
1.6.4 High-Voltage Experiments	11
1.6.5 Conclusions	11
2 Literature Review	12
2.1 Chapter Overview	12
2.2 The PV Module	12
2.2.1 History	12
2.2.2 PV Cell Operation	14
2.2.3 PV Module Performance Specifications	15
2.2.4 The Bypass Diode	17
2.3 Lightning	20
2.3.1 Formation and Discharge Mechanics	20
2.3.2 Lightning in a South African Context	24
2.4 Applicable Standards	31
2.4.1 SANS 61215:2015	31
2.4.2 SANS 62305:2011	33
2.4.3 SANS 60364-7-712:2016	37
2.4.4 SANS 61643-12:2009	38
2.5 Lightning and PV Installations	39
2.5.1 PV Cell, String, and Module Degradation	39
2.5.2 An Air Termination System for the Protection of PV Systems	45
2.5.3 PV Module Layout	47
2.5.4 Influence of the Frame of a PV Module on the Induced Voltages	49
2.5.5 Bypass Diode Failures	56
2.5.6 Mutual Inductance of a PV Module	56
2.6 Chapter Conclusion	61

3	Impulse Generator	62
3.1	Chapter Overview	62
3.2	Lightning Impulse Waveform Parameters	63
3.2.1	Standard Lightning Impulses	64
3.2.2	Combination Wave Generator Layout	66
3.3	Pulse-Shaping Network	67
3.3.1	Design of Pulse-Shaping Network	67
3.3.2	Simulation of Pulse-Shaping Network	71
3.4	Marx Generator	74
3.4.1	Marx Generator Principles	74
3.4.2	Marx Generator Design	76
3.5	Simulation of Impulse Generator	80
3.6	Charge-Controlling Module	83
3.7	Distribution Board	84
3.8	PC Software	85
3.9	Microcontroller	87
3.10	Impulse Generator Testing	89
3.11	Diode Testing	92
3.11.1	Forward Bias	93
3.11.2	Reverse Bias	95
3.11.3	Degradation Testing	98
3.11.4	Alternative Diode Testing	101
3.11.5	MOV Protection of Bypass Diodes	106
3.12	Chapter Conclusion	109
4	Electromagnetic Modelling	110
4.1	Chapter Overview	110
4.2	CAD Model	110
4.3	Electromagnetic Modelling Assumptions	113
4.3.1	PV Module Modelling Assumptions	113
4.3.2	Lightning Modelling Assumptions	114
4.4	Electromagnetic Simulation Setup	115
4.5	Results	116
4.5.1	Open-Circuited PV Module	116
4.5.2	Short-Circuited PV Module	124
4.5.3	Module Interconnections	128
4.6	Challenges Encountered with Electromagnetic Modelling	132
4.7	Chapter Conclusion	132
5	High-Voltage Testing	134
5.1	Chapter Overview	134
5.2	High-Voltage Impulse Generator	134
5.3	Impulse Generator Simulation	134
5.4	Test Setup	138
5.5	Results	140
5.5.1	PV Module Model Results	141
5.5.2	PV Module Results	146
5.5.3	Actual Bypass Diodes	149

5.6	Wiring Guidelines for Decreased EMI Susceptibility	157
5.7	Challenges Encountered with High-Voltage Testing	160
5.8	Chapter Conclusion	161
6	Conclusions and Recommendations	163
6.1	Impulse Generator	163
6.2	Electromagnetic Modelling	164
6.3	High-Voltage Testing	164
6.4	Recommendations	164
	Bibliography	171
A	Derivation of Pulse-Shaping Network Equations	A
B	Justification of Chosen Electromagnetic Simulation Frequencies	L
C	Justification of Lightning Polarity in Electromagnetic Simulations	Q
D	PCB Schematics	S
E	Construction of Impulse Generator	U

List of Figures

1.1	Global electricity capacity additions and retirements (2016) [1].	1
1.2	A stand-alone solar PV plant [4].	2
1.3	The locations of the three utility-scale PV power plants covered in this study. Image exported from Google Earth.	3
1.4	An example of lightning flash data, as provided by the South African Weather Service.	4
1.5	The number of lightning flashes per current for the period 2006-2016. . . .	5
1.6	Plant A: number of lightning flashes per month for the period 2006-2016. . .	5
1.7	Plant B: number of lightning flashes per month for the period 2006-2016. . .	6
1.8	Plant C: number of lightning flashes per month for the period 2006-2016. . .	6
1.9	Lightning flashes near Plant B during a single thunderstorm [9].	8
1.10	Lightning flashes and recorded fault locations Plant B for 23/11/2016 [9]. . .	9
1.11	An example of the type of thin-wire approximation used in many electromagnetic simulations of PV modules [10].	10
2.1	From left to right, Willoughby Smith, William Grylls Adams, Charles Edgar Fritts, Albert Einstein [13].	14
2.2	The operation of a PV cell [11].	14
2.3	Figures illustrating the definitions of open-circuit voltage and short-circuit current [11].	15
2.4	The single-diode model for a PV cell [11].	15
2.5	The BYD 310P6C-36 PV module.	16
2.6	An I-V curve [11].	17
2.7	I-V curves for a BYD 310P6C-36 PV module for varying irradiance values [2].	17
2.8	A bypass diode functioning to mitigate the effects of shading [9].	18
2.9	The inside of the junction box of a BYD 310P6C-36 PV module, showing the connections of the three bypass diodes.	19
2.10	The original dipole electrification structure for a thundercloud, as proposed in [17].	22
2.11	The stages leading up to a cloud-to-ground discharge [17].	23
2.12	South African mean number of thunder days per year for the interval between 1961 and 1990, as provided by the SAWS. [3].	25
2.13	Global annual lightning flash density, detected by the LIS. [3].	25
2.14	The locations of the sensors which make up the South African Lightning Detection Network [3].	26
2.15	The 2006 ground flash density distribution for South Africa [3].	27
2.16	The 2006 ground flash multiplicity distribution for South Africa [3].	27
2.17	The 2006 median peak current distribution for South Africa [3].	28
2.18	The 2006 Lightning Intensity Risk Index for South Africa [3].	29
2.19	The 2006 Positive Lightning Risk Index for South Africa [3].	30
2.20	The 2006 Total Lightning Risk for South Africa [3].	30

2.21	The flow diagram for determining the necessary level of lightning protection [30].	36
2.22	The connection of three one-port SPDs, as often seen in a PV power plant.	38
2.23	The two-stage operation of a DEHNguard PV SCI 500 [34].	38
2.24	The circuit diagram of the high-current impulse generator used in [35].	39
2.25	Current impulse injected into the centre of the module frame [35].	40
2.26	Current impulse injected into a flat conductor at the back of a frameless module [35].	41
2.27	A plot showing the reduction in the fill factor of a SOLAREX MSX60 frameless module with successive exposure to nearby current impulses [35].	41
2.28	The reduction in the fill factor of a Siemens Solar M55 frameless module with successive exposure to nearby current impulses [35].	42
2.29	Defects in the front grid of a Siemens monocrystalline PV cell, resulting from a nearby high-current impulse [35].	42
2.30	Defects in the rear grid of a Siemens monocrystalline PV cell, resulting from a nearby high-current impulse [35].	43
2.31	Defects in the rear grid of a Telefunken Systemtechnik polycrystalline PV cell, resulting from a nearby high-current impulse [35].	43
2.32	The schematic of the PV system used in [35] to model the effects of induced current impulses [35].	44
2.33	The test setup used in [36] in order to determine the effects of increased separation distance between a PV module and a high-current impulse [36].	45
2.34	A test of the air termination system mentioned in [36]. A 1.2/50 μ s impulse of 2 MV was used at a separation distance of 3 m [36].	46
2.35	The air termination system consisting of upright metallic rods mentioned in [36], installed at Ingenieurschule ISB [36].	47
2.36	An example of the internal wiring layout of an additive module with an even number of rows.	48
2.37	An example of the internal wiring layout of a compensating module with an even number of rows.	48
2.38	An example of the internal wiring layout of a compensating module with three rows.	49
2.39	Three Kyocera KC60 modules stacked vertically on their long edges in the impulse generator used in [37].	50
2.40	A diagram of the vertical experimental setup described in [37].	50
2.41	Induced voltage waveforms in a Kyocera KC60 PV module, with and without its aluminium frame [37].	51
2.42	Induced voltages within a vertically-mounted Kyocera KC60 PV module [37].	52
2.43	The horizontal experimental setup described in [37].	52
2.44	Induced voltages within a horizontally-mounted Kyocera KC60 PV module [37].	53
2.45	Frame reduction factors for three PV modules of differing internal layout [37].	54
2.46	The induced voltages within a vertically mounted Kyocera KC60 PV module, with and without its aluminium frame, with and without a sheet of aluminium foil placed on the front and rear of the module [37].	55

2.47	Test setup used to measure the induced voltage within a PV module when in close proximity to a large current impulse [36].	57
2.48	The recorded current waveform applied to the U-channel in [36] in order to determine the mutual inductance of a PV module [36].	57
2.49	The recorded induced voltage waveform measured at the output terminals of the PV module in [36], used to determine the mutual inductance of a PV module [36].	58
2.50	The setup used in the derivation of the expression for the estimated induced voltages within a PV module.	59
2.51	The setup used for the derivation of the expression for the magnetic flux density resulting from a vertical current flow.	59
3.1	An overview of the impulse generator.	62
3.2	Time parameters for a full voltage impulse [38].	63
3.3	Time parameters for a full impulse current [39].	64
3.4	Circuit diagram of 1.2/50 μ s-8/20 μ s waveform generator [39].	66
3.5	The circuit diagram of the chosen pulse-shaping network topology.	67
3.6	The theoretical open-circuit voltage and short-circuit response of the pulse-shaping network after adjustment of the computed component values.	71
3.7	The circuit used for the simulation of the pulse-shaping network.	72
3.8	The simulated open-circuit voltage and short-circuit response of the pulse-shaping network.	72
3.9	The simulated current and voltage waveforms at the output of the capacitor.	73
3.10	Charging mechanism of a spark gap switched Marx generator.	74
3.11	Discharging mechanism of a spark gap switched Marx generator.	75
3.12	A simplified diagram of the designed Marx generator module [9].	76
3.13	The relationship between I_C (1 ms pulse) and V_{CE} for the Toshiba GT40WR21 IGBT [46].	77
3.14	The concept of deadtime [47].	78
3.15	A two-stage solid-state Marx generator.	80
3.16	The open-circuit voltage and short-circuit current, using component values from Table 3.5.	81
3.17	The open-circuit voltage and short-circuit current, after adjusting V_{C_0} and R_4	81
3.18	The circuit used for the simulation of the impulse generator.	82
3.19	An overview of the charge-controlling module.	84
3.20	A render of the PCB of the distribution board.	84
3.21	The impulse generator PC software.	85
3.22	Impulse generator PC software program flow diagram.	86
3.23	Microcontroller program flow diagram.	88
3.24	Impulse generator open-circuit voltage and short-circuit current output for a source voltage of 50 V (air core inductor).	89
3.25	Impulse generator open-circuit voltage and short-circuit current output for a source voltage of 50 V (no inductor).	90
3.26	Impulse generator Level 1 open-circuit voltage and short-circuit current waveforms (no inductor).	91
3.27	Impulse generator open-circuit voltage and short-circuit current output for a source voltage of 50 V (simplified pulse-shaping network).	92

3.28	Voltage and current waveforms recorded during the testing of Diode 8. . .	94
3.29	Voltage and current waveforms recorded during the testing of Diode 70. . .	94
3.30	Voltage and current waveforms recorded during the testing of Diode 79. . .	95
3.31	Voltage and current waveforms recorded during the testing of Diode 25. . .	96
3.32	Voltage and current waveforms recorded during the testing of Diode 64. . .	97
3.33	Voltage and current waveforms recorded during the failure of Diode 15. . .	97
3.34	Voltage and current waveforms recorded during the failure of Diode 65. . .	98
3.35	Voltage and current waveforms recorded during the degradation testing of Diode 8.	99
3.36	Voltage and current waveforms recorded during the degradation testing of Diode 38.	100
3.37	Voltage and current waveforms recorded during the degradation testing of Diode 64.	100
3.38	Voltage and current waveforms recorded during the testing of Diode A3. .	101
3.39	Voltage and current waveforms recorded during the testing of Diode B3. . .	102
3.40	Voltage and current waveforms recorded during the testing of Diode A8. .	103
3.41	Voltage and current waveforms recorded during the testing of Diode B8. . .	103
3.42	Voltage and current waveforms recorded during the failure of Diode A7. . .	104
3.43	Voltage and current waveforms recorded during the failure of Diode B15. .	104
3.44	Voltage and current waveforms recorded during the degradation testing of Diode A8.	105
3.45	Voltage and current waveforms recorded during the degradation testing of Diode B8.	105
3.46	MOV operation parameters	107
3.47	Voltage and current waveforms recorded during the testing of Diode 44 and MOV 7.	108
3.48	Voltage and current waveforms recorded during the testing of Diode 60 and MOVs 16 & 17.	108
4.1	The front view of the CAD model of a BYD 310P6C-36 PV module.	111
4.2	The junction box in the CAD model of a BYD 310P6C-36 PV module. . .	111
4.3	The conductive tracks on a PV cell.	112
4.4	The conductive tracks representing a row of PV cells within a PV module.	112
4.5	The conductive traces for the conventional modelling approach (left) and the approach hypothesised to be more representative (right).	113
4.6	A time domain plot of a 20 kA, 8/20 μ s current waveform.	114
4.7	The power spectrum of a 20 kA, 8/20 μ s current waveform.	115
4.8	Open-circuited PV module with lightning stroke (modelled as an impressed current) at 1 m along the positive X-axis.	117
4.9	Induced voltages over the bypass diodes at a distance of 1 m from the lightning stroke (with frame).	118
4.10	Induced voltages over the bypass diodes at a distance of 1 m from the lightning stroke (no frame).	118
4.11	A comparison of the Y-component of the H-Field at the centre of the loop connected to Diode 3 (open-circuit case).	119
4.12	Induced currents within the frame of the PV module, viewed from the positive Y-axis.	119

4.13	Induced currents through bypass diodes at a distance of 1 m from the lightning stroke (with frame).	120
4.14	Induced currents through bypass diodes at a distance of 1 m from the lightning stroke (no frame).	120
4.15	A comparison of the Y-component of the H-Field at the centre of the loop connected to Diode 3 (short-circuit case).	121
4.16	Induced currents through bypass diodes at a distance of 5 m from the lightning stroke (with frame).	122
4.17	Induced currents through bypass diodes at a distance of 5 m from the lightning stroke (no frame).	122
4.18	Induced currents through bypass diodes at a distance of 10 m from the lightning stroke (with frame).	123
4.19	Induced currents through bypass diodes at a distance of 10 m from the lightning stroke (no frame).	123
4.20	The CAD model of a PV module with the addition of a short-circuit between the output terminals.	124
4.21	Induced currents at a distance of 1 m from the lightning stroke (with frame and short-circuit loop).	125
4.22	Induced currents at a distance of 1 m from the lightning stroke (no frame, with short-circuit loop).	125
4.23	Induced currents at a distance of 5 m from the lightning stroke (with frame and short-circuit loop).	126
4.24	Induced currents at a distance of 5 m from the lightning stroke (no frame, with short-circuit loop).	126
4.25	Induced currents at a distance of 10 m from the lightning stroke (with frame and short-circuit loop).	127
4.26	Induced currents at a distance of 10 m from the lightning stroke (no frame, with short-circuit loop).	127
4.27	Simulation setup with multiple PV modules and poor inter-module wiring.	128
4.28	Simulation setup with multiple PV modules and better inter-module wiring.	129
4.29	Induced currents in a PV installation where poor inter-module wiring practice was used.	129
4.30	Induced currents in a PV installation where better inter-module wiring practice was used.	130
4.31	Induced currents in a PV installation where poor inter-module wiring practice was used (without frames).	131
4.32	Induced currents in a PV installation where better inter-module wiring practice was used (without frames).	131
5.1	Initial short-circuit current waveform obtained from the HV impulse generator.	135
5.2	The circuit used for the simulation of the impulse generator.	136
5.3	The circuit used for the simulation of the impulse generator (with external inductor).	136
5.4	The short-circuit current waveforms obtained from simulation.	137
5.5	The short-circuit current waveform obtained from the HV impulse generator (with external inductor).	137
5.6	The complete high-voltage test setup.	138

5.7	The full-scale model of a PV module.	139
5.8	A close-up showing the three traces used to model each row of PV cells in the model of a PV module.	140
5.9	The junction box of the model of a PV module.	140
5.10	Induced currents within the model of a PV module at a separation distance of 1 m.	141
5.11	Induced currents within the model of a PV module at a separation distance of 1.6 m.	142
5.12	Induced currents within the model of a PV module (with an external short-circuit) at a separation distance of 1 m.	143
5.13	Induced currents within the model of a PV module (with an external short-circuit) a separation distance of 1.6 m.	143
5.14	Induced currents within the model of a PV module (with bypass diodes) at a separation distance of 1 m.	144
5.15	Induced currents within the model of a PV module (with bypass diodes) at a separation distance of 1.6 m.	144
5.16	Induced currents within the model of a PV module (with bypass diodes and an external short-circuit) at a separation distance of 1 m.	145
5.17	Induced currents within the model of a PV module (with bypass diodes and an external short-circuit) a separation distance of 1.6 m.	145
5.18	Induced currents within the PV module at a separation distance of 1 m.	147
5.19	Induced currents within the PV module at a separation distance of 1.6 m.	147
5.20	Induced currents within the PV module (with an external short-circuit) at a separation distance of 1 m.	148
5.21	Induced currents within the PV module (with an external short-circuit) a separation distance of 1.6 m.	148
5.22	Induced currents within the PV module (with bypass diodes) at a separation distance of 1 m.	149
5.23	Induced currents within the PV module (with bypass diodes) at a separation distance of 1.6 m.	150
5.24	Induced currents within the PV module (with bypass diodes and an external short-circuit) at a separation distance of 1 m.	150
5.25	Induced currents within the PV module (with bypass diodes and an external short-circuit) a separation distance of 1.6 m.	151
5.26	The simulated induced currents at a separation distance of 1 m with an $-4.4\text{ kA } 8/20\text{ }\mu\text{s}$ current impulse.	152
5.27	The simulated induced currents at a separation distance of 1 m with an $-4.4\text{ kA } 8/20\text{ }\mu\text{s}$ current impulse.	152
5.28	The adjusted simulation setup, with a thin-wire approximation of the frame of a PV module.	153
5.29	The simulated induced currents at a separation distance of 1.6 m with an $-4.4\text{ kA } 8/20\text{ }\mu\text{s}$ current impulse (with thin-wire frame).	153
5.30	The simulated induced currents at a separation distance of 1.6 m with an $-4.4\text{ kA } 8/20\text{ }\mu\text{s}$ current impulse (with thin-wire frame).	154
5.31	The simulated induced currents at a separation distance of 1.6 m with an $-4.4\text{ kA } 8/20\text{ }\mu\text{s}$ current impulse (with thin-wire frame and short-circuit loop).	155

5.32	The simulated induced currents at a separation distance of 1.6 m with an $-4.4\text{ kA } 8/20\text{ }\mu\text{s}$ current impulse (with thin-wire frame and short-circuit loop).	155
5.33	Looping of excess inter-module wiring at a solar plant.	157
5.34	A string of 6 series-connected PV modules with looping of excess inter-module wiring.	157
5.35	Methods of neatening excess wiring: A loop (left) versus a figure-of-eight (right).	158
5.36	A string of 12 PV modules with looping of excess inter-module wiring. . .	158
5.37	A string of 12 PV modules without looping of excess inter-module wiring. .	158
5.38	A string of 6 series-connected PV modules with the "leapfrog" wiring method.	159
5.39	A string of 12 series-connected PV modules with the 'leapfrog' wiring method.	159
5.40	A recorded current waveform, before and after low-pass filtering.	160
A.1	The labelled diagram of the chosen pulse-shaping network topology for use in deriving suitable component values.	A
B.1	Induced currents per frequency for 30 discrete frequency steps.	L
B.2	Induced currents per frequency for 60 discrete frequency steps.	M
B.3	Induced currents per frequency for 120 discrete frequency steps.	M
B.4	Time domain induced currents for 30 discrete frequency steps.	N
B.5	Time domain induced currents for 60 discrete frequency steps.	N
B.6	Time domain induced currents for 120 discrete frequency steps.	O
B.7	Time domain induced currents for an interpolated range of frequencies. . .	O
B.8	Induced currents per frequency for interpolated frequency range.	P
C.1	Induced currents through bypass diodes at a distance of 1 m from the positive polarity lightning stroke (with frame).	Q
C.2	Induced currents through bypass diodes at a distance of 1 m from the negative polarity lightning stroke (with frame).	R
D.1	The PCB schematic for a single impulse generator module.	S
D.2	The PCB schematic for the distribution board.	T
D.3	The PCB schematic for the charge-controlling module.	T
E.1	The constructed six stage Marx generator.	U
E.2	The LEDs within the Marx generator module.	V
E.3	A photograph of the Marx generator module.	V
E.4	From left to right, the charge-controlling module, the microcontroller, and the distribution board.	W
E.5	The constructed pulse-shaping network.	X

List of Tables

1.1	Parameters calculated from the gathered lightning flash data.	4
2.1	The classification categories for lightning risk, as proposed by [3].	28
2.2	Expected surge currents resulting from lightning flashes on low-voltage systems [28].	35
2.3	The relevant risk components for each type of loss [30].	36
2.4	Labels for the I-V curves shown in Figure 2.27 [35].	41
2.5	Labels for the I-V curves shown in Figure 2.28 [35].	42
3.1	Definitions of 1.2/50 μ s and 8/20 μ s waveform parameters [39].	65
3.2	The test levels specified by [39].	65
3.3	Specifications extracted from the open-circuit voltage and short-circuit current curves computed in MATLAB.	70
3.4	The target performance specifications for the pulse-shaping network.	70
3.5	The component values chosen for the pulse-shaping network.	71
3.6	Toshiba GT40WR21 IGBT specifications [46].	77
3.7	Metalised Polypropylene vs Aluminium Electrolytic Capacitors [48],[49].	79
5.1	A comparison of the peak current magnitudes from simulation, with the model of a PV module, and an actual PV module (with short-circuited bypass diodes).	156

Nomenclature

A	-	Ampere
AC	-	Alternating Current
ADC	-	Analog to Digital Converter
bps	-	Bits per Second
COM	-	Communications
dB	-	Decibel
DC	-	Direct Current
EM	-	Electromagnetic
EMC	-	Electromagnetic Compatibility
EMI	-	Electromagnetic Interference
F	-	Farad
GUI	-	Graphical User Interface
H	-	Henry
Hz	-	Hertz
IC	-	Integrated Circuit
IEC	-	International Electrotechnical Commission
IDE	-	Integrated Development Environment
IGBT	-	Insulated-Gate Bipolar Transistor
k	-	Kilo
K	-	Kelvin
LED	-	Light Emitting Diode
LPF	-	Low Pass Filter
LPL	-	Lightning Protection Level
LPS	-	Lightning Protection System
LPZ	-	Lightning Protection Zone
m	-	Milli
MOV	-	Metal Oxide Varistor
n	-	Nano
PC	-	Personal Computer
PCB	-	Printed Circuit Board
PV	-	Photovoltaic
PVC	-	Polyvinyl Chloride
Rx	-	Receive
s	-	Second
SANS	-	South African National Standards
SPD	-	Surge Protective Device
Tx	-	Transmit
μ	-	Micro
USB	-	Universal Serial Bus
V	-	Volt
Ω	-	Ohm

Chapter 1

Introduction

In 2016, renewable energy sources represented approximately 2/3 of the new net global generation capacity (additions minus retirements) - a total of 165 GW (as shown in Figure 1.1). New solar photovoltaic (PV) capacity alone increased by 50 %, over 74 GW in total. This was the first year in which the increase in capacity of solar PV was larger than any other source of energy (including coal). [1]

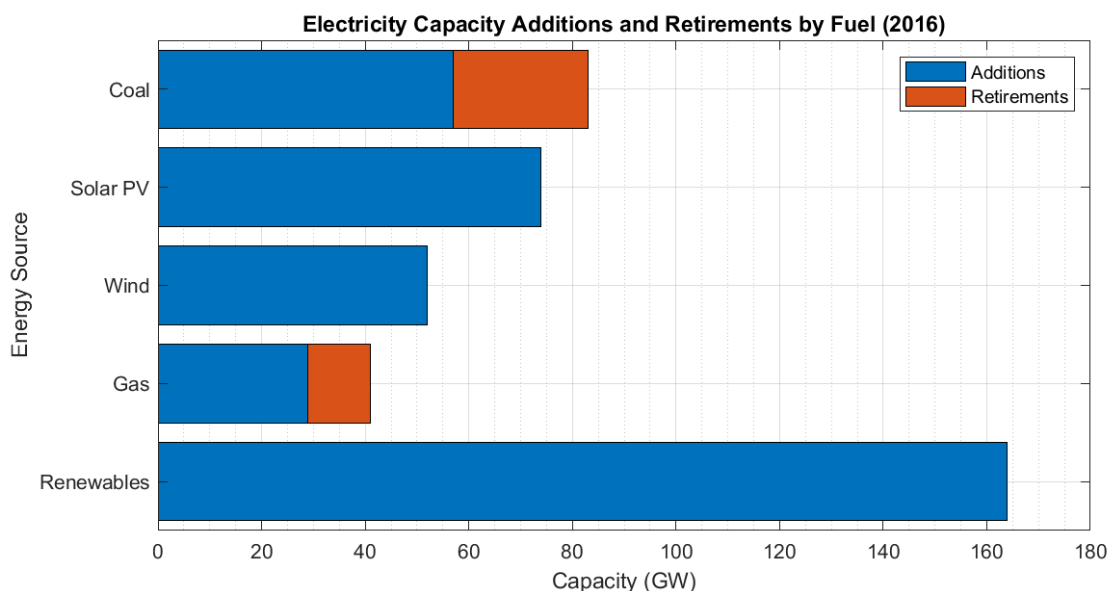


Figure 1.1: Global electricity capacity additions and retirements (2016) [1].

More than half of this growth was due to new installations in China. Solar PV companies began issuing auction bids as low as \$30 (USD) per megawatt-hour (MWh). Between 2017 and 2022, it is forecasted that global renewable electricity capacity will increase by 43 % (an increase of over 920 GW). Annual solar PV additions are forecasted to contribute the largest proportion of this increase (80.4 %, or 720 GW), greater than wind and hydroelectric power. This forecasted increase in solar PV capacity is greater than the 2017 total power capacities of Japan and India, combined. In 2017, China accounted for half of the global solar PV demand, with Chinese companies representing approximately 60 % of the global solar PV manufacturing capacity. [1]

Although the rates of solar PV adoption are increasing (due to a lowering barrier to entry), the rates are likely to increase further if governments around the world further develop legislation allowing increased grid integration of solar PV. Due to factors such as the increasing availability and decreasing cost of solar PV technologies, an increasing desire for global electrification, and increasing global increase in clean energy, solar PV is

being installed (in both off-grid and grid-tied configurations) in regions previously deemed unsuitable, uneconomical, or unnecessary. PV module manufacturers typically guarantee a long service life (a module should produce at least 80 % of its rated maximum power after 20 years [2]), therefore it is in the interest of the plant owner to ensure that the plant remains sufficiently protected in order to remain operational for the full intended service life.

Lightning presents a significant risk to person and property wherever it occurs [3]. Stand-alone PV installations are typically composed of multiple series-connected PV modules, often with aluminium frames and supported by steel structures, as shown in Figure 1.2. As a result, the direct and indirect effects of a lightning flash near or to a PV installation are of concern to the solar PV plant owner.



Figure 1.2: A stand-alone solar PV plant [4].

Global lightning activity is expected to increase in the future. Lightning flash rate has been correlated with the product of the convective available potential energy (CAPE) of an air parcel (a measure of atmospheric instability) and the precipitation rate. When this method was applied to 11 climate models for the contiguous United States (CONUS), it was predicted that the estimated frequency of lightning flashes will increase by 12 ± 5 % per degree Celsius ($^{\circ}\text{C}$) resulting from global warming - a total estimated increase in the frequency of lightning flashes of 50 % over the duration of the current century [5]. An estimate which made use of satellite lightning data suggested that an increase in average wet-bulb (a term used to describe the recorded temperature at a relative humidity of 100 %) temperature increase of 1 Kelvin (K) may result in a global increase in lightning activity of approximately 40 % [6]. An estimate based on using the fundamental mode of the Schumann resonances (resonances in the earth-ionosphere cavity caused by lightning activity [7]) as a proxy for lightning flash rate described an increase in global lightning activity of 100 % for every 1°C rise in average global temperature [8].

Increased global lightning activity, coupled with an increased global rate of adoption of solar PV technologies, prompted an investigation into the susceptibility of a PV module or installation to lightning-related damage. As protection measures exist for the prevention of damage resulting from a direct lightning flash to a structure (such as the frames

or supporting structure of a solar PV installation) or service (such as the power lines connected to the solar PV installation), it was of particular interest to examine the indirect effects a lightning flash may have on a solar PV installation.

1.1 Chapter Overview

This chapter identifies the phenomenon of failing bypass diodes within PV modules within three utility-scale (larger than 10 MW) PV power plants as a result of nearby lightning strikes, and discusses the research approach used to investigate this phenomenon.

The historical lightning activity in and around three utility-scale PV power plants is examined in order to establish a lightning climatology of the areas in which the three plants are located. The repair log data from these three utility-scale PV power plants is then inspected and correlated with lightning flash data in order to gain further insight into what may have caused the recorded failures.

The problem statement is then defined, leading to the formulation of three research goals. From these research goals, three interlinked studies are proposed. The research objectives and thesis outline are discussed in the final section of this chapter.

1.2 Lightning Activity Near PV Power Plants

Lightning flash data was received from the South African Weather Service (SAWS) for a 20 km by 20 km square surrounding three utility-scale PV power plants in South Africa for the period beginning 1 January 2006 and ending 31 December 2016. The physical locations of these plants, Plant A, Plant B, and Plant C, are shown in Figure 1.3.



Figure 1.3: The locations of the three utility-scale PV power plants covered in this study. Image exported from Google Earth.

The lightning flash data indicates the time and date of the sensor reading (to the milli-second), the latitude and longitude of the flash (to nine decimal places), the peak current recorded (both polarity and magnitude in kA), the multiplicity (the number of strokes within a flash), and the number of sensors taking part in each reading. An example of the data gathered is shown in Figure 1.4.

TIME	LAT	LON	PEAK_KA	MULTI	NUM_DFRS
2014-01-04 16:16:11.176	-30.094882965	24.325805664	-19	2	10
2014-01-04 16:19:05.086	-30.105485916	24.227323532	-34	1	14
2014-01-04 16:24:25.173	-30.055427551	24.298139572	-19	1	12
2014-01-04 16:27:28.595	-30.099042892	24.285482407	-11	2	5
2014-01-04 16:29:10.493	-30.113193512	24.302942276	-22	2	12
2014-01-04 16:30:20.749	-30.063613892	24.314313889	-20	1	12

Figure 1.4: An example of lightning flash data, as provided by the South African Weather Service.

Analysis of the received lightning flash data produced the key figures shown in Table 1.1. The large number of flashes and the substantial currents (of up to 308 kA) recorded further reinforced lightning poses a very real threat to person and property. The area surrounding the Plant B had a lower mean flash multiplicity (2.11) and lower positive lightning ratio (9.85) than the areas surrounding Plant A and Plant C. A mean peak flash current of approximately 20 kA was recorded at all plants.

Table 1.1: Parameters calculated from the gathered lightning flash data.

	Number of Flashes	Max. Negative Current [kA]	Max. Positive Current [kA]	Mean Current Magnitude [kA]	Ratio Positive Lightning [%]	Mean Flash Multiplicity
Plant A	89955	-213	308	19.87	11.93	2.76
Plant B	81555	-250	234	19.50	9.85	2.11
Plant C	67073	-240	302	19.16	11.10	2.70

Figure 1.5 shows the number of lightning flashes recorded for each current magnitude. All regions exhibit a similar distribution, where most of the occurrences of lightning flashes are negative with a median peak current magnitude of approximately -15 kA. Negative polarity lightning flashes were recorded with as little peak current as -1 kA, whilst the minimum positive polarity lightning flash peak current recorded was 10 kA.

Figure 1.6, Figure 1.7, and Figure 1.8 show the number of flashes per month near each PV power plant for the period 2006-2016. As expected, lightning activity is high in the summer months of December to January. In contrast, lightning activity is greatly reduced in winter months - with some months having no lightning activity whatsoever. October 2009 was a particularly active month for the areas surrounding Plant A and Plant C (and less so for the areas surrounding the Plant B) when compared with other years.

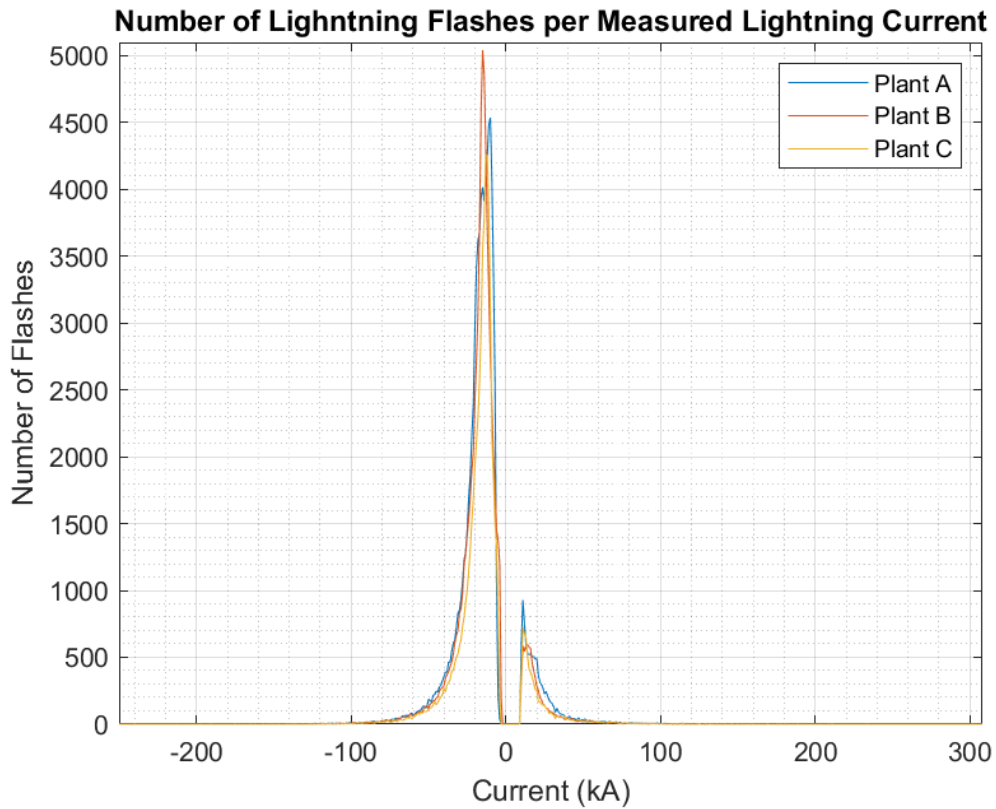


Figure 1.5: The number of lightning flashes per current for the period 2006-2016.

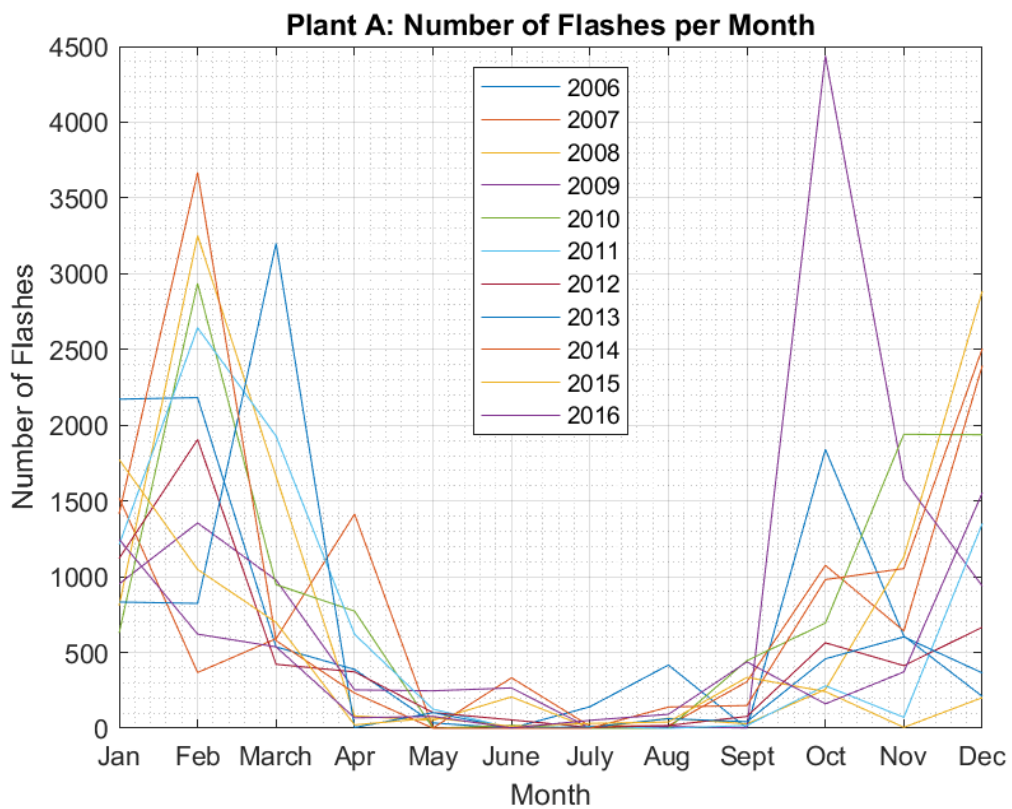


Figure 1.6: Plant A: number of lightning flashes per month for the period 2006-2016.

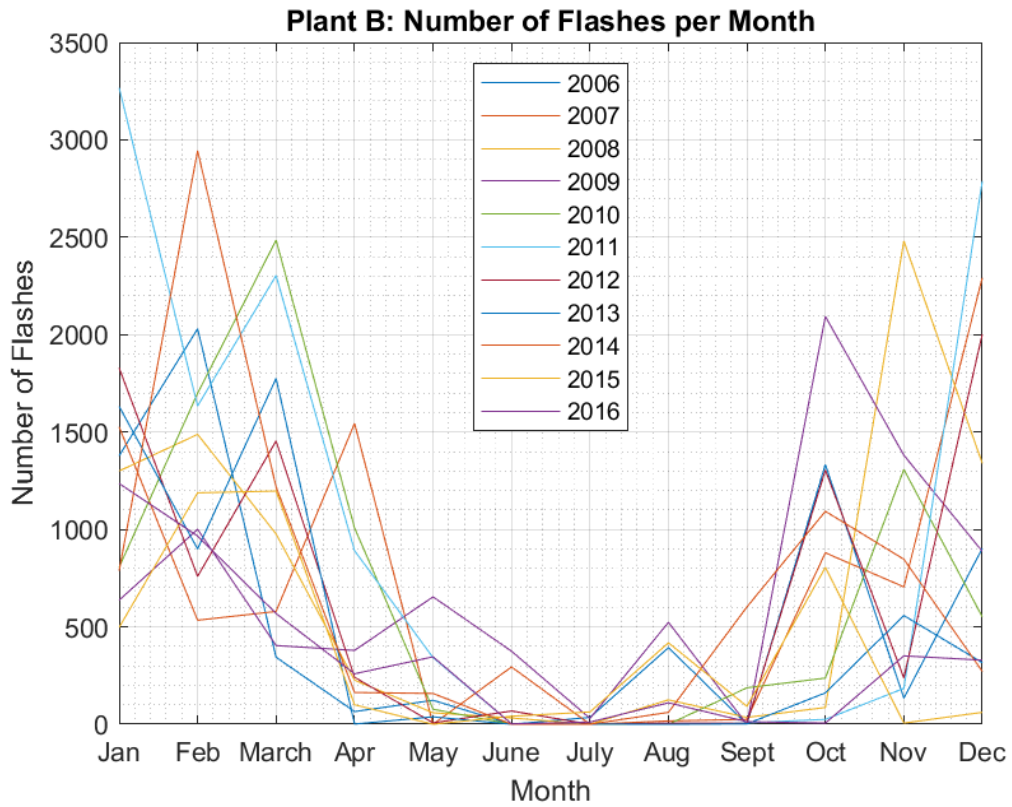


Figure 1.7: Plant B: number of lightning flashes per month for the period 2006-2016.

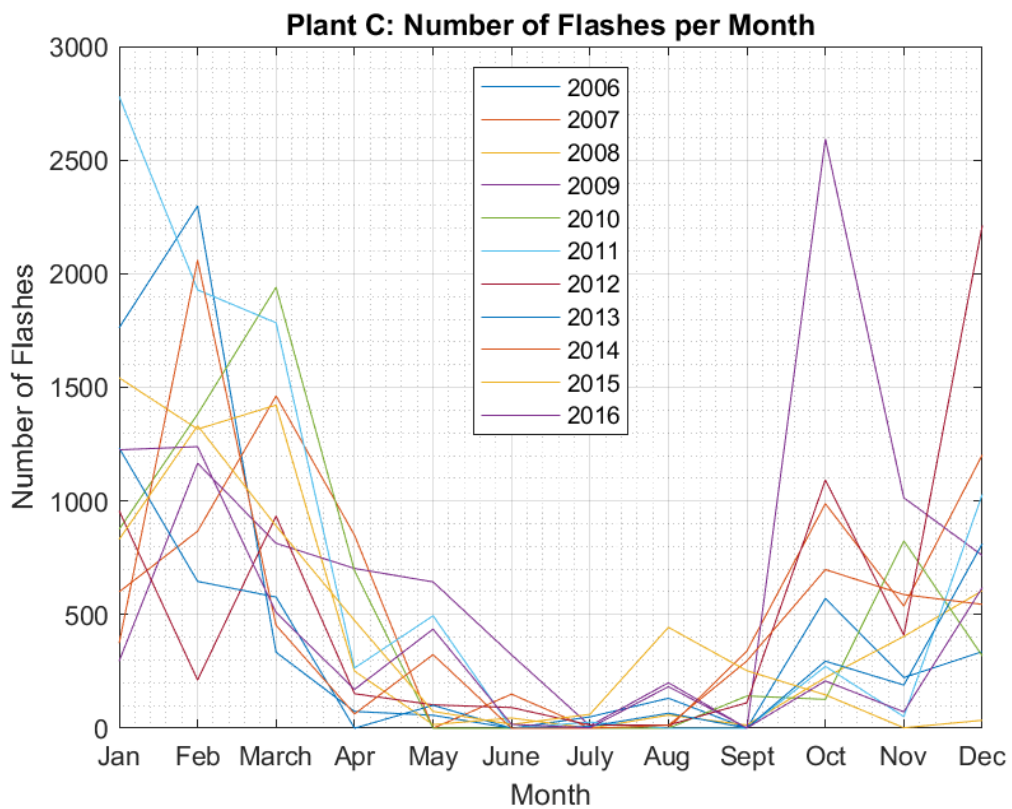


Figure 1.8: Plant C: number of lightning flashes per month for the period 2006-2016.

1.3 Bypass Diode Failures at PV Power Plants

Repair log data, specifically relating to lightning-related faults, was requested from these three utility-scale PV power plants. Data was received for the period 2015-2016. The following information was presented:

- The time and date that the fault was detected.
- The location of the fault (transformer compact station number, inverter number, string number, module number).
- A brief description of the fault logged.
- The remedial action, including the date it was performed.
- Whether or not the surge protective device (SPD) in the combiner box had activated.

In each case, a "low power" fault had been detected in the string monitor placed in the combiner box which the string was connected to. Upon inspection, it was noticed that the SPDs had been activated.

It is worth mentioning that the failure of a bypass diode (the purpose of which is explained later in Section 2.2.4) in the short-circuit or open-circuit position would result in a string under-performing, and therefore triggering a "low power" fault. A short-circuited bypass diode would cause the current produced by the PV cells it is placed in parallel with to flow through the bypass diode, instead of contributing to the string - rendering those cells functionally purposeless. A module with open-circuited bypass diodes would produce power at a normal level when no shading occurs. When shading occurs across one or more series-connected loops, those loops would begin to heat up, therefore reducing the power production of the total string, as well as damaging the PV cells themselves. The latter case would be more difficult to detect than the former as it would only occur during shading.

At Plant C, 70 % of lightning-related failures explicitly cite a faulty bypass diode as the reason for the replacement of an entire PV module - a relatively costly expense resulting from the failure of an inexpensive component. The remaining 30 % of faults refer to "low voltage output", which could be caused by either short-circuited bypass diodes or damaged PV cells.

Plant A replaced the most PV modules in the two-year period due to lightning damage - 110 in total. For comparison, during the same period only 19 PV modules were replaced at Plant A due to wind damage.

Since there is very little solar irradiance during thunderstorms, it was noted that faults were often recorded the morning after the occurrence of a lightning flash. One particular example of this was the recording of a fault on a particular string at Plant A at 10:00 on the 13th of March 2016. Upon investigating, it was discovered that modules 1-6 had been damaged. Reviewing the lightning flash data from the SAWS showed that a lightning flash of unity multiplicity, with a peak current of -10 kA had occurred nearby during the previous night.

Plant B suffered the most damage during a single thunderstorm. A total of 51 modules connected to one inverter and 21 modules connected to another inverter were damaged

during a storm in 2016. The lightning flashes for this particular thunderstorm are plotted in Figure 1.9; the plant is represented by the green polygon.

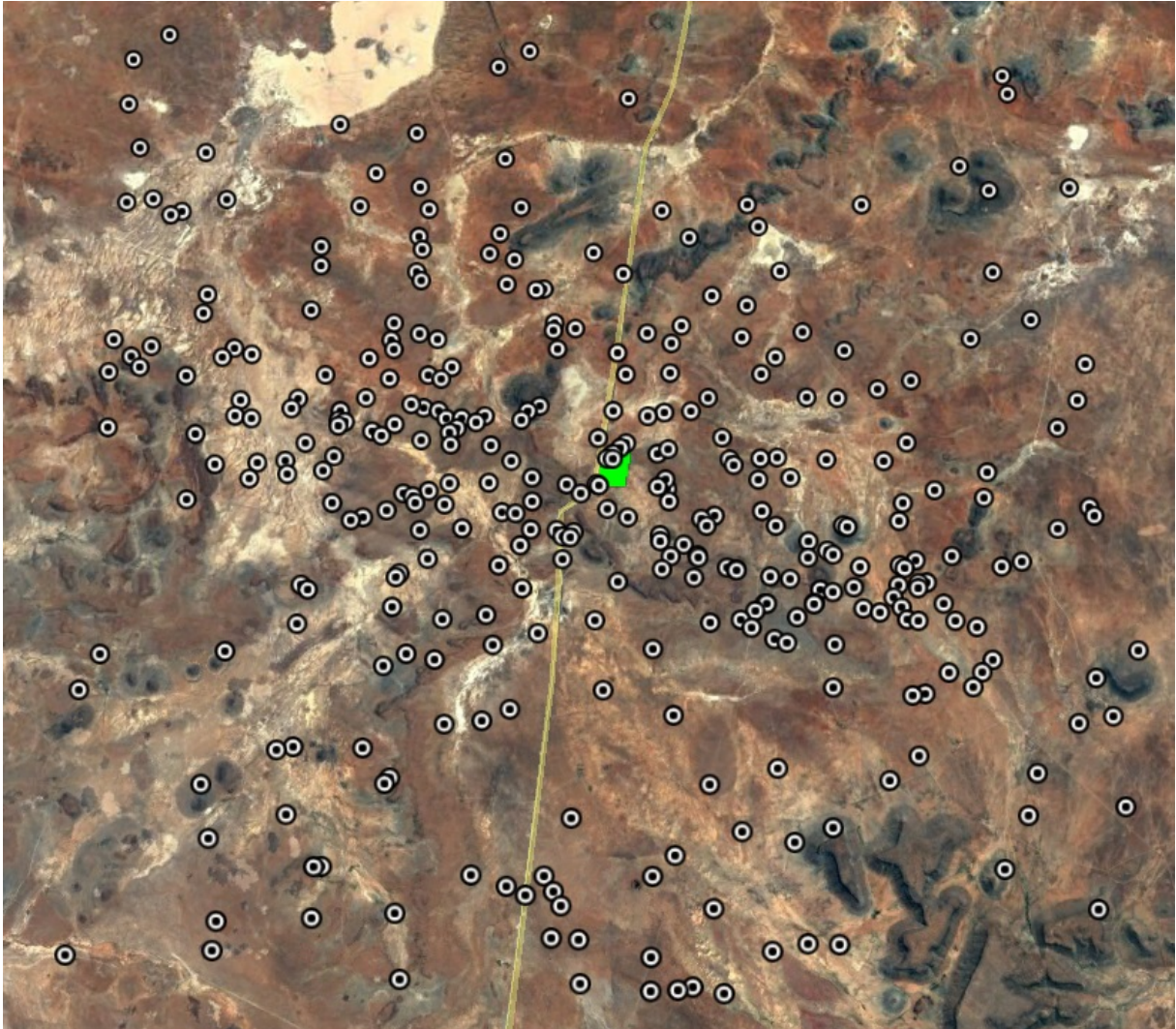


Figure 1.9: Lightning flashes near Plant B during a single thunderstorm [9].

The locations of the faults recorded during this storm were overlaid on the the plot shown in Figure 1.9; zooming in produced Figure 1.10. The faults had been detected at 18:17 on the 23rd of November 2016. Strong correlation had occurred, showing a lightning flash at, or very near to, each fault location. The one flash occurred at 18:17:347, had a peak current of -26 kA, and a multiplicity of 6; while the other flash occurred at 18:18:05.345, had a peak current of -18 kA, and a multiplicity of 1. Although other flashes did occur within the plant throughout this particular storm, no corresponding faults were recorded.



Figure 1.10: Lightning flashes and recorded fault locations Plant B for 23/11/2016 [9].

1.4 Problem Statement

It has been observed that PV installations are susceptible to the effects of nearby lightning strikes, often resulting in the failure of the bypass diodes within the PV modules. Research is required relating to both the conditions under which which bypass diodes may fail, as well as the mechanisms by which these conditions may be created.

1.5 Research Goals

1. Investigate the failure modes of a bypass diode.
2. Once the failure modes of a bypass diode have been established, propose an appropriate protection measure to increase bypass diode resilience.
3. Investigate how the configuration of a PV installation (including the frame and internal layout of a PV module, as well as the inter-module wiring) may influence the magnitudes of the currents induced within the installation.

1.6 Research Objectives and Thesis Outline

1.6.1 Literature Review

Chapter 2 acquaints the reader with both photovoltaics as a technology, and lightning as a natural phenomenon. Once these concepts are explained, technical standards relating to them are discussed, followed by an analysis of previous research relating to induction effects within photovoltaic modules. This lays the groundwork from which the three related studies in this thesis were proposed. The details of these studies are presented in the following chapters.

1.6.2 Bypass Diode Failure Mechanisms

In order to begin to consider manners in which a bypass diode could be protected, it was first necessary to gain an understanding of how a bypass diode may fail.

To gain this understanding, an impulse generator was designed and constructed for the purpose of discovering the levels and polarities at which a bypass diode may fail. The impulse generator was capable of producing waveforms akin to IEC standard current and voltage waveforms, as well as longer waveforms. This directly relates to the first research goal defined in Section 1.5.

Once any weaknesses of a typical bypass diode were discovered, a protection measure could be investigated and tested. This directly relates to the second research goal stated in Section 1.5.

The details and results of this study are presented in Chapter 3.

1.6.3 Electromagnetic Modelling of a PV Module and String of Modules

Electromagnetic modelling of PV modules and arrays is commonly performed using highly-simplified models. These models often approximate the frames, module interconnections, and the traces within a module as thin wires of unspecified thickness - as can be seen in Figure 1.11. Due to the broad simplifications made, it is hypothesised that insightful interactions are being ignored.

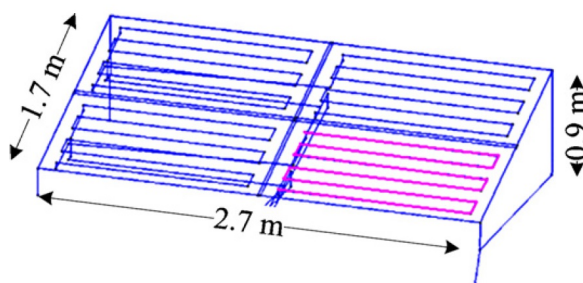


Figure 1.11: An example of the type of thin-wire approximation used in many electromagnetic simulations of PV modules [10].

In this study, a highly detailed model of a PV module is developed. This model is used as the basis for electromagnetic simulations designed to replicate how the currents induced in a PV module (resulting from nearby lightning strokes) are affected by:

- The position of the lightning stroke, at various distances from the module.
- The presence of the metallic frame of the PV module.
- The presence of a short-circuit between the output terminals of the PV module.
- Module interconnections in an array of four modules, and the functional differences between poor and better wiring practices.

This model takes the geometry of the frame and junction box into account in order to increase the accuracy of the simulation. The three conductive connections within a row of series-connected cells are modelled as three continuous traces, and not as a single trace going through the centre of gravity of each cell. Bypass diodes are approximated as either open-circuits or short-circuits, depending on the aim of the particular simulation.

This study directly relates to the third research goal stated in Section 1.5, and its details and results are presented in Chapter 4.

1.6.4 High-Voltage Experiments

Experiments were performed in a high-voltage laboratory in order to examine the correlation between the results of the studies in Chapter 3 and Chapter 4 and the real-world measurements taken in the presence of a current impulse of similar order of magnitude and shape as that found in a lightning stroke.

Both an actual PV module and a full-scale thin-wire approximation of a PV module were used in this study in order to examine the differences in the magnitudes of the induced currents measured. This provides further insight into how a PV module should be modelled accurately in future lightning-related studies.

This study also directly relates to the the third research goal stated in Section 1.5, and its details and results are presented in Chapter 5.

1.6.5 Conclusions

The conclusions drawn from the simulations and experiments performed in Chapter 3, Chapter 4, and Chapter 5, as well as relevant recommendations resulting from these conclusions, are collectively presented in this final chapter, Chapter 6.

Chapter 2

Literature Review

2.1 Chapter Overview

This chapter provides background information relating to all important topics covered throughout the study - including photovoltaics, lightning, technical standards, and previous related research.

Firstly, the PV module as a device is discussed. A brief history of photovoltaics is given, and the operation of a PV cell is explained. The metrics by which the performance of a PV module is characterised are described, and an explanation of the function and importance of the bypass diode is given.

Secondly, the natural phenomenon of lightning is discussed. The formation and discharge mechanics of a thunderstorm are explained, and an overview of the lightning climatology of South Africa is provided. This allows for the development of an understanding of lightning as an electrical process.

Thirdly, the SANS (South African National Standards) standards relating to the design of PV modules, the specification of surge protective devices, the installation requirements for PV power plants, as well as the general lightning protection standard, are reviewed in order to gauge the durability a PV module or installation is expected to possess.

Finally, research relating to the damage of PV modules from the nearby presence of large current impulses is examined. This includes how the internal design of a PV module, as well as the presence of the metal frame, may influence the magnitudes of currents and voltages induced within the module.

2.2 The PV Module

2.2.1 History

The photoelectric effect was first demonstrated by Edmund Becquerel, a 19 year-old French physicist, in 1839. Becquerel was able to produce a voltage by illuminating a metal electrode, submerged in a weak electrolyte solution. [11]

Willoughby Smith, an English electrical engineer, first described the effect of light on the resistance of Selenium rods in 1873 in [12]. Smith was employed by the Gutta Percha Company, where he supervised the laying of underwater telegraph cables between Dover

and Calais. Smith required a method of testing the cables during installation, and determined that a high-resistance semiconductor was required. Selenium, a material known to have a high resistance, was chosen. Initial experiments showed a discrepancy in the measured resistance of bars of selenium. When the cause of the inconsistent resistance measurements, it was discovered that the intensity of light the material was subjected to influenced the measured resistance [12], [13].

William Grylls Adams, a professor at Kings College, and his student, Richard Evans Day, were able to prove that it was feasible to convert solar energy into electrical energy without the use of any thermal or mechanical mechanism. In one set of experiments, a lit candle was placed an inch away from some of the same bars used by Willoughby Smith. The measuring device used reacted immediately to the presence of the lit candle. When the light from the candle was blocked, the measurement quickly fell to zero. Adams and Day concluded that the presence of light causes selenium to produce an electric current. [11]

Charles Edgar Fritts, an American inventor, is credited with the construction of the first "real" photovoltaic (PV) module in 1883. The module was built using a plate of copper with selenium, covered in a thin layer of gold leaf. Fritts noted that the electrical current produced was "continuous, constant, and of considerable force", leading to his speculation that electrical energy produced by a photovoltaic plate may compete with fossil fuel-powered power plants. These early PV modules had efficiencies of approximately 1 % and were not seen as financially viable due to the high costs of selenium and gold. Fritts later sent one of his PV modules to Werner von Siemens. Impressed by the function of the module, von Siemens presented it to the Royal Academy of Prussia. [13]

Albert Einstein, a German theoretical physicist, published a theoretical explanation for the photoelectric effect in 1905. Einstein hypothesised that light contained packets of energy (now known as photons), with light of shorter wavelengths containing more energy than light of longer wavelengths [13]. This hypothesis could be used to explain how energy-carrying photons were able to knock electrons within a photoelectric material from their atomic orbits. If the photoelectric material were to be connected in a circuit, usable electrical energy could be produced. For this work, Einstein was awarded the Nobel Prize in 1923 [11].

Bell Telephone Laboratories unveiled a "solar cell" in 1954. The development of the Bell solar cell was the result of an offshoot from transistor-related research being performed at the time. It had an efficiency of 6%, which was on par with the efficiency of an average gasoline engine of the time. A one square yard area of these cells could produce 50 W of electrical power. [13]

The first commercial PV module became available in 1956. It had an output power of 1 W and cost \$300, putting it beyond the reach of the average consumer. The use of PV modules on satellites appeared in the late 1950s. For implementation in satellites, a low cost was not as important a design objective as durability, size, and efficiency. [13]

A few of the pioneers of photovoltaics mentioned in this section are shown on the following page, in Figure 2.1.

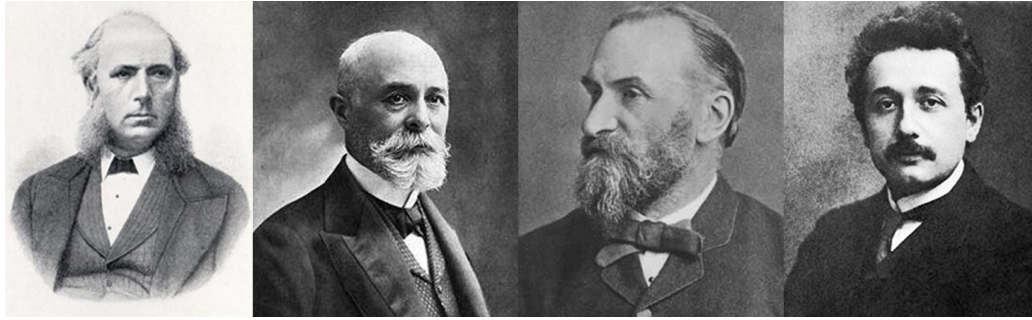


Figure 2.1: From left to right, Willoughby Smith, William Grylls Adams, Charles Edgar Fritts, Albert Einstein [13].

2.2.2 PV Cell Operation

A silicon PV cell has the same fundamental basis as a diode, whereby a PN-junction is established in a silicon crystal. A PN-junction is formed when two semiconductor materials, each containing a different impurity, are placed adjacent to each other within the same silicon crystal. Hole-electron pairs are formed when exposed to sunlight. The positive, or P-type, semiconductor contains excessive "holes", and the negative, or N-type, semiconductor contains excessive movable electrons. Due to the presence of the electric field across the junction, electrons from the N-type region near the junction diffuse into the P-type region. Similarly, holes from the P-type region near the junction diffuse into the N-type region. A difference of potential (a voltage) is present across the junction, creating an electric field. Connection of an external electrical circuit between the positive and negative electrical contacts results in the electrons flowing from the negative contact, through the circuit, and to the positive contact of the PV cell. Electrons recombine with holes when reaching the P-type semiconductor, resulting in the recombination of electrons and holes, and the completion of the circuit. This process is visualised in Figure 2.2. [11]

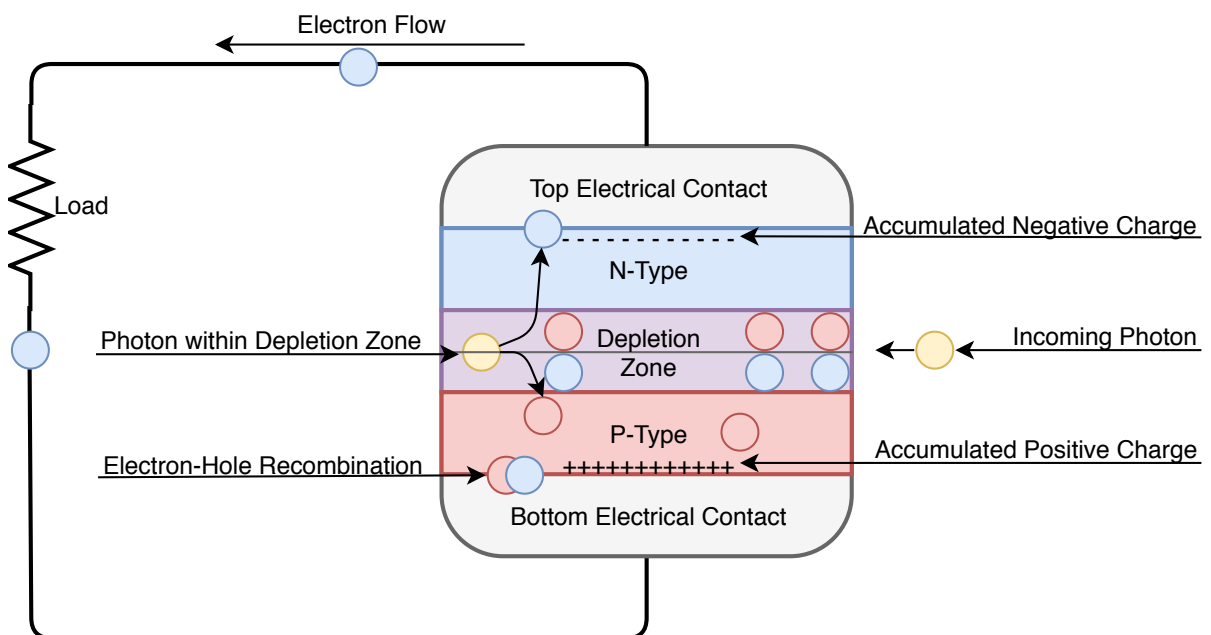


Figure 2.2: The operation of a PV cell [11].

2.2.3 PV Module Performance Specifications

Two fundamental parameters when discussing PV cells are the open-circuit voltage V_{oc} and short-circuit current I_{sc} . Figure 2.3 shows the two configurations for which these parameters are defined.

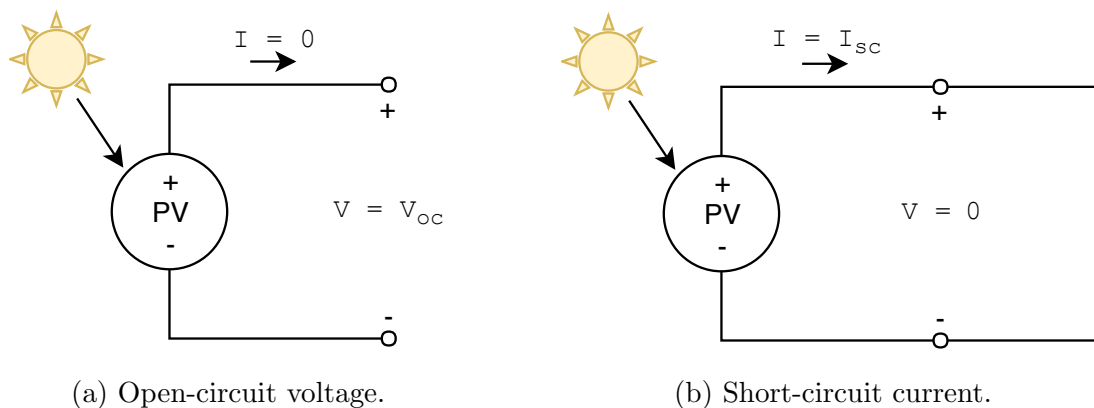


Figure 2.3: Figures illustrating the definitions of open-circuit voltage and short-circuit current [11].

The single-diode model (as shown in Figure 2.4) is a simple equivalent electrical circuit used for modelling a PV cell. The current source produces a current I_1 which is proportional to the intensity of the solar irradiance which falls upon the PV cell. The diode represents the PN junction of the PV cell, and the parallel resistance R_p exists in order to take leakage currents into account. The output voltage of the PV cell is represented by V , and conduction losses are modelled by the series resistance R_s . In the ideal scenario, $R_s = 0\Omega$ and $R_p = \infty\Omega$.

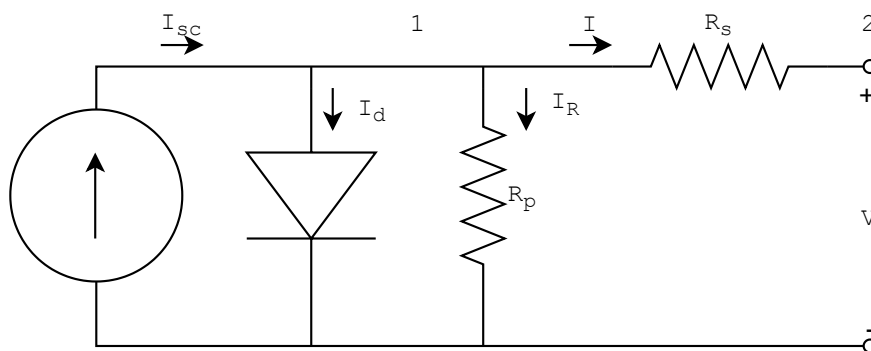


Figure 2.4: The single-diode model for a PV cell [11].

Applying Kirchoff's current law to Node 1 in Figure 2.4 allows for an equation describing the relationship between the voltage and the current (Equation 2.1) at the output of the PV cell to be derived [11].

$$I = I_{sc} - I_d - I_R = I_{sc} - I_s \left(e^{\frac{q(V+IR_s)}{kT}} - 1 \right) - \frac{V + IR_s}{R_p} \quad (2.1)$$

- I_{sc} represents the short-circuit current of the PV cell.
- I_s represents the reverse saturation current of the PN junction.
- k represents Boltzmann's constant (1.381×10^{-23} [J/K]).
- T represents the temperature in Kelvin [K].
- q represents the charge on an electron (1.602×10^{-19} [C]).

Due to the voltage produced by a PV cell being low (about 0.5 V), multiple cells are usually connected together in a PV *module*. Series-connected PV cells or modules are often referred to as a *string*. The BYD 310P6C-36 (shown in Figure 2.5) is a popular PV module, and is made up of 72 series-connected PV cells. Multiple PV modules can be connected in series or parallel in order to produce either a larger voltage or larger current, respectively. Multiple interconnected PV modules are collectively referred to as an *array*. In large installations, it is usually preferable to connect PV modules in series up until the system voltage is reached, and then to connect multiple of these strings in parallel in order to increase the current supplied. This allows for an entire string of modules to be removed without influencing the output voltage of the array, which may be required to remain above a certain threshold for proper operation of the load. Thinner inter-module wiring can also be used as the total current through each string is the same as the current through each module. [11]

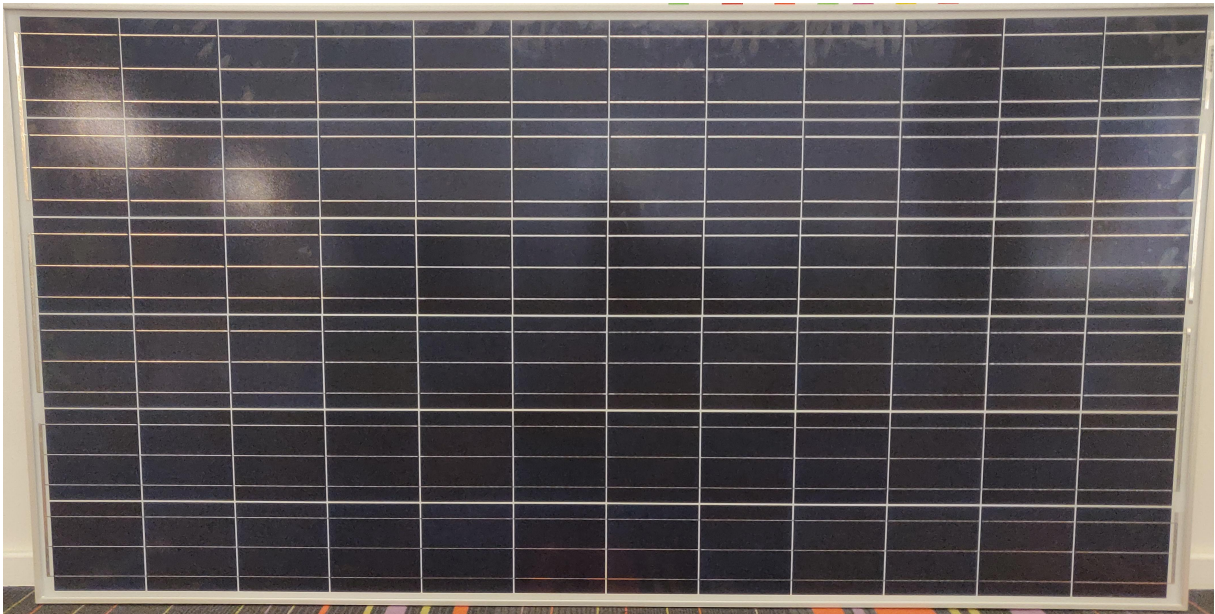


Figure 2.5: The BYD 310P6C-36 PV module.

An I-V curve (as shown in Figure 2.6) is a plot of the current and voltage at the output of a PV cell, module, or array. The maximum power point P_{max} refers to the point at which the device is producing maximum power. Fill factor is a parameter often used to characterize the performance of a PV device. It is defined as the ratio of the maximum power P_{max} to the product of the open-circuit voltage V_{oc} and short-circuit current I_{sc} . [11]

As an example, the I-V curve of a BYD 310P6C-36 is shown in Figure 2.7. As previously mentioned, the current delivered by the current source is directly proportional to the

solar irradiance falling upon the PV module. This relationship is demonstrated in the measured I-V curves shown in Figure 2.7.

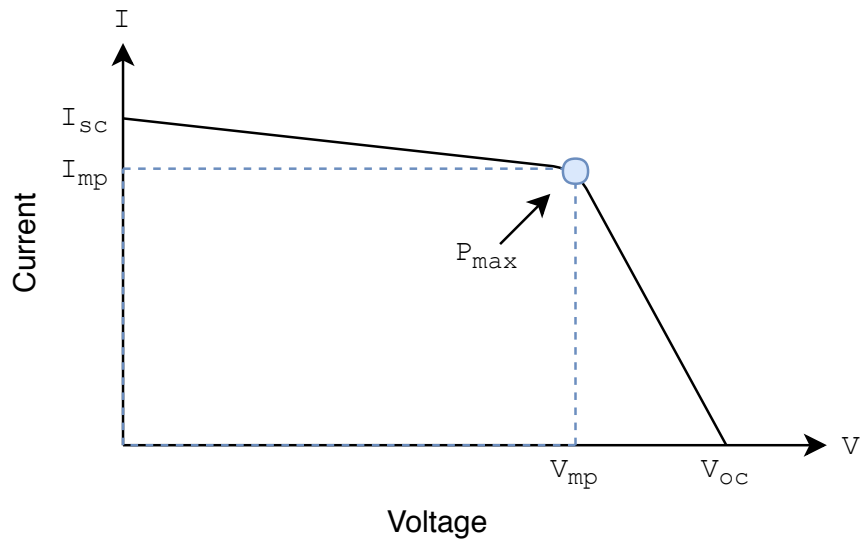


Figure 2.6: An I-V curve [11].

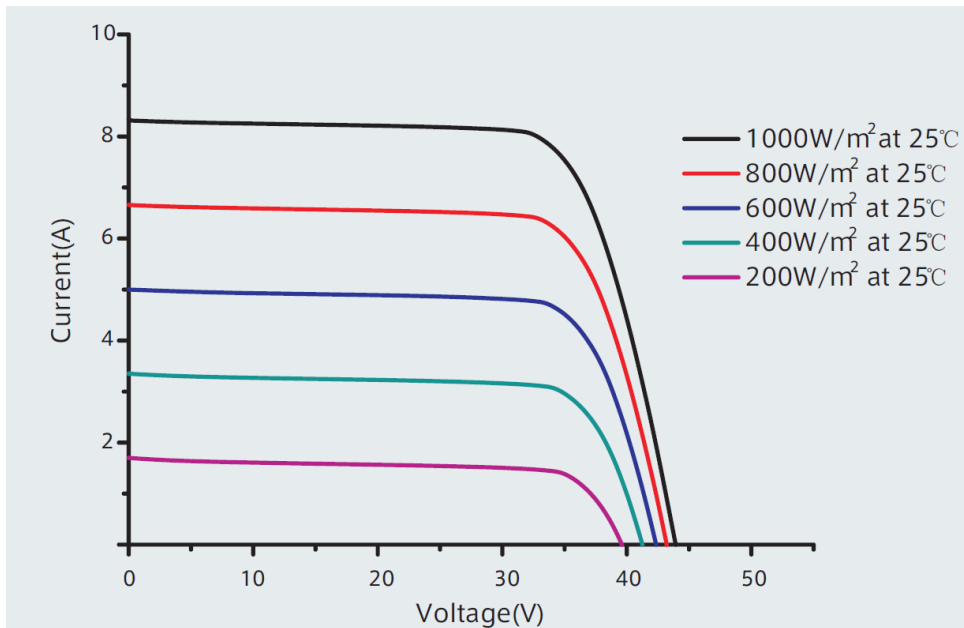


Figure 2.7: I-V curves for a BYD 310P6C-36 PV module for varying irradiance values [2].

2.2.4 The Bypass Diode

Currently, most PV modules make use of monocrystalline or polycrystalline silicon PV cells. When a PV cell is shaded its ability to produce power is reduced to zero. With reference to the single-diode model shown in Figure 2.4, the current provided by the current source becomes zero when the PV cell is shaded. Since PV cells within a PV module are often series-connected, the current through all PV cells is identical.

The current in the shaded cell flows through resistor R_p . The voltage drop over resistor R_p causes the diode to be reverse-biased, therefore the current through the diode is generally negligible (unless the diode is sufficiently reverse-biased to cause avalanche breakdown).

The power dissipated in the resistor R_p and the diode cause what is known as the *hot spot phenomenon*, whereby the PV cell begins heating up. PV cells have a *critical power dissipation* P_c , which if exceeded may result in the destruction of the cell. Manufacturers often define a breakdown voltage V_c , which is dependent on the PV technology and manufacturing process used. The voltage drop over a shaded cell reduces the total string voltage. From a power production perspective, it would therefore be more beneficial to remove the shaded cell from the string than to have it negatively impacting the total power produced [11], [14].

A bypass diode is an extra diode placed in parallel with a PV cell or string of cells, as shown in Figure 2.8. During normal operation the bypass diode is reverse biased. When the PV cell (or string of cells) is shaded, the bypass diode is forward biased, and therefore provides an alternative path for the current originating from the unshaded PV cells to flow through. Ideally, a bypass diode would be placed in parallel with each cell in a PV module, however due to cost limitations this is generally not the case. A compromise is usually made by placing a bypass diode over multiple cells.

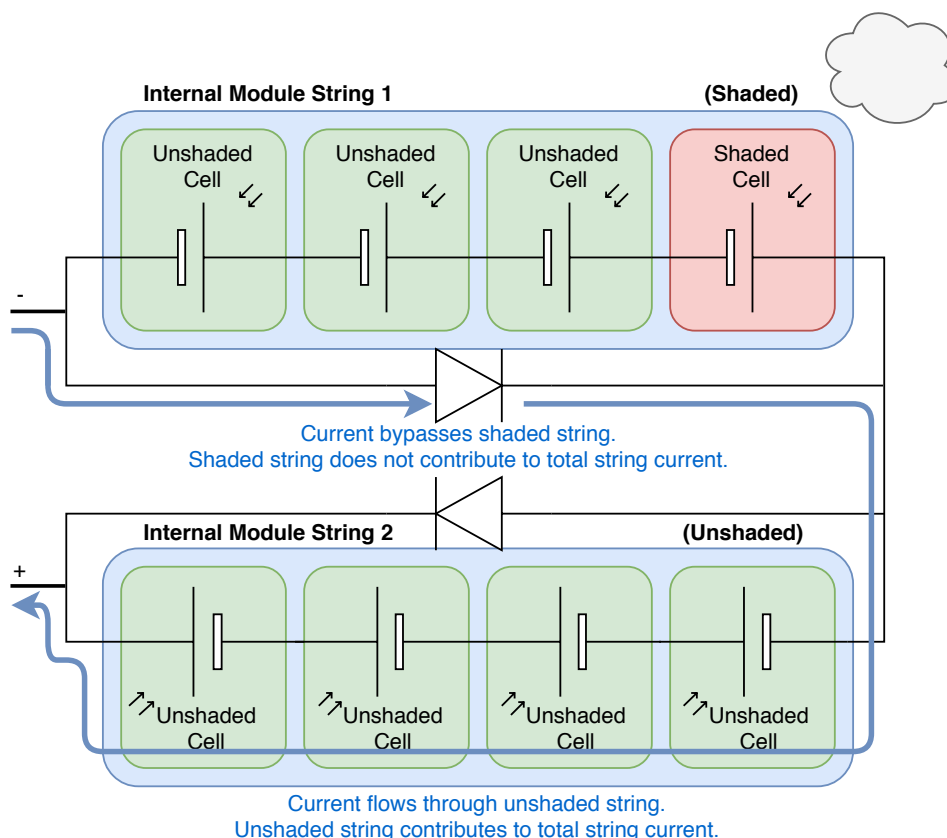


Figure 2.8: A bypass diode functioning to mitigate the effects of shading [9].

When choosing a bypass diode, the first parameter to consider is the maximum repetitive reverse voltage V_{rrm} . The maximum repetitive reverse voltage is required to be greater than the maximum voltage produced by the PV cell (or string of cells) across which it is

connected in order to prevent avalanche breakdown of the bypass diode, resulting in that PV cell (or string of cells) not producing any output power. [14]

The second parameter to consider is the forward voltage V_f of the diode. The forward voltage is required to be lower than the breakdown voltage V_c of the shaded PV cell. When placed over a string of cells, the bypass diode is required to conduct current when one cell is shaded. Schottky diodes are often chosen as bypass diodes due to their low forward voltages. A lower forward voltage also results in lower conduction losses within the diode. [14]

Bypass diodes are usually housed in a container at the rear of the PV module called the *junction box*. Some manufacturers seal the junction box in order to prevent corrosion, making access to the the bypass diodes difficult. Figure 2.9 shows the bypass diodes placed within an accessible junction box.



Figure 2.9: The inside of the junction box of a BYD 310P6C-36 PV module, showing the connections of the three bypass diodes.

Now that an understanding of the operation of a PV module had been developed, it was decided to perform an investigation into the physics behind lightning, as well as the prevalence of lightning in South Africa, in order to determine the real-world environment that a PV installation may be subjected to. Processes such as cloud formation, electrification, charge separation, and the manners in which a cloud may discharge had to be understood in order to be modelled correctly.

2.3 Lightning

This section provides an overview of lightning as a natural phenomenon, both in general and in a South African context.

2.3.1 Formation and Discharge Mechanics

This section covers the mechanisms by which a thundercloud may form, become electrified, and electrically discharge in the form of a lightning stroke.

2.3.1.1 The Formation of Storm Cells

Lightning results from the formation of convective storm cells. There are three main mechanisms of importance in the formation of thunderstorms - instability, moisture, and a triggering mechanism. [15]

In an unstable atmosphere, convection causes warmer pockets of air to rise due to their lower density than the surrounding air. These warm pockets contain moisture, and expand as they rise due to the lowered atmospheric pressure. As these pockets expand they begin to cool. Many warm pockets of rising air result in the formation of updrafts or *thermals*, which are able to extend to impressive altitudes. [3]

If the air within the thermals cools to dew-point temperature, water droplets begin to form and latent heat is released in the process. The airborne water droplets form cumulus clouds, and the latent heat released stimulates the upward growth of the cloud. [3]

With a constant supply of moist air and the continued upward development of the cumulus cloud, the size of the water droplets increases. If a droplet grows too large for its weight to be sustained in the upper regions of the cloud then it will begin to fall, often leaving the cloud in the form of precipitation. A downward airflow termed a *downdraft* is formed when many of these larger droplets begin to fall within the cloud. [3]

As the cloud extends further upwards, it passes the *freezing level*. The freezing level is the lowest altitude in an area at which the air temperature is 0 °C - the freezing point of water. As a result, a phase separation occurs within the cloud. The lower regions of the cloud are largely comprised of water droplets, the middle region is largely comprised of water and ice particles (for this reason, it is often termed the *mixed phase layer*), and the upper regions are largely comprised of ice crystals and hailstones. [3]

2.3.1.2 Electrification of the Cloud

It is commonly accepted that the electrification of the cloud is a result of the interactions between the water and ice particles within the mixed phase layer [16, 17]. The *Ice-Graupel Mechanism*, as first suggested in [18], is the most probable manner in which charge generation, and therefore electrification, may occur within a cloud.

The ice-graupel mechanism suggests that electrical charge within a cloud is produced by collisions between precipitation particles (usually water droplets or soft ice particles known

as graupels) and cloud particles (usually ice crystals) in the presence of supercooled water droplets. Fall speed is used to differentiate precipitation particles from cloud particles. Precipitation particles have a fall speed of over 0.3 m s^{-1} , while cloud particles have a fall speed of under this threshold. Due to this association with fall speed, precipitation particles fall downward, while cloud particles either rise upward in thermals or remain suspended. A charge transfer between particles occurs during these collisions, resulting in particles becoming negatively or positively charged [18], [19].

It was suggested in [16], [19], [20], and [21] that, for a fixed effective liquid water content (ELWC), the polarity of the charge transfer became increasingly negative with lowered temperature. The change from positive to negative charge occurred around a critical temperature, termed the *reversal temperature*. It was claimed in [21] that with increased ELWC came decreased reversal temperature.

It was shown in [20] that the reversal temperature was also a function of the size of the precipitation and cloud particles, with particles smaller than $10 \mu\text{m}$ possibly having more than one reversal temperature, and particles smaller than $4 \mu\text{m}$ possibly having up to four reversal temperatures.

The surfaces of ice crystals have a tendency to gather water and vapour (a process termed *riming*). The general consensus is that a faster growing ice particle will acquire a more positive charge [16]. The level of water saturation within a cloud therefore has a linked effect on the electrification of the cloud [21].

The velocity of updrafts with the cloud is another factor which influences the electrification of the cloud. A continental thundercloud is more likely to produce an increased number of lightning strokes when compared with a maritime thundercloud. The theory which explains this occurrence is based on the observation that continental thunderclouds often have higher updraft speeds than maritime thunderclouds. Faster updrafts tend to result in the increased formation of ice particles in the upper regions of the cloud, resulting in an increased frequency of collisions between cloud and precipitation particles, leading to the increased generation of charged particles within the cloud [22].

2.3.1.3 Charge Separation within the Cloud

The bipolar model of a thunder cloud, known as the *dipole electrification structure*, was first proposed in [17] in 1963. Negative field changes were observed when a cloud was far away, and positive field changes were observed when it was closer. This information was used to deduce that a cloud has a bipolar charge separation, with a negatively charged region lower than a positively charged. It was proposed that these oppositely charged regions do not necessarily have to be exactly stacked upon each other, and that there was a possibility of a small region of positive charge situated at the bottom of the cloud. This charge distribution is shown in Figure 2.10.

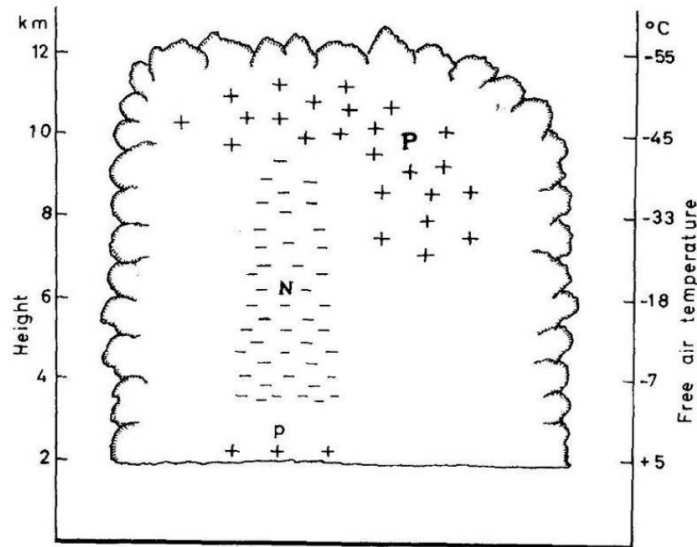


Figure 2.10: The original dipole electrification structure for a thundercloud, as proposed in [17].

The dipole electrification structure was expanded on in [23], where it was mentioned that lightning flashes originating below 7.43 km were far more prevalent than those originating above 7.43 km. It was also noted in [23] that lightning flashes tended to originate lower in the cloud during the earlier phases of the development of the cloud, while in later phases the lightning flashes emerged from further up. The author of [23] was able to establish the polarity of 165 out of 214 lightning flashes; only one flash had a positive polarity.

The dipole electrification structure was further expanded on in [24]. It was shown in [24] that the positive region in the cloud is often found at an altitude of around 12 km above the ground and has a temperature of around -25°C . The negatively charged middle region in the cloud is often found at about 7 km and has a temperature of around -10°C . If the positively charged lower region is present, it is usually found at an altitude of around 2 km [24].

2.3.1.4 Electrical Discharge of the Cloud

Electrical discharges between regions of opposing electrical charge can occur within a cloud (intra-cloud lightning) or between another nearby cloud (inter-cloud lightning) [16]. These discharges are common during the formation of the thunderstorm, and often act as a harbinger to cloud-to-ground lightning [3].

A detailed theory of the mechanism by which cloud-to-ground lightning may occur was proposed by [17]. In this theory, it is postulated that a strong electric field is produced between the large negatively charged regions within the cloud and the earth. Objects on the earth expel positively charged particles in the form of corona, with taller objects producing higher corona. The positively charged particles are moved upwards due to the movement of air moving in the direction of the cloud - the electric field does also contribute to this movement, but to a lesser extent. The distribution of these positively charged particles is therefore largely influenced by the wind, and it is this distribution which determines the course a cloud-to-ground discharge will take. [17]

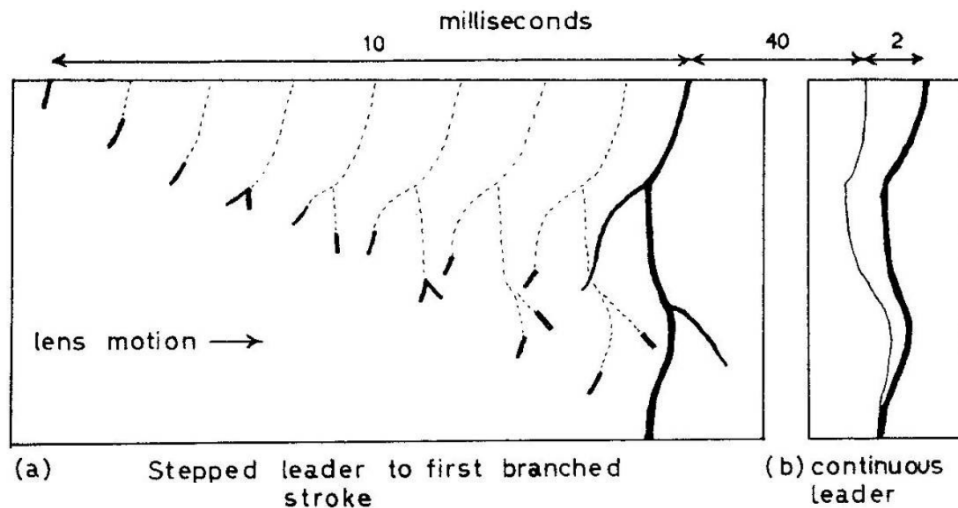


Figure 2.11: The stages leading up to a cloud-to-ground discharge [17].

Due to the presence of the negatively charge region in the cloud, a *leader stroke* begins to form in a downward direction, moving through the regions of positively charged particles, in an attempt to reach earth. The distribution of the regions of positively charged particles influences the path taken by the leader stroke. A leader stroke may split up and begin taking multiple paths (known as branches) in the presence of multiple regions of equal positive charge below it. This owes to the often unpredictable nature of the leader stroke, often appearing as a "stepping" motion during moments where it appears to hesitate. As a result, leader strokes are also known as *stepped leaders*. This process is illustrated in Figure 2.11. A channel is formed between the tips of the leader stroke and the negatively charged centre of the cloud. [17]

When a tip of the leader stroke is near to the ground, a positive discharge known as an *upward leader* forms. This upward leader meets the nearby tip of the leader stroke, forming a ionized channel between the cloud and the ground. The branch which makes contact with the ground first is known as the *main channel*. At the moment at which the main channel is established, a luminous return stroke carrying positive charge is formed in order to equalise the negative charge within the channel. The diameter of a leader stroke can be 1-10 m, while average diameter of a return stroke is around 16 cm. Average currents in a leader stroke are about 300 A, while a return stroke may have currents 1-3 orders of magnitude greater than this. A *lightning stroke* is composed of both a leader stroke and a return stroke. [17]

After the neutralization of the channel by the return stroke, the channel often conducts smaller strokes (if there is sufficient negative charge in the cloud), remaining luminous as it does so. Due to the existence of the channel, subsequent strokes are less ragged in appearance since the formation of a new path to ground is not necessary. These subsequent discharges are referred to as *dart leaders*, and occur usually 40-50 ms apart. A *lightning flash* is a collection of multiple lightning strokes. If a duration of 100 ms passes, it is unlikely that the channel will have sufficient conductivity for subsequent dart leaders, resulting in the end of the flash. [17]

In the case that the channel remains open and a large region of negative charge is rapidly reformed in the cloud after the first return stroke, a *long stroke* (often at least 40 ms in

duration) may occur. Long strokes rarely occur as either a single stroke, or the first stroke within a flash, as they mostly make use of a channel which is already formed. [25]

Positive polarity lightning strokes (strokes which deliver positively charged particles to ground) are less common than negative polarity lightning strokes, although they are often more damaging. It is possible for positively charged regions in a cloud to be positioned alongside negatively charged regions. It was noted in [17] that positively charged regions in the upper reaches of a cloud also had a tendency to move more slowly than negatively charged regions, resulting in the rear of a moving cloud having a net positive charge.

It was noted in [26] that positive polarity lightning strokes dissipated the most energy to ground either during the dissolution of the thunderstorm (once the previously negatively charged regions had been mostly neutralized by negative polarity lightning), or when the thunderstorm was fully developed with high internal wind shear, or during colder seasons. In all cases, a positively charged region exists in the lower reaches of the cloud. Unlike negative leader strokes, positive leader strokes do not exhibit a stepped path to ground, but rather follow a more direct path. As a result, positive lightning strokes often continue to conduct for longer durations, dissipating more energy to ground per stroke.

2.3.2 Lightning in a South African Context

In the years before the installation of advanced lightning detection equipment, it was difficult to gather data relating to the incidence of lightning flashes in South Africa. Thunder is the sound produced by the rapid expansion of gasses during a lightning discharge. The number of *thunderstorm days*, defined in [16] as "a local calendar day during which thunder is heard at least once at a given location", was used to provide an estimate of the level of lightning activity in an area. Figure 2.12 shows a plot from the South African Weather Service (SAWS) of the mean number of thunderstorm days recorded in South Africa for the interval between 1961 and 1990.

As technology developed, satellites began to be utilized for the recording of lightning distribution data. The Lightning Imaging Sensor (LIS), installed in the NASA Earth Observing System (EOS) as part of the Tropical Rainfall Measuring Mission (TRMM), is able to detect cloud-to-ground, inter-cloud, and intra-cloud lightning discharges [3].

Figure 2.13 shows the global annual lightning flash density, as recorded by the LIS. South Africa appears to have a varying lightning flash density distribution (from as low as 4 flashes per square kilometre to as high as 30 flashes per square kilometre). The distribution shown in Figure 2.13 appears to agree with the distribution shown in Figure 2.12.

The South African Lightning Detection Network (SALDN) was installed in 2005. It is a state-of-the-art ground-based system, one of only three ground-based lightning detection networks in the Southern Hemisphere (the other two being in Australia and Brazil). The original network was made up of 19 sensors (the locations of which are shown in Figure 2.14), but has since been expanded to 24 sensors. It is able to detect 90% of cloud-to-ground lightning over South Africa. The SALDN is capable of detecting individual lightning strokes within a lightning flash. [3]

Average Number of Thunder Days in South Africa (1961-1990)

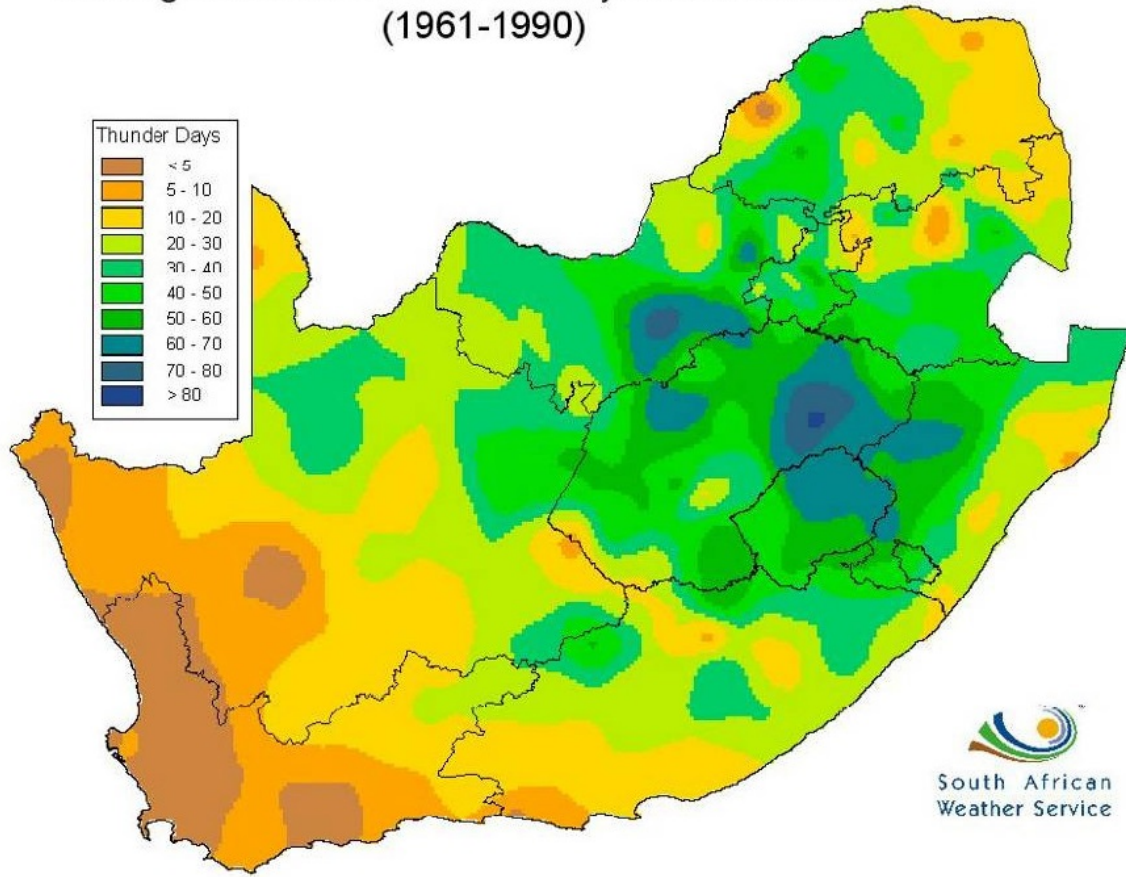


Figure 2.12: South African mean number of thunder days per year for the interval between 1961 and 1990, as provided by the SAWS. [3].

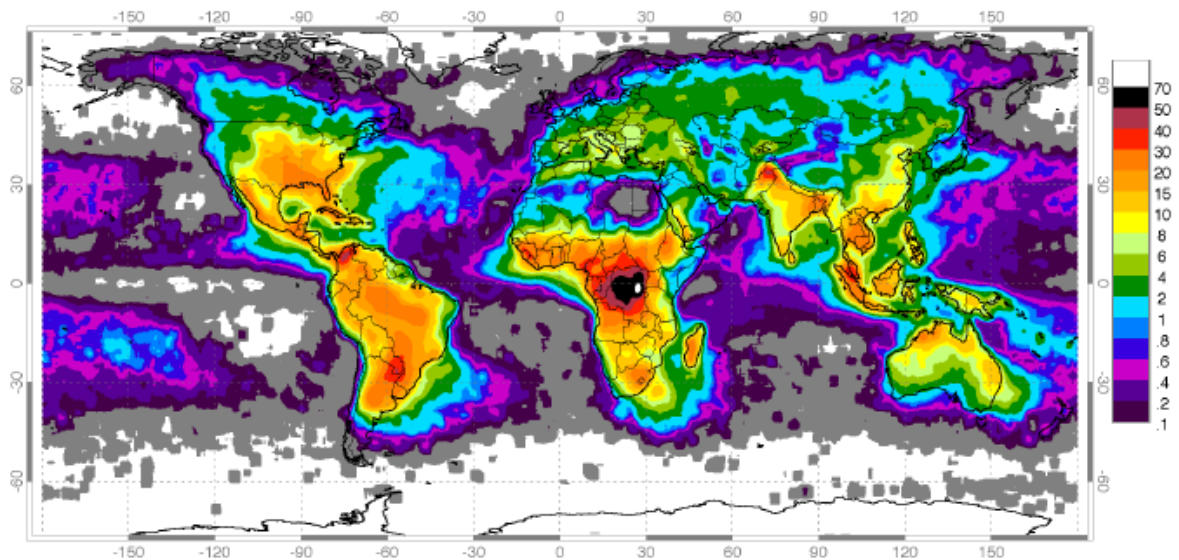


Figure 2.13: Global annual lightning flash density, detected by the LIS. [3].

Either lightning flash or lightning stroke data can be requested from the SAWS. Lightning flash data indicates the date and time of the flash, the latitude and longitude, the peak

current recorded, the multiplicity of the flash, and the number of sensors taking part in the reading.

The installation of the SALDN allowed far more complex studies into the lightning climatology of South Africa to be performed. The availability of accurate lightning stroke data allowed for the author of [3] to plot distributions for the lightning ground flash density, median peak current, and ground flash multiplicity.

SAWS LIGHTNING DETECTION NETWORK

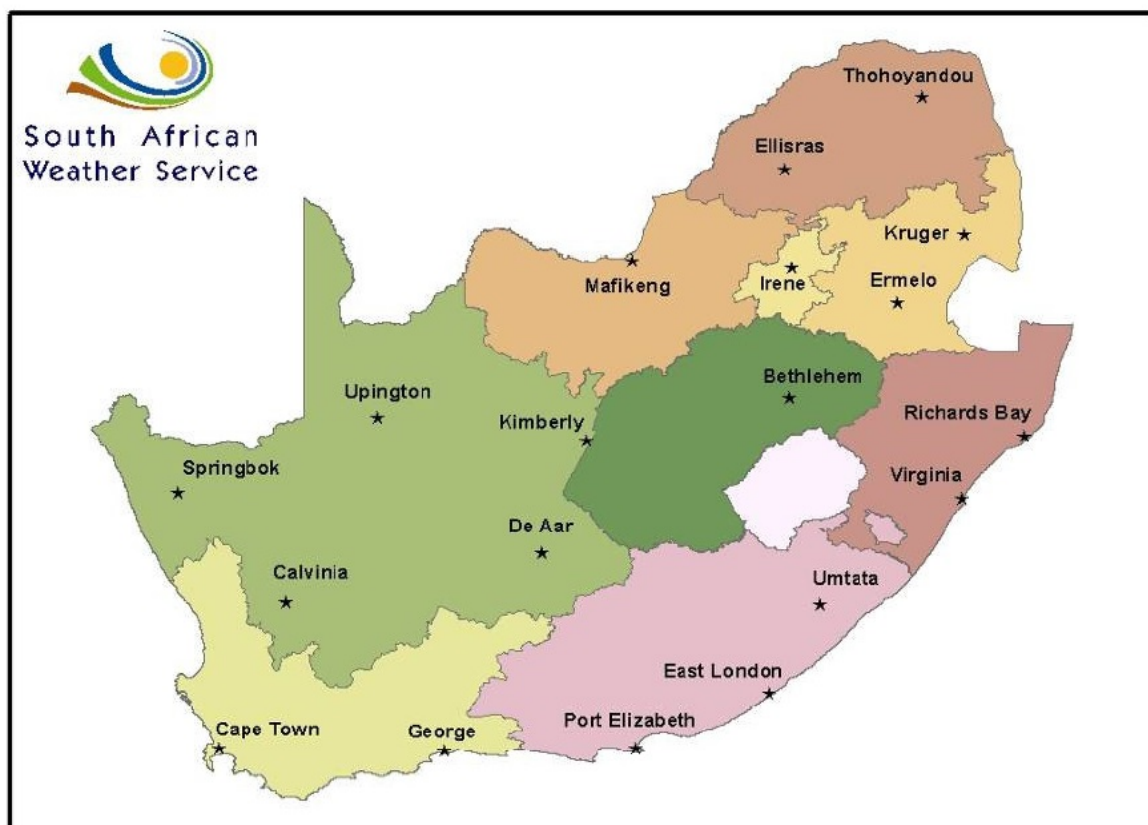


Figure 2.14: The locations of the sensors which make up the South African Lightning Detection Network [3].

The 2006 ground flash density and ground flash multiplicity distributions (shown in Figures 2.15 and 2.16, respectively) are similarly located across South Africa. Most of South Africa experiences ground flash densities of 5-10 flashes per square kilometer, with an average flash multiplicity of 2-2.5. The highest ground flash density is experienced near the border of the Mpumalanga and KwaZulu-Natal provinces, while the highest ground flash multiplicities are mostly located south of this border, in the centre of the KwaZulu-Natal province.

The 2006 median peak current distribution is shown in Figure 2.17. Most of the median peak currents recorded are between 1-15 kA, however there is a band that runs through the the country in a north-westerly to south-easterly direction through parts of the Northern Cape and Eastern Cape provinces where median peak currents of 15-20 kA were recorded. The locations of the three utility-scale PV power plants considered in Section 1.3 are

within this band, therefore the distribution shown in Figure 2.17 correlates with the magnitudes of the median peak currents of approximately 15 kA shown in Figure 1.5.

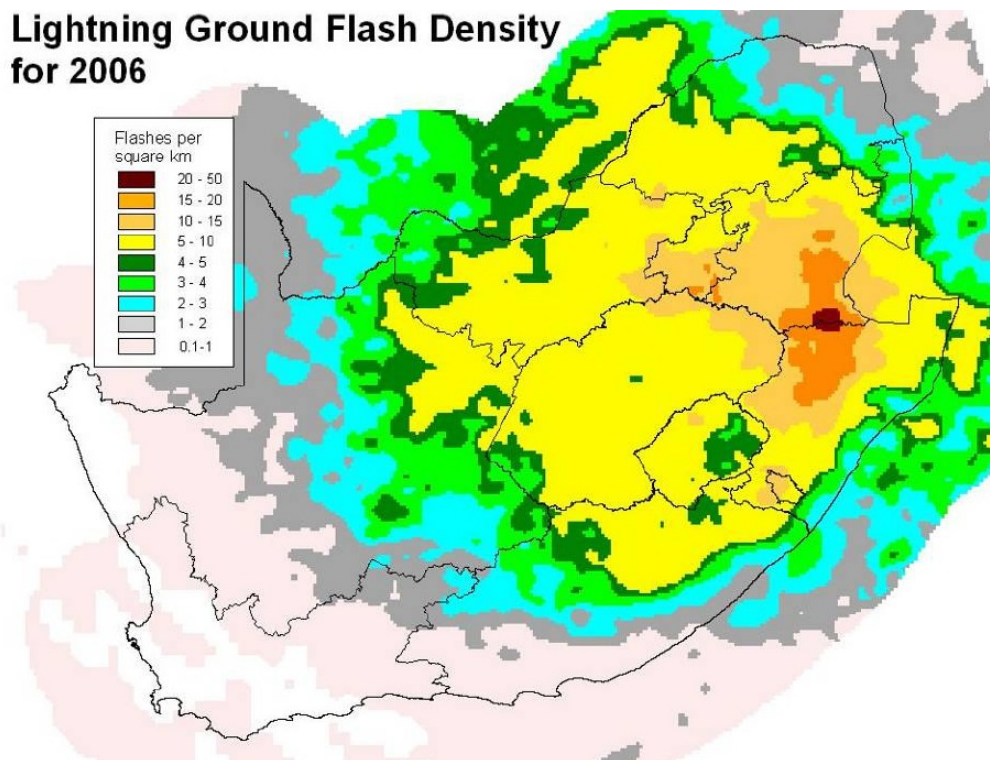


Figure 2.15: The 2006 ground flash density distribution for South Africa [3].

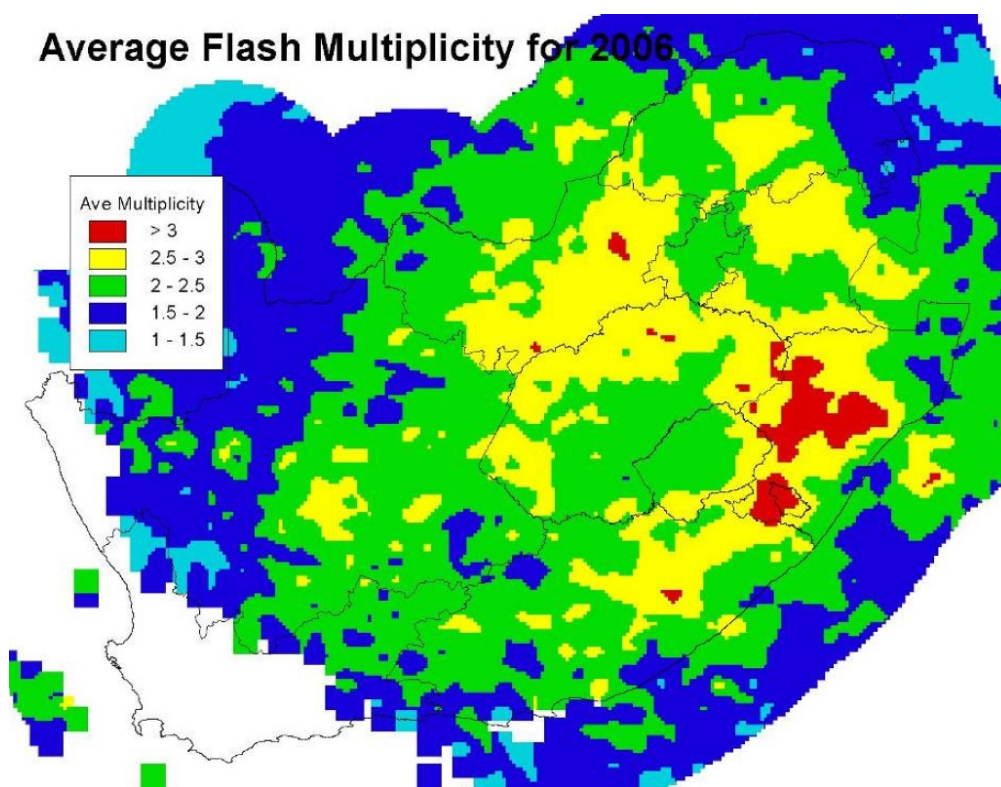


Figure 2.16: The 2006 ground flash multiplicity distribution for South Africa [3].

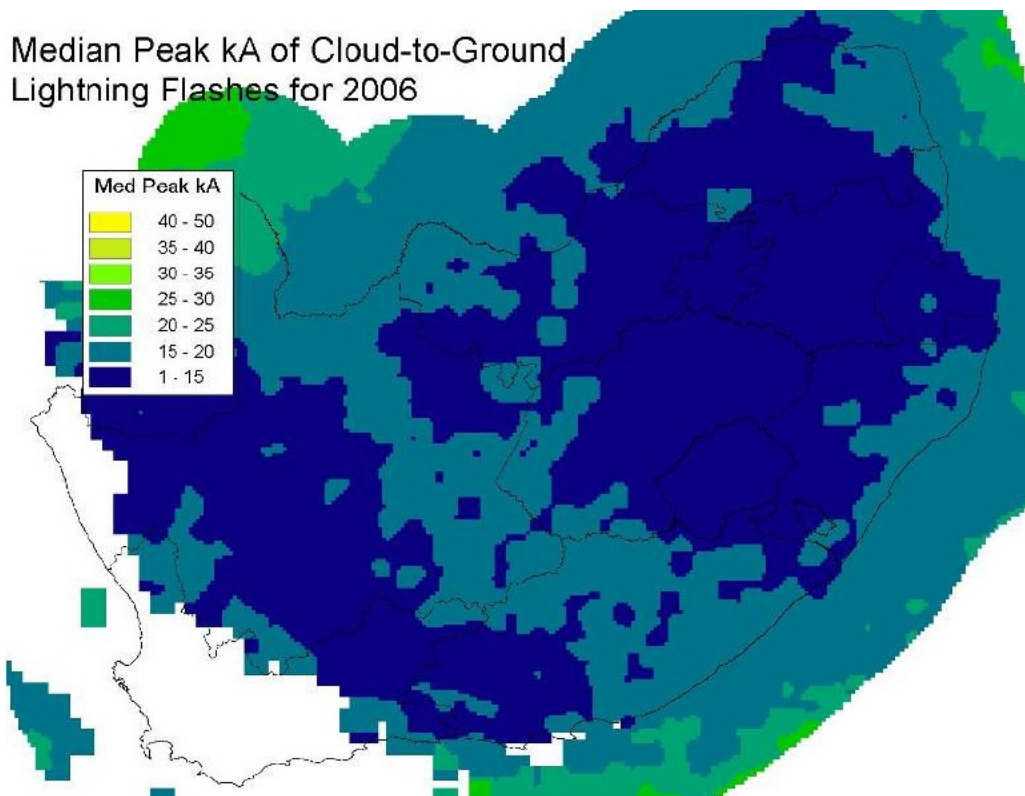


Figure 2.17: The 2006 median peak current distribution for South Africa [3].

In Figure 2.15, Figure 2.16, and Figure 2.17, it is clearly shown that the western coast of South Africa experiences little-to-no lightning activity when compared with the rest of the country.

In order to identify areas in South Africa which could potentially suffer damage as a result of lightning activity, the author of [3] proposed three lightning risk indexes. Each of these lightning risk indexes make use of five classification categories, as shown in Table 2.1.

Table 2.1: The classification categories for lightning risk, as proposed by [3].

Category	Score
Almost Risk Free	0.0-0.2
Minimal Risk	0.2-0.4
Moderate Risk	0.4-0.6
Severe Risk	0.6-0.8
Extreme Risk	0.8-1.0

The first lightning risk index is the Lightning Intensity Risk Index (LIRI). It takes overall ground flash density, median peak current, and average flash multiplicity into account, with the goal of identifying areas where a large number of flashes occur, and where these flashes consist of many strokes. These areas would therefore experience the discharging of substantial energy to ground. The 2006 LIRI for South Africa is shown in Figure 2.18; it indicates that most of the country is at a moderate to severe risk on the lightning intensity scale [3].

Lightning Intensity Risk for 2006

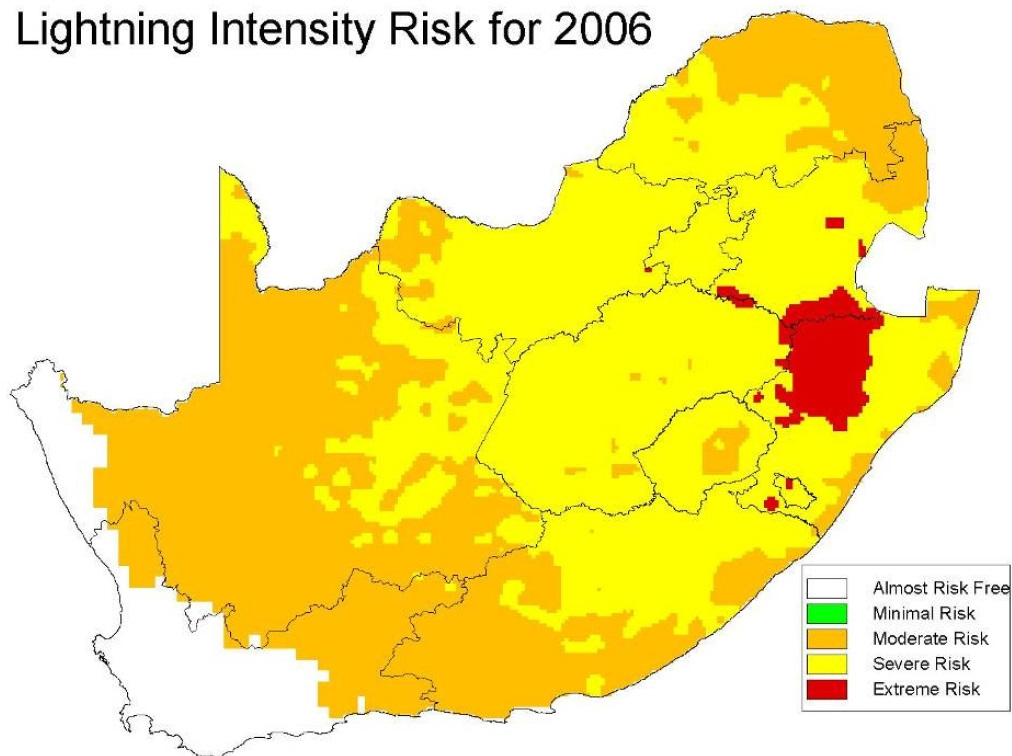


Figure 2.18: The 2006 Lightning Intensity Risk Index for South Africa [3].

The second lightning risk index is the Positive Lightning Risk Index (PLRI). It takes the ground flash density, the median peak current, and the average flash multiplicity of positive polarity lightning, as well as the proportion of positive polarity lightning, into account. The author of [3] motivated that positive polarity lightning should be considered as a separate index as it results in the highest fire risk. This is due to the notion that in positive polarity cases where the flash multiplicity is greater than one, the initial stroke has a high peak current and the subsequent stroke has continuing current (a long stroke). This combination of strokes can often lead to the ignition of fires. The 2006 PLRI for South Africa is shown in Figure 2.19; it indicates that most of the country is at a severe or extreme risk to positive lightning flashes [3].

The third lightning risk index is the Total Lightning Risk Index (TLRI). It is derived from the equally-weighted sum of the LIRI and PLRI, and then scaled from 0 to 1, and makes use of the same classification categories mentioned in Table 2.1. The TLRI aims to provide a single indication of the total lightning risk for any area in South Africa. The 2006 TLRI for South Africa shows that most of the country is at severe risk to lightning. Parts of north-western KwaZulu-Natal, southern Mpumalanga, northern Eastern Cape, western Free State, and southern North-West provinces have large areas which are at an extreme risk to lightning. The western coast of South Africa is almost risk free as far as lightning is concerned [3].

The high lightning risks discussed in this chapter further support the notion that lightning is a very real risk in South Africa, and that appropriate steps should be taken to ensure the safety of life and property.

Positive Lightning Risk for 2006

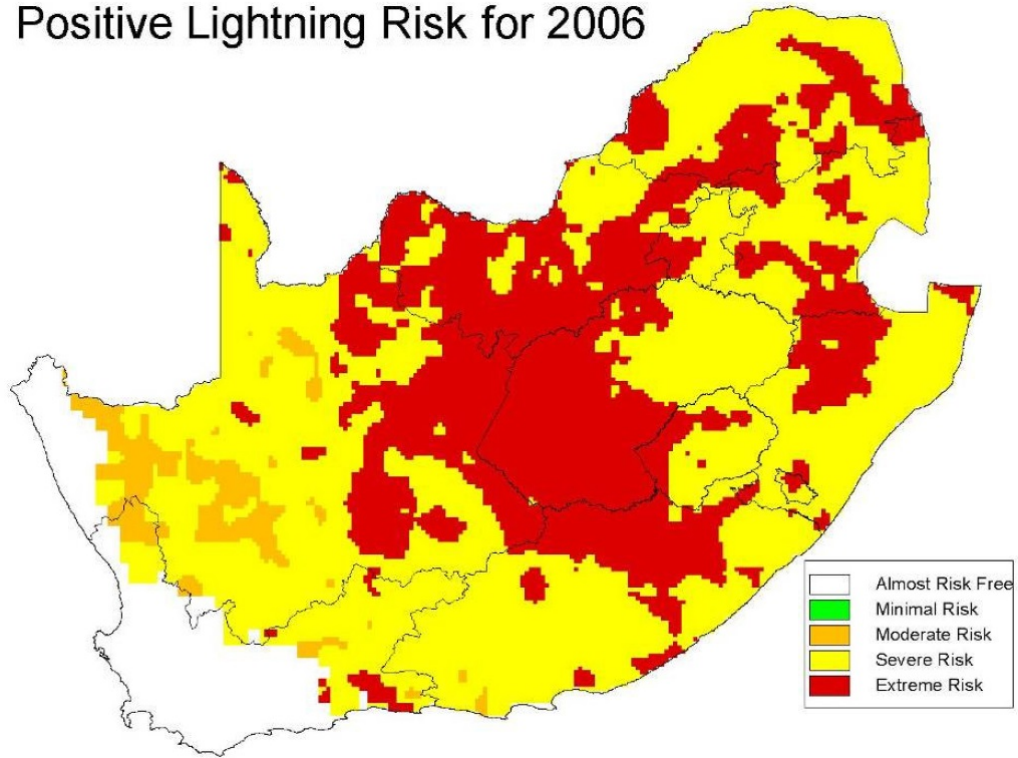


Figure 2.19: The 2006 Positive Lightning Risk Index for South Africa [3].

Total Lightning Risk for 2006

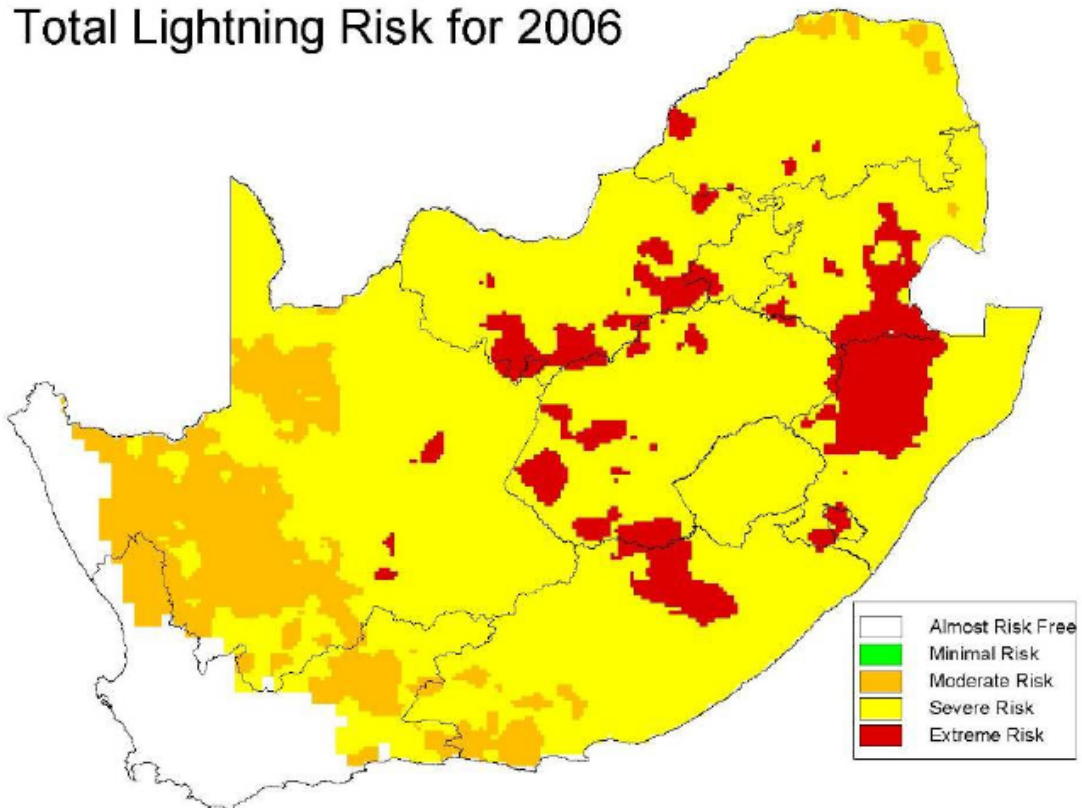


Figure 2.20: The 2006 Total Lightning Risk for South Africa [3].

2.4 Applicable Standards

This section reviews standards relating to the design of PV modules, as well as when and how lightning protection measures should be implemented. This analysis was done in order to understand the guidelines in place which are designed to assist both the manufacturers and installers of photovoltaic modules to ensure that their product is adequately up to standard for the intended purpose.

2.4.1 SANS 61215:2015

The IEC standard 61215:2005 is adopted in South Africa as [27] for the design qualification and type approval of crystalline silicon terrestrial PV modules. In this standard, many tests relating to the conditions which a PV module are expected to operate in are described - tests such as thermal cycling, hail test, maximum power determination, among others.

2.4.1.1 Insulation Test

There are no tests described in [27] designed to assess the ability of a PV module to withstand the effects of direct or indirect lightning activity. The *insulation test* is the closest to a test of this kind. It is the third test described in [27], and its purpose is "to determine whether or not a module is sufficiently well-insulated between current-carrying paths and the frame or the outside world."

The procedure for this test is as follows:

1. The output terminals of the PV module are short-circuited and attached to the positive terminal of a current-limited DC insulation tester.
2. The negative terminal of the insulation tester is connected to an exposed metal part of the PV module. If no exposed metal part exists, then a conductive foil is wrapped around the edges and over the back of the module. The foil is then connected to the negative terminal of the insulation tester.
3. The output voltage of the insulation tester is increased at a rate slower than 500 V/s until a voltage of 1000 V plus twice the maximum system voltage is reached. If the maximum system voltage is less than 50 V then a total voltage of 500 V must be applied. The voltage should be maintained for one minute.
4. The applied voltage is reduced to zero, and the output terminals of the insulation tester are short-circuited in order to discharge any voltage build-up in the module.
5. The short-circuit between the output terminals of the insulation tester is removed.
6. The output voltage of the insulation tester is increased at a rate slower than 500 V/s until a voltage of 500 V, or the maximum system voltage, is reached (whichever is higher). This voltage should be maintained for two minutes.
7. As before, the applied voltage is reduced to zero, and the output terminals of the insulation tester are short-circuited.
8. The short-circuit and test equipment are removed from the PV module.

In order to pass the test, the following is required:

- No dielectric breakdown or insulation breakdown (known as *surface tracking*) may occur in step 3 of the test.
- The insulation resistance for PV modules of area less than 0.1 m^2 may not be less than $400 \text{ M}\Omega$.
- For modules of area larger than 0.1 m^2 , the product of the module area and the measured insulation resistance must not be lower than $40 \text{ M}\Omega\text{m}^2$.

Although not specifically designed for lightning, this test gives an indication of the voltage levels which a PV module is expected to handle between its conducting paths and any nearby metallic parts (including the frame).

2.4.1.2 Bypass Diode Thermal Test

The only test described in [27] addressing the specification of bypass diodes for crystalline PV modules is the *bypass diode thermal test*. This is the final test described in [27], and its purpose is "to assess the adequacy of the thermal design and relative long-term reliability of the by-pass diodes used to limit the detrimental effects of module hot-spot susceptibility".

The procedure for this test is as follows:

1. Short-circuit any blocking diodes fitted to the module.
2. Determine the short-circuit current of the module, either from its label or from its datasheet.
3. Connect wiring of the minimum recommended gauge (as specified by the manufacturer) to the output terminals of the module.
4. Heat the module to $75 \text{ }^\circ\text{C} \pm 5 \text{ }^\circ\text{C}$ and apply a current equivalent to the short-circuit current under standard test conditions (STC) $\pm 2 \%$.
5. Measure the temperature, the voltage over, and the current through each bypass diode after a duration of one hour. Using the manufacturer-provided documentation, calculate the junction temperature of each diode.
6. Increase the applied current to 1.25 times the short-circuit current of the module at STC.
7. After one hour, verify that the diode is still operational.

The module is then given a visual inspection, followed by a test of the maximum power output and an insulation test. As this is the last test described in the standard, these tests would already have to have been performed, therefore a baseline for them would have been established.

In order to pass the test, the following is required:

- The diode junction temperature must not exceed the maximum diode junction temperature as specified by the manufacturer.
- No major visual defects may be present.
- The module should still pass any required insulation tests in order to ensure that current carrying sections of the module remain sufficiently insulated from the outside world.
- The degradation of the maximum output power must not exceed 5% of the value measured before the test.
- The diode must still function as a diode after the test.

This test does not relate in any way to the ability of a bypass diode to cope with the transients it may be exposed to during the lifetime of the PV module. This shortfall in the standard leaves possible room for improvement. Recommendations or specifications for bypass diode protection measures should be added for instances where PV modules are expected to operate in regions where there is a high likelihood of exposure of a PV installation to the effects of nearby lightning strikes.

2.4.2 SANS 62305:2011

SANS standard 62305:2011, which is the identical adoption of IEC standard 62305:2010, is designed to act as a generic lightning protection guideline. It is divided into four parts, each approaching a different aspect of lightning protection.

2.4.2.1 SANS 62305-1:2011

Part one of SANS 62305, [28], serves as an introductory part which details the general principles and definitions used when discussing lightning protection measures.

Firstly, the following important definitions are covered in [28].

A *lightning flash to earth* is defined as an "electrical discharge of atmospheric origin between cloud and earth consisting of one or more strokes" [28].

A lightning flash may be either downward or upward in direction. A *downward flash* is a "lightning flash initiated by a downward leader from cloud to earth", while an *upward flash* is a "lightning flash initiated by an upward leader from an earthed structure to cloud". A downward flash is usually made up of an initial impulse, which could possibly be followed by successive impulses. A few impulses may be followed by a long stroke [28].

A lightning flash may be made up of multiple strokes, often 3-4 in number and with an interval of around 50 ms between them. A *lightning stroke* is a "single electrical discharge in a lightning flash to earth". A *short stroke* is the "part of a lightning flash which corresponds to an impulse current" (a current with a time to half the peak value on the tail of the waveform of less than 2 ms). A *long stroke* is the "part of a lightning flash which corresponds to a continuing current" (with a time of between 2 ms and 1 s from 10% on the front of the waveform to 10 % on the tail of the waveform). [28]

The term *lightning electromagnetic impulse* (abbreviated to LEMP) describes "all the electromagnetic effects of lightning current via resistive, inductive, and capacitive coupling that creates surges and radiated electromagnetic fields" [28].

Four possible sources of damage from lightning are described in [28]:

- **S1** - Flashes to the structure.
- **S2** - Flashes near to the structure.
- **S3** - Flashes to a service.
- **S4** - Flashes near to a service.

Three possible types of damage resulting from any of the above sources of damage are described in [28]:

- **D1** - Injury to living beings by electric shock.
- **D2** - Physical damage (fire, explosion, mechanical destruction, chemical release) due to lightning current effects, including sparking.
- **D3** - Failure of internal systems due to LEMP.

Four possible types of loss may occur as a result from the damages caused by lightning [28]:

- **L1** - Loss of human life.
- **L2** - Loss of service to the public.
- **L3** - Loss of cultural heritage.
- **L4** - Loss of economic value.

For a PV power plant, any of the above-listed sources of damage, as well as any of the above-listed types of damage, are a concern. Types of loss L1, L2, and L4 are applicable in this context. This emphasizes the need for appropriate and well-designed lightning protection systems for utility-scale PV power plants.

Four lightning protection levels (LPLs), ascertained from data in published technical papers, are described in [28]. Each lightning protection level specifies parameters (such as the maximum impulse current and waveform) for each lightning protection level. Table 2.2 contains the expected surge currents and waveforms for each possible source of damage S1-S4 for low-voltage systems. According to [29], a standard which details the specification of surge protective devices (SPDs) for low-voltage power distribution systems, the scope for standards relating to low-voltage installations covers AC systems of frequency 50-60 Hz and up to 1000 V_{rms}, and DC power circuits up to 1500 V. It is worth noting that [29] references SANS standard 62305, and is therefore a related standard with the same definitions for low-voltage systems.

Table 2.2 specifies the levels for which a surge protective device will need to conform to in order to provide sufficient protection to satisfy the desired lightning protection levels. A waveform shape and peak current values are defined for each source of damage. For induced currents, the 8/20 μ s waveform is specified, with peak current values ranging from 0.1 kA to 10 kA, depending on the source of the surge and the required lightning protection level. Explanations of voltage and current impulse waveform parameters are given in Section 3.2.

Apart from Table 2.2, Section E.4 of [28] specifically refers to surges resulting from induction effects. It is mentioned that surges due to induction effects due to the magnetic fields produced by a nearby lightning flash (source S2) or lightning currents flowing in an external LPS or the spatial shield of LPZ 1 (source S1) usually have an 8/20 μs current waveform [28].

Table 2.2: Expected surge currents resulting from lightning flashes on low-voltage systems [28].

LPL (class)	Low-voltage systems	
	Direct and indirect flashes to the service	
	Source of damage S3 (direct flash) Current shape: 10/350 μs [kA]	Source of damage S4 (indirect flash) Current shape: 8/20 μs [kA]
III-IV	5	2.5
II	7.5	3.75
I	19	5
	Flash near the structure	Flash to the structure
	Source of damage S2 (induced current) Current shape: 8/20 μs [kA]	Source of damage S1 (induced current) Current shape: 8/20 μs [kA]
	III-IV	0.1
II	0.15	7.5
I	0.2	10

The concept of Lightning protection zones (LPZs) were introduced in [28] to assist in the design of lightning protection systems (LPSs). Different LPZs are defined according to the required level of protection from the electromagnetic effects of lightning, where zones of a higher number are expected to handle lower levels of electromagnetic disturbances. LPZs are typically used within a structure in order to protect sensitive equipment to the levels necessary for that equipment to remain operational.

2.4.2.2 SANS 62305-2:2011

Part two of SANS 62305, [30], covers the assessment and management of the risks associated with lightning activity. It aims to define tolerable levels of risk, and then use these levels to determine the extent to which a LPS is required to protect a structure or service from the losses associated with these risks.

The process followed in [30] is best described using the flow diagram shown in Figure 2.21. The process involves identifying the potential types of loss which a structure or service may be susceptible to. A tolerable level of risk is then defined for each possible loss. The risk components for each risk are then defined and summed together. The components to be considered for each source of damage are shown in Table 2.3.

It should be noted that although specific formulae for the determination of the value of each risk are described in [30], they were not included in this section for the sake of brevity and relevance to the study. If the total (summed) risk is greater than the corresponding tolerable level of risk, then further lightning protection measures are required, either in the form of an adequate LPS or SPDs.

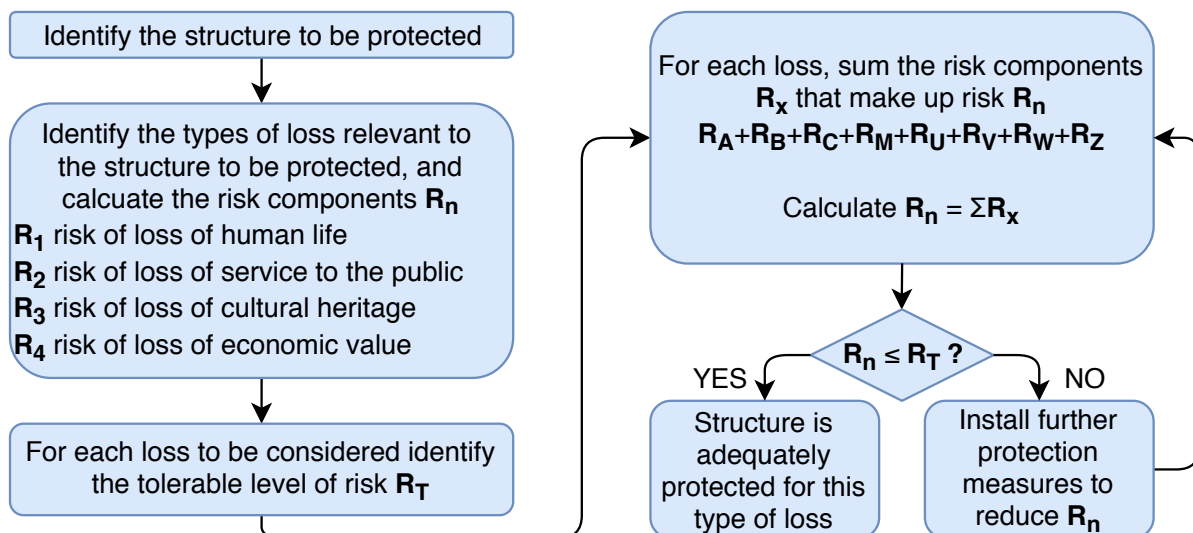


Figure 2.21: The flow diagram for determining the necessary level of lightning protection [30].

Table 2.3: The relevant risk components for each type of loss [30].

Source of damage	Flash to a structure			Flash near a structure	Flash to a line connected to the structure			Flash near a line connected to the structure
	S1				S3			
Risk component	RA	RB	RC	RM	RU	RV	RW	RZ
R1	*	*	*	*	*	*	*	*
R2		*	*	*		*	*	*
R3		*				*		
R4	*	*	*	*	*	*	*	*

2.4.2.3 SANS 62305-3:2011

Part three of SANS 62305, [31], covers the methods for the determination of the class of LPS required, as well as the design of an appropriate LPS.

The required class of lightning protection (LPS) required correlates exactly with the required lightning protection level (LPL) defined in [28]. For example, a structure or service requiring a LPL of I will require a class I LPS.

There are two classes of lightning protection systems - external and internal.

An external LPS is placed on the outside of a structure or service, and is made up of the following three parts: the air termination system (responsible for capturing the lightning discharge current), the down conductor system (responsible for conducting the captured lightning discharge current), and the earth termination system (responsible for dispersing the captured lightning discharge current into the ground). An external LPS may either be isolated from a structure in the case that the structure poses a fire or explosion risk. An air termination system may be made up of vertical free-standing rods, suspended conductors, or a conductive mesh. A down conductor system is usually made up of conductive wiring, however it may make use of conductive parts (such as reinforcing bars or steel frames) within the structure. An earth termination system is made up of an electrically conductive and corrosion resistant material placed underground in a rod or grid layout. Methods of determining the appropriate layout of an air termination system, down conductor system, and earth termination system for the required lightning protection level are described in [31].

An internal LPS is designed to avoid sparking within a structure. Equipotential bonding (the connection of separate conductive paths) is often used, either in the form of a direct connection or by using a surge protective device (SPD), in order to reduce large potential differences between metallic parts - thereby avoiding sparking.

2.4.2.4 SANS 62305-4:2011

Part four of SANS 62305, [32], covers lightning and surge related protection for electrical and electronic systems within structures. The methods for the determination of the placement of lightning protection zones (LPZs), as well as the placement of SPDs and shielding, are presented in [32].

As this part specifically applies to electrical and electronic systems within structures, it will not be further elaborated in this thesis.

2.4.3 SANS 60364-7-712:2016

SANS standard 60434-7-712:2016, [33], which is the identical adoption of IEC standard 60364-7-712:2002, is intended to act as a guideline for the installation of solar PV power supply systems.

It should be noted that [33] is rather brief in nature, and it currently covers all PV power supply systems (despite its full title specifically referring to the electrical installations of buildings). As this standard was originally published in 2002, when requirements for stand-alone PV power supply systems were still under consideration, it is rather outdated. The latest update on the IEC standard 60464-7-712 was published in 2017, which SANS should consider adopting.

No references to surge protective devices are made in [33], and the only mention of the prevention of electromagnetic interference (EMI) resulting from lightning declares that the area of all wiring loops should be as small as possible. No guidelines (specifying how this should be accomplished) are given.

2.4.4 SANS 61643-12:2009

SANS standard 61643-12:2009, [29], which is the identical adoption of IEC standard 61643-12:2008, acts as a guideline for the specification of surge protective devices in low-voltage power distribution systems.

Low-voltage power distribution systems are often susceptible to overvoltages and currents resulting from lightning activity. Surge protective devices are used to mitigate the potential damage caused by these overvoltages and currents.

A one-port SPD is a surge protective device designed to be connected between two conductive paths in order to protect sensitive equipment from harm. These SPDs are usually voltage-sensitive (voltage switching type SPDs) - they have a high impedance during normal operation but have a low impedance when a high voltage is present. Voltage switching SPDs make use of spark gaps, gas-discharge tubes, or metal-oxide varistors (MOVs) as the voltage-switching device used in the SPD.

In a PV installation, three one-port SPDs are often connected between the positive string terminal (DC+), the negative string terminal (DC-), and ground in a combiner box. A *combiner box* is a device which combines the current of many PV strings in parallel with each other, and feeds the combined current to an inverter for the production of AC power - this configuration is shown in Figure 2.22. Some SPDs make use of both voltage and current limiting components. The DEHNguard PV SCI 500, for example, utilizes a MOV for an initial voltage transient, but quickly transfers the conducted current to a fuse in order to handle a large current transient, preventing the failure of the MOV. This process shown in Figure 2.23.

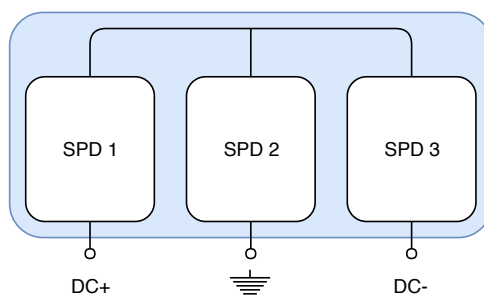


Figure 2.22: The connection of three one-port SPDs, as often seen in a PV power plant.

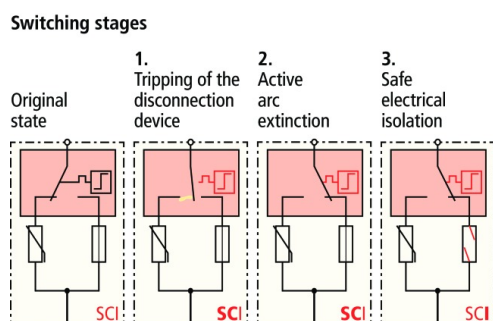


Figure 2.23: The two-stage operation of a DEHNguard PV SCI 500 [34].

Now that an understanding of the standards to which PV modules and installations should abide to has been gained, literature relating specifically to both lightning and PV modules is reviewed in order to discern the level of relevant research which has been performed.

2.5 Lightning and PV Installations

This section reviews published literature relating to the effects of nearby lightning strokes and PV installations.

Firstly, it begins by reviewing experiments designed to examine the degradation of the performance of a PV module resulting from nearby current surges.

Secondly, it covers an experiment aiming to minimize the damage to a PV module by increasing the distance between it and a nearby current surge.

Thirdly, this section examines the possible effect of the internal layout of a PV module on the induced currents and voltages within the module.

Fourthly, this section examines the influence of the conductive frame of a PV module on the induced currents and voltages within the module.

Fifthly, this section describes cases of bypass diode failures within PV modules when exposed to nearby current surges.

Finally, the mutual inductance of a PV module, as well as the factors influencing it, are discussed.

2.5.1 PV Cell, String, and Module Degradation

In [35], a high-voltage impulse generator was converted into a high-current impulse generator in order to gather information about the sensitivity of solar cells, modules, and systems. The generator was made up of 10 capacitors (each rated at $1.2 \mu\text{F}$ and 50 kV) in parallel, discharged through a sphere gap. The circuit diagram can be seen in Figure 2.24.

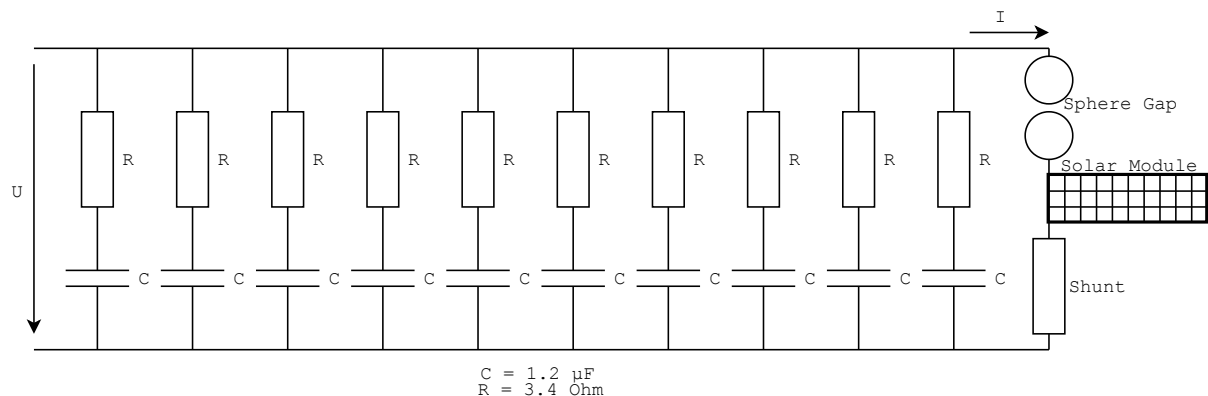


Figure 2.24: The circuit diagram of the high-current impulse generator used in [35].

The peak values reached in [35] were $I_{\text{peak}} = 108 \text{ kA}$ and $di/dt_{\text{peak}} = 53 \text{ kA}/\mu\text{s}$. It was recognised by the authors that these values exceeded those of typical lightning currents, however it was explained that they were necessary in order to obtain typical values for the electrical charge Q since budgetary constraints had forced the authors to make use of smaller than ideal capacitors. The largest value for electric charge obtained was 0.6 A s . [35]

In order to measure any possible degradation in the performance of a PV module, a testing apparatus was created. This testing apparatus was made up of 30 Osram Biolux fluorescent lamps, and a homogeneous irradiance of 300-400 W/m² in a 130 cm by 50 cm rectangular shape was claimed by the authors. The testing apparatus was used to measure the I-V characteristics of PV modules before and after exposure to simulated lightning currents. [35]

Tests were carried out with single cells as well as strips of three cells. For these tests, the current impulse flowed through a wire 1-4 mm from the edge of the cell(s). Tests were also carried out with entire modules, of both the framed and frameless varieties. For framed modules, the current was injected into either the shortest edge (as shown in Figure 2.24), or the centre of the frame (as shown in Figure 2.25). For frameless modules, a flat conductor was placed under the back of the module (as shown in Figure 2.26). The authors intended these configurations to enable them to simulate direct lightning strikes into the frames of framed modules, or the supporting structures of frameless modules. [35]

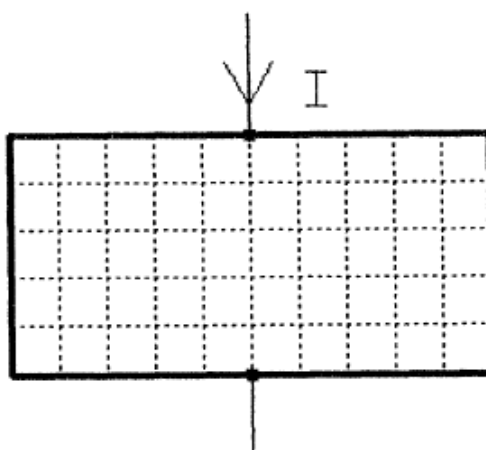


Figure 2.25: Current impulse injected into the centre of the module frame [35].

The authors expected to observe damage as a result of direct breakdown between the frame and solar cells within a module, resulting in the complete failure of the module. Such an event was never observed. The authors did observe a successive degradation of the I-V curve of a solar cell as a result of a nearby lightning current flowing very nearby, specifically noting a reduction of the fill factor as a result of the fast changing electromagnetic field of the currents (as shown in Figure 2.28). Cells which had considerable degradation of fill factor had visible defects in the metallic grid on the front and back side (as seen in Figures 2.29 and 2.30). The authors speculated that this degradation may be caused by eddy currents induced in the closed loops of the metallic grid. Similar defects were observed in the back contact of a polycrystalline solar module (as seen in Figure 2.31). [35]

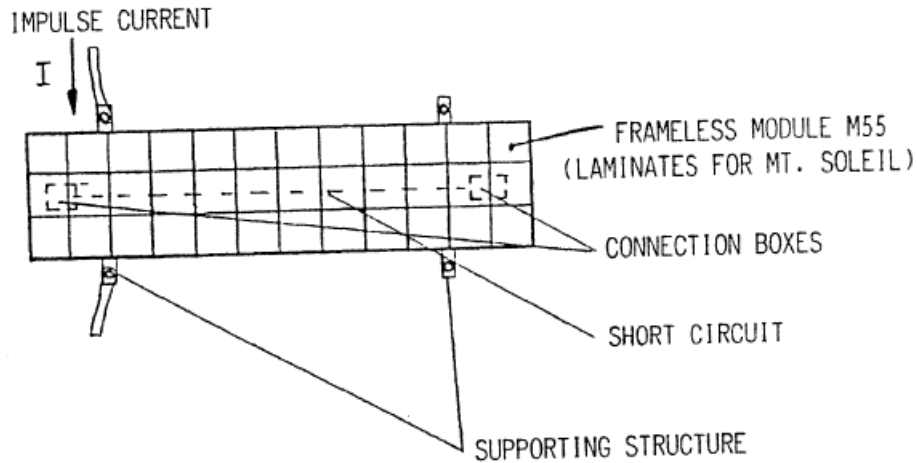


Figure 2.26: Current impulse injected into a flat conductor at the back of a frameless module [35].

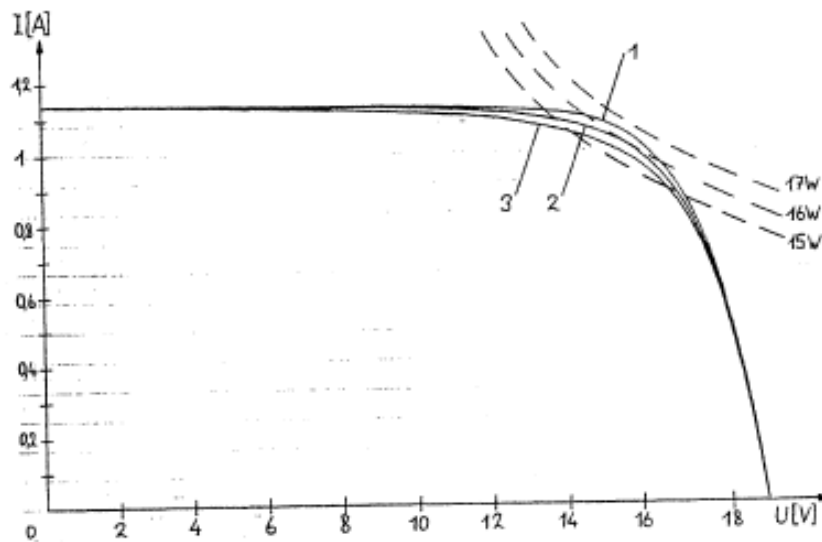


Figure 2.27: A plot showing the reduction in the fill factor of a SOLAREX MSX60 frameless module with successive exposure to nearby current impulses [35].

The properties of each current impulse from Figure 2.27 are noted in Table 2.4.

Table 2.4: Labels for the I-V curves shown in Figure 2.27 [35].

I-V Curve ($G_{sc} = 300 \text{ W/m}^2$)	I_{peak} [kA]	$\frac{di}{dt}_{\text{peak}}$ [kA/s]
1	N/A (Before Impulses)	N/A (Before Impulses)
2	53	43
3	69	43
4	80	53

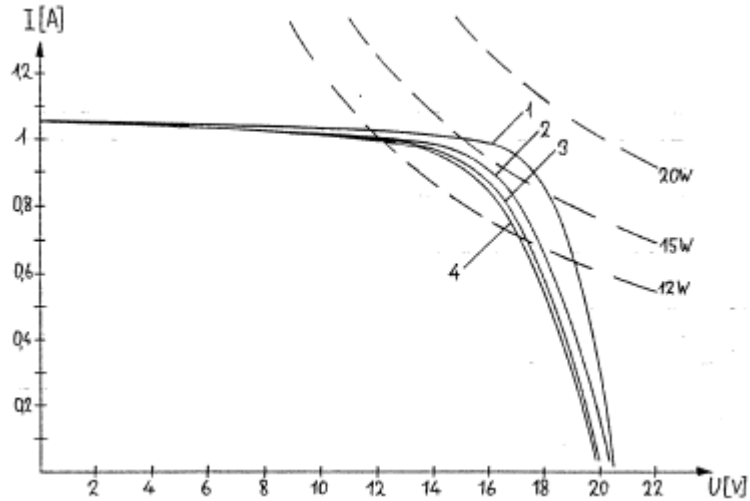


Figure 2.28: The reduction in the fill factor of a Siemens Solar M55 frameless module with successive exposure to nearby current impulses [35].

Table 2.5: Labels for the I-V curves shown in Figure 2.28 [35].

I-V Curve ($G_{sc} = 320 \text{ W/m}^2$)	I_{peak} [kA]	$\frac{di}{dt}_{\text{peak}}$ [kA/s]
1	N/A (Before Impulses)	N/A (Before Impulses)
2	53	43
3	69	43
4	80	53

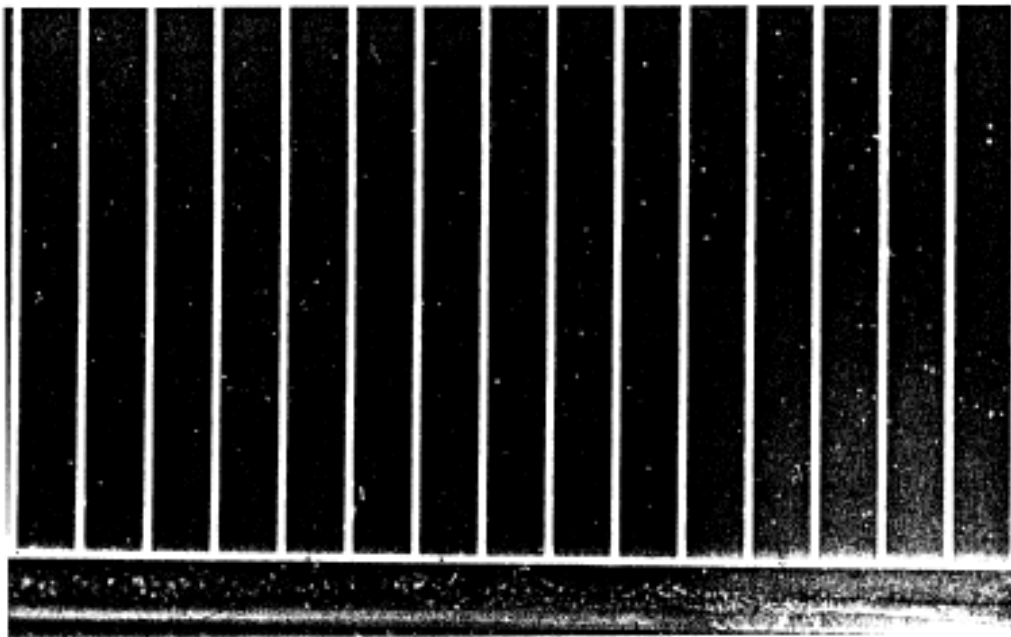


Figure 2.29: Defects in the front grid of a Siemens monocrystalline PV cell, resulting from a nearby high-current impulse [35].

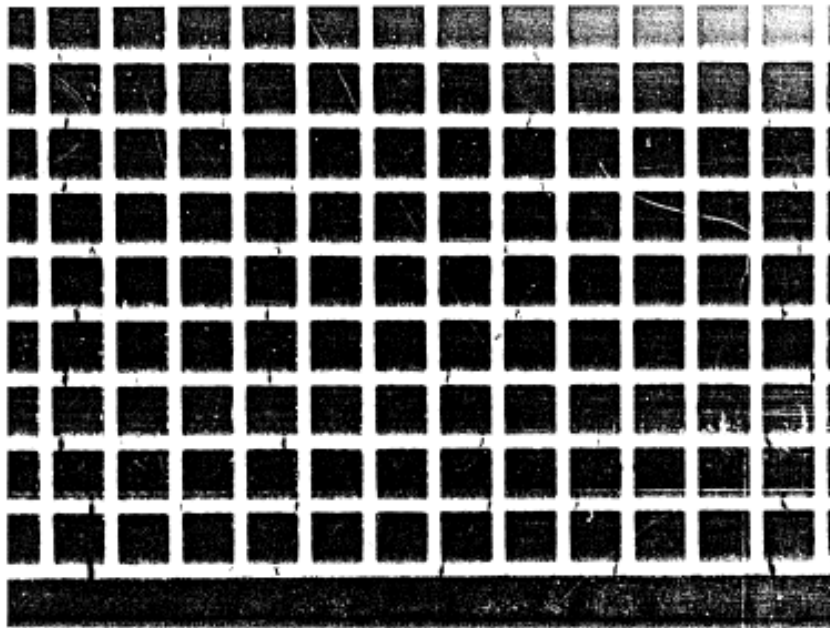


Figure 2.30: Defects in the rear grid of a Siemens monocrystalline PV cell, resulting from a nearby high-current impulse [35].

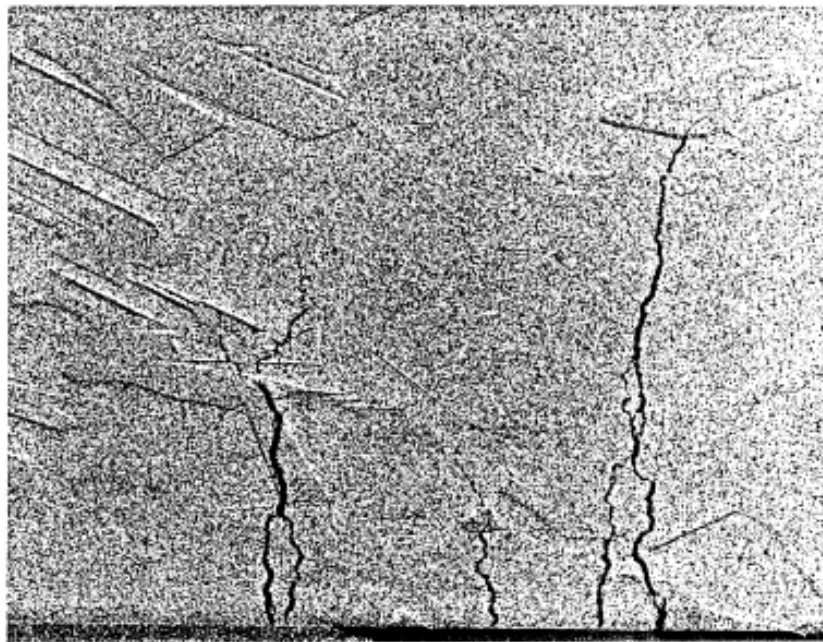


Figure 2.31: Defects in the rear grid of a Telefunken Systemtechnik polycrystalline PV cell, resulting from a nearby high-current impulse [35].

It was postulated in [35] that the degradation of the I-V characteristics was possibly not only a result of the increase in the series resistance due to damaged front and back contacts, but also as a result of the degradation of the semiconductor material caused by the magnetic field. The degradation of an entire cell's I-V curve was observed to be a result of the degradation of the part of the cell very close to the lightning current [35].

The authors found that degradation as a result of lightning current impulses within the frame is largely dependant on the layout of the module. Modules with smaller frame-to-cell distances (1.2 mm) suffered more profound defects than modules with larger frame-to-cell distances (5.0 mm). The fast changing magnetic field were found to be greatly attenuated by eddy currents in a metallic foil on the back side of a Kyocera module (LA361J48). With this module, no degradation of I-V characteristics was observed. Modules without this metallic foil and with smaller frame-to-cell distances suffered from the defects shown in Figures 2.27 and 2.28. The tests found that the same current impulse caused more damage when cells or modules were connected in the short-circuit position than when they were in the open-circuit position, therefore most of these tests were carried out with short-circuited modules. [35]

The authors used the setup shown in Figure 2.32 in order to observe the effects of a lightning strike to the frame of a module on a PV system which included two surge arresters - one near the PV module and one near the inverter. A 6 m long steel pipe was placed to provide partial shielding to the wiring between each surge arrester. Current and voltage measurements were recorded at each of the surge arresters. The authors observed that modules within this setup did not degrade more than those tested in the short-circuit position, despite the surge arresters beginning to conduct during high di/dt values recorded at the front of the waveform of the induced current impulse. Modules with three parallel rows of ten cells (such as the Siemens M20 or M65) produced less induced voltage than those with four rows of nine cells (such as the Kyocera LA361J48). Less voltage was induced in modules with three rows when the lightning current flowed along the short sides of the frames. Bypass diodes mounted in a single connection box (such as in a Kyocera LA361J48) failed in the short-circuit position. Modules which made use of bypass diodes across 2/3 of the module and mounted within the module experienced no bypass diode failures. The authors hypothesised that the series resistance of the remaining 1/3 of the module limited the current in the bypass diodes sufficiently to prevent failure. [35]

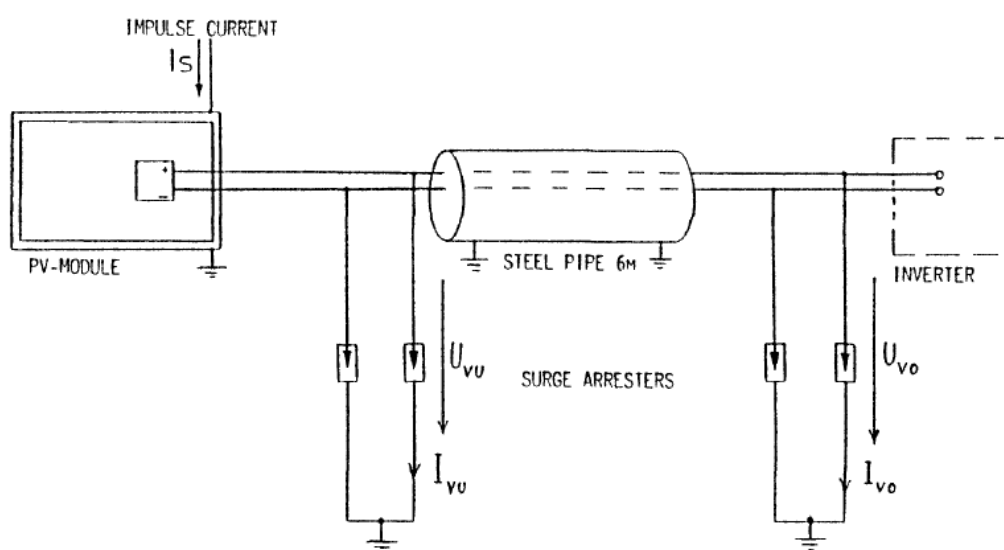


Figure 2.32: The schematic of the PV system used in [35] to model the effects of induced current impulses [35].

A wire model of a PV module was constructed in order to examine the effect of the dual surge arrester configuration without PV cell degradation influencing results. Experiments were conducted using the same test setup as before and concluded that by placing surge arresters on both sides of the wiring between the PV module and the inverter, the current entering the inverter-side surge arrester was only 30% of that induced at the PV module. Slightly higher induced voltages were recorded with the wire model when compared to those recorded with an actual PV module, however the results gathered showed the effectiveness of the dual surge arrester configuration at reducing the transient voltages and currents entering the input terminals of the inverter. Substituting the steel pipe for an iron pipe did not provide any significant further reduction in the induced currents and voltages, and neither did substituting the steel pipe and wiring for copper-shielded wiring. [35]

2.5.2 An Air Termination System for the Protection of PV Systems

The authors of [35] conducted further research, which was documented in [36]. In [36], the same configuration of current impulse generator as shown in Figure 2.24 is used with similar high-current impulses ($I_{\text{peak}} = 111 \text{ kA}$ and $di/dt_{\text{peak}} = 56 \text{ kA}/\mu\text{s}$).

The test setup shown in Figure 2.33 was used in [36] in order to examine the effects of increasing the separation distance between a PV module and a nearby high-current impulse. The current from the current impulse generator was passed through an aluminium U-profile (of cross sectional dimensions 50 mm by 40 mm, with a thickness of 4 mm) mounted on a Siemens Solar M65.

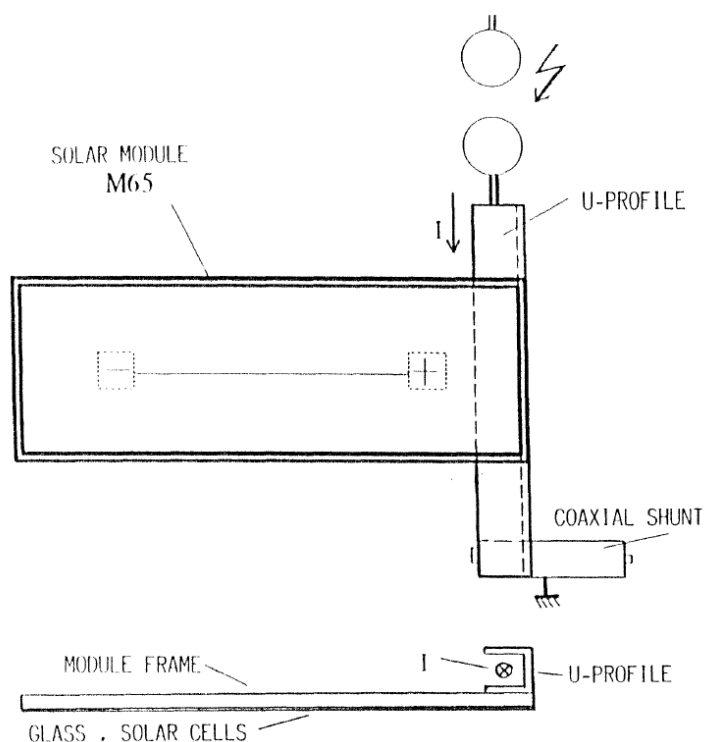


Figure 2.33: The test setup used in [36] in order to determine the effects of increased separation distance between a PV module and a high-current impulse [36].

The first conclusion reached in [36] was that by increasing the separation distance between the current impulse and the solar cells to a few centimetres eliminated the possibility of solar cell degradation as a result of the electromagnetic field.

Based on this observation, the authors attempted to create an air termination system which would decrease the probability of a direct strike to the frames of the PV modules themselves. Earlier design attempts included large vertical metallic rods or horizontal metallic ropes. The shading created by these designs brought about concerns relating to decreased energy production, and the physical layouts did not suit every installation. Finally, a design was chosen which consisted of a number of upright metallic rods of length 30 cm and diameter 1 cm, connected to the PV modules' supporting structure, a few centimetres below the frames of the PV modules. Tests were conducted in the high voltage laboratories at the Swiss Federal Institute of Technology in Lausanne and at Emil Haefely in Basel. Voltage impulses of up to 2 MV, using a 1.2/50 μ s impulse, at separation distances of up to 3 m were used. Over 40 tests were conducted using the air termination system and a Siemens M55 PV module, and no simulated lightning strikes contacted the frame of the PV module. Figure 2.34 shows the air termination system effectively capturing the lightning discharge current and routing it away from a single PV module, preventing a direct lightning strike to the module frame and any resulting damage to the PV module. Figure 2.35 shows the air termination system installed on the 60 kWp PV installation at Ingenieurschule ISB. [36]

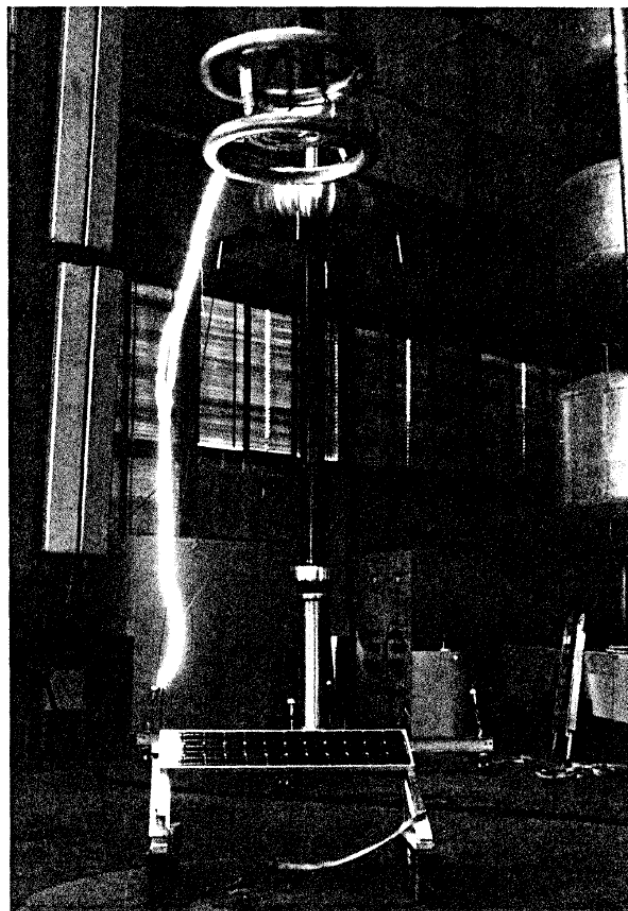


Figure 2.34: A test of the air termination system mentioned in [36]. A 1.2/50 μ s impulse of 2 MV was used at a separation distance of 3 m [36].

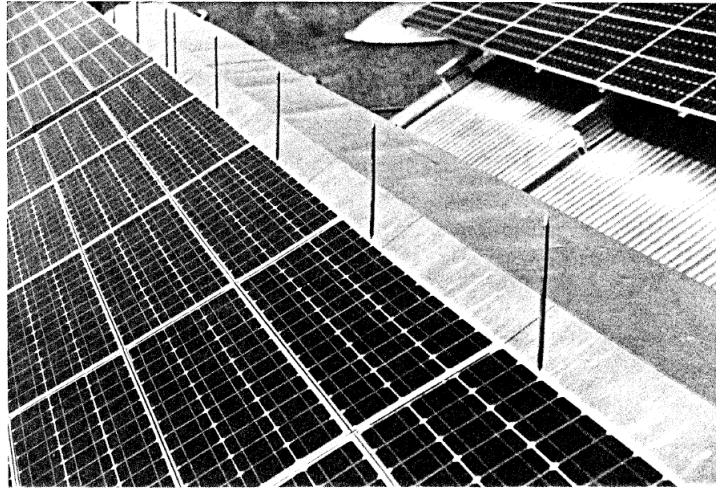


Figure 2.35: The air termination system consisting of upright metallic rods mentioned in [36], installed at Ingenieurschule ISB [36].

One criticism of the work presented in [36] is the use of only the Siemens M55 PV module. In [35], the authors observed no defects in the bypass diodes found in Siemens M65 PV modules as a result of simulated lightning currents injected into the module's frame. Modules with a single junction box containing bypass diodes across all the strings suffered complete failure of all bypass diodes at medium lightning currents. The authors hypothesised that due to the PV module containing bypass diodes across 2/3 of the strings, the remaining 1/3 of the module provided a sufficient impedance to limit the induced current to a safe level. The Siemens M55 shares the same bypass diode configuration as the M65, therefore it would have been advantageous to examine the effectiveness of separating the simulated lightning currents from a PV module by a few centimetres using PV modules which contained single junction boxes with bypass diodes across all strings.

2.5.3 PV Module Layout

Following on from the work presented in [35] and [36], [37] documents the influence of the internal layout of a PV module on the voltages induced by nearby simulated lightning currents.

Three types of PV module layouts are identified in [37]. These classifications are valid with the PV module in the open-circuit position, and take the effects of a module's bypass diodes into account.

An additive module with an even number of rows (e.g. Kyocera KC60) is the first type of PV module layout. When lightning currents flow in one direction (resulting in the reverse biasing of the bypass diodes), the voltages induced in each loop add together. When the lightning currents flow in the opposite direction (resulting in the forward biasing of the bypass diodes), no voltage is induced. [37]

Figure 2.36 shows an example of a PV module with this type of internal layout. With the magnetic field resulting from the lightning current travelling into the page, an induced voltage occurs. In this case, the induced voltage results in the reverse biasing of the bypass diodes, further resulting in an induced voltage at the output terminals of the PV

module. If the magnetic field resulting from the lightning current were to travel out of the page, then the induced voltage would result in the forward biasing of both bypass diodes, resulting in an induced current flowing within the internal loops of the module and a negligible induced voltage at the output terminals of the PV module.

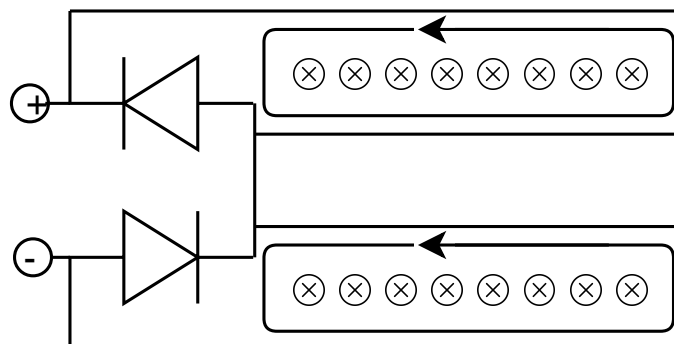


Figure 2.36: An example of the internal wiring layout of an additive module with an even number of rows.

A compensating module with an even number of rows (e.g. Solarex MSX 60/64) is the second type of PV module layout. Due to the module's internal layout, voltages of opposing polarity are induced in the internal loops of the module, resulting in the forward biasing of half of the bypass diodes and the reverse biasing of the other half of the bypass diodes, as can be seen in Figure 2.37. The loops with the forward biased bypass diodes do not contribute to the induced voltage measured at the output terminals of the PV module, whereas the loops with the reverse biased bypass diodes do contribute to this induced voltage. The opposite loops are conducting when the the polarity of the lightning current is reversed. [37]

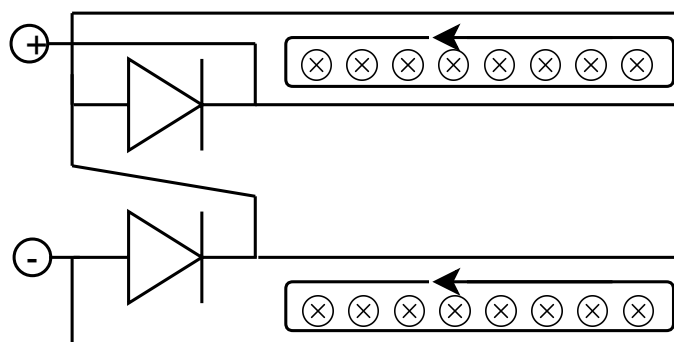


Figure 2.37: An example of the internal wiring layout of a compensating module with an even number of rows.

A compensating modules with three rows (e.g. Siemens SM46/SM55) is the third type of PV module layout. As can be seen in Figure 2.38, these modules typically have bypass diodes across two of the three internal PV strings. Due to the module's internal layout, only one loop contributes to the induced voltage measured at the output terminals of the PV module. If the magnetic flux were to travel into the page, a voltage would be induced which results in the forward biasing of the upper bypass diode and the reverse biasing of the lower bypass diode, therefore only the lower loop would contribute to the total induced voltage of the module. If the magnetic flux were to travel out of the page, the opposite would occur.

Since this type of PV module typically has bypass diodes across two of the three internal PV strings, it is not usually prone to bypass diode failures (according to [35]). As mentioned in Section 2.5.1, the authors of [35] hypothesised that the series resistance of the internal PV string which did not have a bypass diode was sufficient to sufficiently limit the current in the active bypass diode to prevent its failure.

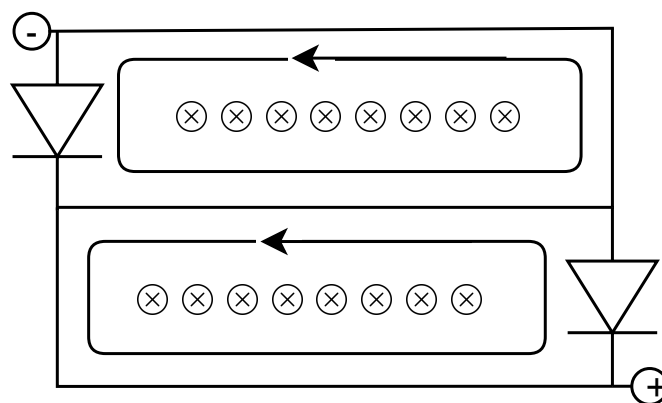


Figure 2.38: An example of the internal wiring layout of a compensating module with three rows.

2.5.4 Influence of the Frame of a PV Module on the Induced Voltages

Physical tests were performed in [37] in order to determine the influence of the frame of a PV module on the induced voltages. A larger impulse generator was used (up to $I_{\text{peak}} = 120 \text{ kA}$ and $di/dt_{\text{peak}} = 40 \text{ kA}/\mu\text{s}$) than that in [35]. In addition to increased current capacity, this larger generator allowed for the exposure of multiple series-connected PV modules (up to a total area of 2.25 m in height and 1.25 m in width) to the magnetic field resulting from the high-current impulse, as can be seen in Figure 2.39. For all the tests described in [37], the output terminals of the PV modules were in the open-circuit position.

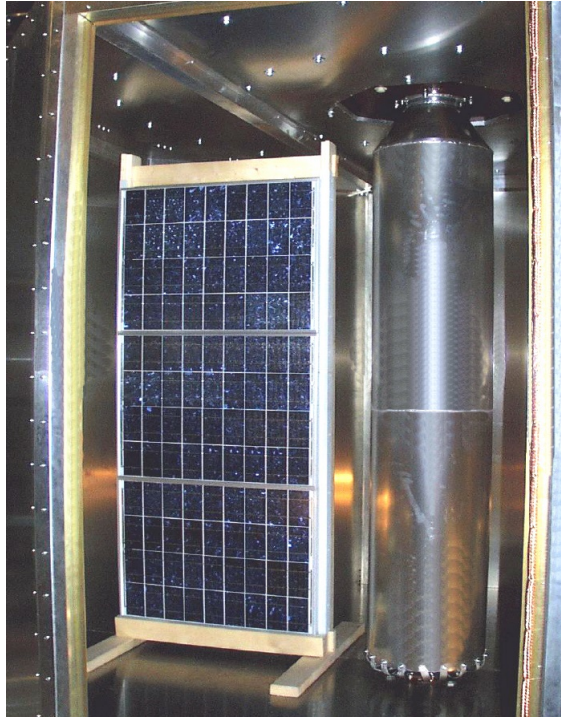


Figure 2.39: Three Kyocera KC60 modules stacked vertically on their long edges in the impulse generator used in [37].

2.5.4.1 Vertical Orientation

Figure 2.40 shows the test setup used in [37] for the examination of the induced voltages within an additive PV module with an even number of rows. The chosen module was a Kyocera KC60, distance $d_{m1} = 450$ mm, and distance $d_{m2} = 900$ mm. [37]

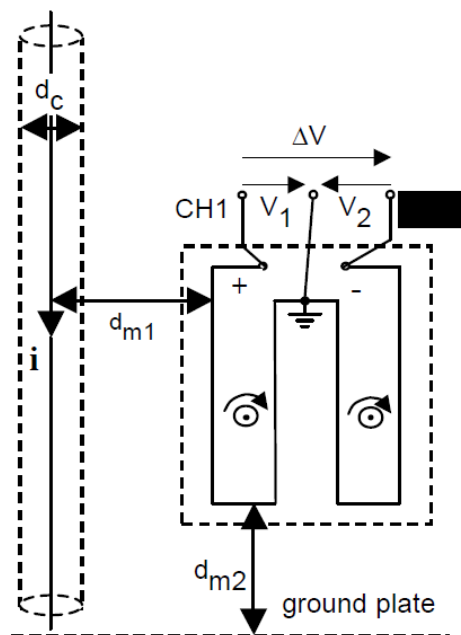
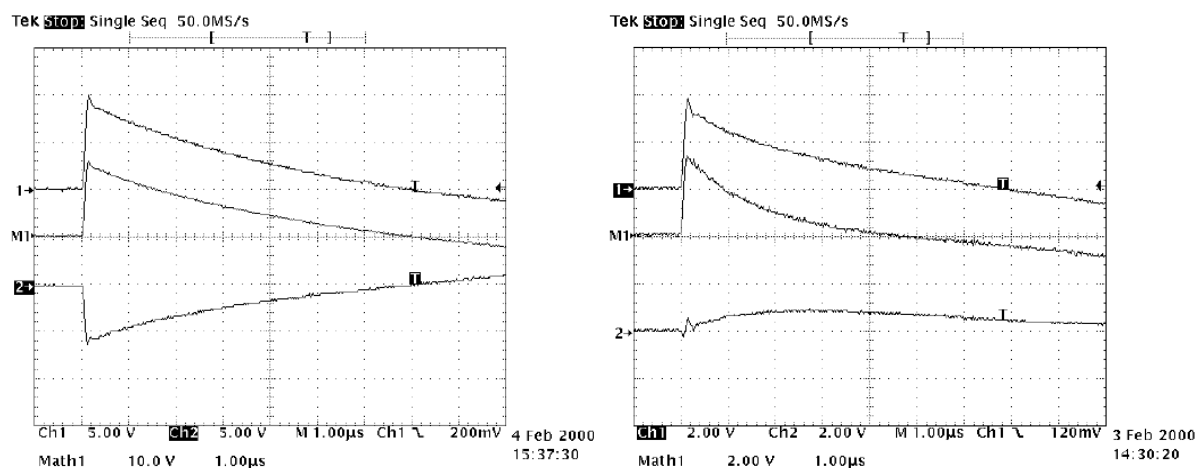


Figure 2.40: A diagram of the vertical experimental setup described in [37].

Figure 2.41 shows the induced voltages in a Kyocera KC60 PV module recorded in [37]. A voltage was induced within each loop, and these voltages combined to produce a larger induced voltage. This was expected due to the additive nature of the loops within the Kyocera KC60 PV module. It should be noted that the voltage recorded over the inner loop (Channel 1) was larger than the voltage recorded at the outer loop (Channel 2) in both cases. This observation was also as expected, since the proximity of the inner loop to the current impulse was closer than that of the outer loop to the current impulse, therefore the magnetic flux cutting the outer loop was lower than the magnetic flux cutting the inner loop. In Figure 2.41, the current impulse had a maximum rate of rise of $di/dt_{\text{peak}} = 25 \text{ kA}/\mu\text{s}$. Voltages were measured using a 100x probe, therefore actual voltages are 100x larger. The vertical scale also changes between plots.

Without the aluminium frame, a total induced voltage of up to around 1500 V was recorded. With the aluminium frame, a total induced voltage of up to 300 V was recorded. The authors of [37] attributed this significant reduction in the magnitude of the induced voltages to the counteracting current flowing in the frame, which would reduce the magnetic flux cutting the loops of the PV module.



(a) Induced voltages without aluminium frame. (b) Induced voltages with aluminium frame.

Figure 2.41: Induced voltage waveforms in a Kyocera KC60 PV module, with and without its aluminium frame [37].

Further experiments were performed with the Kyocera KC60 PV module, with and without its aluminium frame, at different distances from the current impulse. The recorded results are presented in Figure 2.42. Voltages as large as 1.12 kV were induced within the module without the aluminium frame, while a voltage of around 0.6 kV was induced at the same distance with the aluminium frame present. The results were extrapolated in order to provide estimates of the estimated magnitudes of the induced voltages at closer and further distances than measurements were taken at. In Figure 2.42, measurements were taken for different separation distances from the current impulse, both with and without the presence of the aluminium frame. The recorded values were normalised for a maximum rate of rise of the current impulse of $di/dt_{\text{peak}} = 25 \text{ kA}/\mu\text{s}$. [37]

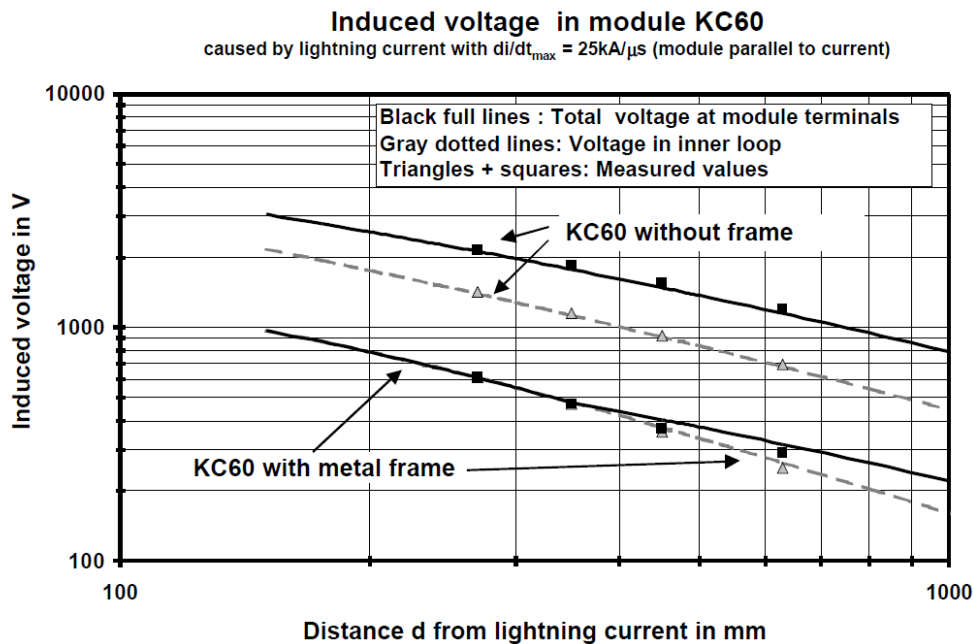


Figure 2.42: Induced voltages within a vertically-mounted Kyocera KC60 PV module [37].

2.5.4.2 Horizontal Orientation

The experiments performed in Section 2.5.4.1 with a single Kyocera KC60 PV module were repeated with the module in a horizontal orientation, as can be seen in Figure 2.43. In Figure 2.43, distance d_{m1} is 450 mm, and distance d_{m2} is 1000 mm. [37]

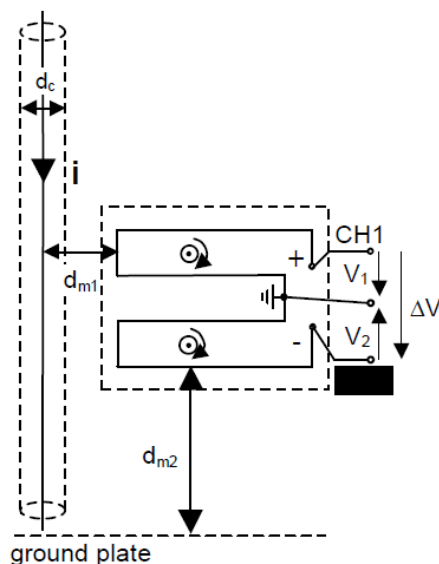


Figure 2.43: The horizontal experimental setup described in [37].

For the horizontal orientation, it would be expected that the voltages induced in each loop would be more similar to each other than for the vertical orientation. This expectation is due to the distance between each loop to the current impulse being more equal than for the vertical orientation (where one loop is closer to the current impulse than the other

loop). Unfortunately, the authors of [37] did not provide data or descriptions relating to the induced voltages on a per-loop basis for the horizontal orientation, as was done for the vertical orientation.

The authors of [37] did provide a plot of the total induced voltages for the Kyocera KC60 PV module, with and without its aluminium frame, at different distances from the current impulse for the horizontal orientation case. This plot is shown in Figure 2.44, and shows a similar response as shown in Figure 2.42. The overall induced voltages are slightly lower for the horizontally orientated module, likely due to the lower total magnetic flux cutting the loops of the PV module in this orientation (the total loop area is closer to the current impulse in the vertical case than in the horizontal case). In Figure 2.44, measurements were taken for different separation distances from the current impulse, both with and without the presence of the aluminium frame. The recorded values were normalised for a maximum rate of rise of the current impulse of $di/dt_{\text{peak}} = 25 \text{ kA}/\mu\text{s}$. [37]

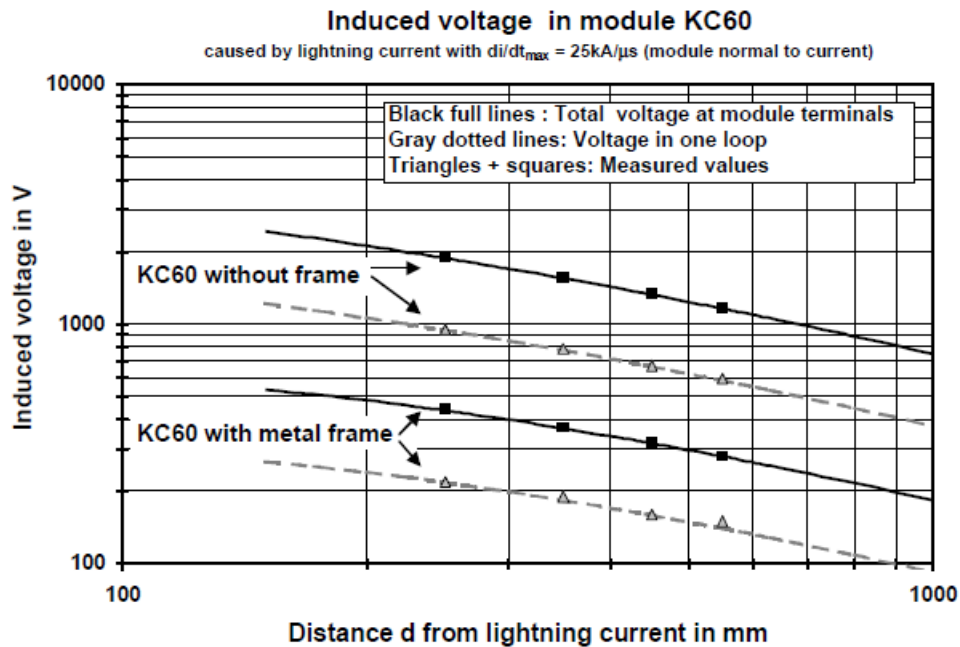


Figure 2.44: Induced voltages within a horizontally-mounted Kyocera KC60 PV module [37].

2.5.4.3 Frame Reduction Factor

Tests similar to those described in Sections 2.5.4.1 and 2.5.4.2 for PV modules of different internal layout were detailed in [37]. The authors determined that a manner of quantifying the amount by which the induced voltages were reduced by the inclusion of the aluminium frame was required. For this purpose, a *frame reduction factor* was defined in [37] as "the ratio between the peak induced voltage in a PV module without its frame and the peak induced voltage in a PV module with its frame."

Frame reduction factors were plotted (as shown in Figure 2.45) for the three types of PV modules in both the vertical and the horizontal orientations, and a mathematical model allowed for an estimated extrapolation of the recorded results to larger separation

distances between the PV modules and the current impulse. In Figure 2.45, legend labels ending in "p" denote tests performed in the vertical orientation, while legend labels ending in "n" denote tests performed in the horizontal orientation. [37]

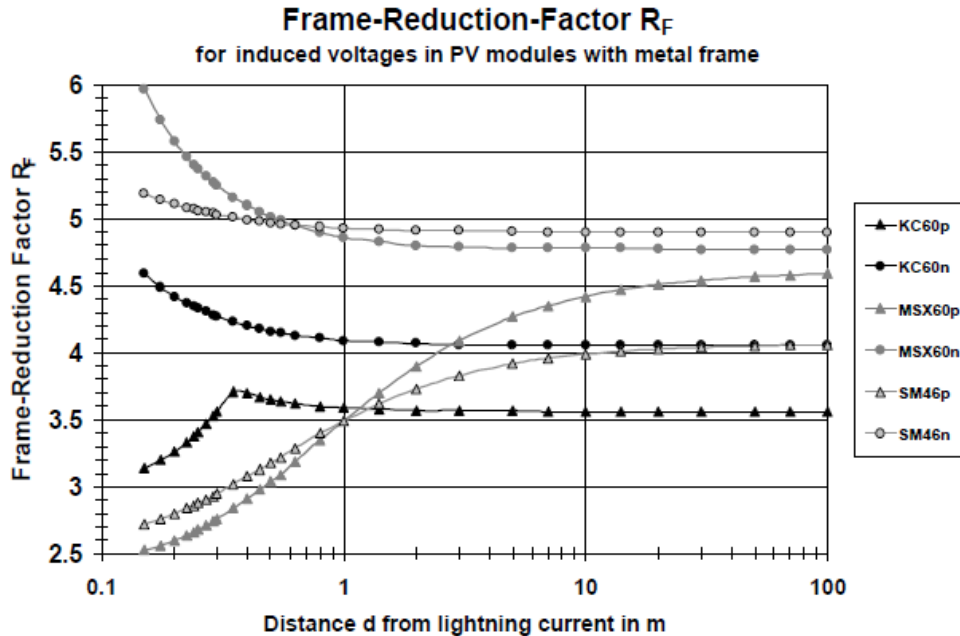


Figure 2.45: Frame reduction factors for three PV modules of differing internal layout [37].

Examining the results in Figure 2.45, one can observe that for the test setup used, the frame reduction factor decreased with increasing distance from the current impulse for all horizontally orientated PV modules and increased with increasing distance from the current impulse for most vertically orientated PV modules. The additive module (Kyocera KC60) differed slightly from this trend. In the vertical orientation, the KC60 exhibited an initial rise in the frame reduction factor up to a separation distance of about 0.35 m before stabilising at a lower value. For all PV modules, the frame reduction factors were higher when the module was in the horizontal orientation. For low separation distances, the compensating modules (Siemens SM46 and Solarex MSX60), exhibited a far greater difference in frame reduction factors for the vertical and horizontal orientations than the additive module. Overall, a frame reduction factor of between 3.5 and 5 could be expected for either of the three modules considered for all but the closest separation distances.

2.5.4.4 Influence of Aluminium Foil Sheeting on Induced Voltages

Brief testing of the influence of a sheet of aluminium foil on the induced voltages in a PV module were performed in [37]. The PV module in question was an additive PV module (Kyocera KC60), and a sheet of aluminium foil was placed on the rear of the module. The authors of [37] attempted to negate the effects of differing PV module internal layouts by also placing a sheet of aluminium foil on the front of the PV module (i.e. on the glass), maintaining a separation distance of around 5 mm between the sheet and the frame of the module in order to prevent flashover from occurring.

The results gathered by the authors of [37] can be seen in Figure 2.46. Measurements were taken for varying distances and extrapolated in order to estimate the expected induced voltages for other distances. One can observe that the aluminium foil provides a significant reduction in the magnitude of the induced voltages. The recorded values were normalised for a maximum rate of rise of the current impulse of $di/dt_{\text{peak}} = 25 \text{ kA}/\mu\text{s}$.

At a separation distance of about 280 mm, the magnitude of the induced voltage in the module without its aluminium frame or the aluminium foil sheet is around 2000 V. With the addition of the aluminium foil, the induced voltage dropped to an expected magnitude of about 280 V. At the same distance, the module with the aluminium frame and without the aluminium foil sheet experienced an induced voltage of about 600 V. With the addition of the aluminium foil, the induced voltage dropped to an estimated magnitude of about 60 V. [37]

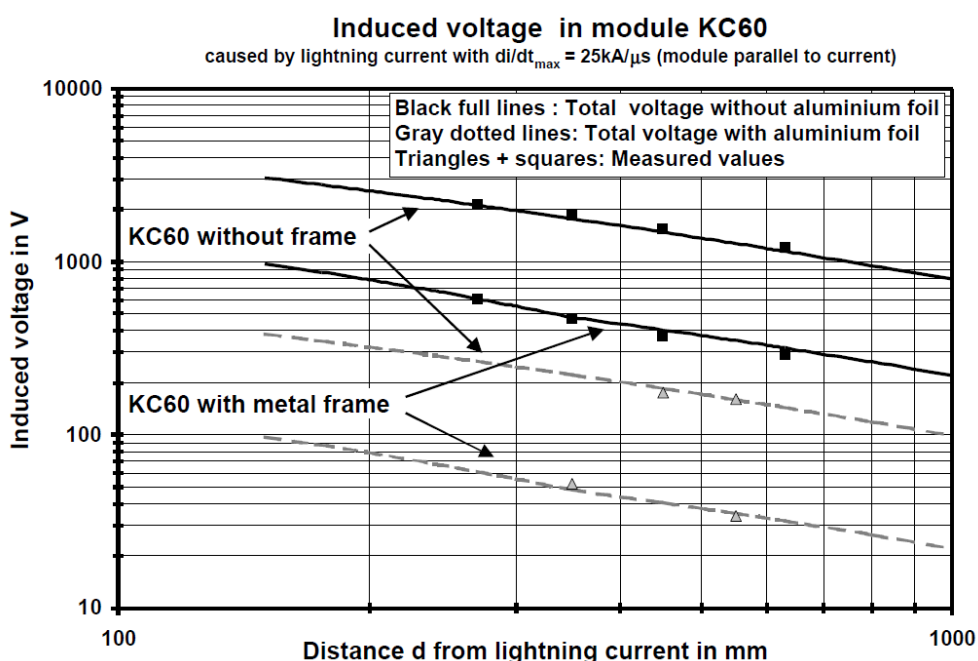


Figure 2.46: The induced voltages within a vertically mounted Kyocera KC60 PV module, with and without its aluminium frame, with and without a sheet of aluminium foil placed on the front and rear of the module [37].

According to [37], the addition of the aluminium foil sheet resulted in a reduction in the induced voltages by a factor of between 7 and 10. This is roughly double that of the frame reduction factor described in Section 2.5.4.3. The authors of [37] therefore concluded that the addition of an aluminium foil sheet would be an effective measure for reducing voltages induced by nearby lightning strokes. The authors did note a concern expressing that sufficient back side insulation and a distance of a few mm may be necessary to ensure adequate withstand voltages.

One criticism of the work relating to the addition of an aluminium foil sheet to the PV module was the application of the extra sheet of aluminium foil to the glass. Since this would not be a realistic mitigation measure, it would have been more useful from a research perspective to only include the sheet applied to the back side when investigating possible mitigation measures for the reduction of the induced voltages.

2.5.5 Bypass Diode Failures

Short-circuit failures of the bypass diodes within PV modules were documented in both [35] and [37].

It was suggested in [37] that bypass diodes with a reverse voltage rating of at least 1000 V should be used in PV installations designed to handle nearby lightning strokes - along with the use of overcurrent protection devices in installations with many strings connected in parallel.

Diodes (even Schottky diodes) with such high reverse voltages, which are still capable of conducting the necessary forward current, often have forward voltages of at least six times that of the standard bypass diodes within a PV module, as well as costs of at least two times higher. Even if the cost of these diodes could be justified, the heat produced by them would need to be strongly taken into consideration. Measures may be necessary to ensure that the bypass diode thermal test is passed, and that the PV cells within the module are not damaged.

2.5.6 Mutual Inductance of a PV Module

In [36], it attempted to devise a method of calculating the expected induced voltages within an open-circuit PV module. The chosen method involved developing a manner in which to calculate the mutual inductance between a PV module and a nearby current flow using Equation 2.2.

$$v = -M \frac{di}{dt} = U_2 - U_1 \quad (2.2)$$

In [36], a Siemens M55 PV module was placed in a coaxial impulse generator. This module fits the description of a compensating module with three rows, as described in Section 2.5.3. The test setup was the same as that described in Section 2.5.2, with a separation distance between the U-profile and the solar cells was 6 cm in order to prevent damage to the module. The total induced voltage was defined as the voltage measured between the output terminals of the PV module. An initial estimate of the mutual inductance M was calculated using the loops formed by approximating the strings within the PV module as a wire running through the centre of gravity of each PV cell, as can be seen by the thick outline shown in Figure 2.47). Although the exact estimation method used is not given, it is likely that it was similar to the method described in Section 2.5.6.1.

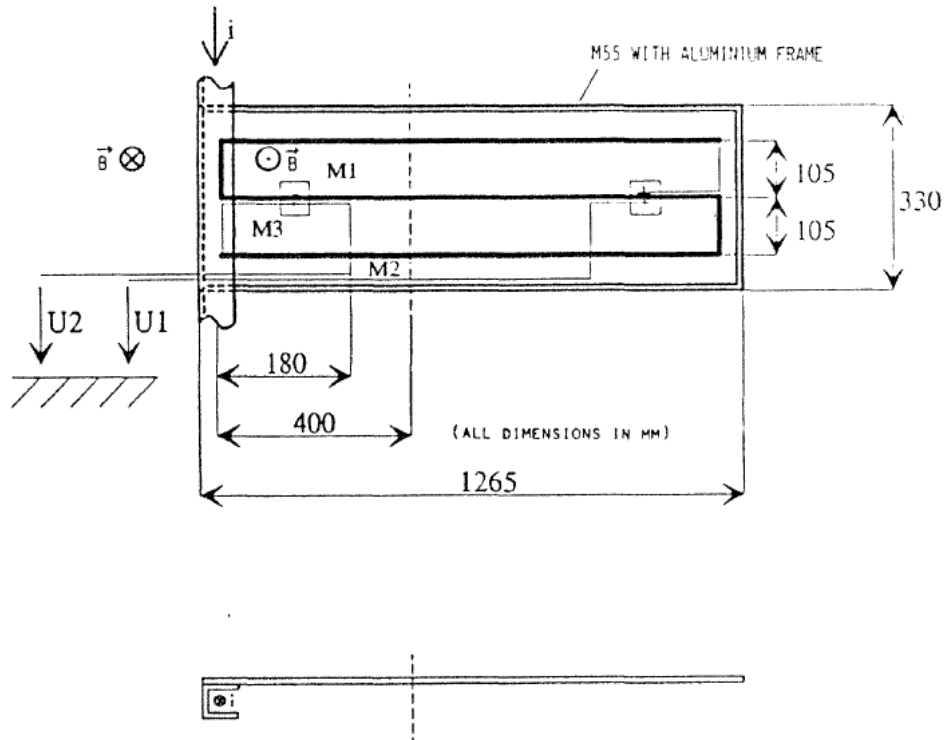


Figure 2.47: Test setup used to measure the induced voltage within a PV module when in close proximity to a large current impulse [36].

The induced voltage was defined as the voltage measured between the two output terminals of the PV module, as can be seen in Equation 2.2. Due to the coaxial design of the impulse generator used, the magnetic fields were attenuated rapidly at distances greater than 400 mm from the current impulse [36].

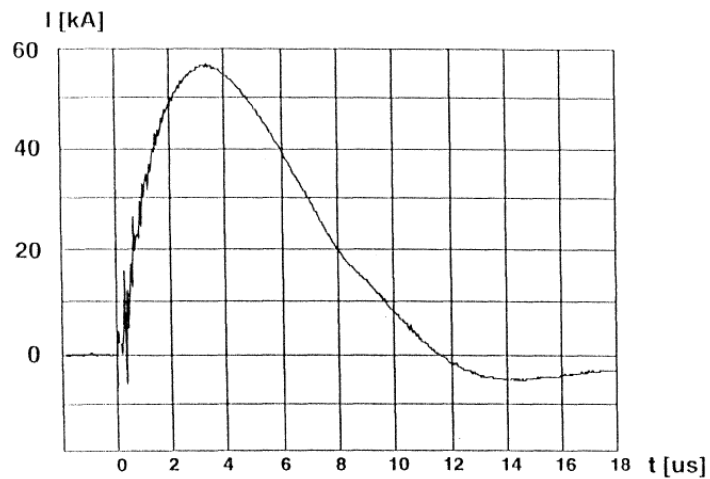


Figure 2.48: The recorded current waveform applied to the U-channel in [36] in order to determine the mutual inductance of a PV module [36].

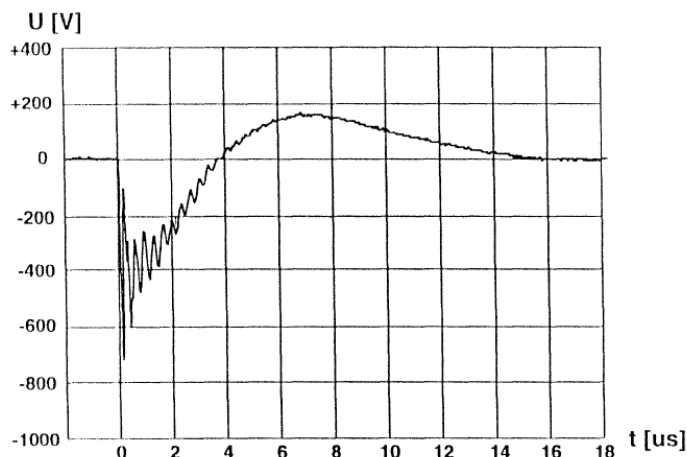


Figure 2.49: The recorded induced voltage waveform measured at the output terminals of the PV module in [36], used to determine the mutual inductance of a PV module [36].

The recorded current waveform applied to the U-channel can be seen in Figure 2.48, and the respective recorded induced voltage waveform can be seen in Figure 2.49. After observing the initial oscillatory behaviour shown in Figure 2.49 between times $t = 0 \mu\text{s}$ and $t = 6 \mu\text{s}$, the authors decided to make use of the values recorded at $t = 8 \mu\text{s}$ ($U = 150 \text{ V}$, $di/dt = -7.5 \text{ kA}/\mu\text{s}$) for the calculation of the mutual inductance. The authors calculated an estimated effective mutual inductance of approximately 21 nH. When the experiment was performed using the impulse generator, an effective mutual inductance of 20 nH was claimed to be recorded. Based on these results, the authors calculated that the total mutual inductance for a single Siemens M55 PV module, placed in the described configuration, should have a total mutual inductance of approximately 46 nH. [36]

2.5.6.1 Calculation of the Induced Voltage within a Conductive Loop

It was mentioned in [36] that a method of estimating the induced voltages within an open-circuit PV module was desirable. This section details the derivation of a simple theoretical method of estimating the induced voltages within a PV module. Although not explicitly stated in [36], this is likely the same method used in Section 2.5.6.

The lightning stroke is modelled as a vertical current flow, from which the magnetic fields radiate radially. The PV module is modelled as an almost short-circuited wire loop of length l and width w , at a distance of r from the vertical current flow, as shown in Figure 2.50.

Firstly, Ampere's Law (shown in Equation 2.3) is used to derive an expression for the magnetic flux density B at a point P_1 , which is at a distance r from the current flow shown in Figure 2.51. Applying Equation 2.3 to the setup shown in Figure 2.51 allows for the the equation for the magnetic field strength at point P_1 (Equation 2.7) to be derived.

$$\oint_c \vec{B} \cdot d\vec{l} = \mu_0 I \quad (2.3)$$

$$\oint_c \vec{B} \cdot d\vec{l} = \mu_0 I \quad (2.4)$$

$$\therefore \oint_0^{2\pi r} \vec{B} \cdot d\vec{l} = \mu_0 I \quad (2.5)$$

$$\therefore B(2\pi r) = \mu_0 I \quad (2.6)$$

$$B = \frac{\mu_0 I}{2\pi r} \quad (2.7)$$

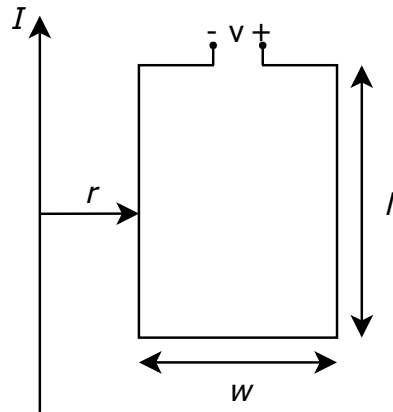


Figure 2.50: The setup used in the derivation of the expression for the estimated induced voltages within a PV module.

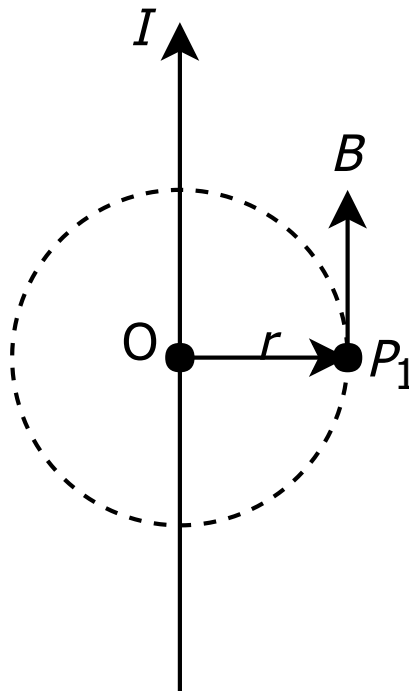


Figure 2.51: The setup used for the derivation of the expression for the magnetic flux density resulting from a vertical current flow.

Secondly, an expression for the total magnetic flux passing through the loop is derived by integrating the magnetic field equation over the surface encompassed by the wire loop.

$$\Phi_B = \int_s \vec{B} \cdot d\vec{A} \quad (2.8)$$

Inserting Equation 2.7 into Equation 2.8 allows for an expression for the total magnetic flux passing through the wire loop to be derived (shown in Equation 2.14).

$$\Phi_B = \int_s \vec{B} \cdot d\vec{A} \quad (2.9)$$

$$= \int_s \frac{\mu_0 I}{2\pi r} dA \quad (2.10)$$

$$= \int_0^l \int_r^{r+w} \frac{\mu_0 I}{2\pi r} dr dl \quad (2.11)$$

$$= \frac{\mu_0 I l}{2\pi} \int_r^{r+w} \frac{1}{r} dr \quad (2.12)$$

$$= \frac{\mu_0 I l}{2\pi} [\ln r]_r^{r+w} \quad (2.13)$$

$$= \frac{\mu_0 I l}{2\pi} \left[\ln \frac{r+w}{r} \right] \quad (2.14)$$

Thirdly, Faraday's Law (shown in Equation 2.15) is used to derive an expression for the induced EMF ξ within the wire loop.

$$\xi = -\frac{d\Phi_B}{dt} \quad (2.15)$$

For the setup shown in Figure 2.50, the magnitude of the current is chosen to be the only time-variant parameter. Inserting Equation 2.14 into Equation 2.15 gives an expression for the total EMF induced in the wire loop as a function of the rate of change of the magnitude of the current. It should be noted that for all open-circuited cases described in this thesis, the term "induced voltage" is used to refer to the induced EMF.

$$\xi = -\frac{d\left(\frac{\mu_0 I(t)l}{2\pi} \left[\ln \frac{r+w}{r}\right]\right)}{dt} \quad (2.16)$$

$$= -\frac{\mu_0 l}{2\pi} \left[\ln \frac{r+w}{r}\right] \frac{dI(t)}{dt} \quad (2.17)$$

Equation 2.17 can be applied to the geometry of the loops formed by the traces of a PV module in order to gain a rough estimate of the induced open-circuit voltages. For modules with a frame which is able to form a conductive loop, a frame reduction factor should be taken into account, therefore actual induced voltages could be 3-5 times lower than calculated (according to [37]), depending on the orientation and separation distance between the module and the current impulse.

2.6 Chapter Conclusion

The first conclusion gathered during the literature review process was that lightning presents a very real risk to life and property throughout most of South Africa. Appropriate steps should be taken during the structural design process in order to prevent the possible losses resulting from these risks from occurring.

The second conclusion reached was that although general SANS standards exist for the prevention of damage resulting from lightning activity, not many of these lightning-related standards explicitly refer to the design or installation of PV modules.

The third conclusion reached was that many factors, such as the internal trace layout or the presence of the aluminium frame, influence the magnitudes of the induced voltages within a PV module. When modelling the effects of lightning activity on PV modules, great attention to detail should therefore be exercised when creating models in order to increase simulation accuracy.

Chapter 3

Impulse Generator

3.1 Chapter Overview

The design, testing, and operation of a modular impulse generator is discussed in this chapter. The purpose of this impulse generator was to provide a platform for the impulse testing of Schottky barrier diodes, which are commonly found as bypass diodes in solar photovoltaic modules. This generator was therefore fundamental in achieving the first and second research goals defined in Section 1.5. This particular generator was designed for component-level testing, and was not intended to replicate voltage and current waveforms of the same magnitude as present in a direct lightning strike. An overview of the interactions occurring within the impulse generator is shown in Figure 3.1.

In this chapter, relevant impulse testing standards waveforms are discussed in Section 3.2. The concept of a combination wave generator is introduced, and its design is split up into two sections - the pulse-shaping network and the Marx generator, which are presented in Section 3.3 and Section 3.4, respectively. The full impulse generator circuit is simulated in Section 3.5. Ancillaries of the impulse generator, such as the charge controlling module, PC software, microcontroller, and distribution board are covered in Section 3.6, Section 3.7, Section 3.8, and Section 3.9, respectively. The construction of the impulse generator is covered in Section E. The impulse generator is tested in Section 3.10, and its waveforms are examined for conformance to IEC standards. The diode testing methodology used and results of the testing are discussed in Section 3.11.

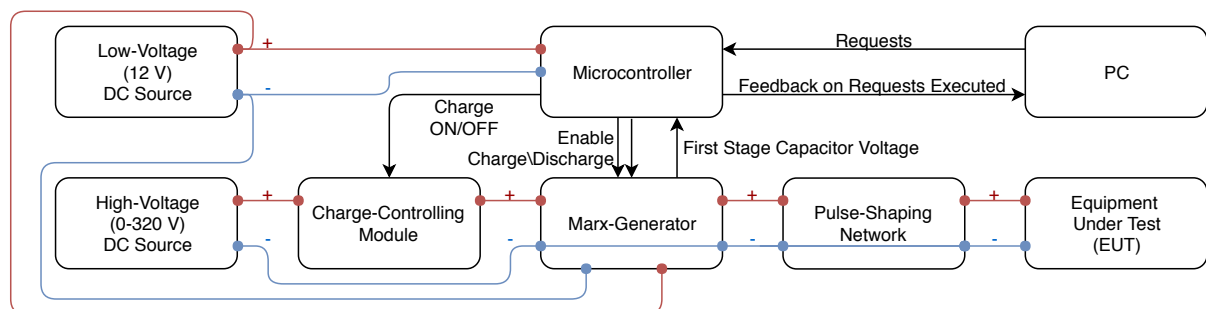


Figure 3.1: An overview of the impulse generator.

3.2 Lightning Impulse Waveform Parameters

The IEC standard 60060-1:2010, adopted in South African as [38], details the general definitions and test requirements for high-voltage test techniques. In order for the standard to be interpreted correctly, some important definitions are discussed.

An *impulse voltage* is defined as an "intentionally applied aperiodic transient voltage, which usually rises rapidly to a peak value and then falls more slowly to zero" [38].

A *lightning-impulse voltage* is an "impulse voltage with a front time less than 20 μs " [38].

A *full lightning-impulse voltage*, is a "lightning-impulse voltage, which is not interrupted by a disruptive discharge" [38].

Figure 3.2 shows a full voltage impulse waveform with time parameters [38].

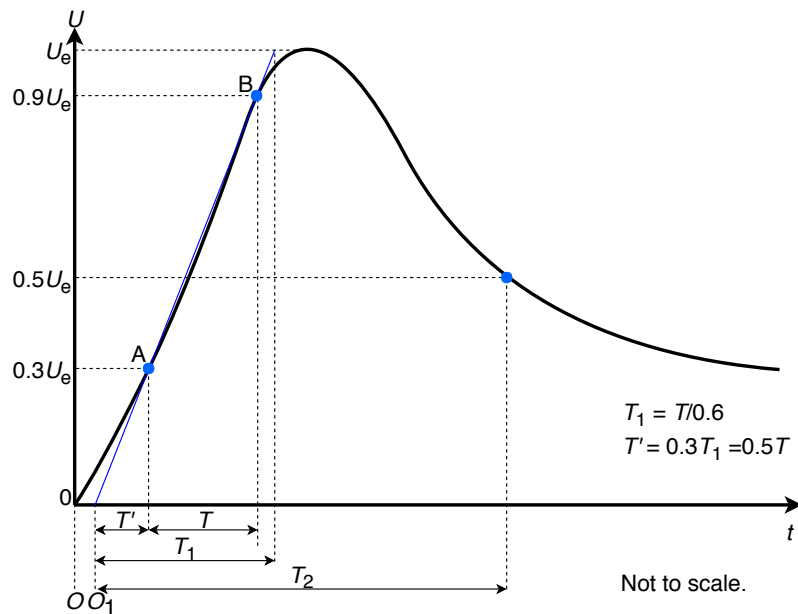


Figure 3.2: Time parameters for a full voltage impulse [38].

T refers to the time difference between the instants when the impulse reaches 30% and 90% of the peak value on the rising edge of the test voltage curve.

T_1 refers to the *front time* and is calculated as $T/0.6$.

O_1 refers to the *virtual origin*, which is the point on the time-axis which precedes the projection of point A onto the time-axis by $0.3T_1$.

U_e refers to the *maximum value of the test voltage*, which is the peak value of the test voltage curve.

T_2 refers to the *time to half-value*, which is the time interval between the virtual origin, O_1 , and the instant when the test voltage curve has decreased to half U_e .

The *average rate of rise* refers to the gradient of the straight line which best fits the region on the rising edge of the test voltage curve between the 30% and 90% points, usually expressed in $\text{kV}/\mu\text{s}$.

According to [39], the definitions of time parameters T , the front time T_1 , and the virtual origin O_1 differ when discussing an current impulse from when discussing a voltage impulse. The time parameters for a current impulse are shown in Figure 3.3.

For a current impulse, T is defined as the time difference between the instants when the impulse reaches 10% and 90% of the peak value on the rising edge of the recorded current curve.

T_1 refers to the *front time* and is calculated as $1.25T$.

O_1 refers to the *virtual origin*, which is the point on the time-axis which precedes the projection of point C onto the time-axis by $0.1T_1$ (which is the same magnitude as $0.125T$).

The maximum undershoot of an current impulse is limited to 30% by [39].

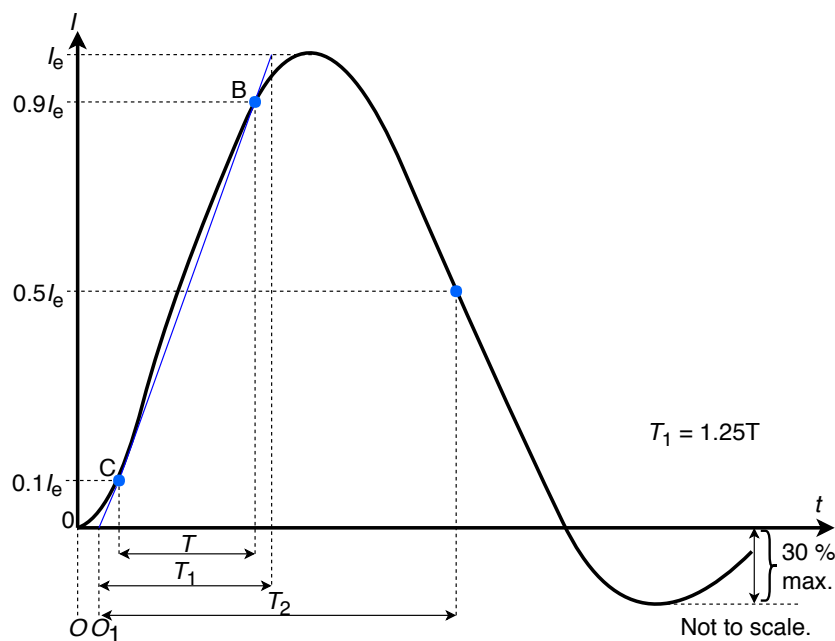


Figure 3.3: Time parameters for a full impulse current [39].

3.2.1 Standard Lightning Impulses

The IEC standard 61000-4-5:2005, which is adopted in South Africa as [39], details the testing and measurement techniques for surge immunity testing, and falls under the umbrella of electromagnetic compatibility (EMC). The purpose of [39] is to detail immunity requirements and test methods, and provide a range of recommended test levels for equipment which may be subject to unidirectional surges caused by overvoltages from switching and lightning transients.

An impulse waveform is often defined using the format T_1/T_2 μs . Tests in [39] are to be performed using a *combination wave generator*. A combination wave generator is a type of impulse generator with a $1.2/50$ μs or $10/700$ μs open-circuit (load greater than or equal to $10\text{ k}\Omega$) voltage waveform and a corresponding $8/20$ μs or $5/320$ μs short-circuit (load smaller than or equal to $0.1\ \Omega$) current waveform. It is specified in [39] that a $1.2/50$ μs combination wave generator is to be used in all cases, except for those relating to the

testing of ports connecting to communication lines (where a 10/700 μs combination wave generator is specified instead).

According to [39], a combination wave generator should be able to generate impulses in both a positive or a negative polarity, have a floating output, and have a repetition rate of 1 impulse per minute (or faster).

Table 3.1 details the waveform parameters given in [39] for the 1.2/50 μs and 8/20 μs waveforms. It should be noted that in current IEC publications, the 1.2/50 μs and 8/20 μs waveforms are defined according to [38], whereas some other IEC recommendations are based on the definitions from IEC 60469-1. For surge immunity testing, it is stated that both definitions are valid as they describe the same combination wave generator.

Table 3.1: Definitions of 1.2/50 μs and 8/20 μs waveform parameters [39].

Definition	IEC 60060-1		IEC 60469-1	
	Front Time [μs]	Time to Half-Value [μs]	Rise Time (10% - 90%) [μs]	Duration Time (50% - 50%) [μs]
Open-Circuit Voltage	1.2 \pm 30 %	50 \pm 20 %	1.0 \pm 30 %	50 \pm 20 %
Short-Circuit Current	8.0 \pm 20 %	20 \pm 20 %	6.4 \pm 20 %	16 \pm 20 %

A number of test levels (shown in Table 3.2) are specified in [39] to provide a standard to which an object's impulse immunity can be referenced. It should be noted that it is possible for a special test level X to be used. This can be any level (above, below, or in between other levels), and if used should be specified within the product standard. A peak open-circuit voltage is to correspond with its peak short-circuit current at the same level of charge of the combination wave generator.

Table 3.2: The test levels specified by [39].

Level	Open-Circuit Peak Voltage [kV] \pm 10 %	Short-Circuit Peak Current [kA] \pm 10 %
1	0.5	0.25
2	1.0	0.50
3	2.0	1.00
4	4.0	2.00
X	Special	Special

For the sake of convenience, the *effective output impedance* of the combination wave generator is defined as the ratio of the peak open-circuit output voltage to the peak short-circuit current. For test levels 1-4, the effective output impedance is 2 Ω . It is, however, noted in [39] that the output voltage and current waveforms are influenced by the impedance of the equipment under test (EUT). An external resistor may be added in the instance that a particular test setup is required to have an increased output impedance - this, however, may impact the shapes of the current and voltage waveforms. [39]

3.2.2 Combination Wave Generator Layout

The circuit diagram for a 1.2/50 μs - 8/20 μs combination wave generator is given in [39], and can be seen in Figure 3.4.

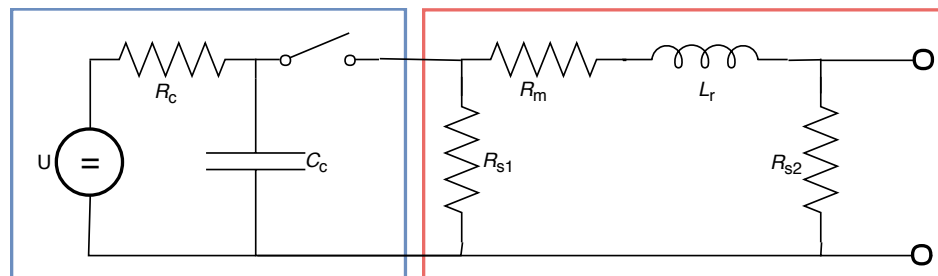


Figure 3.4: Circuit diagram of 1.2/50 μs -8/20 μs waveform generator [39].

In Figure 3.4, U represents a high-voltage source, R_c represents the charging resistor, C_c represents the energy storage capacitor, R_{s1} and R_{s2} represent pulse duration shaping resistors, R_m represents the impedance matching resistor, and L_r represents the rise time shaping inductor. [39]

The combination wave generator seen in Figure 3.4 appeared to be a simple, yet effective, manner of producing the 1.2/50 μs open-circuit voltage and 8/20 μs short-circuit current impulses specified by [39], and it is for these reasons that this topology was chosen when building the impulse generator.

The main obstacle when designing the combination wave generator was obtaining a sufficiently large capacitor C_c , capable of delivering the required peak current, and capable of being charged to the required peak voltage levels, at a reasonable cost. Another obstacle was obtaining a high-voltage source with which to charge capacitor C_c with. A mains-fed transformer with a rectifier at its output could be used as a high-voltage source to charge the capacitor C_c with, however this would require a somewhat bulky autotransformer in order to dial in an exact charge voltage. It was therefore decided to split the topology shown in Figure 3.4 into two sections, denoted by the blue and red rectangles.

The section encompassed by the red rectangle was termed the *pulse-shaping network*, the design and construction of which is documented in Section 3.3.

It was decided to construct the section encompassed by the blue rectangle in Figure 3.4 using a *Marx generator*. This solved the issue relating to finding a sufficiently large source to charge the capacitor C_c with, and the issue relating to finding an appropriate capacitor C_c . The design and construction of the Marx generator is documented in Section 3.4.

The topology shown in Figure 3.4 also does not allow for the applied impulse to ever fall to zero while the switch is closed. One could choose R_c to be sufficiently large to prevent the capacitor C_c recharging to any value of significance while the switch is closed. This would, however, have the undesirable effect of increasing the time taken to recharge the capacitor C_c when the switch was finally opened after a discharge - lowering the repetition rate of the generator. It was decided to replace resistor R_c with a semiconductor-based switching circuit capable of being switched by a microcontroller in order to allow the operator to have complete control over exactly when capacitor C_c can be charged, allowing the

output waveform of the impulse generator to drop to zero. This semiconductor-based switching circuit also has a low on-state resistance, allowing for capacitor C_c to be rapidly recharged. The design and construction of this circuit, labelled the *charge-controlling module*, is documented in Section 3.6.

3.3 Pulse-Shaping Network

3.3.1 Design of Pulse-Shaping Network

In order to pick component values for use in the pulse-shaping network, an understanding of how they influence the open-circuit voltage and short-circuit current waveforms was necessary. To begin the process of gaining this understanding, the equations for the output voltage waveforms were derived from first principles.

3.3.1.1 Mathematical description of open-circuit voltage and short-circuit current waveforms

The chosen pulse-shaping network topology, as shown in Figure 3.5, was based on the section of the combination wave generator mentioned in [39] responsible for ensuring the produced impulse conformed to the required specifications. An adjustable output resistor R_4 was added in order to allow for adjustment of the effective output impedance.

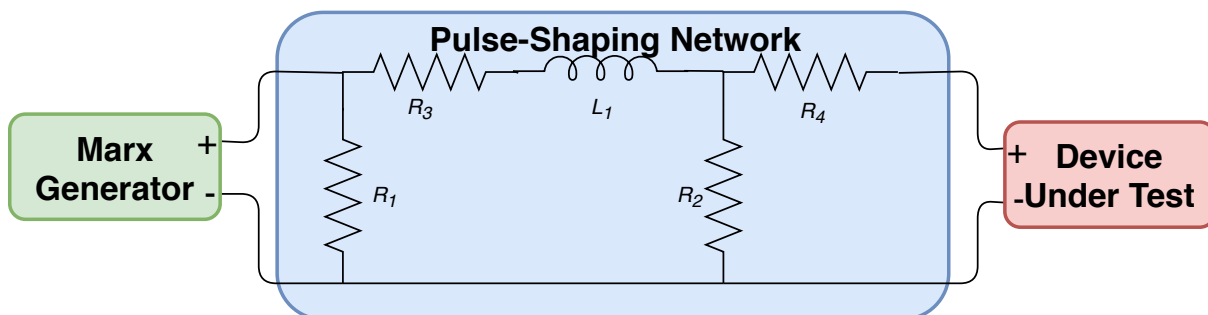


Figure 3.5: The circuit diagram of the chosen pulse-shaping network topology.

Equations A.22 and A.39 describe the theoretical open-circuit voltage and short-circuit current waveforms at the output of the pulse-shaping network. The full derivation of these equations is documented in Appendix A (hence the equation numbers beginning with the prefix label "A.").

$$v_{oc}(t) = V_{C_0} \frac{R_2}{L} \tau_1 e^{\frac{-t}{\tau_2}} (1 - e^{\frac{-t}{\tau_1}}) \quad (\text{A.22})$$

where

$$\tau_1 = \frac{CLR_1}{\sqrt{C^2 R_1^2 (R_2 + R_3)^2 - CL(4R_1^2 + 2R_1(R_2 + R_3) + L^2)}} \quad (\text{A.23})$$

$$\tau_2 = \frac{2CLR_1}{CR_1(R_2 + R_3) + L - \sqrt{C^2R_1^2(R_2 + R_3)^2 - CL(4R_1^2 + 2R_1(R_2 + R_3)) + L^2}} \quad (\text{A.24})$$

$$i_{sc}(t) = \frac{V_{c0} \left(\frac{R_2}{R_2 + R_4} \right) e^{-\frac{t}{\tau_{sc}}} \sin(\omega'_{sc} t)}{\omega'_{sc} L} \quad (\text{A.39})$$

where

$$R_{eq} = R_2 || R_4 = \frac{R_2 R_4}{R_2 + R_4} \quad (\text{A.27})$$

$$\tau_{sc} = \frac{2CLR_1}{L + CR_1 R_3 + CR_1 R_{eq}} \quad (\text{A.31})$$

$$\omega_{sc} = \frac{\sqrt{-R_1^2 C^2 (R_3^2 + 2R_3 R_{eq} + R_{eq}^2) + 2R_1 CL(2R_1 + R_3 + R_{eq}) - L^2}}{2CLR_1} \quad (\text{A.37})$$

An equation for the 1.2/50 μs waveform is documented in [40], shown here in Equation 3.1.

$$V(t) = AV_p (1 - e^{-\frac{t}{\tau_1}}) e^{-\frac{t}{\tau_2}} \quad (\text{3.1})$$

where

$$\tau_1 = 0.4047 \quad \mu\text{s} \quad (\text{3.2})$$

$$\tau_2 = 68.22 \quad \mu\text{s} \quad (\text{3.3})$$

$$A = 1.037 \quad (\text{3.4})$$

Equation A.22 was specifically rearranged into the same form as Equation 3.1, in order to provide ideal values for τ_1 and τ_2 , and for the equivalences shown in Equations 3.5 and 3.6 to be stated.

$$V_p = V_{C_0} \quad (\text{3.5})$$

$$A = \tau_1 \frac{R_2}{L} \quad (\text{3.6})$$

These known values for τ_1 , τ_2 , and A allowed for a quick sensibility-check when choosing component values for capacitor C_1 , inductor L_1 , resistors R_1 , R_2 , R_3 , and R_4 , ensuring that appropriate component values were being chosen.

Equations for the peak open-circuit voltage and peak positive and negative short-circuit currents could then be derived, as shown in Equations A.26, A.41, and A.44, respectively.

$$v_{\text{ocpeak}} = V_{C_0} \frac{R_2}{L} \tau_2 \left(\frac{\tau_1}{\tau_1 + \tau_2} \right)^{\frac{\tau_1 + \tau_2}{\tau_2}} \quad (\text{A.26})$$

$$i_{\text{scpeak}} = \frac{V_{C_0} \tau_{\text{sc}} \left(\frac{R_2}{R_2 + R_4} \right) e^{-\frac{\tan^{-1}(\tau_{\text{sc}} \omega'_{\text{sc}})}{\tau_{\text{sc}} \omega'_{\text{sc}}}}}{L \sqrt{1 + (\tau_{\text{sc}} \omega'_{\text{sc}})^2}} \quad (\text{A.41})$$

$$i_{\text{scmin}} = \frac{-V_{C_0} \tau_{\text{sc}} \left(\frac{R_2}{R_2 + R_4} \right) e^{-\frac{\tan^{-1}(\tau_{\text{sc}} \omega'_{\text{sc}}) + \pi}{\tau_{\text{sc}} \omega'_{\text{sc}}}}}{L \sqrt{1 + (\tau_{\text{sc}} \omega'_{\text{sc}})^2}} \quad (\text{A.44})$$

3.3.1.2 Determination of component values for pulse-shaping network

A function was defined in MATLAB which took the component values for inductor L_1 , resistors R_1 , R_2 , R_3 , and R_4 as inputs, computed the performance specifications using the given inputs, compared the computed performance specifications with the target performance specifications, applied a weighting factor, and returned a vector Y . The component value for capacitor C_1 was not used as an input variable as its value had already been chosen as $18.33 \mu\text{F}$ (the motivation for this choice is given in Section 3.4).

The input variable for the MATLAB function was defined as vector X_0 , as shown in Equation 3.7.

$$X_0 = \begin{bmatrix} L \\ R_1 \\ R_2 \\ R_3 \\ R_4 \\ V_{C_0} \end{bmatrix} \quad (3.7)$$

A vector t was defined, which represented the time-span of interest for the open-circuit voltage and short-circuit current curves. Vector t was made up of 100 001 samples, spanning the region 0-200 μs .

```
samples = 100000+1;
duration_us = 200*10^-6;
t = linspace(0, duration_us, samples);
```

The sampling rate could therefore be calculated as shown in Equation

$$f_s = \frac{100000 \text{ samples}}{200 \mu\text{s}} = 500 \text{ MHz} \quad (3.8)$$

Equation A.22 and Equation A.39 were used to calculate the open-circuit voltage and short-circuit current curves, respectively, over the interval specified by vector t . Performance specifications, shown in Table 3.3, were extracted from these curves. Equations A.26,

A.36, and A.44 were used to calculate their respective parameters, which were validated against the data from the sampling of the open-circuit voltage and short-circuit current equations.

A set of target specifications (represented by the variables shown in Table 3.4) was devised from the Level 2 test level specified in [39] (shown in Table 3.2).

Table 3.3: Specifications extracted from the open-circuit voltage and short-circuit current curves computed in MATLAB.

Parameter	Description
$T_{1,oc}$	The front time of the open-circuit voltage curve.
$T_{2,oc}$	The time to half value of the open-circuit voltage curve.
$T_{1,sc}$	The front time of the short-circuit current curve.
$T_{2,sc}$	The time to half value of the short-circuit current curve.
$V_{oc,peak}$	The peak value of the open-circuit voltage curve.
$V_{sc,peak}$	The peak value of the short-circuit current curve.

Table 3.4: The target performance specifications for the pulse-shaping network.

Parameter	Value
$T_{1,oc,target}$	1.2 μ s
$T_{2,oc,target}$	50 μ s
$T_{1,sc,target}$	8 μ s
$T_{2,sc,target}$	20 μ s
$V_{oc,peak,target}$	1000 V
$V_{sc,peak,target}$	500 A

The ratio of the computed performance specifications to the target performance specifications was then offset by -1 in order for the result to be centred around 0. The absolute value was then taken, followed by multiplication with a weighting factor. The resulting vector Y , as shown in Equation 3.9, was returned to the genetic algorithm. If all target performance specifications were met perfectly, Y would be a vector of zeros.

$$Y = \begin{bmatrix} K_{oc,peak} \times \left| \frac{V_{oc,peak}}{V_{oc,peak,target}} - 1 \right| \\ K_{sc,peak} \times \left| \frac{V_{sc,peak}}{V_{sc,peak,target}} - 1 \right| \\ K_{T_{1,oc}} \times \left| \frac{T_{1,oc}}{T_{1,oc,target}} - 1 \right| \\ K_{T_{2,oc}} \times \left| \frac{T_{2,oc}}{T_{2,oc,target}} - 1 \right| \\ K_{T_{1,sc}} \times \left| \frac{T_{1,sc}}{T_{1,sc,target}} - 1 \right| \\ K_{T_{2,sc}} \times \left| \frac{T_{2,sc}}{T_{2,sc,target}} - 1 \right| \end{bmatrix} \quad (3.9)$$

The genetic algorithm was run, and a matrix of possible component values was returned. Two cost functions were used to provide two possible sets of component values. The first cost function found the combination of component values in Y with the lowest sum, and the second cost function found the combination of component values in Y with the lowest product.

Both results were examined, with the summed cost function providing the more appropriate result. The input variables used in the lowest cost instance were adjusted manually, until the output shown in Figure 3.6 was achieved. The component values which resulted in this response are shown in Table 3.5. Timing parameters were chosen to be more important than magnitude parameters, as magnitude parameters are simpler to adjust. Timing parameters were therefore assigned weights of 20, whilst magnitude parameters were assigned weights of 1.

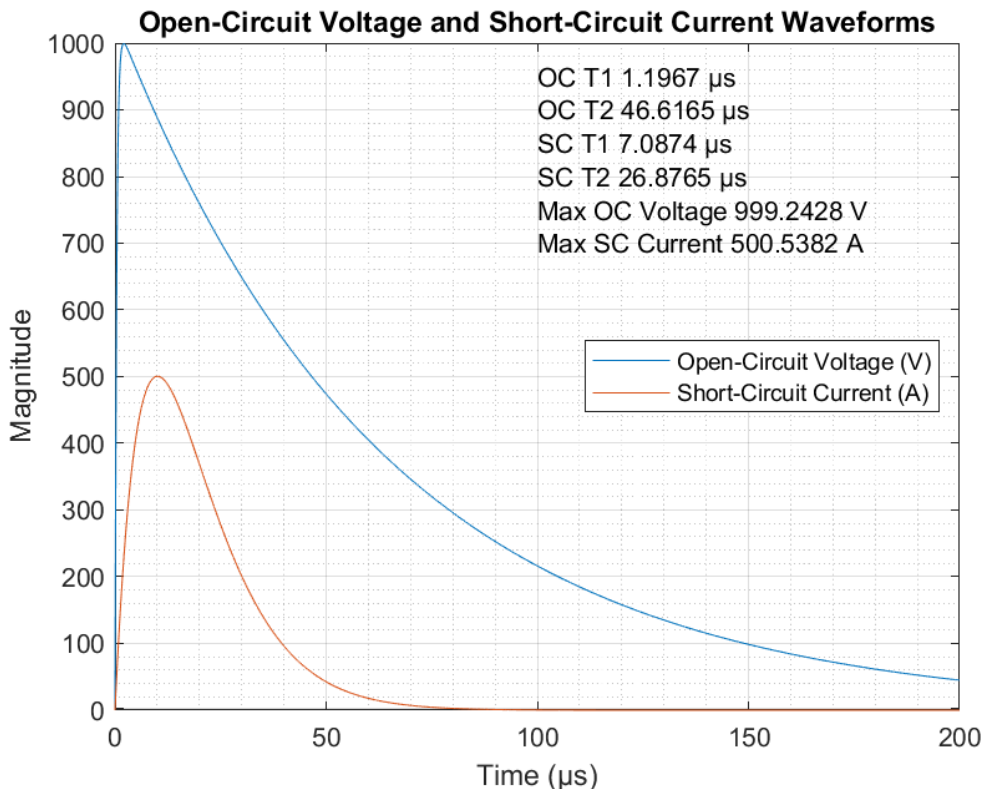


Figure 3.6: The theoretical open-circuit voltage and short-circuit response of the pulse-shaping network after adjustment of the computed component values.

Table 3.5: The component values chosen for the pulse-shaping network.

Variable	Value
L	$7.1 \mu\text{H}$
R_1	4.35Ω
R_2	17.4Ω
R_3	0Ω
R_4	1.41Ω
V_{C_0}	1031 V

It should be noted that all target performance specifications were met within the tolerances shown in Table 3.1, except for the time to half-value of the short-circuit current (which was $2.88 \mu\text{s}$ longer than the tolerance allowed for). A value of 0Ω for resistor R_3 produced good results, indicating that the resistance of the inductor should be as low as possible.

3.3.2 Simulation of Pulse-Shaping Network

The pulse-shaping network was simulated in Simulink in order to verify that the equations for the waveforms derived in Section 3.3.1 were correct.

The circuit (shown in Figure 3.7) was simulated using the component values in Table 3.5, and the resulting waveforms can be seen in Figure 3.8. For simulation of the open-circuit voltage, the LOAD resistor was set to $10\text{ G}\Omega$; for simulation of the short-circuit current, the LOAD resistor was set to $0\ \Omega$.

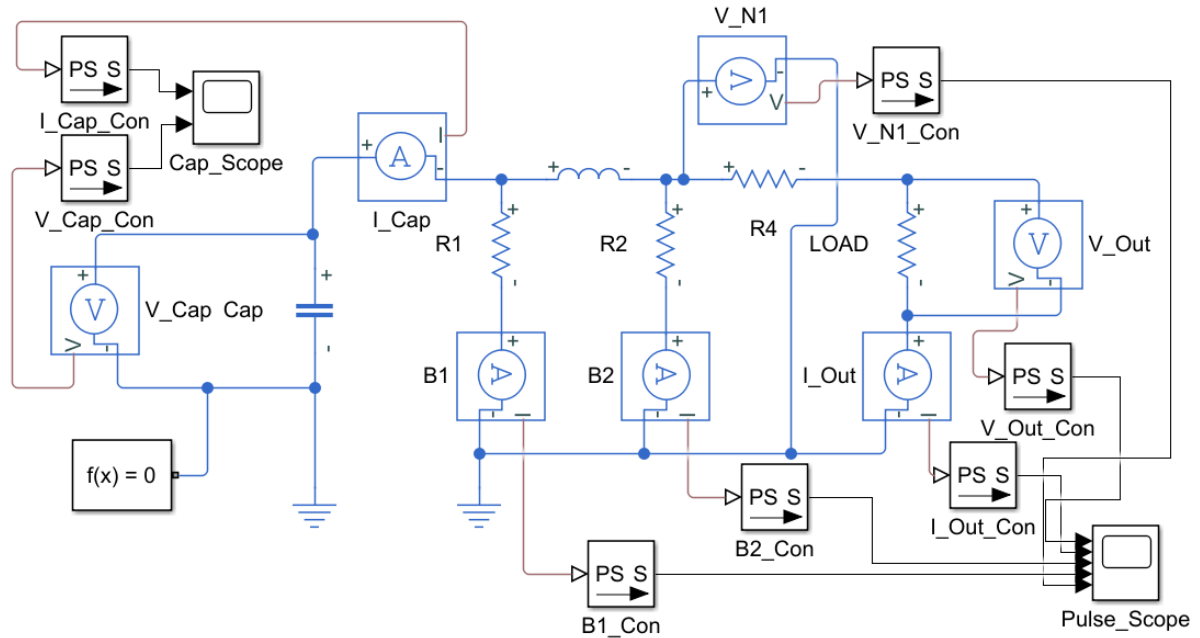


Figure 3.7: The circuit used for the simulation of the pulse-shaping network.

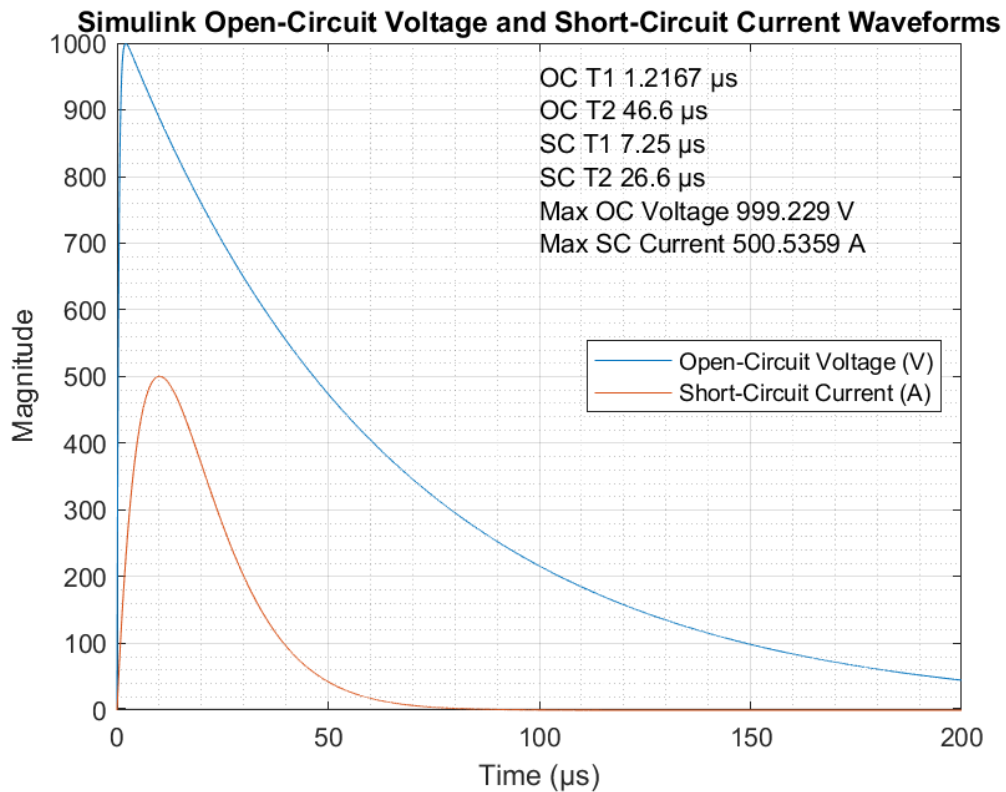


Figure 3.8: The simulated open-circuit voltage and short-circuit response of the pulse-shaping network.

Comparing the simulated waveforms (Figure 3.8) with the derived waveforms (Figure 3.6) shows strong agreement between both the shapes of the waveforms and the extracted parameters. This agreement between the simulated and derived results serves to validate the derivation procedure followed.

This simulation also allowed for the value of the peak current the capacitor would need to deliver to be extracted - an important value in the design of the Marx generator. A peak capacitor output current of 710 A was computed. The simulated voltage and current waveforms at the output of the capacitor can be seen in Figure 3.9.

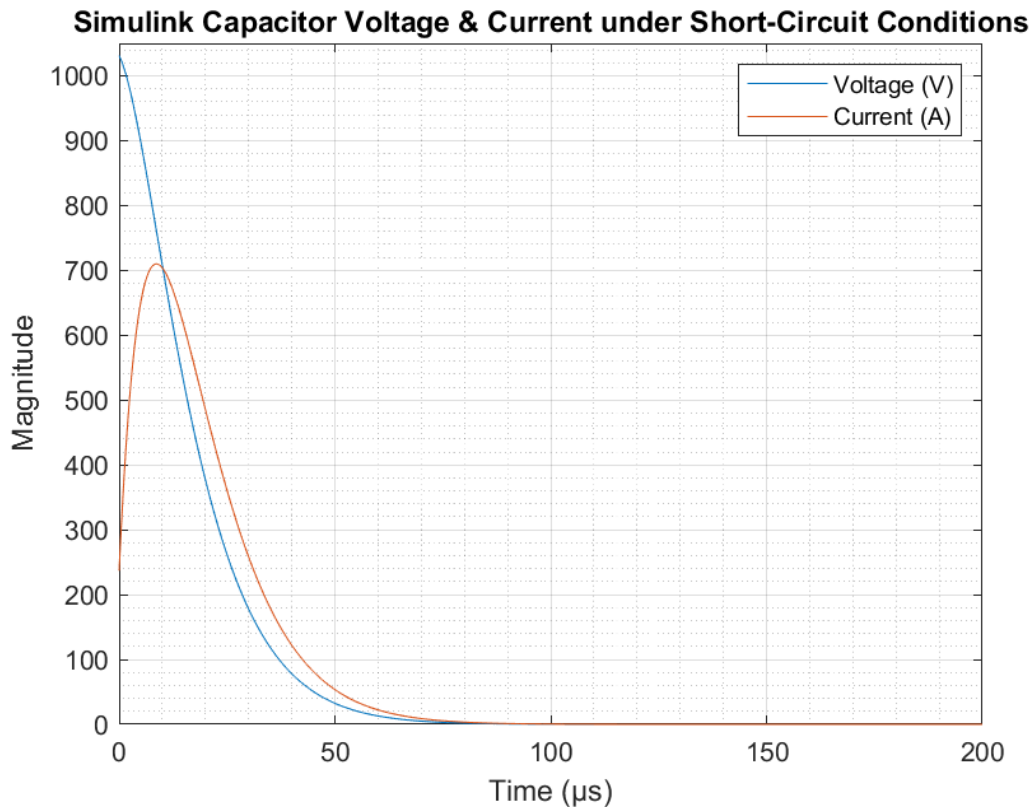


Figure 3.9: The simulated current and voltage waveforms at the output of the capacitor.

3.4 Marx Generator

As mentioned in Section 3.2.2, a Marx generator was chosen in order to avoid potential issues relating to sourcing a suitably high-voltage DC source (with which to charge the capacitor in the impulse generator), as well as capacitor with sufficient capacitance, peak permissible current, and peak rated voltage.

3.4.1 Marx Generator Principles

The Marx generator was first described by Erwin Otto Marx in 1924 [41]. Marx was a German electrical engineer, who invented the Marx generator while working at Hermsdorf-Schomburg-Isolatoren GmbH in order to perform experiments on the breakdown voltages of electrical insulators for high-voltage power lines [42].

At its core, a Marx generator is composed of a bank of capacitors which are charged in a parallel configuration and discharged in a series configuration. This mechanism acts as a voltage multiplier, allowing the generation of a large output voltage using a lower-voltage DC supply. Theoretically, a Marx generator composed of N capacitors charged from a source supplying X V, should produce a peak output voltage (often called the *erected voltage*) of $(X \times N)$ V.

The capacitors within a Marx generator are often charged via a resistor network, as shown in Figures 3.10 and 3.11, where R_c has a large value. The large value of R_c ensures that the current flowing through the charging resistors during the discharge process is negligible. The disadvantage of this large value of R_c is it lengthens the necessary charging time, lowering the repetition rate of the generator.

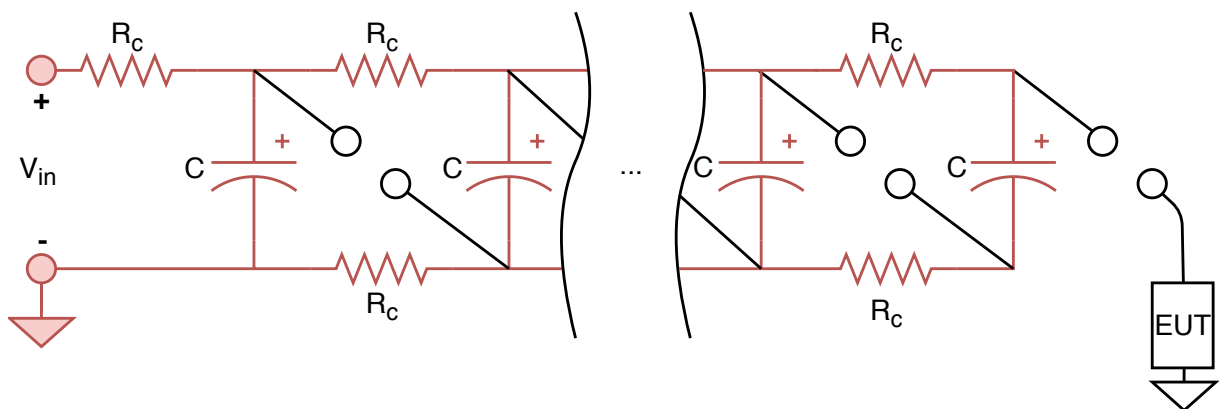


Figure 3.10: Charging mechanism of a spark gap switched Marx generator.

Traditionally, the parallel-to-series switching in Marx generators was accomplished using spark gaps (often in the form of gas discharge tubes) as shown in Figures 3.10 and 3.11. The breakdown voltage of the spark gaps is often chosen to be larger than the maximum capacitor charge voltage V_{in} , but smaller than $2V_{in}$. In Figure 3.10, the voltage over each spark gap is insufficient to trigger its operation, which is desirable during the charging process. The first spark gap is usually triggerable, as shown in Figure 3.11.

When the first spark gap is triggered, the first and second capacitors are placed in series, resulting in a voltage of $2V_{in}$ over the second spark gap. The second spark gap therefore breaks down, resulting in a voltage of $3V_{in}$ over the third spark gap, and so forth. Eventually, the final spark cap begins conducting, resulting in an electrical impulse being delivered to the EUT. If the timing of the impulse is not of importance, then a non-triggerable first spark gap with a breakdown voltage of less than V_{in} may be used. In this case, the capacitors would not finish their full charging cycle.

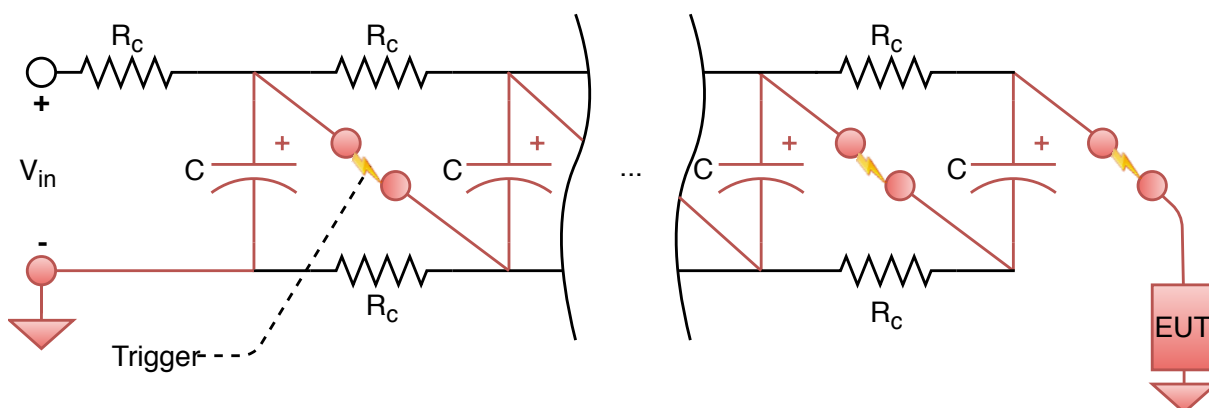


Figure 3.11: Discharging mechanism of a spark gap switched Marx generator.

Marx generators can be classified into four useful categories - large, moderate, compact, and solid-state [43].

Large Marx generators are often found in high energy systems, such as the Z Pulsed Power Facility at Sandia National Laboratories, which is able to deliver up to 5.4 MV and 23 MJ with a 1.5 μ s time to peak, and is used for anything from research involving the extraction of material parameters, to research relating to nuclear fusion as a potential source of energy, to research associated with nuclear weapon reliability [44]. Large Marx generators generally have low repetition rates as a result of their immense energy requirements [43].

Moderate Marx generators are typically able to generate voltages between a few hundred kV to a few MV, with maximum energies up to the low MJ level [43].

Compact Marx generators are able to generate voltages in the region of a few hundred kV to 1 MV, but have relatively lower pulse energies (between 10 J and 1 kJ) [43]. An example is that described in [45], which is used for pulse charging wide band antenna elements. Compact Marx generators are often used as trigger generators for larger systems [43],[45].

Solid-state Marx generators are able to generate voltages up to a few kV, with pulse energies in the range from less than 1 J to few joules. These Marx generators make use of solid-state (semiconductor-based) switches instead of spark gaps in order to accomplish the parallel-to-series switching of the capacitors. Due to the low energies involved, as well as the capabilities of solid-state switches, solid-state Marx generators are able to have repetition rates of 100 kHz or more. [43]

3.4.2 Marx Generator Design

As the levels at which a bypass diode may fail were still unknown, it was decided to design for as high a maximum output voltage and current output as reasonably possible for a PCB-based (printed circuit board) Marx generator. The minimum design goal of satisfying the Level 1 test level of [39] - 500 V (open-circuit) and 0.25 kA (short-circuit) - was chosen, with the capability of achieving higher test levels viewed as an additional benefit. The DC power supply from which the Marx generator would be charged had an output voltage range of 0-320 V. It was decided that a six-stage Marx generator would be constructed in order to produce an output voltage roughly six times that of the input voltage, theoretically allowing for Marx generator output voltages of up to 2 kV to be produced using the available DC power supply.

A modular approach was taken when designing the Marx generator. This allowed for the adaptation of the Marx generator to changing test requirements. The work presented in this section was briefly documented in [9], presented at the 26th South African Universities Power and Engineering Conference (SAUPEC 2018).

As in a traditional Marx generator, multiple modules could be placed in series with each other if an increased output voltage is desired. During the charge phase, each module would charge to the voltage of the previous stage (minus a diode drop). During the discharge phase, the switches would reconfigure the modules into a series configuration, multiplying the output voltage by the number of series-connected modules [9].

Should an increased output current be desired, multiple modules (or strings of series-connected modules) could be placed in parallel in order to increase the discharge current capacity [9]. A basic overview of the designed module is shown in Figure 3.12.

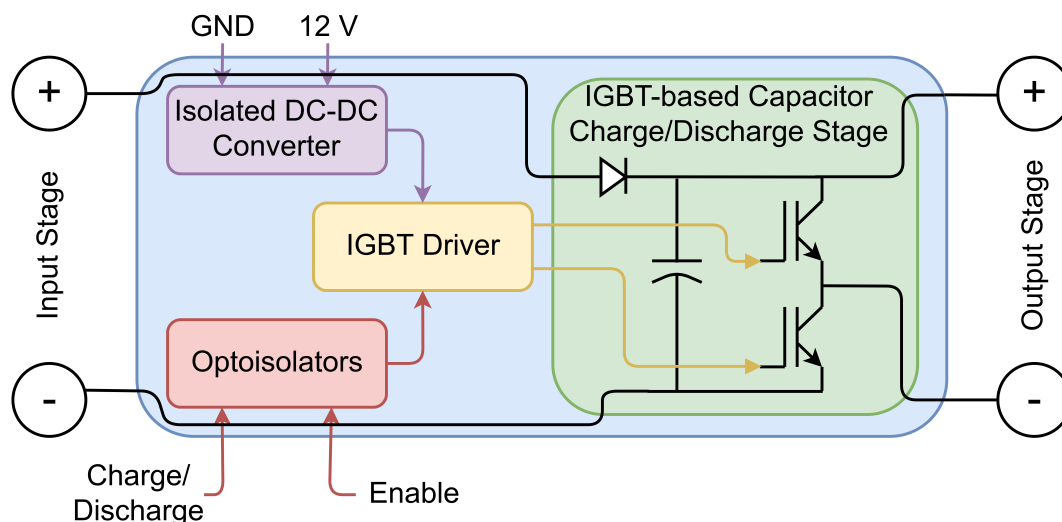


Figure 3.12: A simplified diagram of the designed Marx generator module [9].

It was decided to make use of solid state switches in order to have precise control over when the Marx generator would charge or discharge. Solid-state switches are more compact and predictable than spark-gaps or gas-discharge tubes, further justifying their use in this application. Modern solid-state switches are able to provide large isolation voltages and have fast switching times, while remaining cost-effective.

The Toshiba GT40WR21 N-Channel Insulated-Gate Bipolar Transistor (IGBT) (specifications shown in Table 3.6) was the solid-state switch of choice. Its high isolation voltage (1800 V), high current (maximum 1 ms pulse current of 80 A), and switching time (t_{on} of 0.55 μ s) were the more important specifications considered. As solid-state switches are mainly used in power electronics applications (such as inverters) where switching frequencies are in the kHz range, the manufacturers do not specify maximum pulse currents for durations in the order of microseconds. At this point in the design process, it was also not known at which current magnitudes a bypass diode (usually rated for a maximum forward current of 10-20 A) would fail. A maximum guaranteed 1 ms pulse current of 80 A appeared to be a reasonable choice for the solid-state switch as it was estimated that a bypass diode would fail at a current lower than this. It was also speculated that more current could be conducted by the switch for shorter pulse periods - which turned out to be the case.

Table 3.6: Toshiba GT40WR21 IGBT specifications [46].

	Symbol	Rating	Unit
Collector-Emitter Voltage	V_{CE}	1800	V
Collector Current (DC)	I_C	40	A
Collector Current (1 ms Pulse)	I_{CP}	80	A
Switching Time (Turn-On Time)	t_{on}	0.55	μ s

The relationship between the pulsed (1 ms) conduction current I_C and collector-emitter voltage V_{CE} at room temperature (25 °C) for the Toshiba GT40WR21 IGBT are shown in Figure 3.13. It shows that a higher gate-emitter voltage V_{GE} should be used in order to keep V_{CE} as low as possible during high values of I_C . It is desirable to keep V_{CE} as low as possible in order to minimise the voltage drop over the IGBT, resulting in higher Marx generator output voltages and lower conduction losses within the IGBT. As the microcontroller was only capable of producing an output voltage of 5V, it would not be capable of directly driving an IGBT. An IGBT gate driver was therefore required.

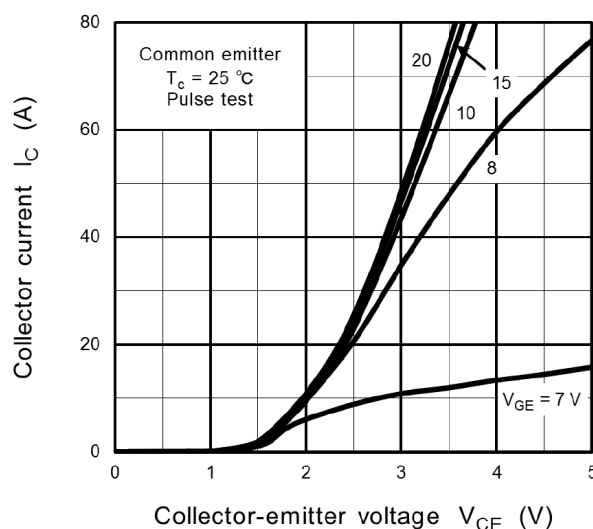


Figure 3.13: The relationship between I_C (1 ms pulse) and V_{CE} for the Toshiba GT40WR21 IGBT [46].

As the maximum rated current for the IGBT was 80 A, graphs for the collector-emitter voltage V_{CE} were only plotted up to this current. At this current, it was shown that V_{CE} was equal to about 3.6 V. Multiplying the equation for a 500 A, 8/20 μ s impulse with this value of V_{CE} resulted in an equation for the instantaneous power dissipated within the IGBT. Integrating this equation with respect to time resulted in the total energy conducted by an IGBT during a discharge pulse - a value of 30.5 mJ. As this energy dissipation per discharge cycle was so small, it was decided that additional cooling for the IGBT would not be necessary, considering the minimum repetition rate of 1 impulse per minute (specified in [39]).

The International Rectifier IR2104SPbF was selected as the IGBT gate driver. This gate driver has a fast typical turn-on rise time t_r of 100 ns, and is capable of delivering output voltages of 10-20 V, a maximum positive output current of 130 mA. Since the switches this Marx generator were required to turn on at the beginning of an impulse and only turn off after the impulse had completed, the propagation delay of the signals within the gate driver was not a factor which needed to be taken into account. This gate driver has two logic inputs, IN and \overline{SD} . IN represented the logic input for the high-side/low-side switching of the IGBTs, and \overline{SD} was the shutdown logic input. The gate driver would not switch either IGBT on without \overline{SD} receiving a logical high input - this led to the \overline{SD} input being used as a safety to prevent accidental discharging of the impulse generator. During the design process, the IN and \overline{SD} signals were referred to as "Charge/Discharge" and "Enable", respectively.

Gate driver outputs with complementary switching were a necessity, as it was critical to avoid an instance where the upper and lower IGBTs within a module would conduct simultaneously, effectively short-circuiting the high-voltage capacitor to which they are connected (a phenomenon commonly referred to as *shoot-through*). The term *deadtime* refers to an intentional delay between the changing of the high-side and low-side IGBT gating signals, in order to prevent the IGBTs conducting simultaneously (as shown in Figure 3.14). A deadtime of 520 ns is provided by the gate driver, which is far longer than the turn-on rise time (t_r of 100 ns) or turn-off fall time (t_f of 50 ns).

It should be mentioned that shoot-through was only a concern when changing from the charging state (low-side IGBT conducting, high-side IGBT not conducting) to the discharging state (low-side IGBT not-conducting, high-side IGBT conducting). At this instant, the capacitor would be fully charged. When changing from the discharging state to the charging state, a module's capacitor would be fully discharged - therefore there would be no concern for potential damage if shoot-through were to occur. The capacitors are only able to recharge when the charge-controlling module (documented in Section 3.6) begins conducting, connecting the high-voltage DC source to the Marx generator.

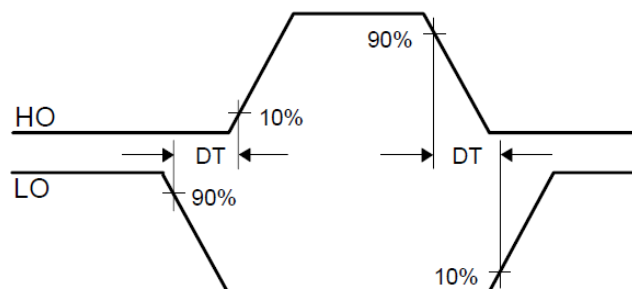


Figure 3.14: The concept of deadtime [47].

A number of factors had to be considered when choosing a suitable capacitor. As previously mentioned in Section 3.2.2, the chosen capacitor would need to be capable of storing a suitable amount of charge, be capable of delivering a sufficiently large peak current, be capable of being charged to adequately large voltage levels, and ideally remain cost-effective.

As mentioned in Section 3.3.2, the simulation circuit used in Figure 3.8 allowed for the maximum current required by the pulse-shaping network under short-circuit conditions to be determined, in order to satisfy the Level 2 test level from [39].

Since the total capacitance of series-connected capacitors is governed by Equation 3.10, the total capacitance of a six-stage Marx generator would be the capacitance used in each stage divided by six. As large a capacitance as reasonably possible was desired when choosing the capacitor in order for the total capacitance to remain sufficiently large.

$$\frac{1}{C_{\text{tot}}} = \frac{1}{C_1} + \frac{1}{C_2} + \frac{1}{C_3} + \frac{1}{C_4} + \frac{1}{C_5} + \frac{1}{C_6} = \frac{6}{C_{\text{stage}}} \quad (3.10)$$

The Panasonic EZPE50117MTA metalised polypropylene film capacitor was found to be a suitable option. This capacitor has a capacitance of 110 μF (which would theoretically result in total Marx generator capacitance of 18.333 μF) and a voltage rating of 500 V (greater than the maximum voltage capable of being supplied by the DC power supply). A polypropylene film capacitor was specifically chosen due to its low equivalent series resistance (ESR) (resulting in losses within the Marx generator) and its high peak current (greater than the minimum required current of 710 A mentioned in Section 3.3.2). For the sake of comparison, the chosen capacitor is compared with an electrolytic capacitor of the same voltage rating and similar capacitance in Table 3.7. The capacitor is the component in the Marx generator with the lowest voltage rating. It would therefore be the first component to consider upgrading if larger output voltages were desired.

Table 3.7: Metalised Polypropylene vs Aluminium Electrolytic Capacitors [48],[49].

	Panasonic EZPE50117MTA	TDK B43541A6107M0
Type	Metalised Polypropylene Film	Aluminium Electrolytic
Capacitance [μF]	110	100
Voltage Rating [V]	500	500
ESR [$\text{m}\Omega$]	4.4	920
Peak Current [A]	1540	1.78

Traditionally, as shown in Figure 3.10, the capacitors in a Marx generator were charged through a large resistor network. These resistances were larger than the resistance of the output path of the generator, therefore little current would flow through them during a discharge cycle. In the design of this Marx generator, it was decided not to make use of a resistor-based charging network in order to decrease the duration necessary to recharge the capacitors. Diodes were added at the input of each module in order to prevent the discharge of a module's capacitor through the IGBT of the previous module when the IGBT begins conducting.

Referring to the two-stage Marx generator shown in Figure 3.15, it can be seen that if it were not for the diode at the input of Module 2, then Module 2's capacitor would be short-circuited through the upper IGBT in Module 1 as soon as it began conducting.

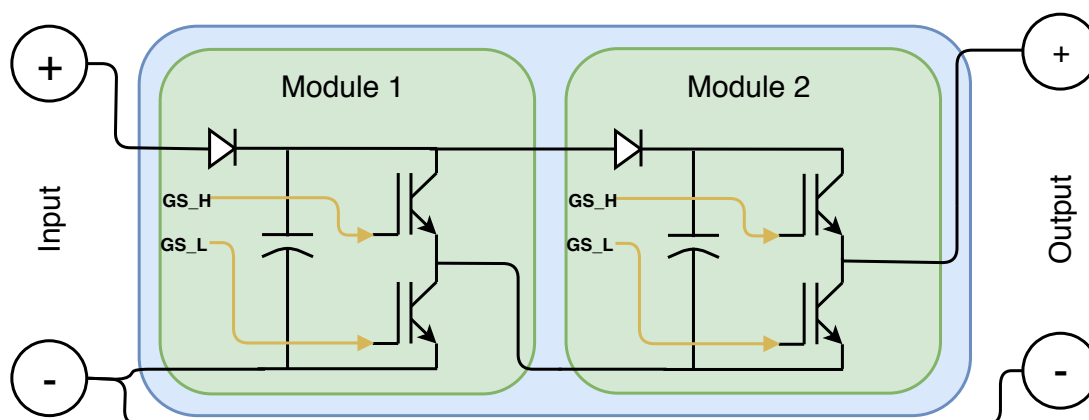


Figure 3.15: A two-stage solid-state Marx generator.

The diode would be required to have a maximum reverse voltage rating of greater than the maximum charge voltage of the capacitor (500 V), and have a maximum forward current greater than the current capacity of the DC power supply used to charge the Marx generator (200 mA). The Fairchild Semiconductor RHRP30120 was chosen due to its maximum reverse voltage rating of 1200 V and its maximum forward current of 20 A [50].

As the ground potential at which each stage would be at during a discharge cycle would be the sum of the total potentials of the previous stages, a method of transferring power and data signals for the IGBT gate drivers to each stage was required. Isolated DC-DC boost converters were used to provide power to the IGBT gate drivers. The chosen DC-DC converter was the XP Power ITV1215SA, which is able of producing an output voltage of 15 V from a source voltage of 12 V, and has DC isolation voltage of 3 kV [51]. Optocouplers were used to transfer the two command signals (Charge/Discharge and Enable) from the microcontroller to each IGBT gate driver. The chosen optocoupler was the Cosmo K1010, which has an isolation voltage of 5 kV [52].

3.5 Simulation of Impulse Generator

The discharge phase of the full impulse generator (pulse-shaping network and Marx generator) was simulated in Simulink. The circuit used can be seen in Figure 3.18. The first capacitor was charged to 173.25 V, and every successive capacitor was charged to the voltage of the previous capacitor, minus a diode drop of 0.5 V - resulting an in average voltage of 172 V per stage (the result of dividing the V_{C_0} of 1031 V from Table 3.5 by the number of stages). The ESR of each capacitor was also taken into account. Figure 3.16 shows the output recorded for this simulation. Upon examination of the simulation output, it was noticed that the waveform timing parameters all agreed with

those previously simulated and calculated, however the peak magnitudes of the open-circuit voltage and short-circuit current were lower than those previously recorded.

All capacitor voltages were increased by 3 V, and the value of R_4 was adjusted to 1.381Ω . These adjustments corrected the peak magnitudes of the open-circuit voltage and short-circuit current waveforms, as can be seen in Figure 3.17.

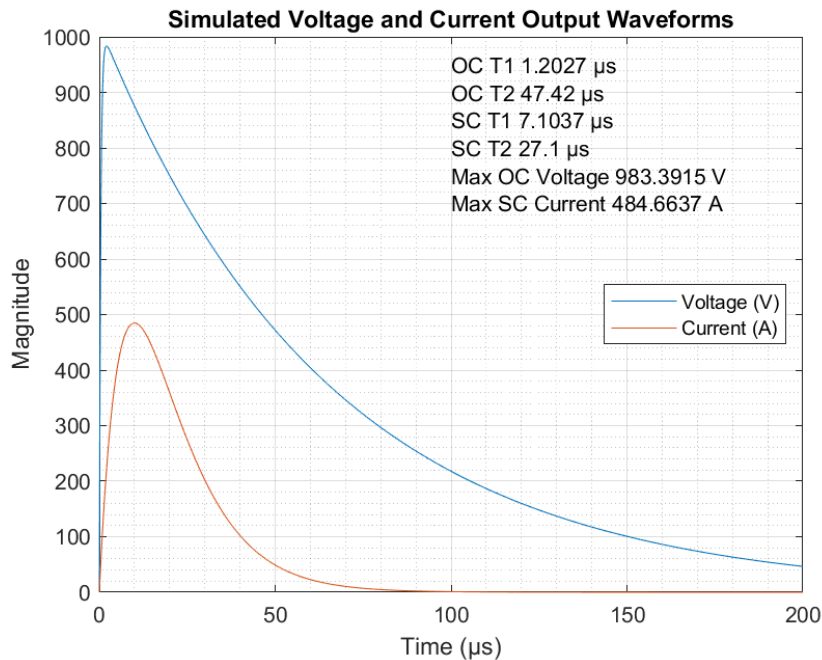


Figure 3.16: The open-circuit voltage and short-circuit current, using component values from Table 3.5.

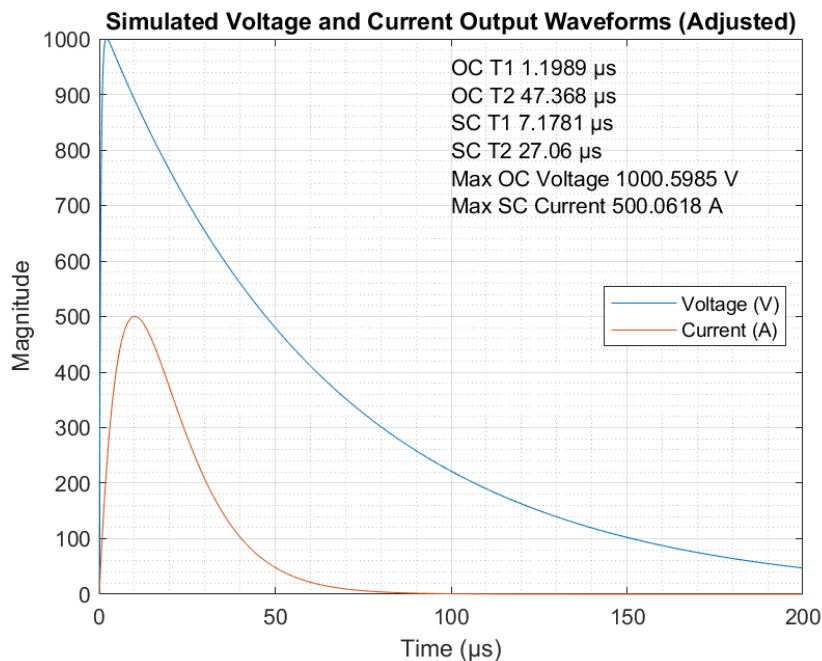


Figure 3.17: The open-circuit voltage and short-circuit current, after adjusting V_{C_0} and R_4 .

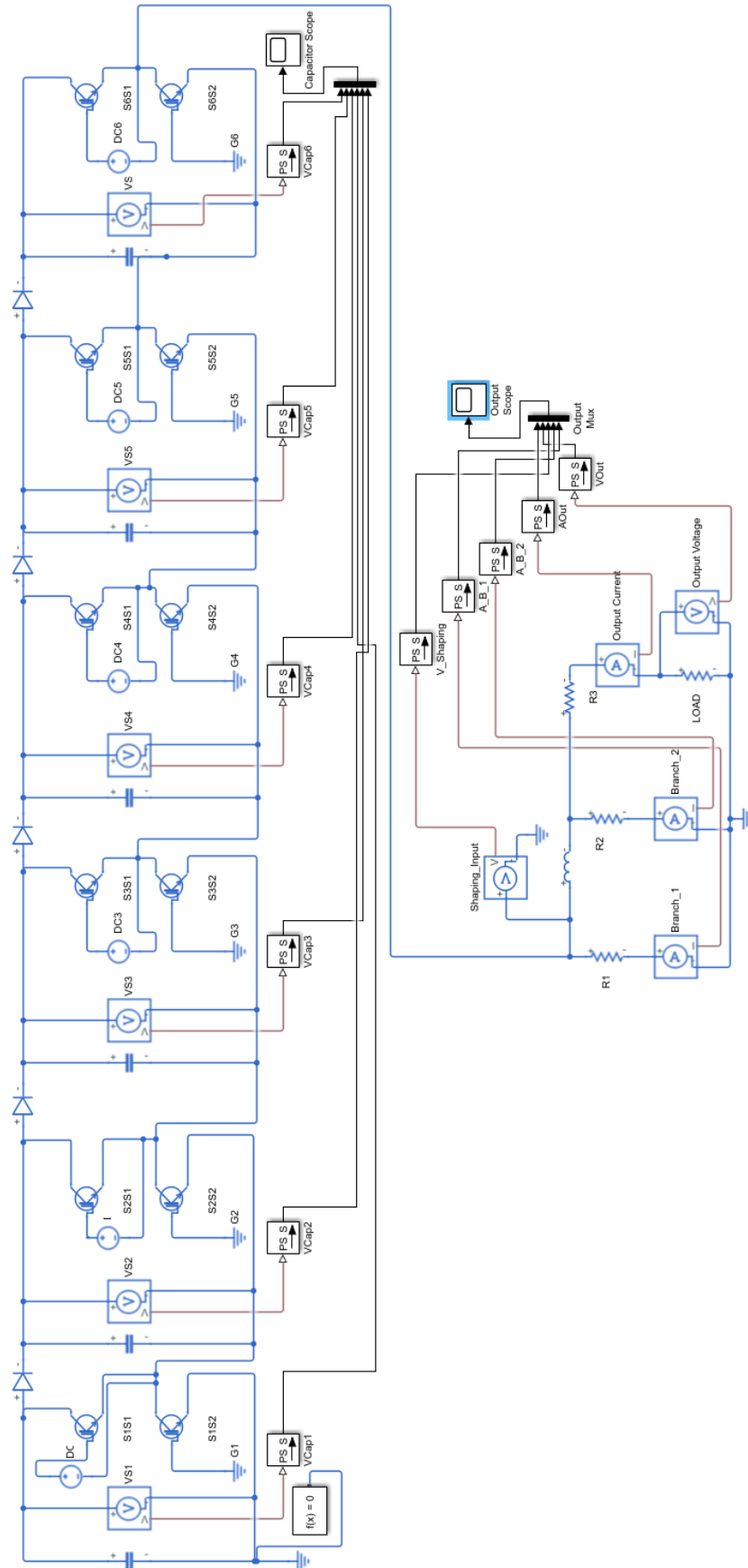


Figure 3.18: The circuit used for the simulation of the impulse generator.

3.6 Charge-Controlling Module

A method of connecting and disconnecting the Marx generator from the high-voltage DC power supply was needed. Before the initiation of a discharge cycle, the DC power supply was to be disconnected from the Marx generator in order for the output voltage of the Marx generator to fall to zero. This was accomplished by isolating the positive terminal of the high-voltage DC power supply from the input of the Marx generator.

A simple circuit with a solid-state switch was decided on. A relay would have sufficed, however a solid-state switch with a suitable isolation voltage (at least 320 V for the high-voltage DC power supply used) would have a smaller footprint than a relay with the same isolation voltage. The solid-state switch used was the same IGBT used in the Marx generator, and it was driven by the low-side output of the same model gate driver as used in the Marx generator. This IGBT had both sufficient isolation voltage 1800 V and sufficient current conduction capacity 40 A (DC), therefore it would easily handle the maximum current which the high-voltage DC power supply could supply (200 mA). Power was provided to the gate driver by the same isolated DC-DC converter used in the Marx generator, and the Charge/Discharge and Enable signals were provided to the gate driver by means of the same optocoupler used in the Marx generator.

The \overline{SD} logic input of the gate driver in the charge-controlling module was pulled permanently high, as it was decided that it was not as necessary to implement the same two-step safety procedure (pulling Enable high, followed by pulling Charge/Discharge high in order to initiate a discharge cycle) used in the Marx generator due to the comparatively lower voltages involved with the charge-controlling module.

The total charge required to charge all six capacitors in the six-stage Marx generator to 320 V is calculated in Equation 3.11.

$$Q_{\text{tot}} = 6C_{\text{tot}}V = 6 \times (110 \times 10^{-6}) \times 320 = 0.2112 \text{ C} \quad (3.11)$$

As the high-voltage DC source would likely be current-limited during the charge cycle (due to the low resistance of the charging circuit), the charging time can be approximated as shown in Equation 3.12. Consulting Figure 3.13, it can be seen that the collector-emitter voltage V_{CE} is negligible or a current of 0.2 A. This suggests that the power dissipated within the IGBT would also be negligible. Due to the short estimated charging duration, it was determined that little energy would be dissipated within the IGBT of the charge-controlling module, negating any need for additional cooling.

$$t = \frac{Q}{i} = \frac{0.2112}{0.2} = 1.056 \text{ s} \quad (3.12)$$

The charge-controlling module had a green LED which would illuminate when the Marx generator was disconnected from the high-voltage DC supply - indicating that the Marx generator was not currently charging. A non-illuminated LED would indicate that either the Marx generator was busy charging, or that the charge-controlling module was not receiving sufficient power - both steps requiring the user to be attentive.

An overview of the charge-controlling module is shown in Figure 3.19. For a more detailed description, please consult the schematic (shown in Figure D.3 in Appendix D).

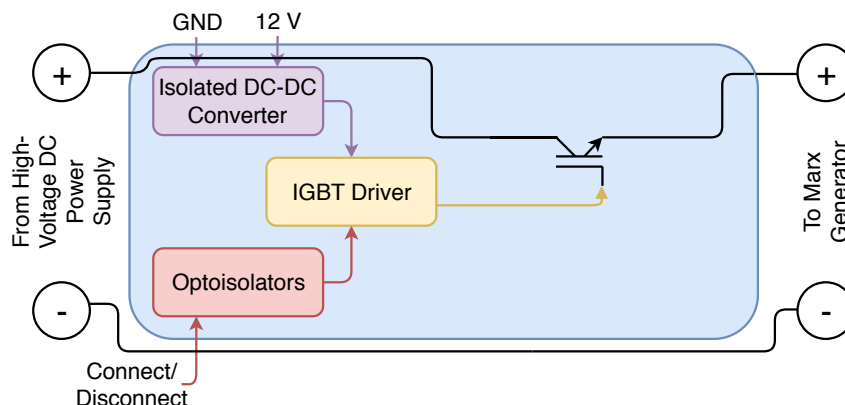


Figure 3.19: An overview of the charge-controlling module.

3.7 Distribution Board

The distribution board was designed to solve two functional problems - distributing the same logic signals from the microcontroller to each module in the Marx generator, and distributing power from the 12 V DC power supply to the microcontroller (as well as to each module). The distribution board solved both of these issues in a simple manner.

A render of the PCB of the distribution board is shown in Figure 3.20. Eight 4-pin MTA100 male connectors occupied headers P1 to P8. For these headers, Pin 1 represented 12 V, Pin 2 represented Enable, Pin 3 represented Charge/Discharge, and Pin 4 represented 0 V. The microcontroller, as well as each Marx generator module, connected to one of these headers via a ribbon cable for power and logic connectivity. Although the microcontroller possessed sufficient digital output pins to provide two logic inputs to each stage, this approach would not work as the timing of the setting of the Charge/Discharge signal to a high logical output (starting a discharge) had to happen at the same time for each module. A delay of up to a few milliseconds between output signals would occur if using a separate output for each module. The same logic signal therefore had to be used to control all modules.

Header P9 was occupied by a 2-pin MTA100 male connector, with Pin 1 connected to 12 V and Pin 2 connected to 0 V. This header acted as the input for the 12 V DC power supply. Diode D1 glowed red when power was supplied to the distribution board. The full schematic is shown in Figure D.2 in Appendix D.

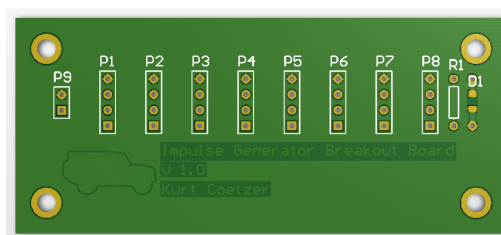


Figure 3.20: A render of the PCB of the distribution board.

3.8 PC Software

PC software (shown in Figure 3.21) was developed in order to allow the user of the impulse generator to operate its functions. The software was written in Python to allow for rapid development.

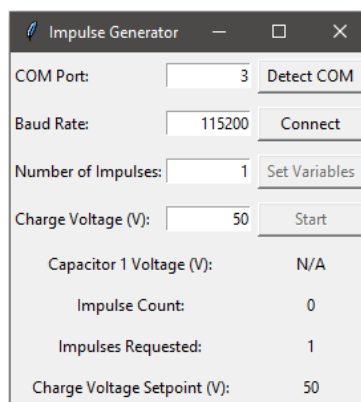


Figure 3.21: The impulse generator PC software.

To begin using the PC software, the user connects the microcontroller to the PC using a Universal Serial Bus (USB) Type B to USB Type A male-to-male cable. The user then launches the PC software and presses "Detect COM". This automatically detects the correct COM port to be used for serial communication between the microcontroller and the PC software. The standard baud rate for the impulse generator is 115200 bps, however the user is able to change the baud rate in the PC software if necessary.

The user is then able to input the desired charge voltage and number of impulses. Once these details are entered, the user clicks the "Start" button, and the impulse generator begins executing the requested number of impulses. It should be noted that the desired charge voltage is not the final output voltage which the impulse generator is able to supply, but rather approximately the voltage to which each stage in the generator will be charged to. The final output voltage is approximately the voltage to which each stage is charged, multiplied by the number of series-connected stages in the Marx generator portion of the impulse generator.

Whilst the impulse generator is in operation, feedback pertaining to the progress of the execution of the impulses is provided to the user. The user can view the total number of requested impulses, as well as how many impulses have been executed thus far. The voltage over the first capacitor in the Marx generator, as well as the requested voltage set-point, are also available. These voltages give the user an indication of the current state of charge of the Marx generator. The voltage over the first capacitor in the Marx generator is particularly useful information, as it gives the user an indication of whether or not the device is safe to handle when reconfiguration or maintenance is required. A notification is given once the requested number of impulses have been executed.

The program flow diagram for the PC software is shown in Figure 3.22. The PC software and microcontroller firmware are designed to work symbiotically. The PC software sends requests to the microcontroller over a USB connection. These requests are performed by the microcontroller, and a confirmation that the request has been successfully executed is echoed back to the PC software. Once the PC software receives this echo, it will progress to the next command in the queue. The software and firmware were designed in this way to prevent the instance where the Marx generator is busy executing a discharge cycle whilst the high-voltage DC power supply is connected to the Marx generator. If this were

3.9 Microcontroller

The ATmega2560 was the microcontroller of choice for controlling the charge and discharge cycles of the impulse generator. This was due to its availability in the form of the Arduino Mega 2560 development board, which allowed for rapid development of the firmware using the Arduino Integrated Development Environment (IDE) and Arduino C libraries.

Three digital outputs were required - two for the Charge/Discharge and Enable logic signals for the gate drivers in the Marx generator and one for the Connect/Disconnect signal in the charge-controlling module.

An analogue input pin was used for the sampling of the voltage of the capacitor in the first stage of the Marx generator (in order to determine whether a charge or discharge cycle had completed). A voltage divider (shown in the module PCB schematic in Figure D.1, in Appendix D) was used to scale the maximum charge voltage down to the input range of the ADC connected to the analog pin on the development board.

The resistive voltage divider used to sample the voltage of the capacitor in the first stage of the Marx generator was made up of a $1\text{ M}\Omega$ (actual resistance $977.2\text{ k}\Omega$) and a $15\text{ k}\Omega$ (actual resistance $14.752\text{ k}\Omega$) resistor. These resistors are referred to as R_1 and R_2 , respectively. The high input resistance ($100\text{ M}\Omega$) and low input capacitance (14 pF) of the analogue-to-digital converter (ADC) were too large and too small (respectively) to load the resistive voltage divider in such a way that it would not represent the true value of the DC voltage being measured [53]. Equation 3.13 was used to convert between the capacitor voltage V_{cap} and the ADC voltage V_{ADC} .

$$V_{\text{ADC}} = V_{\text{cap}} \times \frac{R_2}{R_1 + R_2} = V_{\text{cap}} \times \frac{14.753}{14.752 + 977.2} \quad (3.13)$$

The ADC is capable of reading voltage levels from 0 V to 5 V , outputting the result on a scale from 0 to 1023 (labelled X_{ADC}). Since it was known that the high-voltage DC source from which the generator was to be charged could deliver up to 320 V , the values of R_1 and R_2 were chosen such that the value read by the ADC at a capacitor voltage of 320 V would be 4.76 V - below the maximum input voltage of the ADC. This division results in almost the full input range of the ADC being used, giving maximum resolution. The value provided by the ADC was then calculated back to the true capacitor voltage using Equation 3.14.

$$V_{\text{cap}} = V_{\text{ADC}} \times \frac{5}{1023} \times \frac{R_1 + R_2}{R_2} \quad (3.14)$$

The microcontroller program flow diagram is shown in Figure 3.23. As mentioned in Section 3.8, the PC software and microcontroller firmware were designed to work symbiotically. Although the PC software will not progress to the next command in the queue until it has received an echo stating that the current command has been successfully executed, the microcontroller firmware still manually examines (and corrects) the Charge/Discharge and Connect/Disconnect states in order to ensure that the high-voltage DC power supply cannot be connected to the Marx generator while the Marx generator is busy executing a discharge cycle. This is intended to act as a second level of safety.

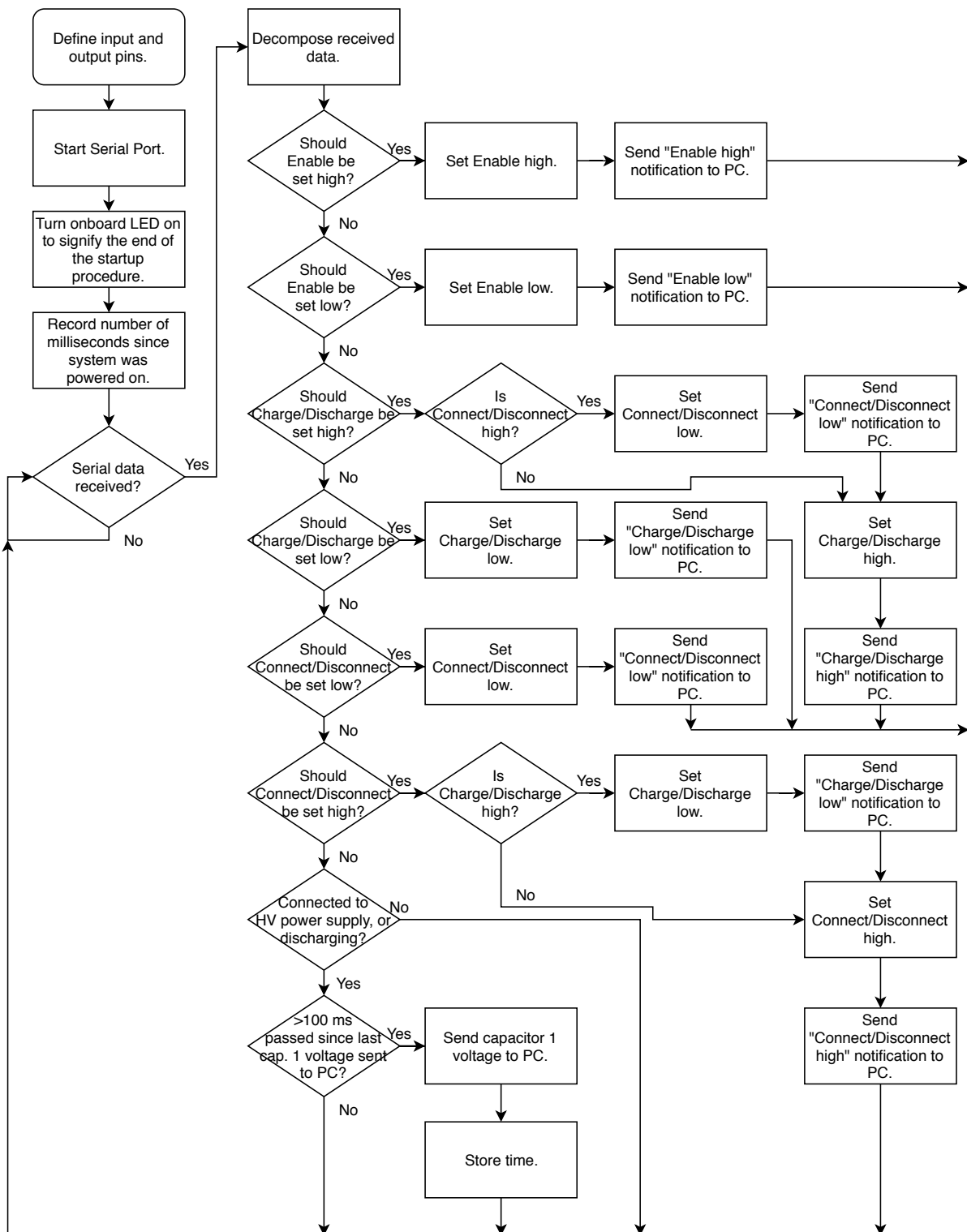


Figure 3.23: Microcontroller program flow diagram.

3.10 Impulse Generator Testing

The complete constructed impulse generator (the construction details are given in Appendix E) was tested in order to examine its conformance to the waveform timing parameters specified in [39].

Figure 3.24 shows the open-circuit voltage and short-circuit current waveforms recorded at the output. The high-voltage DC source from which the impulse generator was charged was set to 50 V when these waveforms were recorded. The recorded front time τ_1 of the open-circuit voltage waveform was 2.23 μs longer than the intended 1.2 μs value for τ_1 (exceeding the allowable $\pm 30\%$ tolerance). The recorded time to half-value τ_2 of the open-circuit voltage waveform was 0.9 μs shorter than the expected 50 μs value for τ_2 - well within the allowable $\pm 20\%$ tolerance. The recorded front time τ_1 and time to half-value τ_2 of the short-circuit current waveform were 7.5 μs and 23.7 μs longer than intended, respectively (both outside of the allowable $\pm 20\%$ tolerance). The peak recorded open-circuit voltage was 252.6 V, and the peak short-circuit current was 122.47 A, giving an effective output impedance (as defined in Section 3.2.1) of 2.06 Ω . Resistor R_4 was set to 0.5 Ω in order to achieve this effective output impedance. From observing the slower than expected short-circuit current waveforms, it was clear that an excessive amount of series inductance was present in the test setup - likely a result of the self-inductance of the rheostat used to represent resistor R_4 . No undershoot was recorded, therefore the undershoot requirement of less than 25% had been met.

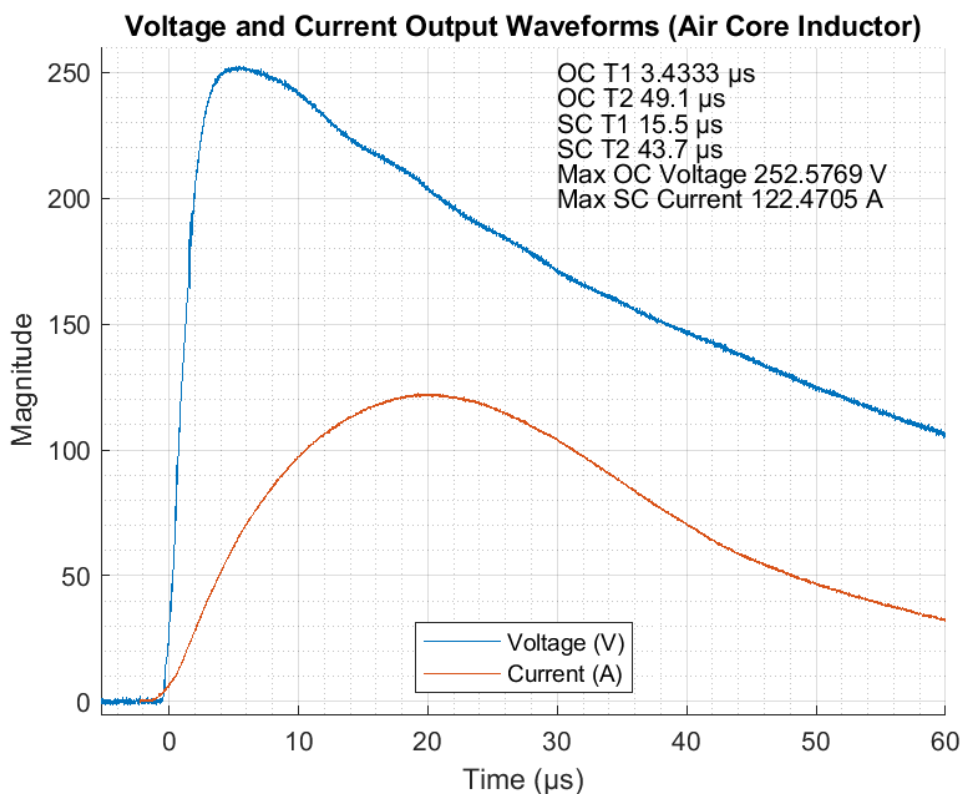


Figure 3.24: Impulse generator open-circuit voltage and short-circuit current output for a source voltage of 50 V (air core inductor).

In an attempt to reduce the amount of series inductance within the test setup, inductor L_1 was replaced with a short-circuit. The rest of the test setup remained unadjusted. The open-circuit voltage and short-circuit current waveforms recorded are shown in Figure 3.25. As would be expected, the front time τ_1 and time to half-value τ_2 of the short-circuit current waveform shortened, to $15.125 \mu\text{s}$ and $42.2 \mu\text{s}$, respectively. Closer to the desired specifications, however outside of the allowable tolerances. The front time τ_1 and time to half-value τ_2 of the open-circuit voltage waveform moved slightly closer to the desired values. The peak open-circuit voltage and short-circuit current values, 252.93 V and 125.72 A , respectively, remained largely unchanged - giving an effective output impedance of 2.01Ω . As before, no undershoot was recorded, therefore the undershoot requirement of less than 25% had been met.

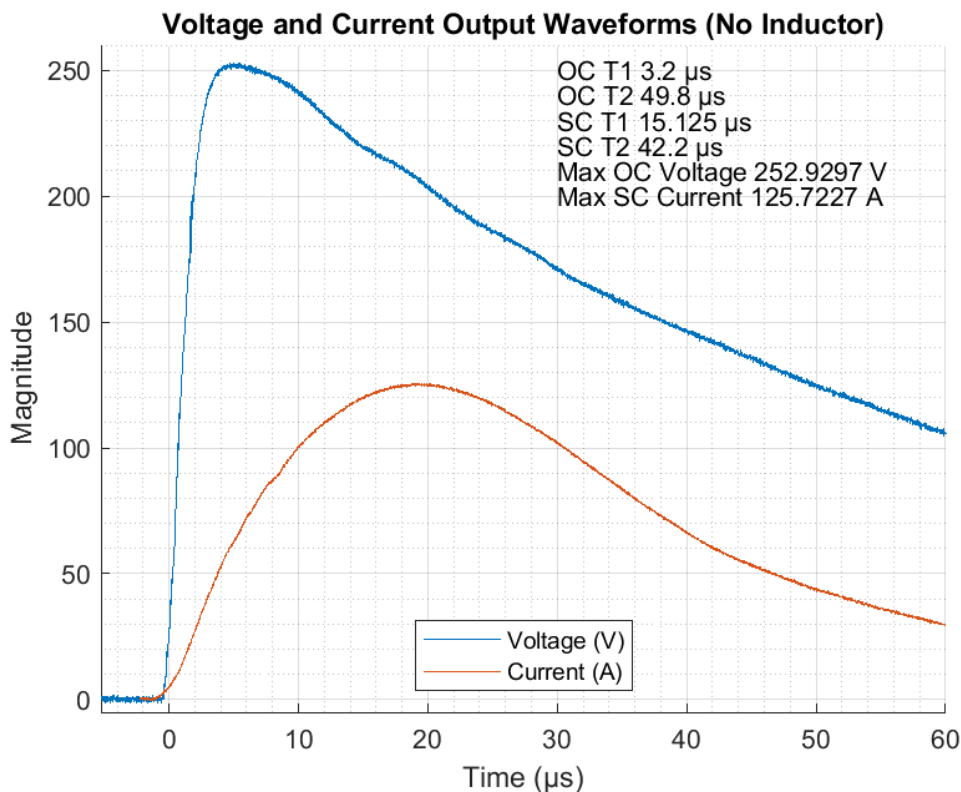


Figure 3.25: Impulse generator open-circuit voltage and short-circuit current output for a source voltage of 50 V (no inductor).

The voltage of the high-voltage DC source from which the impulse generator was increased to 100 V in order to examine if the impulse generator was able to provide the peak open-circuit voltage and short-circuit current levels of the Level 1 test level specified in [39] (the chosen minimum design goal). The recorded open-circuit voltage and short-circuit current waveforms are shown in Figure 3.26. The same waveform shapes from Figure 3.25 were recorded, and, as expected, the doubling of the source voltage resulted in a doubling of the magnitudes of the peak open-circuit voltage and short-circuit current (whilst the timing parameters remained the same). A peak open-circuit voltage of 500 V and a peak short-circuit current of 0.25 kA had been recorded, satisfying the Level 1 test level requirements specified in [39]. As was recorded for the lower charge voltage, no undershoot had occurred, therefore the undershoot requirement of less than 25% had been met.

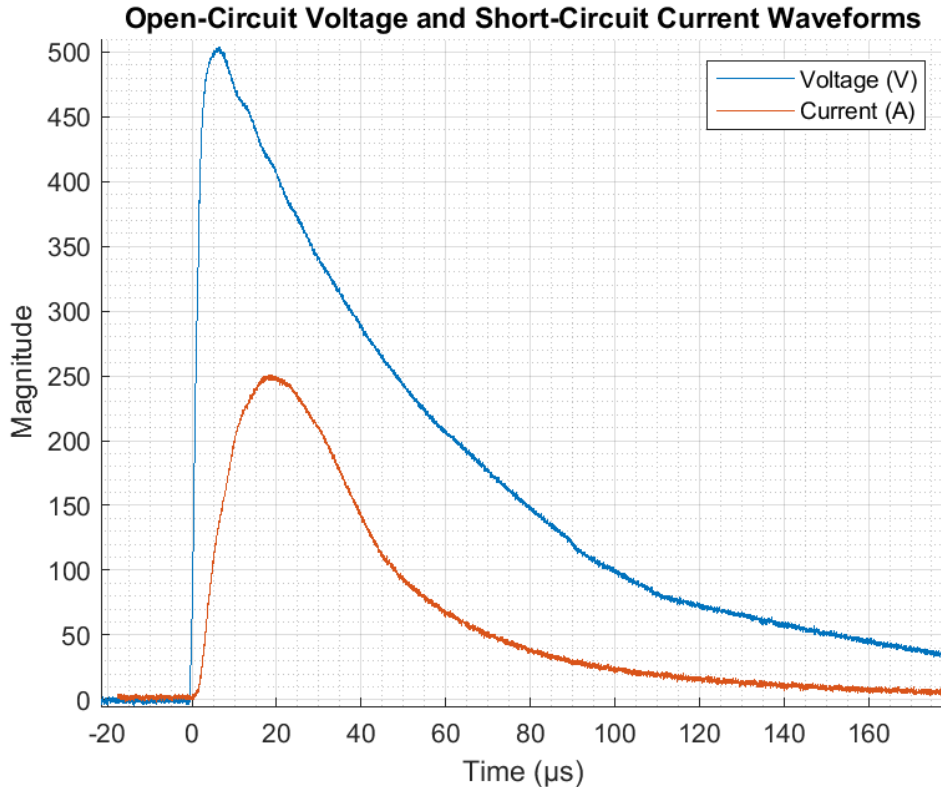


Figure 3.26: Impulse generator Level 1 open-circuit voltage and short-circuit current waveforms (no inductor).

In an attempt to further reduce amount of series-inductance in the circuit, a simplified pulse-shaping network was made by connecting only a rheostat in parallel with the output of the Marx generator. During the short-circuit current case no current would flow through the rheostat, as it would flow through the short-circuit instead. This resulted in a significant shortening of the front time τ_1 and time to half-value τ_2 of the short-circuit current waveform to $9.5 \mu\text{s}$ (within the allowable $\pm 20\%$ tolerance) and $25.5 \mu\text{s}$ ($1.5 \mu\text{s}$ over of the allowable $\pm 20\%$ tolerance), respectively. An undershoot of 3.50% was recorded, which was well under the maximum allowable undershoot of 25% . The voltage of the high-voltage DC source from which the impulse generator was charged remained at 50 V for this case.

This simplified pulse-shaping network also resulted in only the switch-on times of the IGBTs contributing to the front time τ_1 of the open-circuit voltage waveform (as there would be no voltage drop over any external series inductance). As the rheostat was the only path for the Marx generator to discharge through in the open-circuit voltage case, the value of the resistance of the rheostat determined the rate at which the Marx generator was able to discharge. The rheostat was adjusted to 1.2Ω in order for a time to half-value of τ_2 of $43.9 \mu\text{s}$ to be obtained (within the allowable tolerance of 20%). An effective output impedance of 0.62Ω was calculated for this case.

It was decided to make use of both the original pulse-shaping network (with the short-circuited inductor) and the simplified pulse-shaping network in order to provide possible further insight relating to the failure mechanisms of the diodes which were to be tested. Using both of these configurations provided two sets of output waveforms which a diode could be subjected to when testing.

The first configuration used was the original pulse-shaping network (with the short-circuited inductor). As it was not known whether a diode would fail in an open-circuit or a short-circuit, it was decided that a waveform which had an effective output impedance of 2Ω would serve to satisfy the Level 1 test level specified in [39]. The second configuration used was the simplified pulse-shaping network. This configuration allowed for waveforms of shape closer to that specified in [39]. The comparison of the results from these two configurations allowed for the observation of the influence of the pulse duration on the measured results.

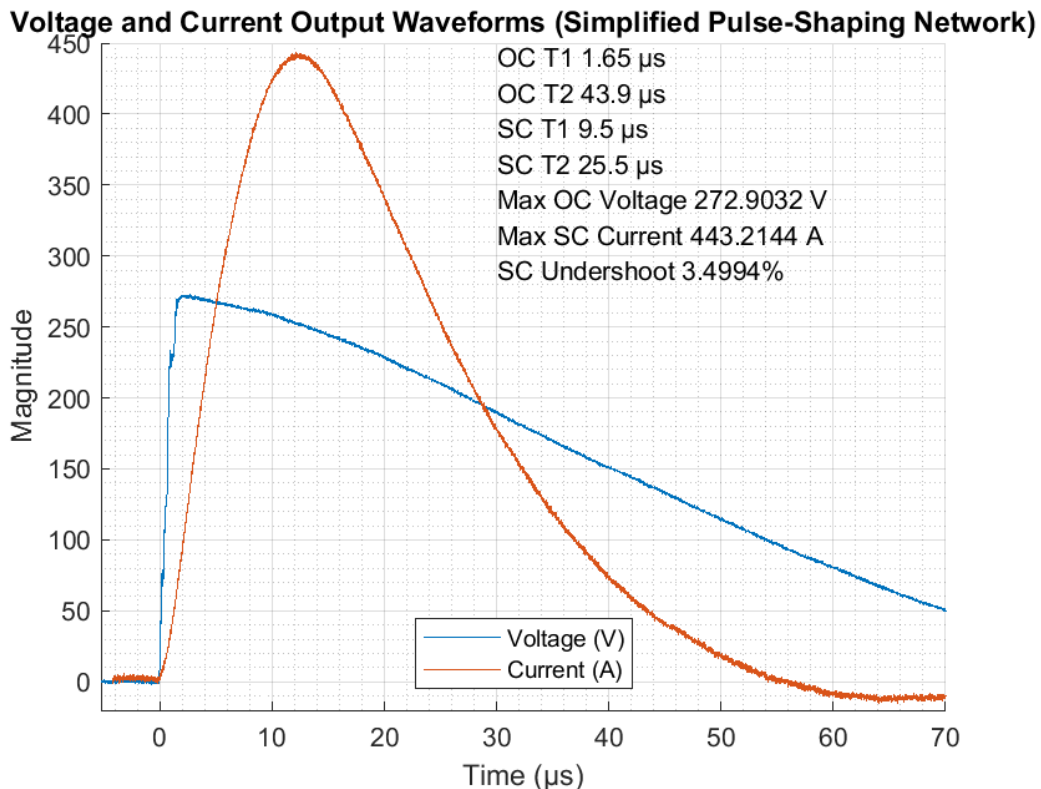


Figure 3.27: Impulse generator open-circuit voltage and short-circuit current output for a source voltage of 50 V (simplified pulse-shaping network).

3.11 Diode Testing

The EUT was the HY 10SQ045 Schottky diode. This diode is typical of one used as a bypass diode in a photovoltaic module due to its high maximum average forward current capacity of 10 A and low forward voltage of 0.55 V. The HY 10SQ045 has a maximum recurrent peak reverse voltage rating of 45 V. Part of the work presented in this section was briefly documented in [54], which was presented at the 5th South African Solar Energy Conference (SASEC 2018).

A new diode would be subjected to an initial impulse. Should this impulse result in a failure, the mode of the failure (short-circuit or open-circuit) would be noted. Should the initial impulse not result in a failure, the diode would be subjected to further impulses in order to ascertain whether subsequent impulses would have a degrading effect on the electrical characteristics of the diode [54].

Firstly, diodes tested in the forward biased position with current impulses of increasing magnitude in order to determine the point at which failure would repeatedly occur [54].

Secondly, diodes were tested in the reverse biased position. Voltage impulses of increasing magnitude were applied. The magnitude of these voltage impulses was larger than that of the maximum recurrent peak reverse voltage rating of the diodes - this resulted in a reverse current beginning to flow.

Two similar diodes from alternative manufacturers (DC Component 15SQ040 and Vishay VSB2045) were also examined in order to determine if the diode failures recorded were a result of poor design or manufacturing of the HY 10SQ045 diode, or if the failures were a consequence of the diode technology used in general.

Over 5000 impulses were executed in total in order to gain an accurate representation of how a diode may fail. The constructed impulse generator performed reliably and consistently throughout the duration of the study. During a test, the voltage over the diode was measured using a Tektronix P5100A 100x (bandwidth 500 MHz) voltage probe, and the current through the diode was measured using a Tektronix TCP0150 or TCP303 (both of bandwidth 20 MHz) current probe. The waveforms were captured and stored using a Tektronix digital storage oscilloscope. The forward voltages of diodes which did not exhibit a failure during the testing procedure were tested for deviation from the manufacturers specifications.

3.11.1 Forward Bias

A total of 10 diodes were examined for the forward biased case. The HY 10SQ045 diodes were found to be resilient to current impulses of peak magnitude far larger than their maximum average forward current rating of 10 A. Tests were performed with both the designed pulse-shaping network (the waveforms for which are shown in Figure 3.28) and the simplified pulse-shaping network (the waveforms for which are shown in Figure 3.29). In both cases, the diode was able to conduct forward currents of about 450 A without failure. The forward voltages, although larger than the rated forward voltage of 0.55 V, remained relatively low (between 2 V and 6 V at currents far exceeding the maximum average forward current of the diode. For the test which used the designed pulse-shaping network, the high-voltage DC power supply was set to 170 V, producing an open-circuit voltage waveform with a peak magnitude of 940 V and a short-circuit current waveform with a peak magnitude of 465 A. For the test which used the simplified pulse-shaping network, the high-voltage DC power supply was set to 50 V, producing an open-circuit voltage waveform with a peak magnitude of 275 V and a short-circuit current waveform with a peak magnitude of 452 A.

The test with the largest peak current magnitude was performed using the simplified pulse-shaping network. The high-voltage DC power supply was set to 88 V, producing an open-circuit voltage waveform with a peak magnitude of 486 V and a short-circuit current waveform with a peak magnitude of 770 A. This test resulted in a current impulse with a peak magnitude of 751 A conducted through the diode (as shown in Figure 3.30). Even with impulses of this peak magnitude, no forward bias failures occurred.

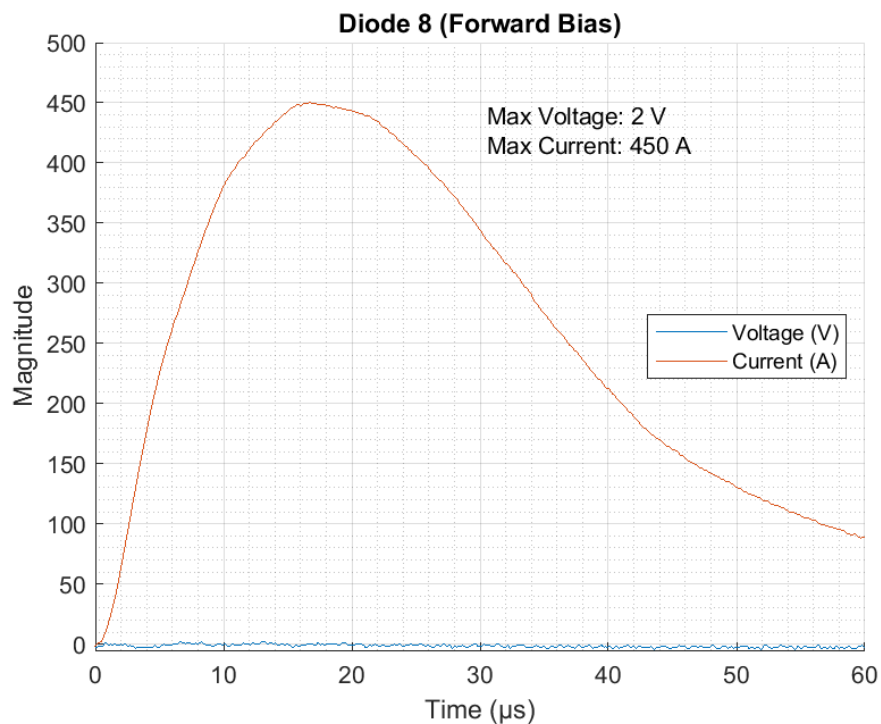


Figure 3.28: Voltage and current waveforms recorded during the testing of Diode 8.

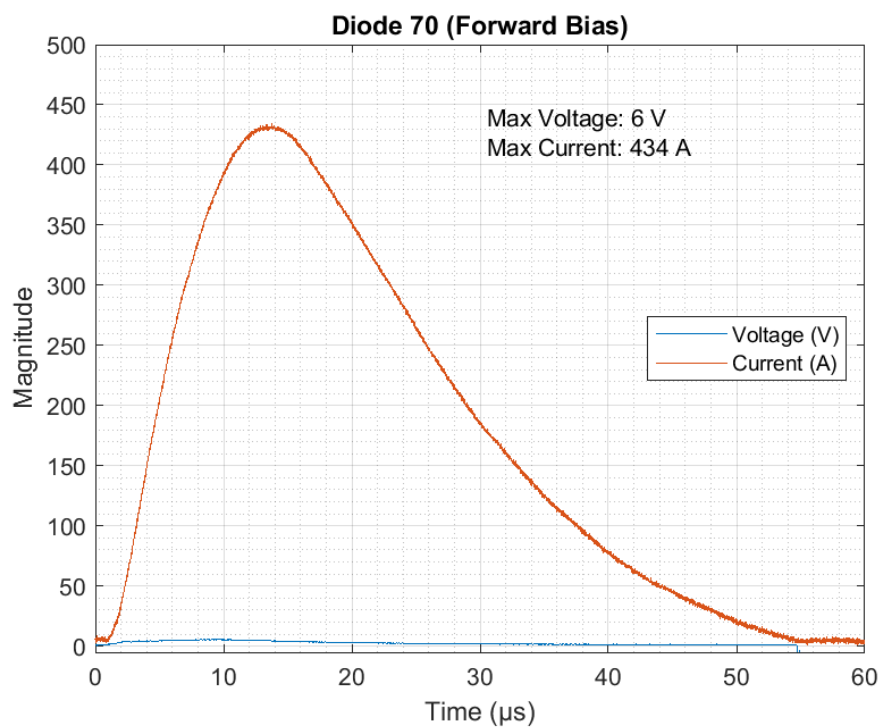


Figure 3.29: Voltage and current waveforms recorded during the testing of Diode 70.

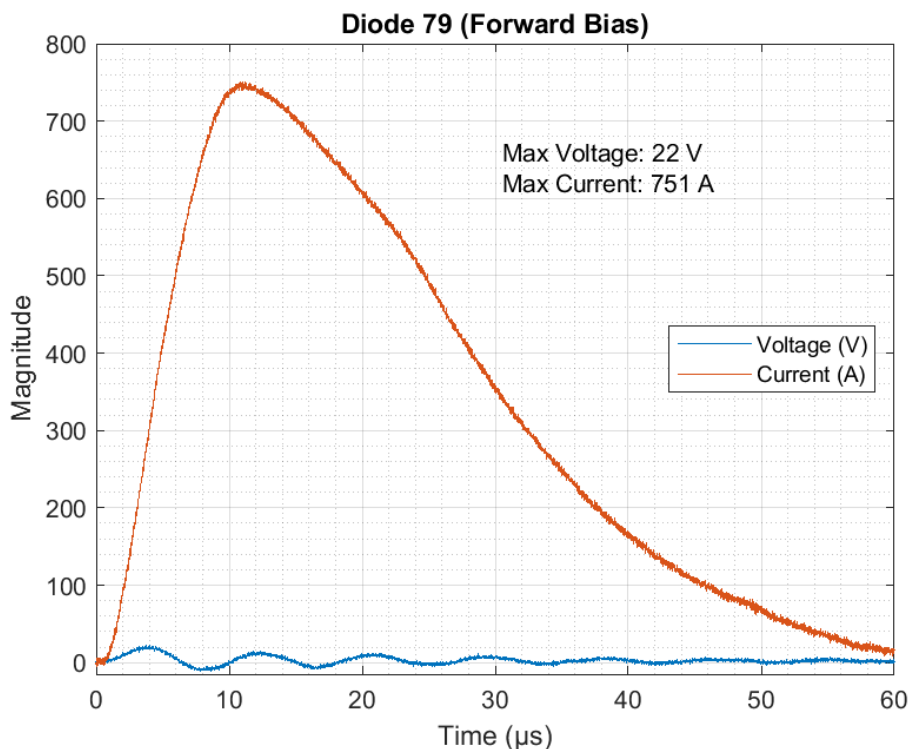


Figure 3.30: Voltage and current waveforms recorded during the testing of Diode 79.

3.11.2 Reverse Bias

As was done for the forward bias case, reverse bias testing of the HY 10SQ045 diodes was performed with both the designed pulse-shaping network and the simplified pulse-shaping network. As the voltages applied to the HY 10SQ045 diodes exceeded the maximum recurring peak reverse voltage of the diode (45 V), a reverse current would begin to flow. A total of 36 diodes were examined for the reverse biased case.

When failure of a diode did not occur, the waveforms recorded using the designed pulse-shaping network (shown in Figure 3.31) and the simplified pulse-shaping network (shown in Figure 3.32) showed similar responses. A steep voltage rise was initially experienced finally stopping at around 70 V. At this point, a reverse current would begin flowing. As the reverse current impulse would flow, the reverse voltage over the diode may climb to between 75 V and 80 V. Once the reverse current impulse had finished flowing, the reverse voltage over the diode would begin to decay exponentially, before eventually reaching zero. For the test which used the designed pulse-shaping network, the high-voltage DC power supply was set to 40 V, producing an open-circuit voltage waveform with a peak magnitude of 206 V and a short-circuit current waveform with a peak magnitude of 98 A. For the test which used the simplified pulse-shaping network, the high-voltage DC power supply was set to 20 V, producing an open-circuit voltage waveform with a peak magnitude of 106.4 V and a short-circuit current waveform with a peak magnitude of 164 A.

When a failure of a diode did occur, the waveforms recorded using the designed pulse-shaping network (shown in Figure 3.33) and the simplified pulse-shaping network (shown in Figure 3.34) again showed similar responses. A steep voltage rise was followed by a reverse current beginning to flow. If the reverse current reached a critical magnitude of

approximately 60 A, the diode had a high probability of failing in the short-circuit position. The failure would not necessarily occur upon reaching this point, but rather above this value the PN-junction would begin to break down. What would follow would be an increase in the voltage over the diode to between 80 V and 90 V, followed by an almost instantaneous short-circuit failure. As this short-circuit failure occurred, the remaining energy in the impulse generator would be executed result in a current impulse flowing through the short-circuit. For the test which used the designed pulse-shaping network, the high-voltage DC power supply was set to 45 V, producing an open-circuit voltage waveform with a peak magnitude of 236 V and a short-circuit current waveform with a peak magnitude of 116 A. For the test which used the simplified pulse-shaping network, the high-voltage DC power supply was set to 25 V, producing an open-circuit voltage waveform with a peak magnitude of 136 V and a short-circuit current waveform with a peak magnitude of 212 A.

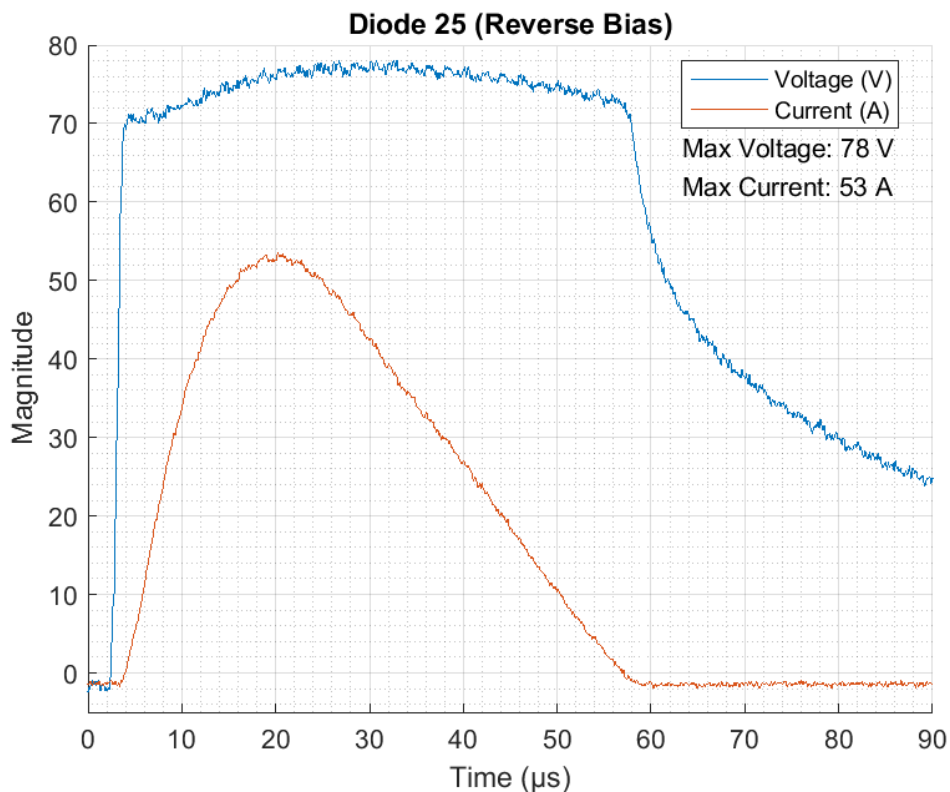


Figure 3.31: Voltage and current waveforms recorded during the testing of Diode 25.

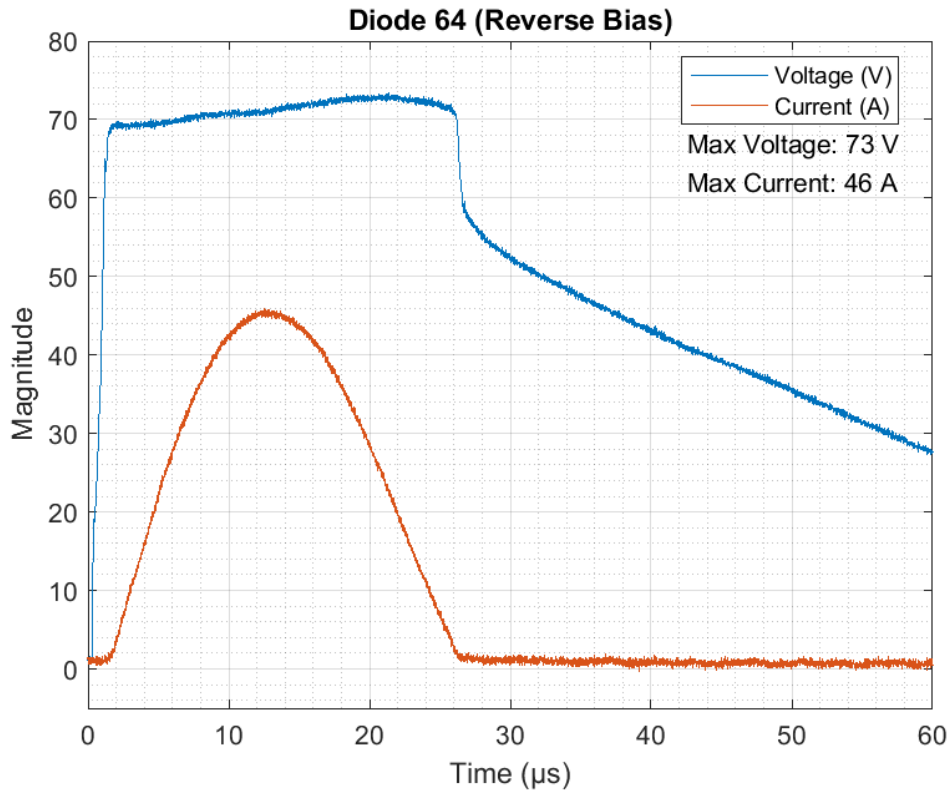


Figure 3.32: Voltage and current waveforms recorded during the testing of Diode 64.

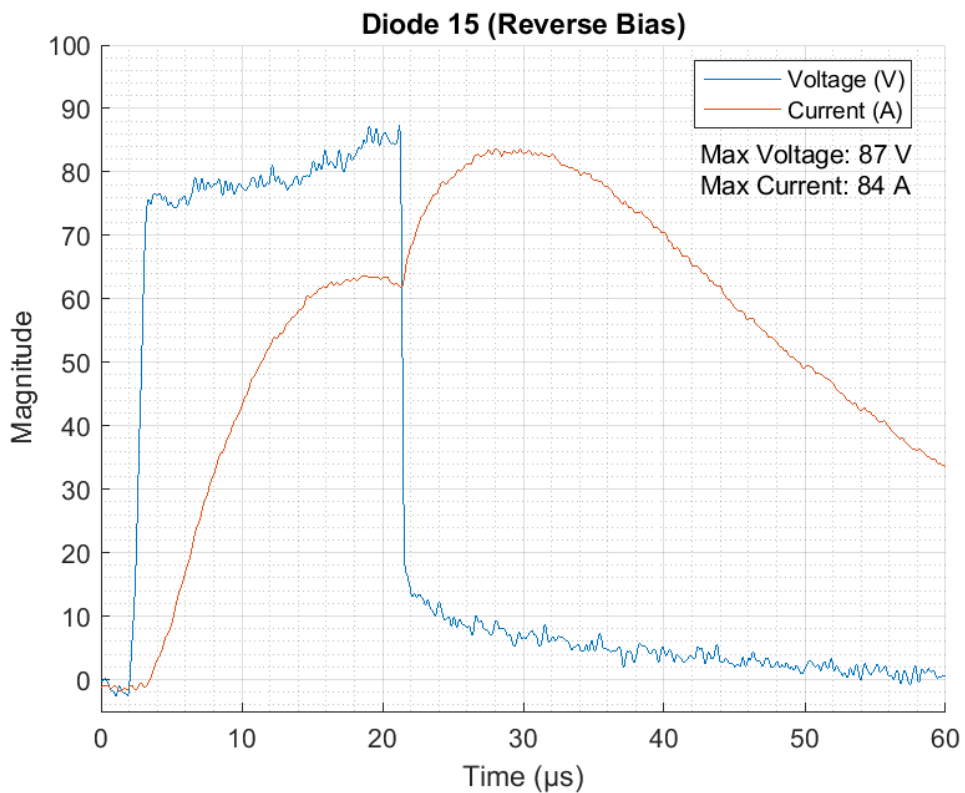


Figure 3.33: Voltage and current waveforms recorded during the failure of Diode 15.

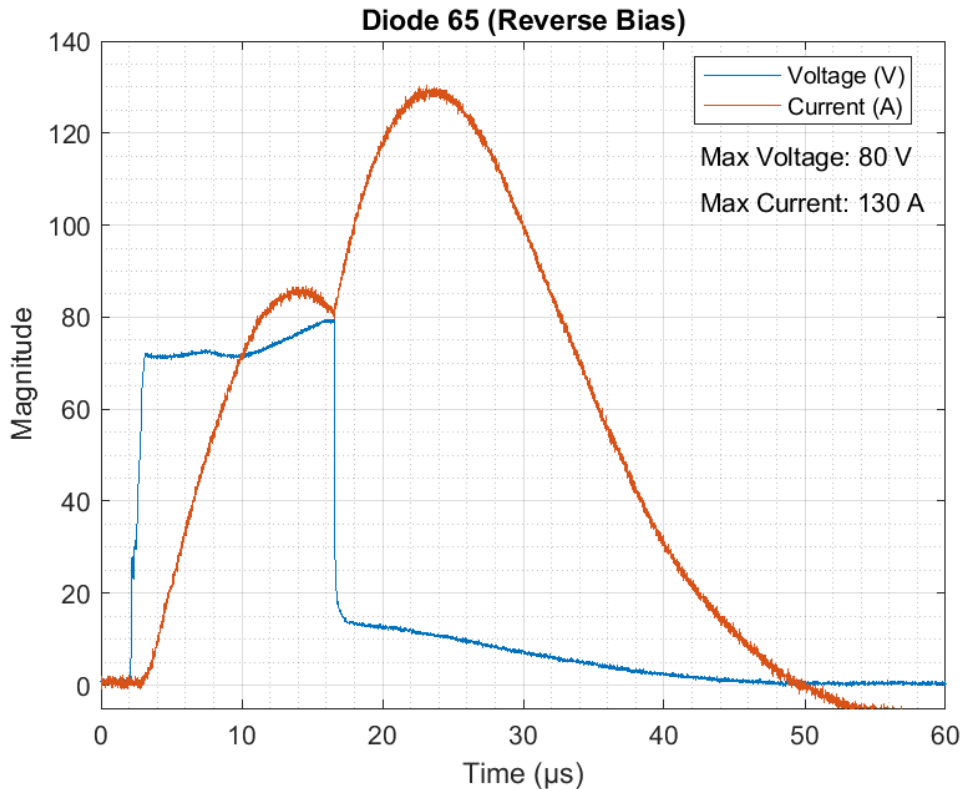


Figure 3.34: Voltage and current waveforms recorded during the failure of Diode 65.

3.11.3 Degradation Testing

Testing was performed in order to determine the resilience of a forward or reverse biased diode to multiple impulses at a level at which the diode had previously shown that it was unlikely to experience failure of the PN-junction. These tests were termed ‘degradation testing’, and were intended to discover whether or not the subjection of a diode to impulses would have an effect on its ability to withstand further impulses.

The first case considered was the forward biased case. As previously shown in Figure 3.28, Diode 8 did not experience a failure when subjected to a current impulse with a peak magnitude of 450 A. Diode 8 was subjected to nine additional impulses of this magnitude, and the measured current and voltage waveforms were recorded. The ten recorded voltage and current waveforms (shown in Figure 3.35) were all identical, indicating that no degradation of the PN-junction had occurred. In addition to the lack of any degradation noticed, the fact that the recorded current and voltage waveforms agree so closely is a testament to the consistency of the constructed impulse generator. The designed pulse-shaping network (with the short-circuited inductor) was used for the forward bias degradation testing.

As failures had previously been documented in the reverse biased case, it was decided to perform extensive reverse biased degradation testing of up to 200 impulses with both the designed pulse-shaping network (with the short-circuited inductor) and the simplified pulse-shaping network - the waveforms for which are shown in Figure 3.36 and Figure 3.37, respectively. For each pulse-shaping network, the impulse generator was set to a level so that the reverse current would not reach the critical level of approximately 60 A

where a failure was likely to occur. For the test which used the designed pulse-shaping network, the high-voltage DC power supply was set to 30 V, producing an open-circuit voltage waveform with a peak magnitude of 160 V and a short-circuit current waveform with a peak magnitude of 86 A. For the test which used the simplified pulse-shaping network, the high-voltage DC power supply was set to 20 V, producing an open-circuit voltage waveform with a peak magnitude of 106 V and a short-circuit current waveform with a peak magnitude of 164 A.

As with the forward biased case, the voltage and current waveforms agreed well enough that they were individually indistinguishable, indicating that no degradation of the PN-junction (and therefore the electrical characteristics of the diode) had occurred.

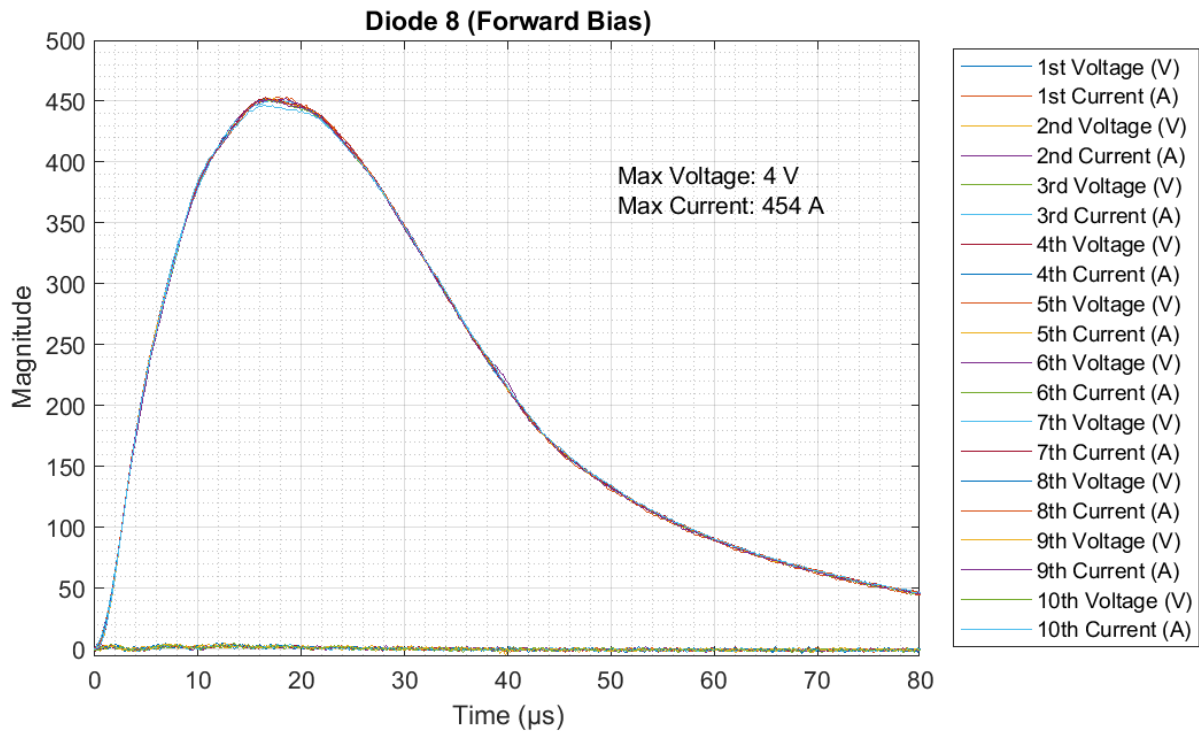


Figure 3.35: Voltage and current waveforms recorded during the degradation testing of Diode 8.

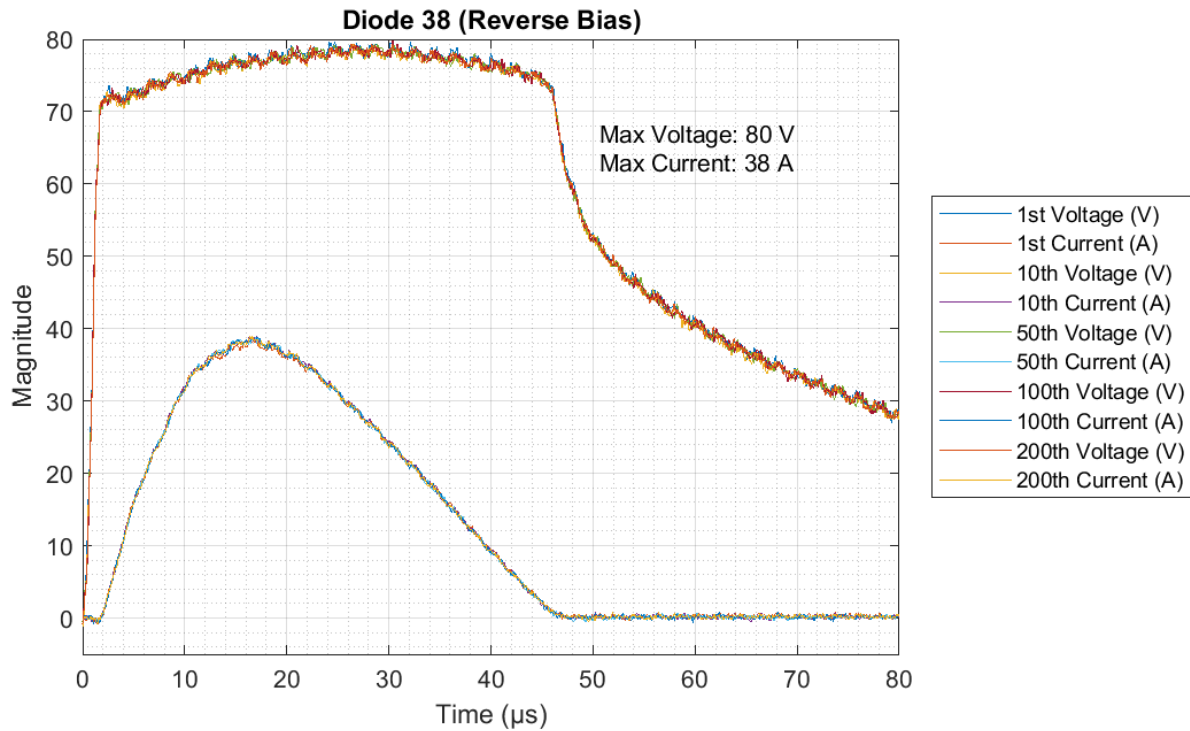


Figure 3.36: Voltage and current waveforms recorded during the degradation testing of Diode 38.

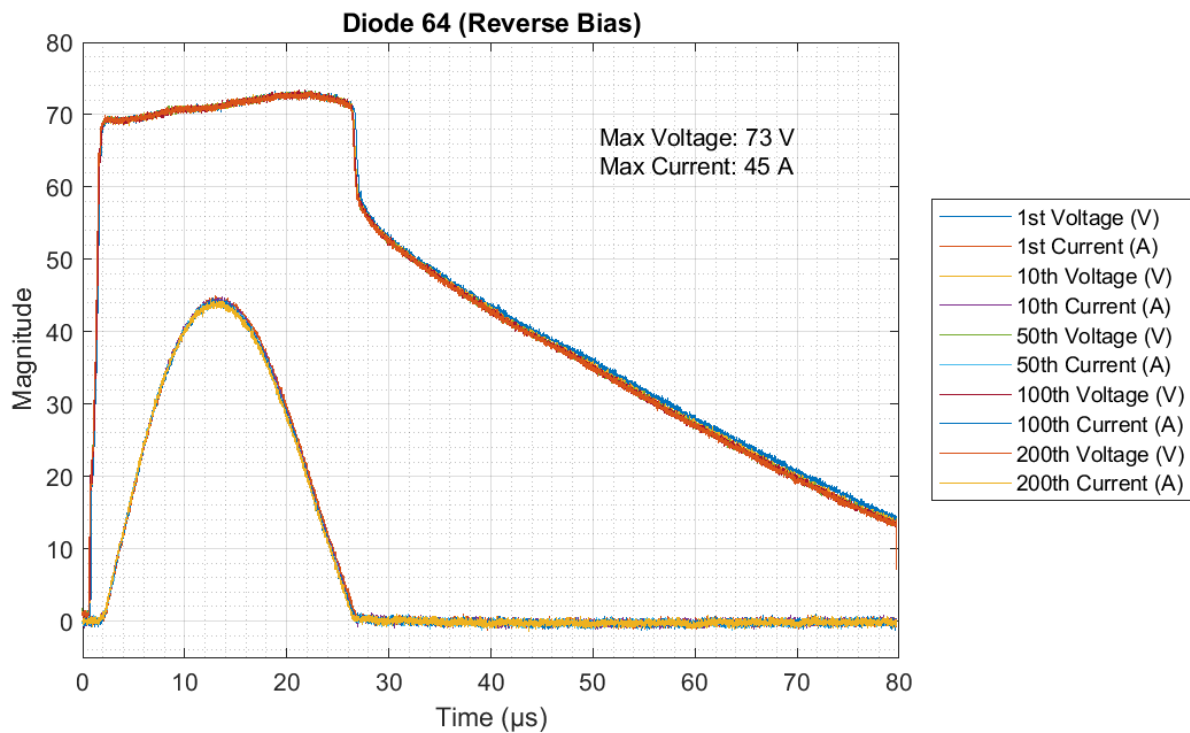


Figure 3.37: Voltage and current waveforms recorded during the degradation testing of Diode 64.

3.11.4 Alternative Diode Testing

Two alternative Schottky diodes were tested in order to determine whether the HY 10SQ045 diode was an outlier, or if the results gathered in Section 3.11.1, Section 3.11.2, and Section 3.11.3 were generally representative of the characteristics of Schottky diodes. The selected diodes were the DC Components 15SQ040 and the Vishay VSB2045. These diodes were rated for maximum average forward currents of 15 A and 20 A, and maximum recurrent reverse voltages of 40 V and 45 V, respectively [55], [56]. For the figures below, diodes denoted with an "A" prefix in the name are the DC 15SQ040 diode, and diodes denoted with a "B" prefix in the name are the Vishay VSB2045 diode. Twenty of each type of diode were examined in the following series of tests.

Firstly, forward bias testing was conducted. The pulse-shaping network (with the short-circuited inductor) was used, and the high-voltage DC power supply was set to 50 V for the test of Diode A3 and Diode B3 - the recorded waveforms for which are shown in Figure 3.38 and Figure 3.39, respectively. At this level, an open-circuit voltage waveform with a peak magnitude of 253 V and a short-circuit current waveform with a peak magnitude of 123 A would be produced. As in the forward bias test of the 10SQ045 diode, the 15SQ040 and VSB2045 diodes simply conducted the applied current impulse without failure.

The 15SQ040 and VSB2045 were not tested to the same level as the 10SQ045 diode as the forward biased case was not the particular case which showed the greatest weakness in previous tests. The 15SQ040 and VSB2045 diodes were therefore tested in forward bias with a sufficiently large current impulse reverse bias failure for the purpose of ensuring that the 15SQ040 and VSB2045 diodes did not possess an inherent weakness in the forward biased configuration (and therefore that the main weakness remained in the reverse biased configuration).

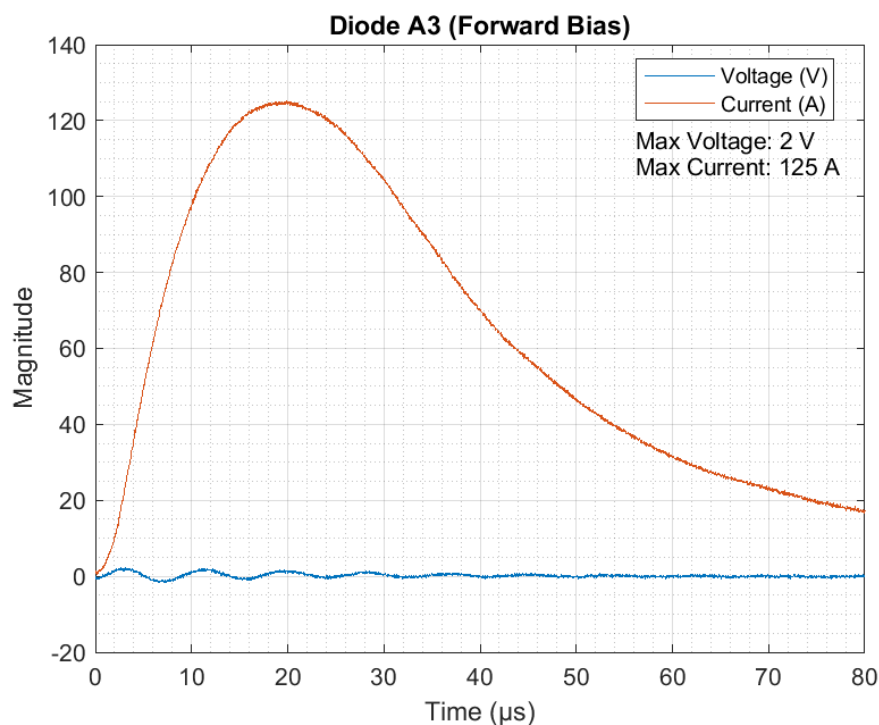


Figure 3.38: Voltage and current waveforms recorded during the testing of Diode A3.

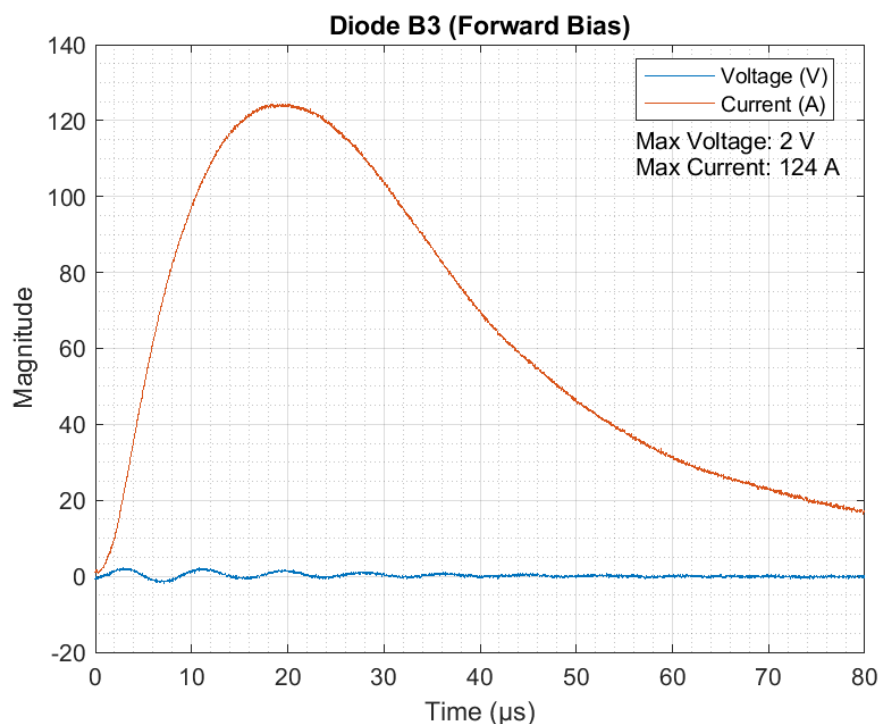


Figure 3.39: Voltage and current waveforms recorded during the testing of Diode B3.

Secondly, reverse bias testing was performed on the 15SQ040 and VSB2045 diodes using the designed pulse-shaping network. When a failure did not occur, a response similar to that seen in the case of the HY 10SQ045 diode was seen (an initial sharp voltage rise, followed by a plateauing of the voltage as the reverse current begins to flow, followed by a collapse of the voltage waveform once the reverse current has finished flowing). The reverse biased waveforms for the 15SQ045 and VSB2045 diodes for when a failure did not occur are shown in Figure 3.40 and Figure 3.41, respectively. For these waveforms, the high-voltage DC power supply was set to 45 V, producing an open-circuit voltage waveform with a peak magnitude of 227 V and a short-circuit current waveform with a peak magnitude of 114 A.

The critical reverse current value above which failure of the diode was certain to occur upon execution of the first impulse was 75 A for the 15SQ045 and VSB2045 diodes. The recorded waveforms for the reverse biased failure of Diode A7 and Diode B15 are shown in Figure 3.42 and Figure 3.43, respectively. As with the case of the HY 10SQ045 diode, if a critical reverse current was exceeded, the voltage over the alternative diodes would begin to increase as a result of the breakdown of the PN-junction, followed by an instantaneous short-circuit failure of the diode. The remaining energy in the impulse generator would then be executed as a current impulse flowing through the short-circuit. The high-voltage DC power supply was set to 50 V for these tests, producing an open-circuit voltage waveform with a peak magnitude of 253 V and a short-circuit current waveform with a peak magnitude of 123 A.

As with the case of the HY 10SQ045 diode, reverse biased degradation testing was performed with the impulse generator set at a level at which a diode was unlikely to fail during execution of the first impulse. Diode A8 showed a similar response (shown in Figure 3.44) to Diode 38 (shown in Figure 3.36), where no degradation seemed to occur. Diode B8 differed in that a clear degradation was observed. The magnitudes

of the recorded current and voltage waveforms would increase gradually with increasing pulse count. During the first impulse, the measured peak current was 67 A. By the 200th impulse, the measured peak current was 73 A. This suggested that with further impulses, the diode may degrade sufficiently to reach the critical level of 75 A where it was likely to fail. The level at which the high-voltage DC power supply was set for these tests was the same as that for the reverse bias testing of Diode A8 and Diode B8 discussed earlier.

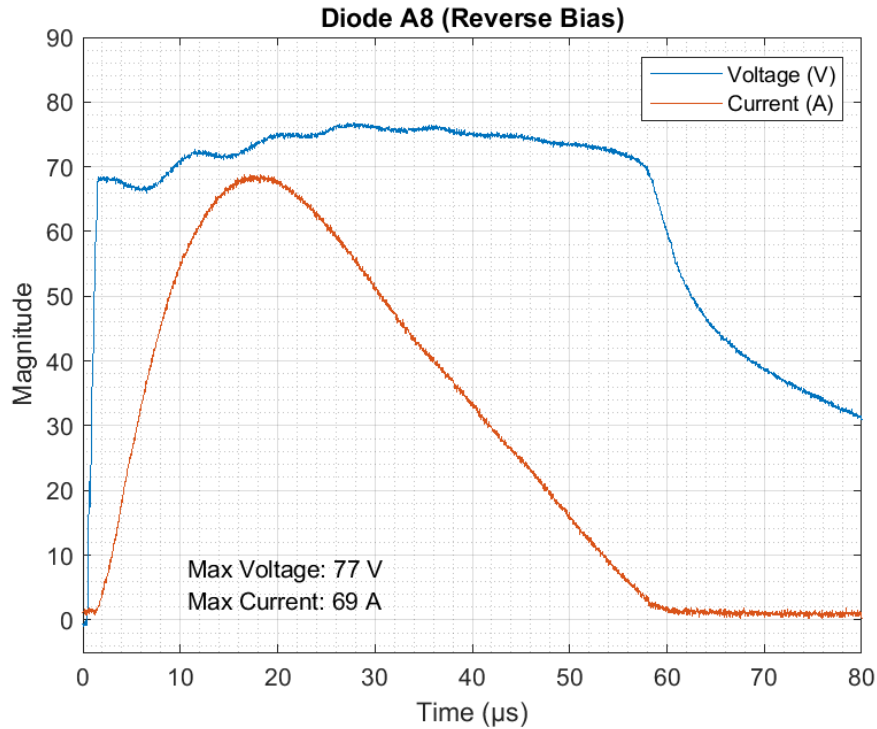


Figure 3.40: Voltage and current waveforms recorded during the testing of Diode A8.

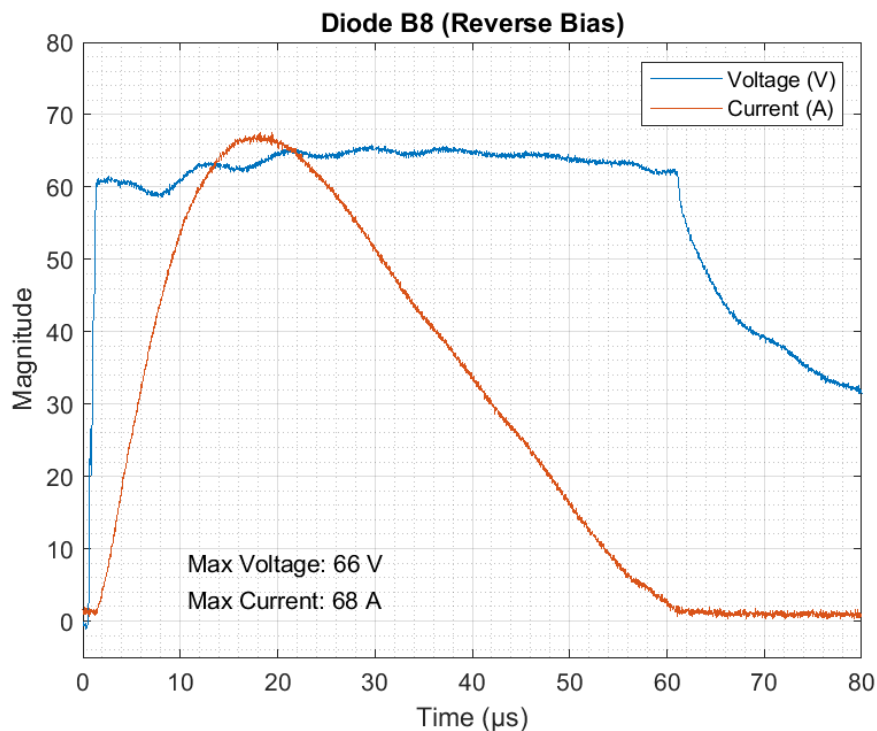


Figure 3.41: Voltage and current waveforms recorded during the testing of Diode B8.

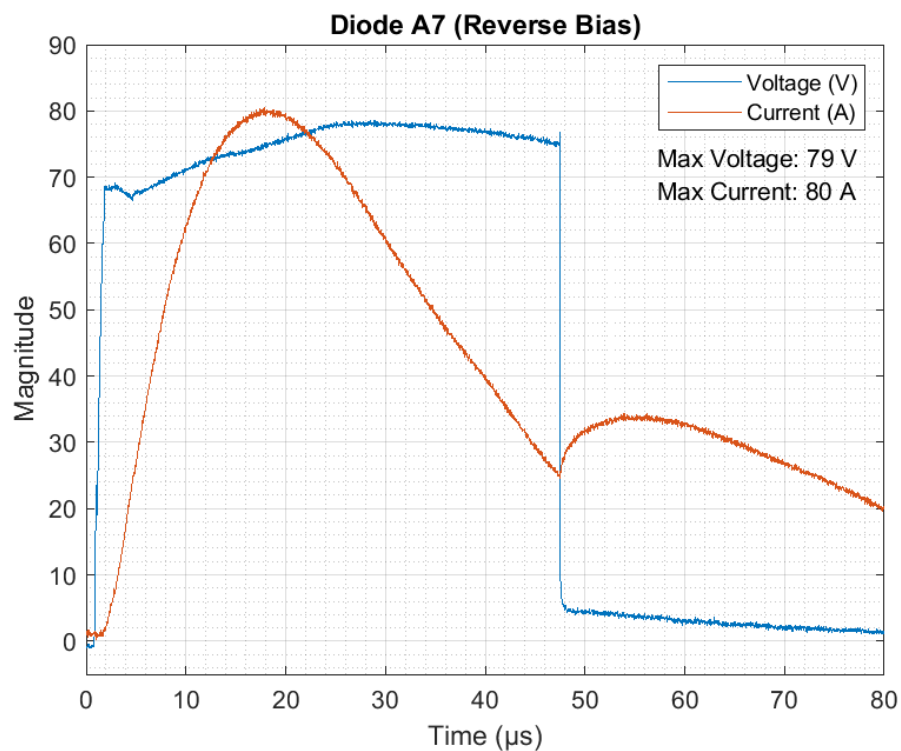


Figure 3.42: Voltage and current waveforms recorded during the failure of Diode A7.

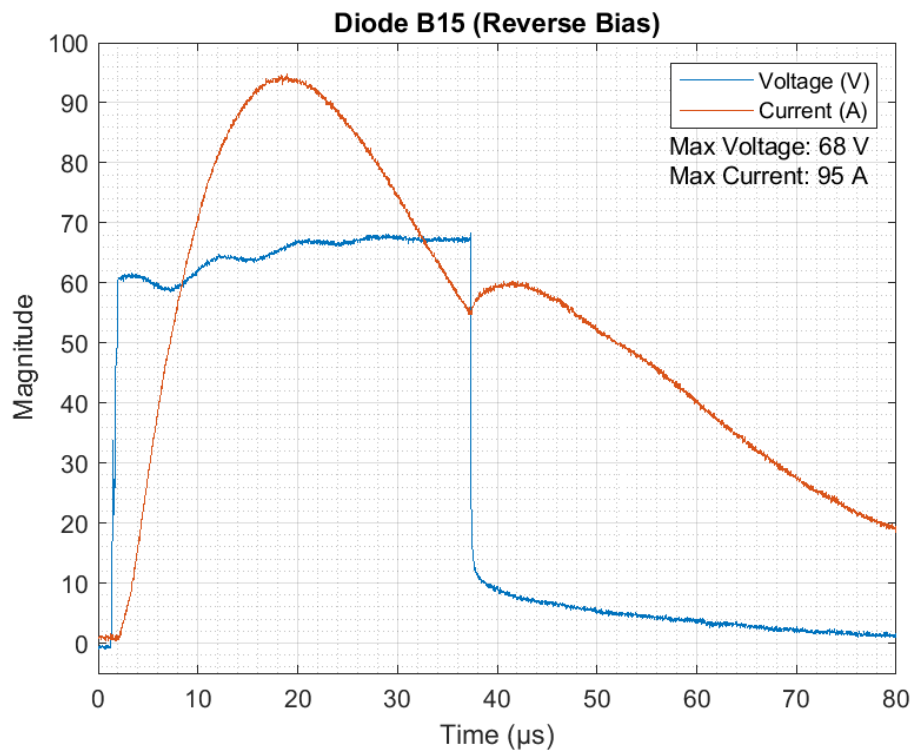


Figure 3.43: Voltage and current waveforms recorded during the failure of Diode B15.

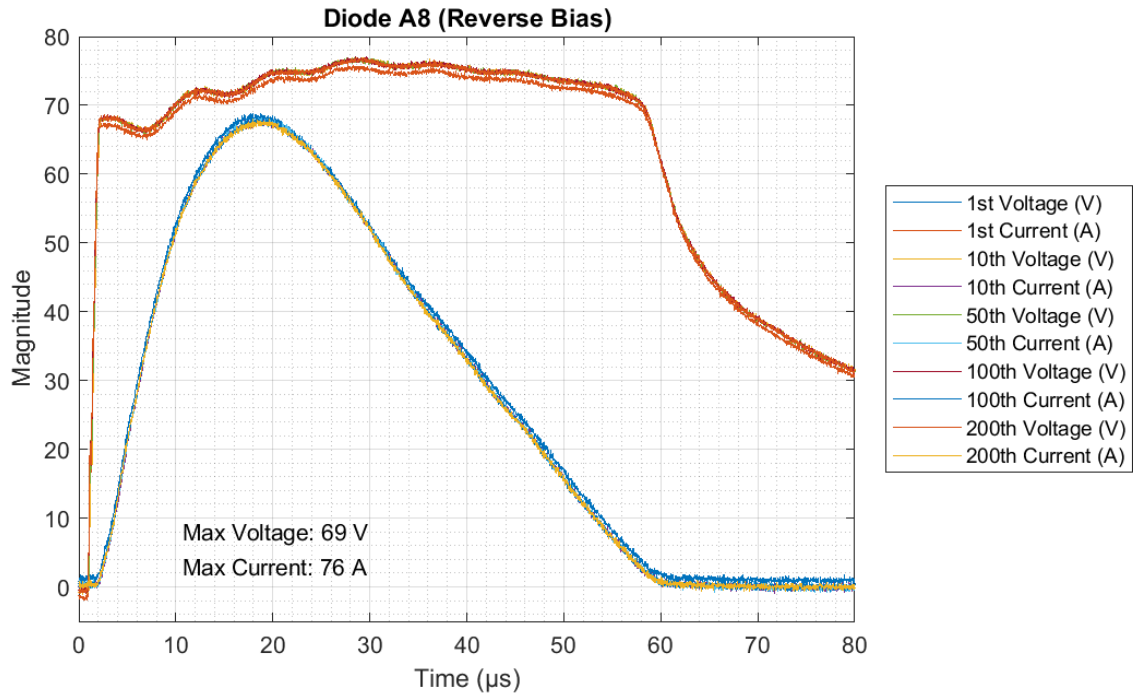


Figure 3.44: Voltage and current waveforms recorded during the degradation testing of Diode A8.

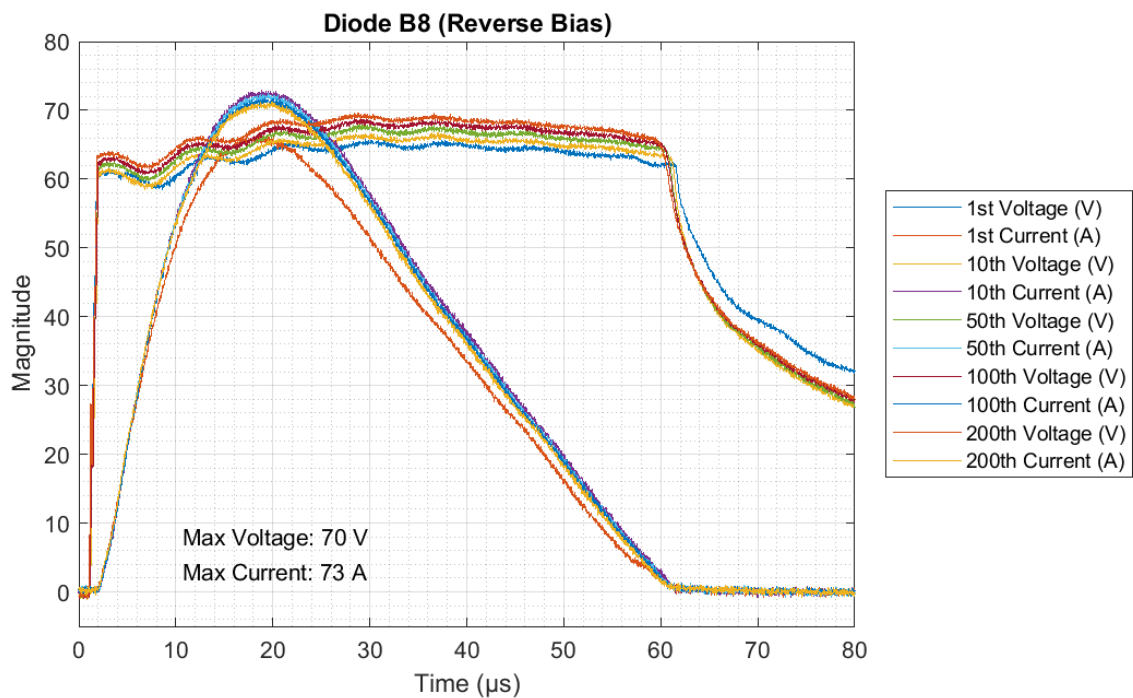


Figure 3.45: Voltage and current waveforms recorded during the degradation testing of Diode B8.

Now that research goal 1 (an investigation of the failure modes of a bypass diode) had been achieved using the impulse generator, research goal 2 (the proposal of an appropriate protection measure) was due to be investigated.

3.11.5 MOV Protection of Bypass Diodes

As it was now understood that a HY 10SQ045 Schottky diode was particularly susceptible to damage from large reverse currents occurring as a result of large reverse voltages, an appropriate protection measure could be investigated in order to satisfy research goal 2 (the proposal of an appropriate mitigation measure to increase bypass diode resilience). It was decided to make use of a voltage-sensitive protection measure, as opposed to a current-sensitive protection measure - for example, a fuse), as the voltage over the reverse biased diode was present before the commencement of the conduction of the reverse current. Ideally, the reverse current would be prevented from flowing, and not simply stopped from flowing when it became too large.

A varistor is an electronic device whose resistance varies depending on the applied voltage. A metal-oxide varistor (MOV) is a varistor manufactured using grains of a metal-oxide, sandwiched between two electrical contacts. Minute PN-junctions form between the grains, and a current is allowed to flow through the device when a sufficiently large voltage is placed across the electrical contacts, resulting in the forward biasing of these many small PN-junctions. MOVs are often employed to protect equipment from damage resulting from abnormal transients. Possible sources of these transients include electrostatic discharge, inductive switching, or lightning.

A MOV is a voltage-sensitive component, often placed in parallel with the equipment requiring protection (or between a line and earth). A MOV, like a resistor, does not have a particular polarity. During normal operation, the MOV acts as an open-circuit (or high impedance), and does therefore not influence the operation of the equipment. If the *breakdown voltage* of the MOV is exceeded, it begins to conduct. The breakdown voltage is often specified for the point at which a current of 1 mA flows through the MOV. A breakdown voltage larger than the maximum voltage the equipment requiring protection is therefore required in order for the MOV to remain in its open-circuit state during the normal operation of the equipment. When the breakdown voltage is exceeded and the MOV begins to conduct, the MOV exhibits a low impedance state, providing an alternative path (around the equipment) for the transient current to flow through while clamping the transient voltage. The *clamping voltage* is the maximum voltage at which a MOV is able to clamp to where damage to the MOV is unlikely to occur, and the *clamping current* is the current conducted through the MOV at this voltage. A *maximum current* is often specified, indicating the peak current a MOV can conduct before failure of the MOV is likely to occur. If a MOV should fail, it is desired that it fail in an open-circuit position in order to allow for continued operation of the protected equipment, and to prevent large currents from flowing between the terminals of the MOV [57], [58]. The current-voltage relationship of a MOV is shown in Figure 3.46.

There are two important voltage levels that should be considered when choosing a MOV for the protection of a bypass diode in a PV module. The first voltage level is the maximum voltage that the MOV would be subjected to during the normal operation of the PV module. In order to prevent power produced by a string within a PV module from being wasted, the breakdown voltage of the MOV should be greater than the open-circuit voltage of the internal cell string to be protected (the maximum voltage that the internal cell string can produce - approximately 15 V for a typical polycrystalline PV module, such as the BYD 300P6C-3). The second voltage level is the maximum recurrent reverse voltage of the bypass diode to be protected. The MOV should begin conducting well

before a reverse current begins to flow through the bypass diode (and ideally preventing a reverse current from flowing at all). The breakdown voltage of the MOV should therefore be chosen as lower than the maximum recurrent reverse voltage rating of the bypass diode (usually around 45 V, such as in the case of the HY 10SQ045 diode).

It proved difficult to source a MOV with a breakdown voltage in the region of 15-45 V with a large maximum current rating. The chosen MOV (TDK B72207S0170K101) had an RMS breakdown voltage of 17 V, a clamping voltage of 53 V (with a corresponding clamping current of 2.5 A), and a maximum current of 250 A (specified for an 8/20 μ s current impulse) [58].

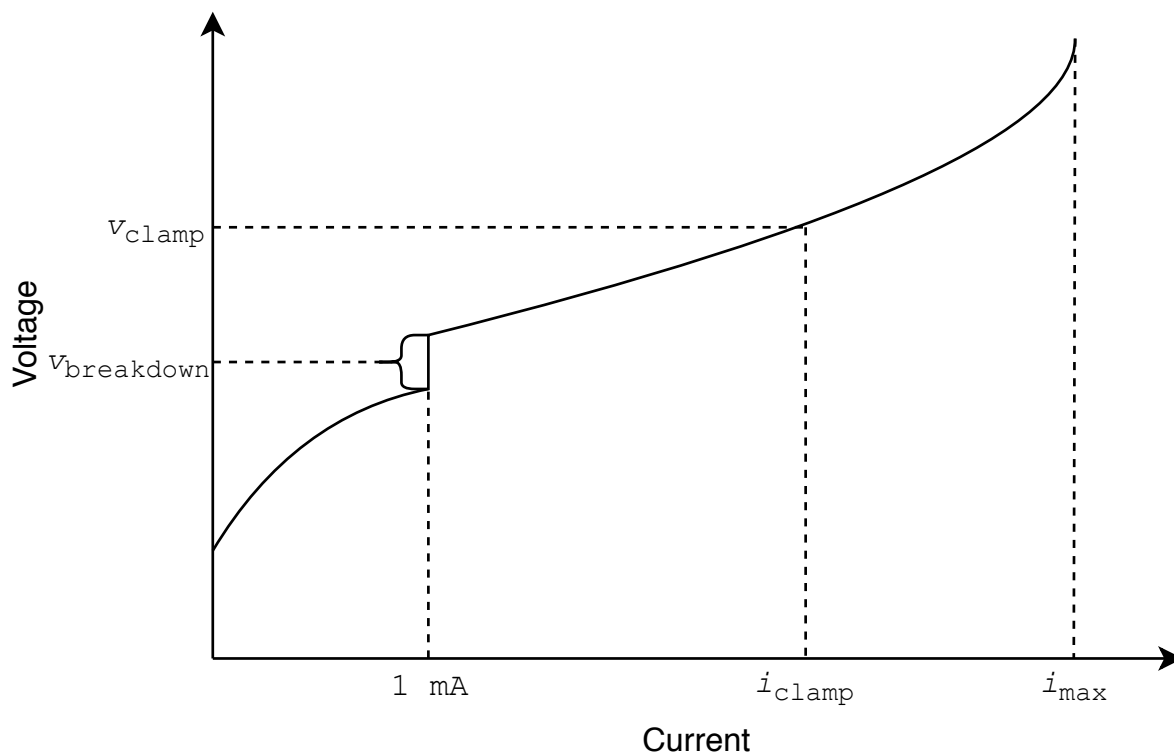


Figure 3.46: MOV operation parameters

Tests were performed with both a single MOV placed in parallel with a HY 10SQ045 diode, as well as two MOVs placed in parallel with a HY 10SQ045 diode (for increased MOV current carrying capacity), using the designed pulse-shaping network (with the short-circuited inductor).

For the case where a single MOV was used (as shown in Figure 3.47), the high-voltage DC power supply was able to be set as high as 80 V (which would produce an open-circuit voltage waveform with a peak magnitude of 406 V and a short-circuit current waveform with a peak magnitude of 203 A) without the reverse current of the diode reaching 60 A. The diode was therefore unlikely to fail at this level.

The addition of a second MOV placed in parallel with the first allowed for the high-voltage DC power supply to be set as high as 105 V (which would produce an open-circuit voltage waveform with a peak magnitude of 556 V and a short-circuit current waveform with a peak magnitude of 277 A), as shown in Figure 3.48. This case therefore protected the diode to a level exceeding the Level 1 protection level specified in [39].

The HY 10SQ045 diode would have failed with the designed pulse-shaping network and the high-voltage DC supply set to 37.5 V (which would provide an open-circuit voltage waveform with a peak magnitude of 195 V and a short-circuit current waveform with a peak magnitude of 96 A).

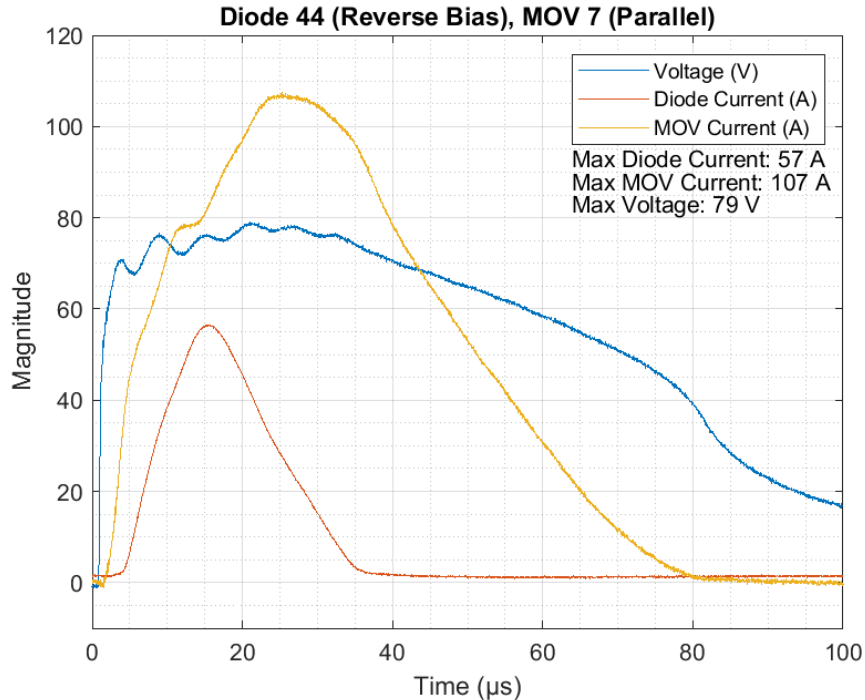


Figure 3.47: Voltage and current waveforms recorded during the testing of Diode 44 and MOV 7.

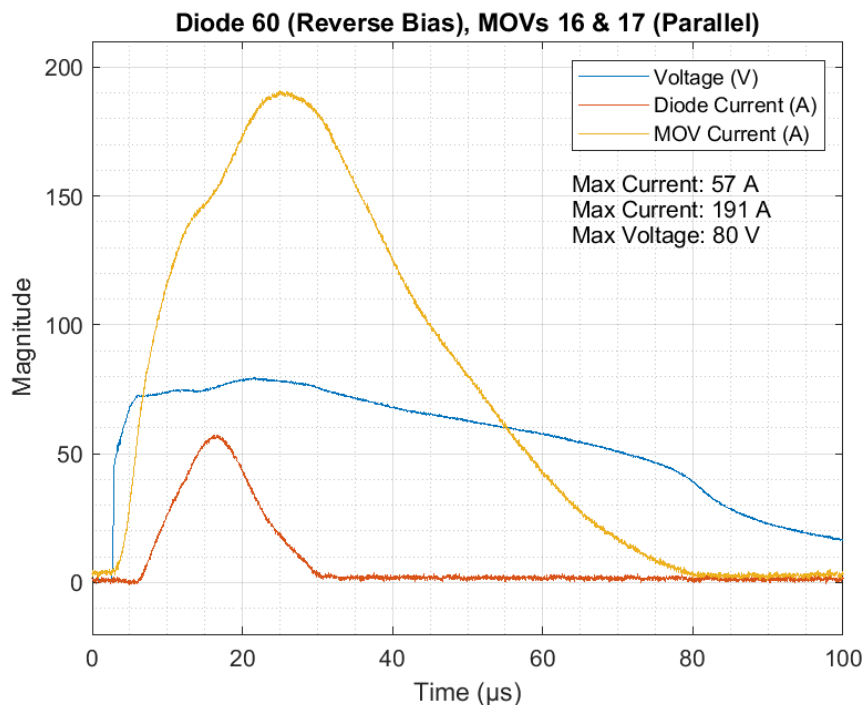


Figure 3.48: Voltage and current waveforms recorded during the testing of Diode 60 and MOVs 16 & 17.

Both the cases with the single MOV and double MOV configurations allowed for a substantial increase in the level to which the impulse generator could be charged to - demonstrating the appropriateness and effectiveness of MOVs for protecting bypass diodes within a PV module. The protection benefit (the increase in generator charge level) gained from the addition of the single MOV was greater than the benefit provided by the protection benefit gained when the additional MOV was added - suggesting a case of diminishing returns.

3.12 Chapter Conclusion

A modular impulse generator was designed and constructed in this chapter. The design of this impulse generator was split up into two main parts - the pulse-shaping network and the Marx generator. These parts were designed to work together to provide impulses in accordance with SANS standards, for the determination of the modes in which a Schottky diode may fail. The constructed impulse generator functioned both reliably and consistently.

Diodes were tested in both forward and reverse bias, and found to be particularly susceptible to damage in the reverse bias configuration. Two alternative diodes (the DC 15SQ040 and VSB2045) were investigated in order to determine whether the weaknesses recorded with the initial diode (the HY 10SQ045) were a consequence of the design and manufacturing of that diode in particular, or if the recorded weaknesses were representative of Schottky diodes in general - the latter was found to be the case. Degradation testing was performed at a level at which a diode would not fail after an initial impulse in order to investigate whether the application of successive impulses would degrade the electrical characteristics of the diode - no degrading effect was noticed for the HY 10SQ045 or DC 15SQ040 diodes, however a reverse bias degradation was noticed for the VSB2045 diode. The use of the two different pulse-shaping networks produced similar results. This testing achieved the first research goal (an investigation into the failure modes of a bypass diode) originally set out in Section 1.5.

The MOV was introduced as a potential bypass diode protection measure. MOVs were shown to provide considerable protection to diodes, while remaining cost effective.

At the time of writing, an average bulk unit cost of a bypass diode was \$ 0.55 (USD). Short-circuit failure of the bypass diodes within a PV module would prevent it from producing power. This would nullify the upfront investment of approximately \$ 100.00 (USD) used to purchase the module, as well as any potential earnings which could have been generated from the intended functioning of the module. The bulk unit cost of the MOV used was \$ 0.09 (USD). If a MOV were to be placed in parallel with each bypass diode, the unit cost of a PV module would increase negligibly. The susceptibility of a bypass diode to damage, however, would be decreased substantially. This testing therefore achieved the second research goal (the proposal of an appropriate bypass diode protection measure in order to increase bypass diode resilience) originally set out in Section 1.5.

This chapter served to establish the conditions under which a bypass diode may fail. The following chapter demonstrates (by means of simulation) the manners in which these conditions may arise within a PV installation - the third research goal set out in Section 1.5.

Chapter 4

Electromagnetic Modelling

4.1 Chapter Overview

This chapter documents the electromagnetic modelling of a PV module in close proximity to a nearby lightning stroke. As mentioned in Section 1.6.3, many studies involving the electromagnetic modelling of lightning strokes and PV installations make use of a model which approximates the traces within a PV module, the module interconnections, and the frame of the module as a thin-wire. These models fail to take the actual geometry of the module into account, and in most cases the junction box (including the bypass diodes) are excluded from the model. The traces within a module are often approximated as a thin-wire passing through the centre of gravity of each PV cell. This study aims to provide better insight into the induced voltages and currents within a PV module by increasing the detail of the model used.

Firstly, the CAD model used in these simulations is discussed.

Secondly, the assumptions made during this modelling study are stated and motivated.

Thirdly, the setup within the electromagnetic simulation package is described, including all variations of the simulation that are considered.

Fourthly, the computed results are examined, and explanations are given.

Finally, the challenges encountered during the electromagnetic modelling process are stated, along with the solutions used.

This chapter directly addresses the third research goal (an investigation into how the configuration of a PV installation may influence the magnitudes of the currents induced within the installation) originally defined in Section 1.5.

4.2 CAD Model

A Computer Aided Design (CAD) model of a BYD 310P6C-36 PV module was constructed in Inventor Professional 2018. This model takes into account the geometries of the frame, the junction box (including the bypass diodes), and the traces which connect the PV cells within the module. Dimensions larger than 200 mm are accurate to within 0.5 mm, and dimensions smaller than 200 mm are accurate to within 0.05 mm. The model was exported in the .stp file format, with an accuracy set to 0.0001 mm, for use in the electromagnetic simulation software package.

The module has a height of 1957 mm and a width of 992 mm. The complete CAD model can be seen in Figure 4.1, and the junction box can be seen in Figure 4.2.



Figure 4.1: The front view of the CAD model of a BYD 310P6C-36 PV module.

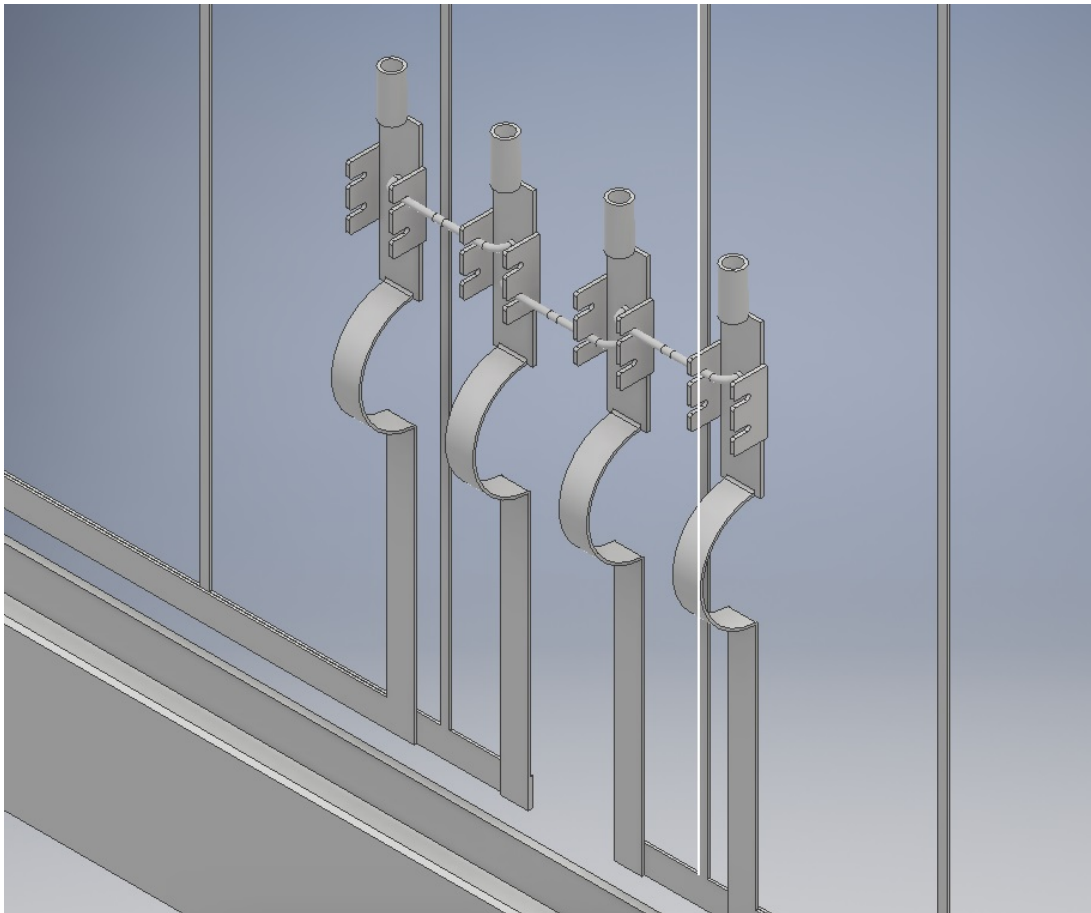


Figure 4.2: The junction box in the CAD model of a BYD 310P6C-36 PV module.

A PV cell usually has three conductive tracks on the top and on the bottom, which act as the positive and negative terminals (as shown in Figure 4.3). The CAD model approximates a PV cell as three parallel metallic traces, as can be seen in Figure 4.4.

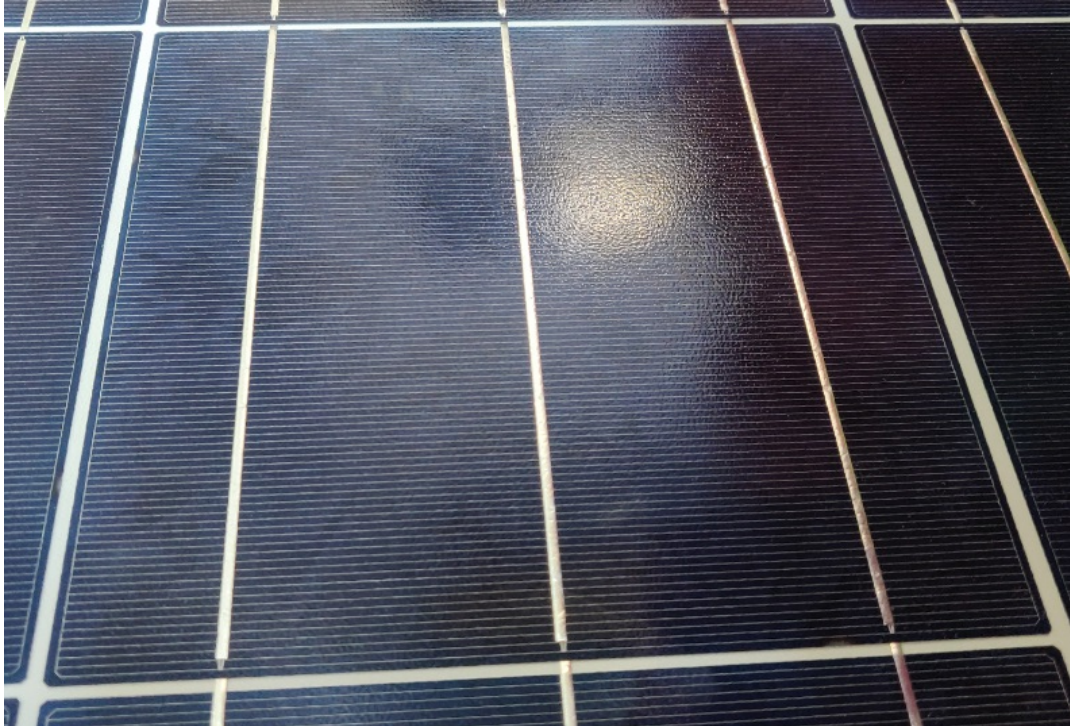


Figure 4.3: The conductive tracks on a PV cell.

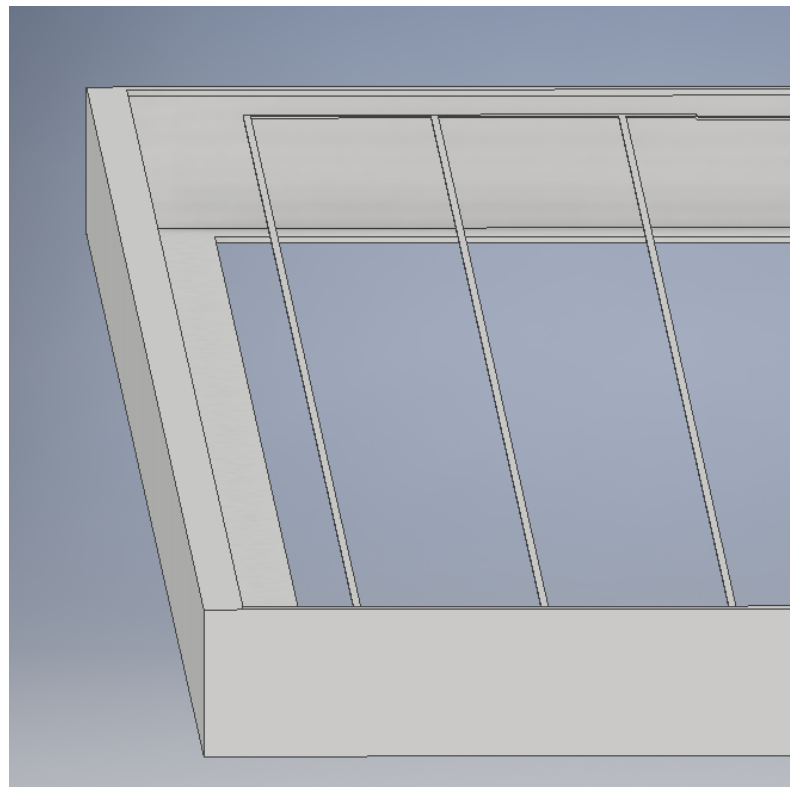


Figure 4.4: The conductive tracks representing a row of PV cells within a PV module.

4.3 Electromagnetic Modelling Assumptions

A number of assumptions were made in this modelling study. These assumptions are stated and motivated in the section below.

4.3.1 PV Module Modelling Assumptions

All surfaces within the model are modelled as perfect electrical conductors within the electromagnetic simulation package. These simulations were intended to simulate the susceptibility of the geometry in a PV module to induced voltages and currents, and not the effect the materials on the induced voltages and currents. The glass sheet at the front of a PV module is omitted, as it would have no effect on the results of the simulations.

All PV cells are approximated as three short-circuited traces. PV cells have low forward bias and reverse breakdown voltages, it is therefore assumed that conduction can occur in either direction with the presence of relatively small induced voltages. This approximation is based off of the intention to simulate a worst-case scenario - as this is a scenario for which protection measures are often designed for.

As previously mentioned, the PV cells within a PV module are approximated as three parallel traces. The assumption is that since the loop connected to the terminals in the junction box has a smaller area, lower induced voltages or currents are measured at the junction box. This is hypothesised to give more realistic results than if a single trace had been used, as it is more representative of the actual layout within a PV module. This concept is illustrated in Figure 4.5.

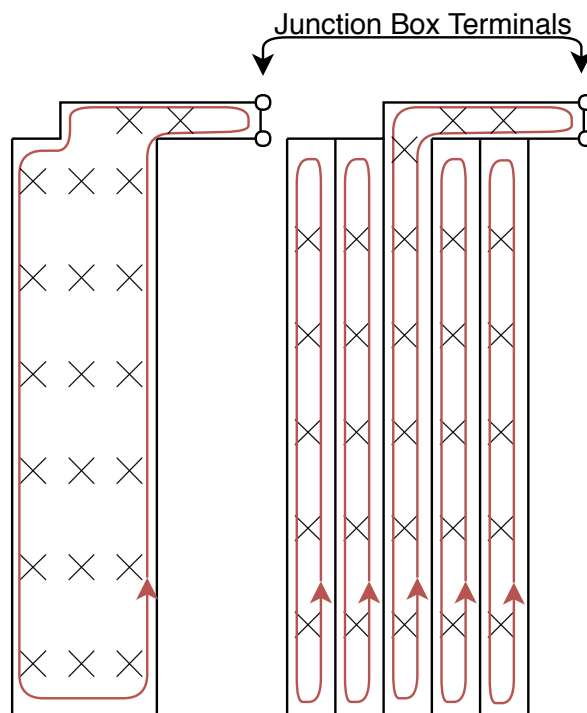


Figure 4.5: The conductive traces for the conventional modelling approach (left) and the approach hypothesised to be more representative (right).

4.3.2 Lightning Modelling Assumptions

The lightning stroke is modelled as vertically orientated impressed current, originating at a height of 2 m and terminating at a height of -2 m along the vertical Z-axis. The main assumption made regarding the orientation was that the last few metres of the lightning stroke were orientated vertically.

A current magnitude of 20 kA was chosen, as this was the average current magnitude measured in the regions surrounding the three solar plants considered in Section 1.2. The 8/20 μ s waveform was selected as it is the expected waveform of currents likely to be induced as a result of a nearby lightning stroke [28]. Due to this fact, it is also the waveform referenced by SPD manufacturers when stating the maximum impulse current rating of their SPDs. A time domain plot of a 20 kA, 8/20 μ s current waveform is shown in Figure 4.6.

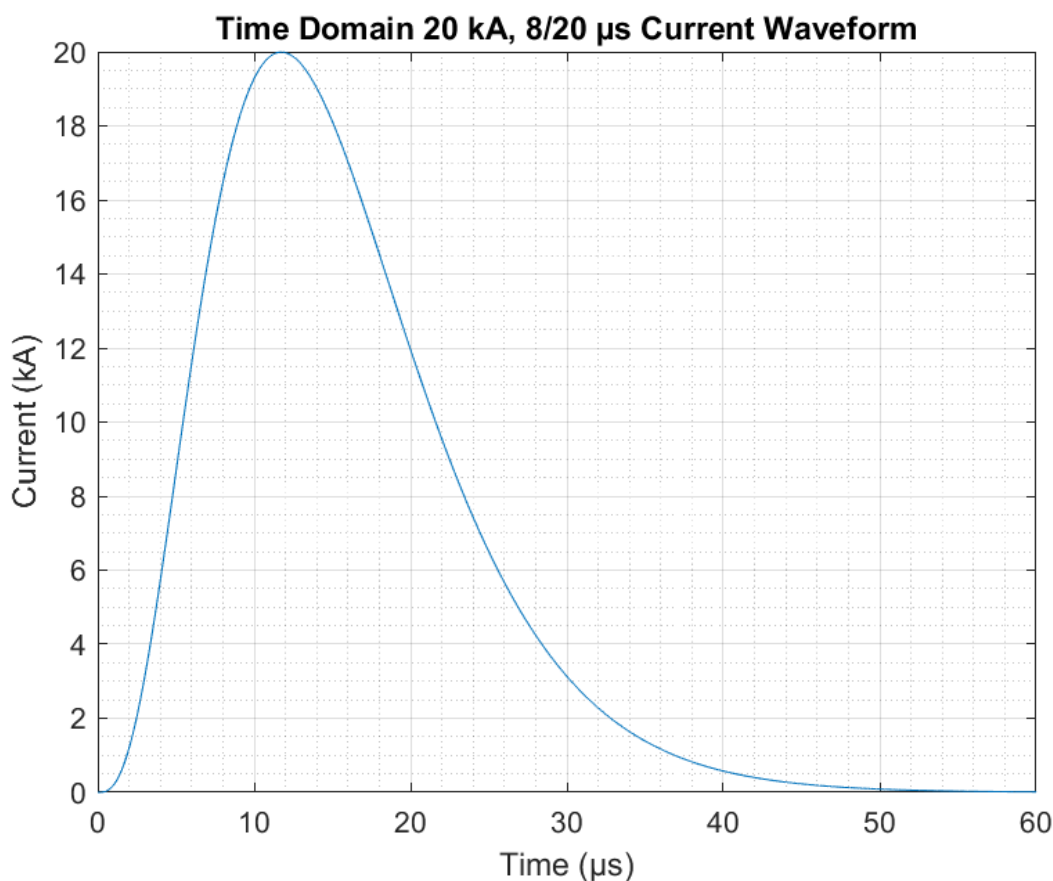


Figure 4.6: A time domain plot of a 20 kA, 8/20 μ s current waveform.

Figure 4.7 shows the computed power spectrum for a 20 kA, 8/20 μ s current waveform. Simulations were run for 30 linearly spaced discrete frequency intervals between 10 kHz and 600 kHz (inclusive), as it was decided that this would give sufficient bandwidth to model the intended lightning waveform. The electromagnetic simulation setup used, including details relating to the electromagnetic solver settings, are covered in the following section (Section 4.4).

In order to come to the understanding that 30 frequencies would be sufficient, test simulations were run for 30, 60, and 120 frequencies in the interval from 10 kHz to 600 kHz. The results of these simulations are presented in Appendix B.

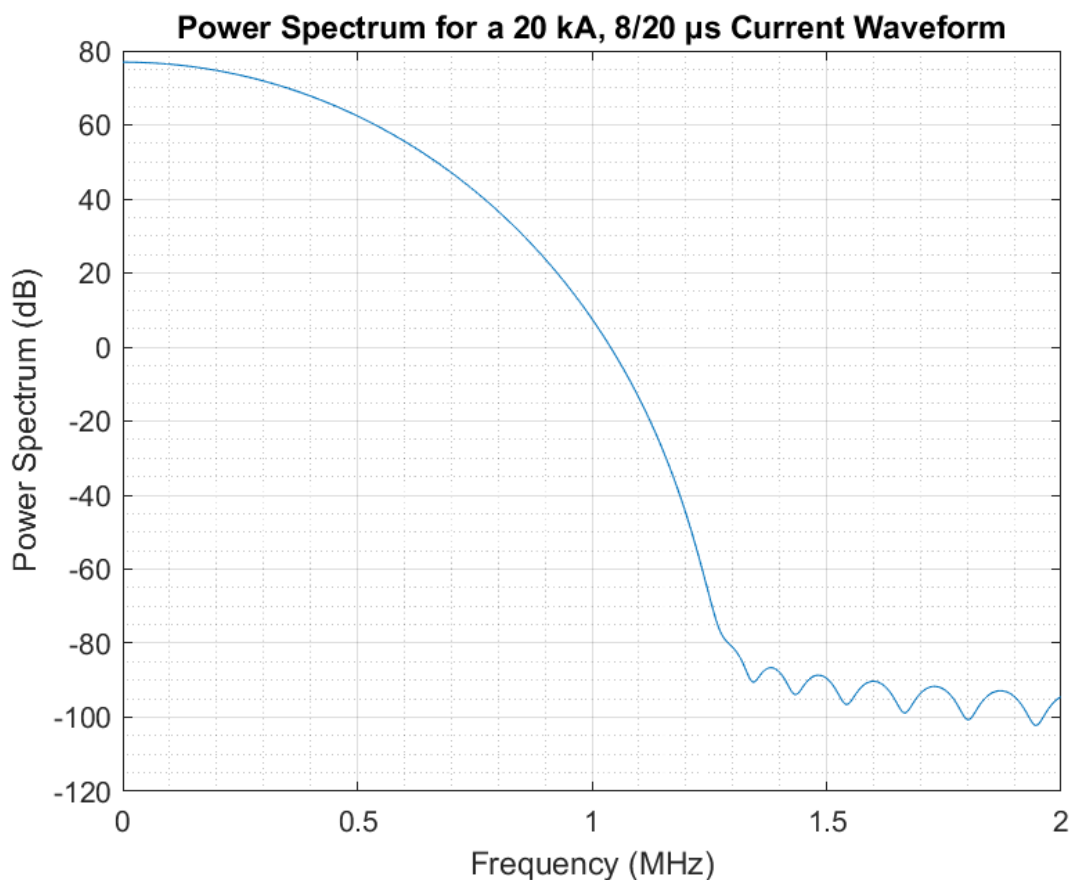


Figure 4.7: The power spectrum of a 20 kA, 8/20 μs current waveform.

The PV module has a slight front-back asymmetry. Simulations were performed in order to determine whether a positive or negative polarity lightning stroke influenced the magnitudes of the induced currents, or just the polarities. The simulations are discussed in Appendix C, and showed that while the polarities are reversed by reversing the polarity of the lightning stroke, the magnitudes are negligibly influenced. As the front-back asymmetry of the module had little influence on the magnitudes of the induced currents, a positive lightning stroke was chosen for all simulations, for the sake of simplicity.

4.4 Electromagnetic Simulation Setup

Altair FEKO ([59]) was the computational electromagnetic simulation software package for all simulations.

The Method of Moments (MoM) solver was utilised. The MoM solver provides a full-wave solution of Maxwell's integral equations in the frequency domain, and is recommended for radiation and coupling analysis [60].

Due to the $8/20\ \mu\text{s}$ impulse waveform consisting of largely low-frequency content, the *low-frequency stabilisation* option was enabled within FEKO. This option allowed for increased solution accuracy in the kHz range (this option is not necessary when solving for frequencies in the MHz-GHz range). It should be noted that the low-frequency stabilisation option is only compatible with the MoM solver [61].

Double precision data storage precision was enabled, on recommendation by the FEKO kernel. The memory requirement for double precision was double that of single precision, however the increased solution accuracy at low-frequencies was a necessity [61].

Surface currents were requested for the entire model geometry in order to give a visual indication of the surface current density for a particular part of the model at a particular frequency. Edge ports were defined wherever a particular current value of interest was to be extracted. Loads with an impedance of $(0 + 0i)\ \Omega$ were defined at each of these ports in order to extract short-circuit currents, and loads of impedance $(10 + 0i)\ \text{G}\Omega$ were defined in order to extract open-circuit voltages.

A time domain $8/20\ \mu\text{s}$ signal was defined, which utilised the frequency domain results from the MoM solver. Extraction of the time domain currents and voltages of interest were plotted on a Cartesian plane.

4.5 Results

Results were computed for cases involving different separation distances between the centre of the PV module and the lightning stroke, both with and without the frame of the module present, in order to examine the effect that the presence of the frame of the module has on the currents induced within the module. A short-circuit loop was then placed between the output terminals of the module, and the results were recomputed in order to ascertain how the presence of this loop would influence the magnitudes of the induced currents. Finally, the simulation of a PV installation with four series-connected modules was performed in order to gauge the influence of good and bad wiring practices on the induced currents.

4.5.1 Open-Circuited PV Module

4.5.1.1 Open-Circuited vs Short-Circuited Bypass Diodes

The first simulation performed involved placing a single PV module vertically centred in the XZ-plane (with the front of the module facing the positive Y-axis), with the lightning stroke at a distance of 1 m along the positive X-axis, as shown in Figure 4.8.

Results were computed for the case in which the bypass diodes were approximated as open-circuits, both with and without the frame of the PV module present. The results are shown in Figure 4.9 and Figure 4.10, respectively.

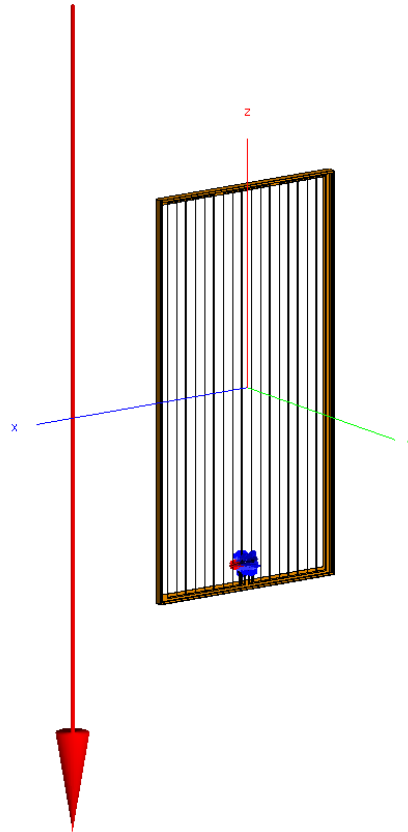


Figure 4.8: Open-circuited PV module with lightning stroke (modelled as an impressed current) at 1 m along the positive X-axis.

For the case with which included the frame, Diode 1 (the diode completing the loop situated closest to the lightning stroke) showed induced voltages of up to 78.2 V. Diode 2 (the diode completing the loop situated in the middle of the module) showed induced voltages of up to 47.0 V. Diode 3 (the diode completing the loop situated furthest from the lightning stroke) showed an induced voltage waveform of opposite polarity to the waveforms seen for Diode 1 and Diode 2. This is a result of a current circulating within the outer frame of the module which produced a magnetic field of opposite polarity to the field caused by the lightning stroke. This counteracting magnetic field was strong enough to result in a reversal of the polarity of the net flux cutting the loop to which Diode 3 was connected, resulting in a negative induced voltage as large as -44.9 V. The summation of these voltages gives the total induced voltage, as would be measured at the output terminals of the PV module - a total of 80.3 V. The occurrence of the negative voltage through Diode 3 is further discussed later in this section.

For the case which did not include the frame - Diode 1 showed induced voltages of up to 223.8 V, Diode 2 showed induced voltages of up to 147.5 V, and Diode 3 showed induced voltages of up to 101.9 V. These induced voltages were each 2-3 times higher than the respective diode voltage in the case where the frame of the PV module was present. The total induced voltage between the output terminals of the PV module was 473.2 V. Referring back to Section 2.5.4.3 and the definition of a *frame reduction factor* (the ratio between the peak induced voltage in a PV module without its frame and the peak induced voltage in a PV module with its frame), a frame reduction factor of 5.89 could be calculated for these simulation results. This value is within a reasonable region, if Figure 2.45 is consulted for the appropriate separation distance (± 0.5 m). It should be noted that the largest values of the induced voltages correlate in time with the largest rate of

changes of the lightning stroke's current waveform - this is as expected, as the induced voltage within an open-circuited loop is dependent on the di/dt of the waveform supplied by the current source (as shown in Equation 2.2).

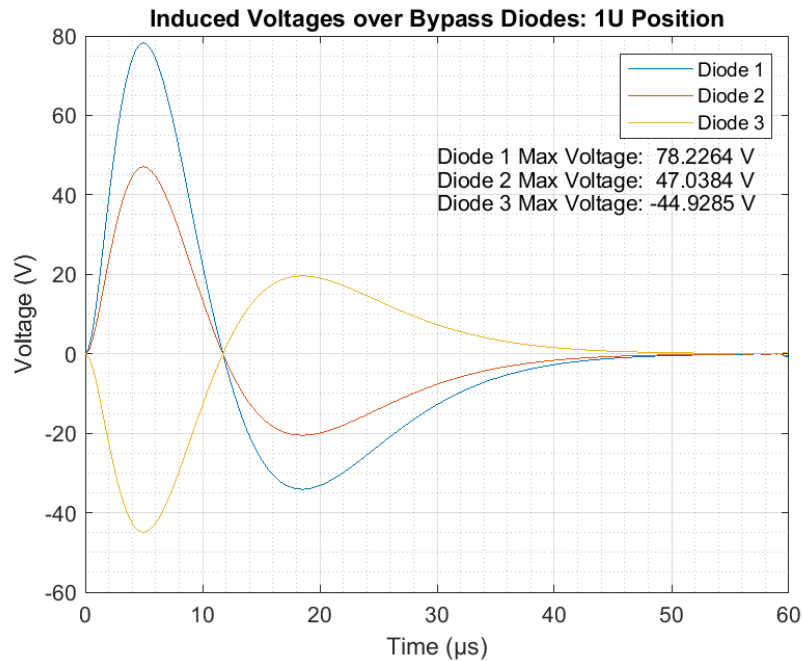


Figure 4.9: Induced voltages over the bypass diodes at a distance of 1 m from the lightning stroke (with frame).

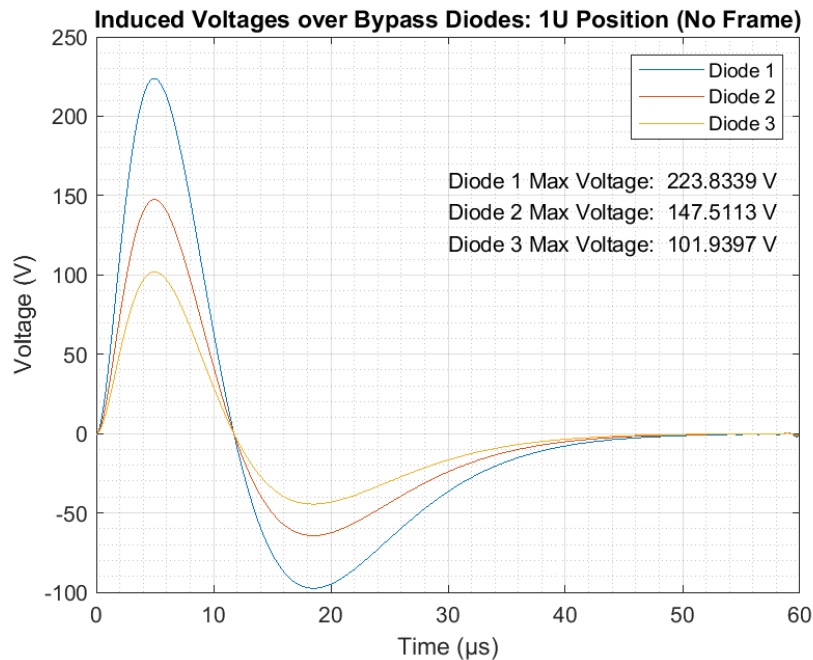


Figure 4.10: Induced voltages over the bypass diodes at a distance of 1 m from the lightning stroke (no frame).

These induced voltages were all larger than the required forward voltage and maximum reverse recovery voltage of a typical bypass diode (approximately 0.2 V and 40 V, respectively).

Therefore it was deduced that if a bypass diode were to be placed within the model, it would begin conducting (in forward or reverse bias).

The reason for the negative polarity of the induced voltage over Diode 3 in the case of the module with the frame is explained by investigating the Y-component of the magnetic field at the centre of the loop formed by the traces connected to Diode 3 (as shown in Figure 4.11). A current is induced within the conductive frame of the PV module (shown by the arrows in Figure 4.12), which creates an opposing magnetic field to the magnetic field from the lightning stroke. The resulting net magnetic flux through this loop has a polarity opposite to that of the magnetic field from the lightning stroke (causing the polarity and magnitudes of the gradient of the flux cutting the loop to change), resulting in a voltage of opposite polarity being induced.

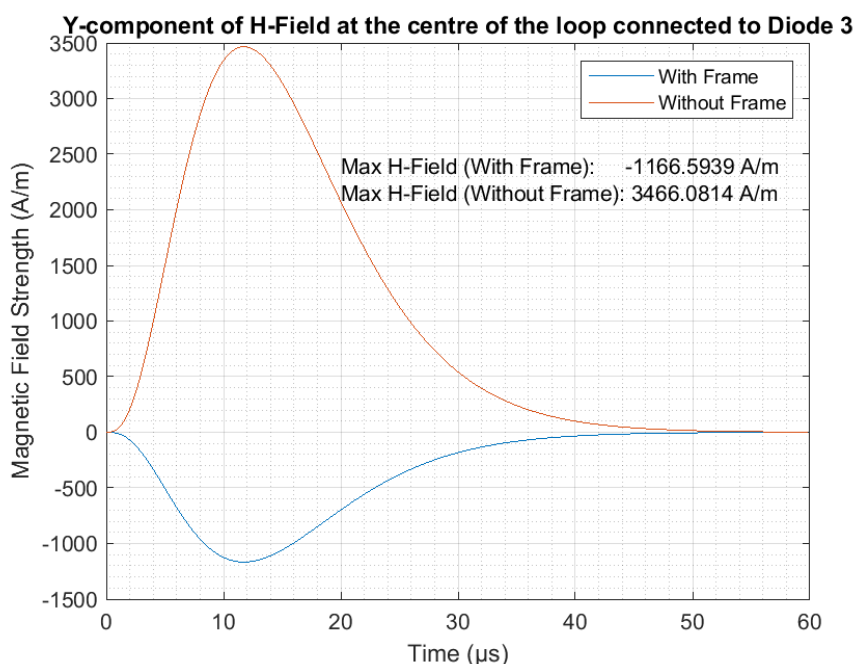


Figure 4.11: A comparison of the Y-component of the H-Field at the centre of the loop connected to Diode 3 (open-circuit case).

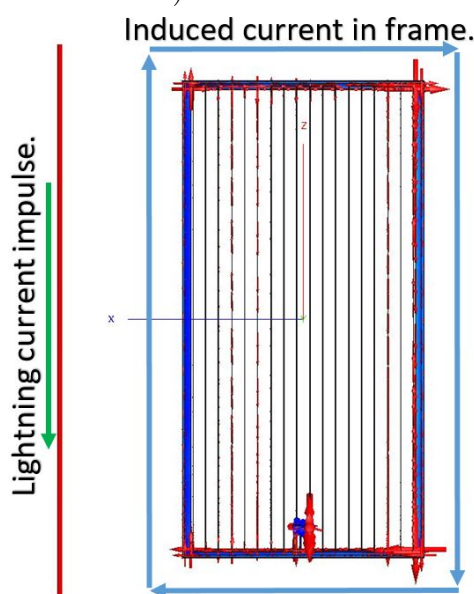


Figure 4.12: Induced currents within the frame of the PV module, viewed from the positive Y-axis.

The currents computed for the short-circuited bypass diode case (with and without the frame) follow a similar pattern. The currents induced in the module with the frame were each lower than the respective currents induced in the module without the frame by a factor of 2-4 times, as can be seen by comparing Figure 4.13 and Figure 4.14. For the case where the frame was present, the current through Diode 1 was 291.9 A, the current through Diode 2 was 189.2 A, and the current through Diode 3 was -123.8 A. For the case where the frame was not present, the current through Diode 1 was 808.6 A, the current through Diode 2 was 616.4 A, and the current through Diode 3 was 399.0 A.

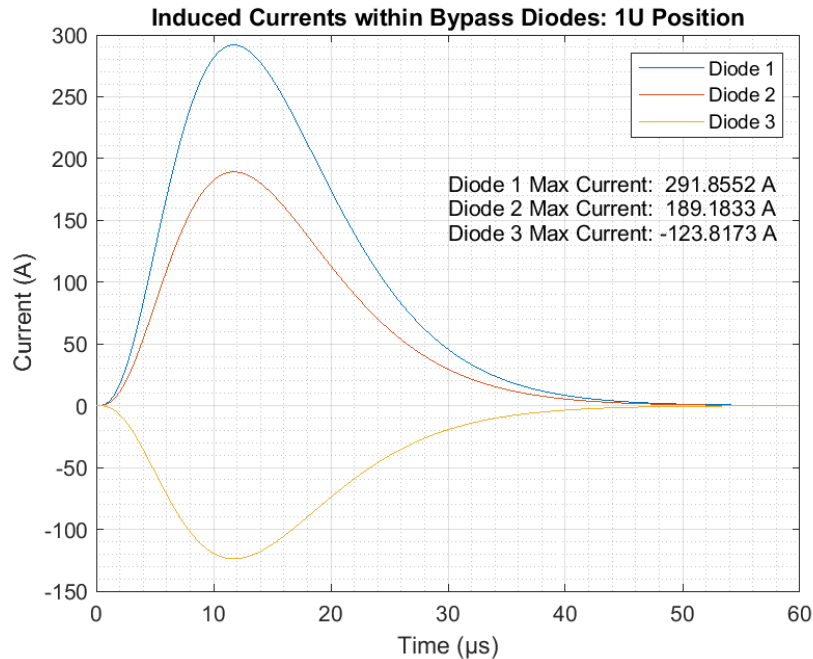


Figure 4.13: Induced currents through bypass diodes at a distance of 1 m from the lightning stroke (with frame).

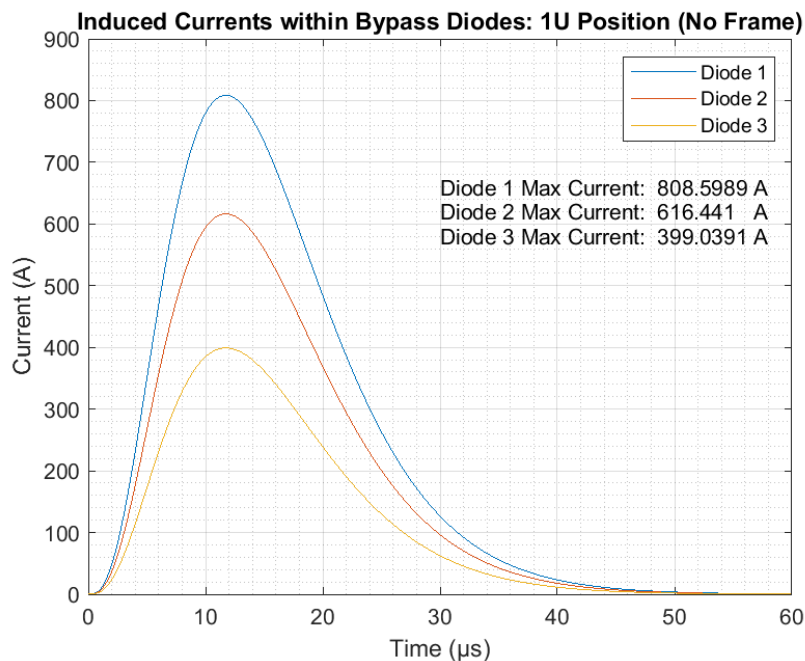


Figure 4.14: Induced currents through bypass diodes at a distance of 1 m from the lightning stroke (no frame).

As with the case of the induced voltage over Diode 3 having an opposite polarity (to the voltage over Diode 1 and Diode 2) in the case with the frame, the current through the Diode 3 also has an opposite polarity (to the current through Diode 1 and Diode 2). This is again explained by examining the Y-component of the H-field at the centre of the loop connected to Diode 3 (as shown in Figure 4.15). It should be noted that Figure 4.15 differs from Figure 4.11 due to the induced current passing through Diode 3 creating an additional magnetic field of its own, thereby influencing the total magnitude of the calculated magnetic field.

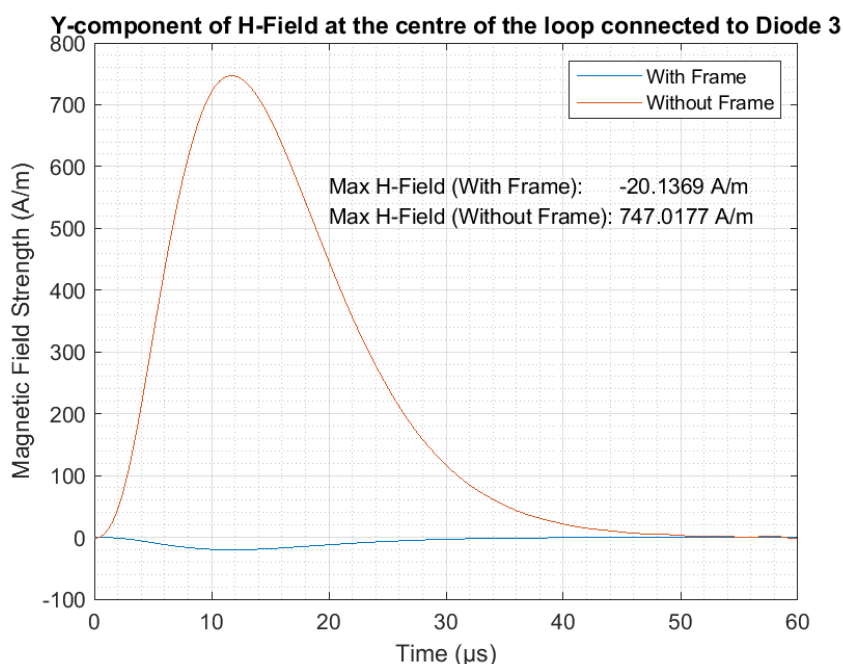


Figure 4.15: A comparison of the Y-component of the H-Field at the centre of the loop connected to Diode 3 (short-circuit case).

4.5.1.2 Influence of separation distance on induced currents.

The short-circuited bypass diode simulations from Section 4.5.1.1 were recomputed for separation distances of 5 m and 10 m (along the X-axis) from the centre of the PV module, for both the cases with and without the frame of the PV module present. The results from the simulations at a separation distance of 5 m are shown in Figure 4.16 and Figure 4.17, respectively.

For the case (with a 5 m separation distance) in which the frame was present, the peak current through Diode 1 was 10.0 A, the peak current through Diode 2 was 17.7 A, and the peak current through Diode 3 was 0.677 A. This was due to a larger proportion of the loops connected to Diode 1 and Diode 3 being in close proximity to the frame than for the loop connected to Diode 2, therefore the influence of the opposing magnetic field caused by the induced current within the frame was stronger for the loops connected to Diode 1 and Diode 3, resulting in lower currents for these loops than for the loop connected to Diode 2. The net flux through the loop connected to Diode 3 was positive at this distance, resulting in a positive current flowing through Diode 3 (as opposed to the negative current through Diode 3 noted in the case with a separation distance of 1 m).

For the case (with a 5 m separation distance) in which the frame was not present, the peak current through Diode 1 was 49.7 A, the peak current through Diode 2 was 50.3 A, and the peak current through Diode 3 was 40.4 A. In contrast with the cases with a separation distance of 1 m, the highest induced current in these cases was through Diode 2. In this simulation, each loop area was much further from the lightning stroke than in the case with a separation distance of 1 m. This higher current through Diode 2 was due to the magnetic fields which radiated from the currents induced in the loops connected to Diode 1 and Diode 3 constructively adding their own magnetic fluxes to that which passed through the loop connected to Diode 2, increasing the total magnetic flux through this loop.

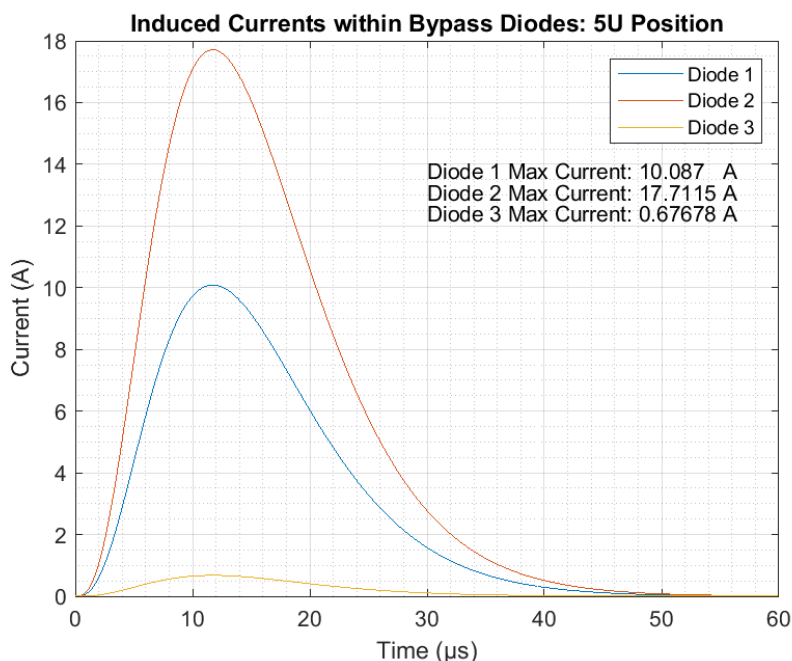


Figure 4.16: Induced currents through bypass diodes at a distance of 5 m from the lightning stroke (with frame).

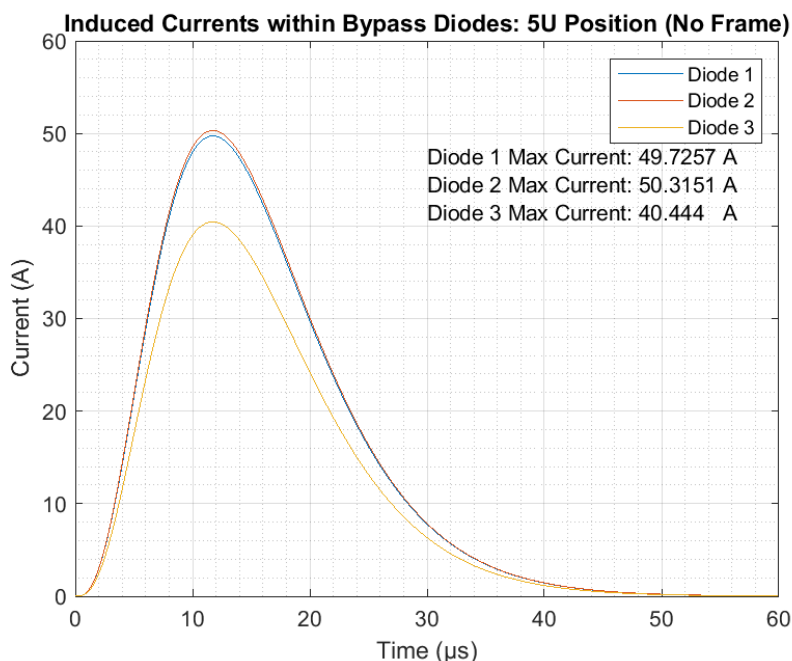


Figure 4.17: Induced currents through bypass diodes at a distance of 5 m from the lightning stroke (no frame).

The results from the simulations at a separation distance of 10 m are shown in Figure 4.18 and Figure 4.19, respectively. For the case (with a 10 m separation distance) in which the frame was present, the peak current through Diode 1 was 2.06 A, the peak current through Diode 2 was 4.74 A, and the peak current through Diode 3 was 0.74 A. For the case (with a 10 m separation distance) in which the frame was not present, the peak current through Diode 1 was 12.6 A, the peak current through Diode 2 was 13.4 A, and the peak current through Diode 3 was 11.3 A. In contrast with the previous cases with a separation distance of 1 m, and in agreement with the previous cases with a separation distance of 5 m, the highest induced current in the cases with a separation distance of 10 m was through Diode 2.

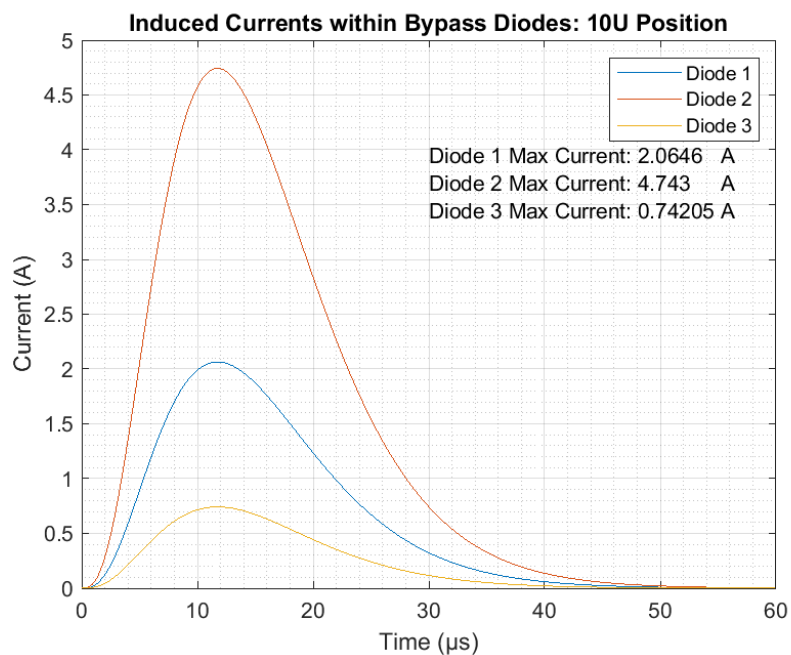


Figure 4.18: Induced currents through bypass diodes at a distance of 10 m from the lightning stroke (with frame).

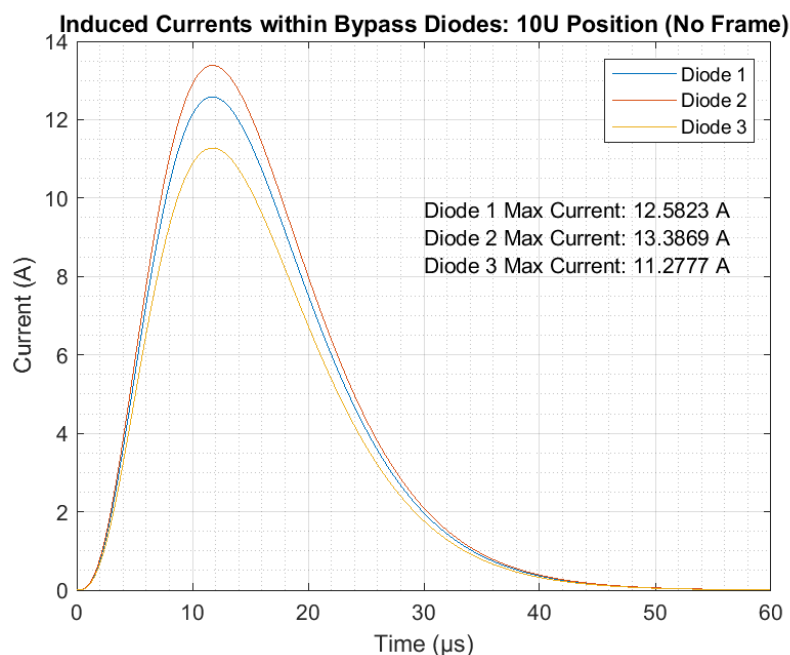


Figure 4.19: Induced currents through bypass diodes at a distance of 10 m from the lightning stroke (no frame).

For the cases in which the frame was not present, the currents through the bypass diodes became more similar in magnitude with each other with increasing separation distance. This was as expected, due to the difference in distance between each loop being much smaller than the separation distance between any of the loops and the lightning stroke.

For the cases in which the frame was present, the induced currents had lower peak magnitudes than the cases where the frame was not present. The trend observed was that the presence of the frame resulted in a larger reduction of the induced currents with increasing distance from the lightning stroke.

4.5.2 Short-Circuited PV Module

A short-circuited loop was added to the CAD model between the output terminals of the PV module in order to determine the contribution that an external loop area may have on the induced currents. The length of the loop was approximately 2 m, the collective length of the wiring which is commonly connected to a PV module at the factory [2]. The CAD model with the short-circuited loop is shown in Figure 4.20. Note that the polarity of the port used to extract the current in the short-circuited loop was opposite to that of the polarity of the ports used to extract the currents in the short-circuited bypass diodes. A negative short-circuit loop current would therefore add constructively to a positive diode current. This allowed for clearer plotting of the induced currents.

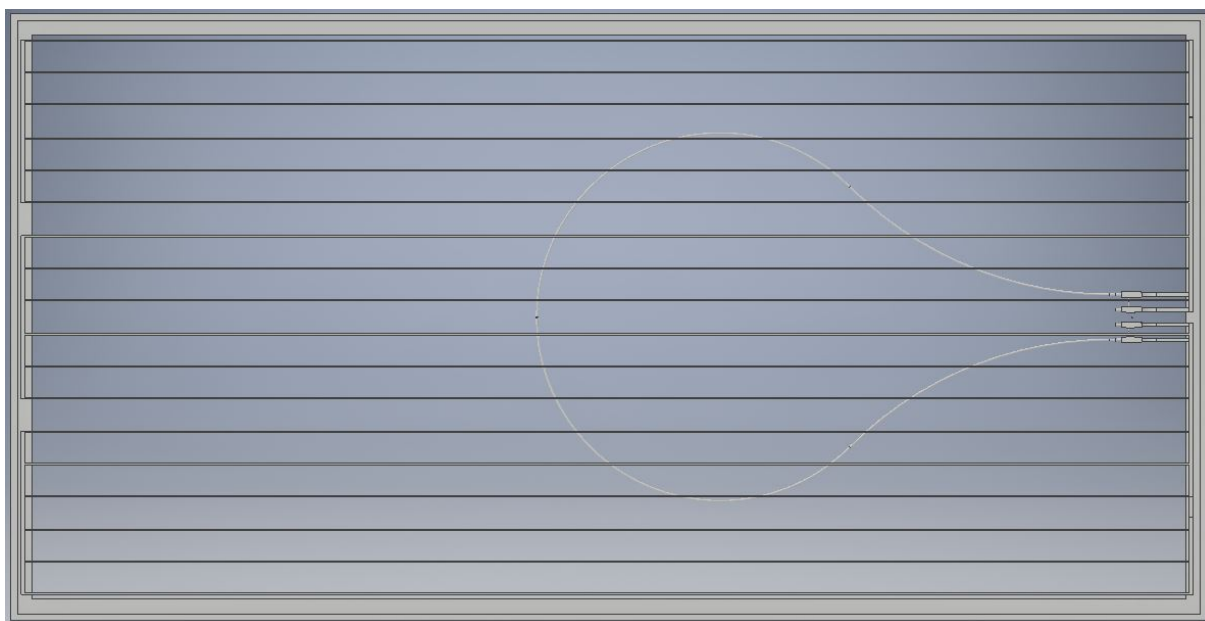


Figure 4.20: The CAD model of a PV module with the addition of a short-circuit between the output terminals.

As in the cases without the short-circuited loop between the output terminals of the PV module, simulations were run for separation distances of 1 m, 5 m, and 10 m between the middle of the module (placed centred in the XZ-plane) and the lightning stroke. Simulations were run for cases both with and without the frame of the module present.

Figure 4.21 the case (with a 1 m separation distance) in which the frame was present, the peak current through Diode 1 was 514.6 A, the peak current through Diode 2 was

358.7 A, and the peak current through Diode 3 was 97.9 A. The peak current through the short-circuit loop was 207.3 A.

Figure 4.22 the case (with a 1 m separation distance) in which the frame was not present, the peak current through Diode 1 was 1245.0 A, the peak current through Diode 2 was 948.0 A, and the peak current through Diode 3 was 834.4 A. The peak current through the short-circuit loop was 416.4 A.

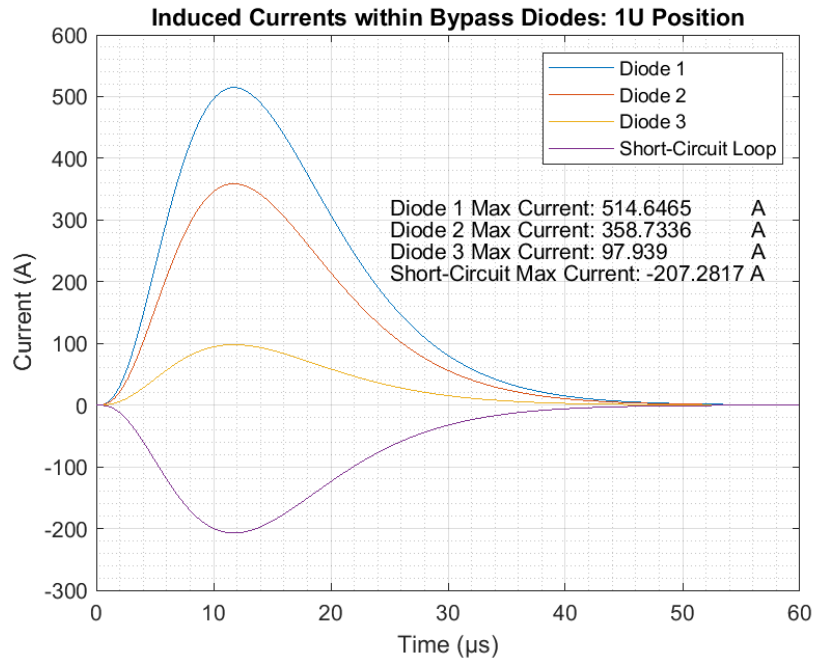


Figure 4.21: Induced currents at a distance of 1 m from the lightning stroke (with frame and short-circuit loop).

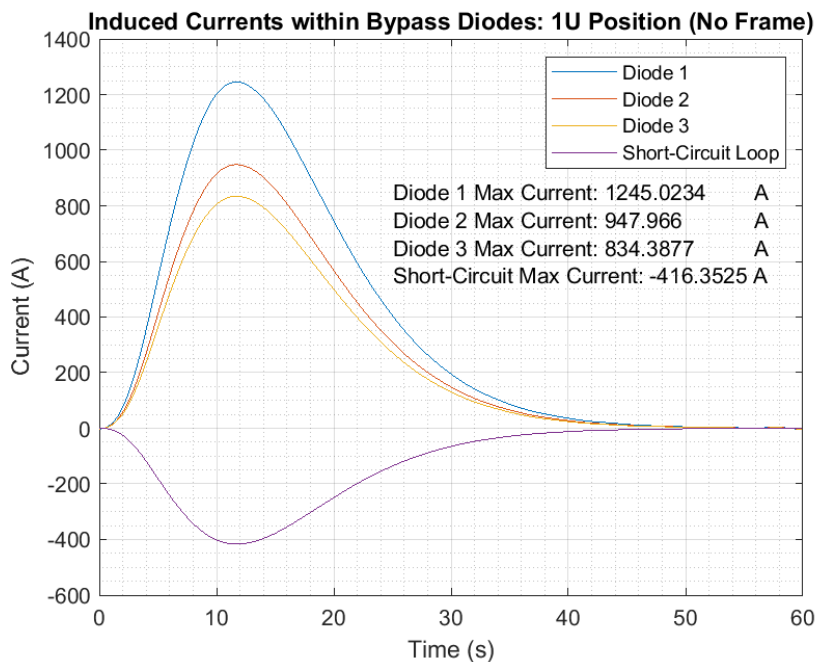


Figure 4.22: Induced currents at a distance of 1 m from the lightning stroke (no frame, with short-circuit loop).

Figure 4.23 shows the case (with a 5 m separation distance) in which the frame was present, the peak current through Diode 1 was 28.8 A, the peak current through Diode 2 was 32.0 A, and the peak current through Diode 3 was 19.4 A. The peak current through the short-circuit loop was 19.4 A.

Figure 4.24 shows the case (with a 5 m separation distance) in which the frame was not present, the peak current through Diode 1 was 84.7 A, the peak current through Diode 2 was 76.9 A, and the peak current through Diode 3 was 75.4 A. The peak current through the short-circuit loop was 33.4 A.

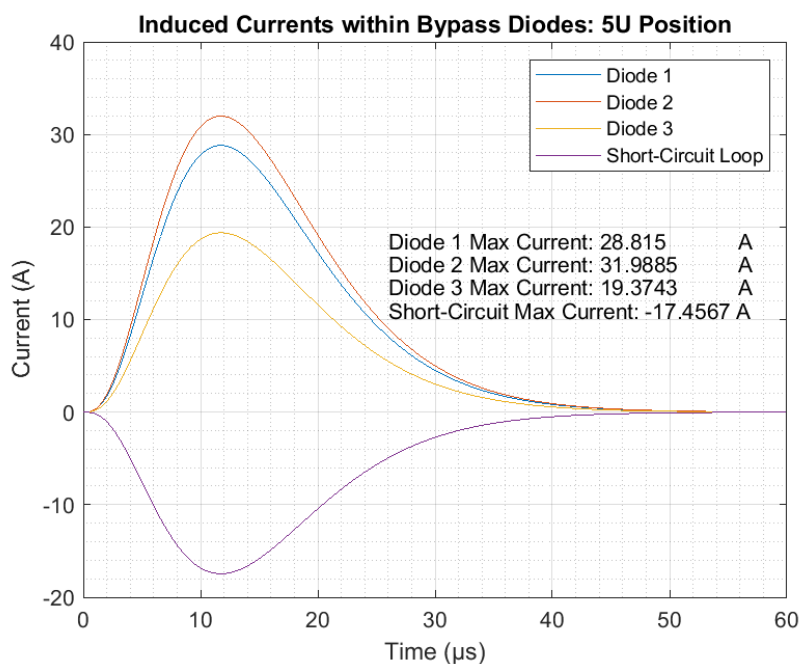


Figure 4.23: Induced currents at a distance of 5 m from the lightning stroke (with frame and short-circuit loop).

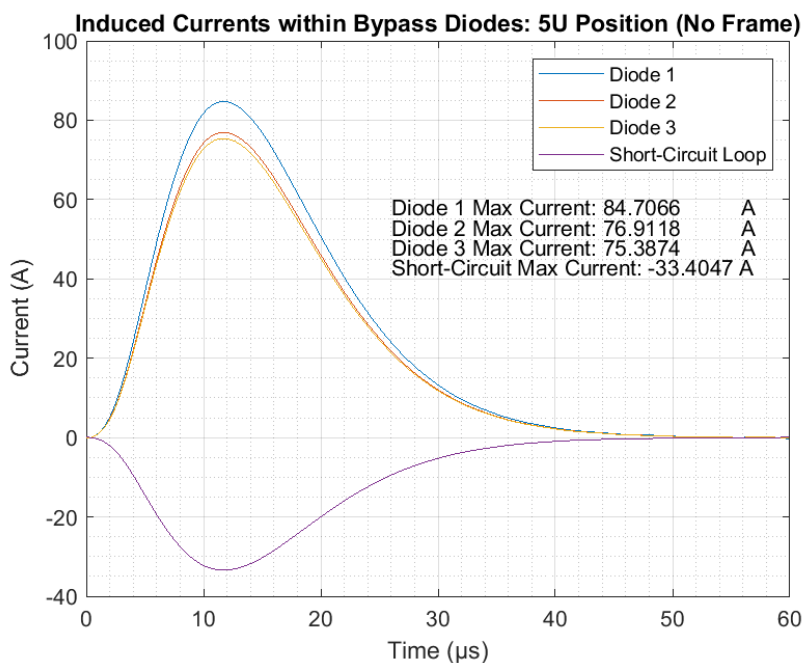


Figure 4.24: Induced currents at a distance of 5 m from the lightning stroke (no frame, with short-circuit loop).

Figure 4.25 shows the case (with a 10 m separation distance) in which the frame was present, the peak current through Diode 1 was 6.99 A, the peak current through Diode 2 was 8.50 A, and the peak current through Diode 3 was 5.66 A. The peak current through the short-circuit loop was 4.59 A.

Figure 4.26 shows the case (with a 10 m separation distance) in which the frame was not present, the peak current through Diode 1 was 21.8 A, the peak current through Diode 2 was 20.4 A, and the peak current through Diode 3 was 20.5 A. The peak current through the short-circuit loop was 8.8 A.

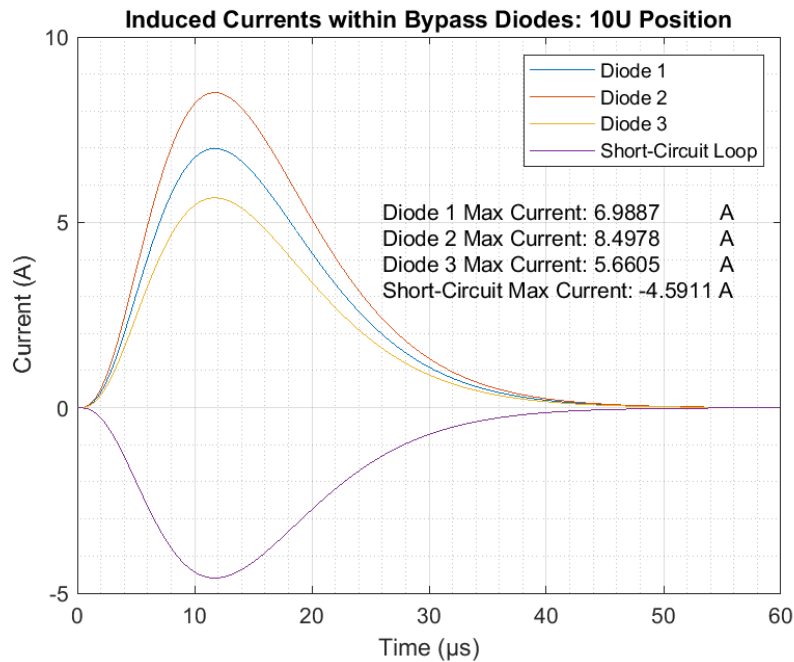


Figure 4.25: Induced currents at a distance of 10 m from the lightning stroke (with frame and short-circuit loop).

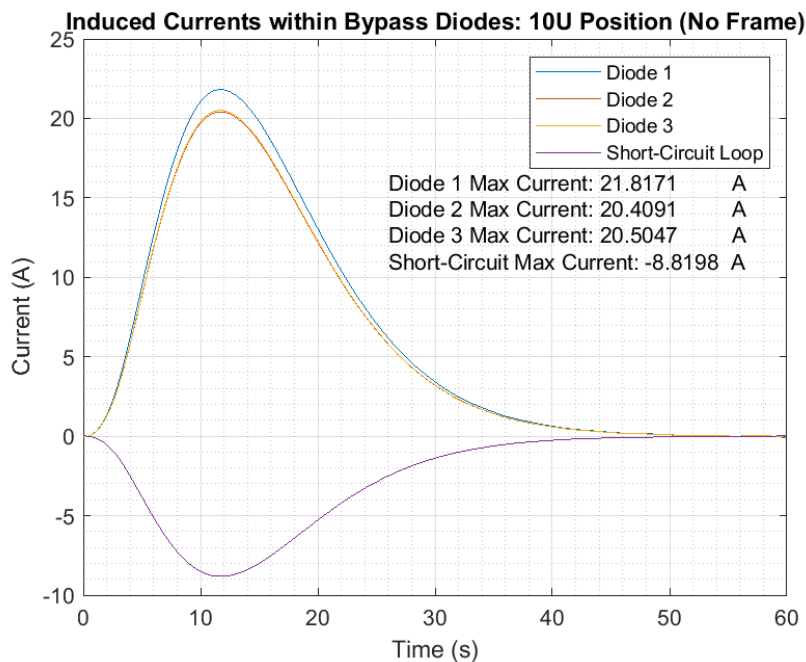


Figure 4.26: Induced currents at a distance of 10 m from the lightning stroke (no frame, with short-circuit loop).

The presence of the short-circuit loop resulted in an additive contribution to the induced currents within the bypass diodes in all cases.

When comparing the simulated currents in the short-circuit loop in the cases with and without the frame, it was found that the current induced when the frame was present was approximately half that of when the frame was not present (for any of the separation distances considered).

For the case without the loop and with the frame present, the induced currents within Diode 1, Diode 2, and Diode 3 become more similar with increasing distance. The same trend was observed for the case without the presence of the frame.

For the framed modules, no negative currents were observed in the loop connected to Diode 3 (or any other diodes) with the presence of the short-circuit loop (at any of the considered separation distances). This suggests that the influence of the current induced within the short-circuit loop was greater than the influence of the counter-active induced current within the frame of the module, preventing the reversal of the net magnetic flux cutting the loop connected to Diode 3 (as previously seen in Figure 4.13).

4.5.3 Module Interconnections

The degree to which poor inter-module wiring practice may influence the currents induced within a PV module was investigated by placing four series-connected modules positioned adjacent to each other in the XZ-plane, with the centre of the first module positioned at the origin (and with the other modules extending into the negative X-axis). The frames of these modules were connected to each other using earth straps located at the bottom of the modules. The same 20 kA, 8/20 μ s positive polarity impressed current impulse used in previous simulations was placed at a distance of 1 m along the positive X-axis. The size of the loop created by the inter-module wiring was altered, with a large loop area being used for the simulation of a poor installation (as shown in Figure 4.27), and a small loop area being used for the simulation of a better installation (as shown in Figure 4.28). The currents through each bypass diode in each module, as well as the short-circuit loop current, were extracted. The induced currents for the poor installation are shown in Figure 4.29, and the induced currents for the better installation are shown in Figure 4.30.

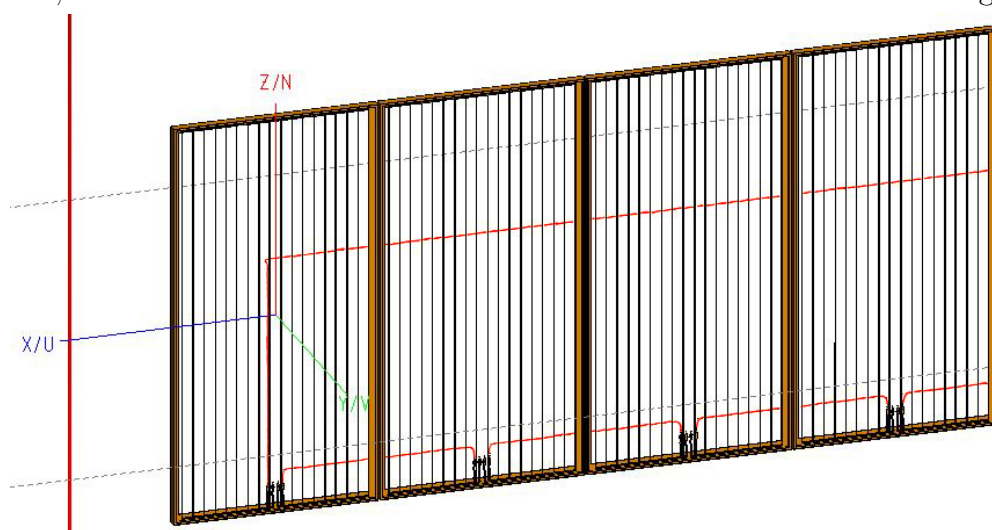


Figure 4.27: Simulation setup with multiple PV modules and poor inter-module wiring.

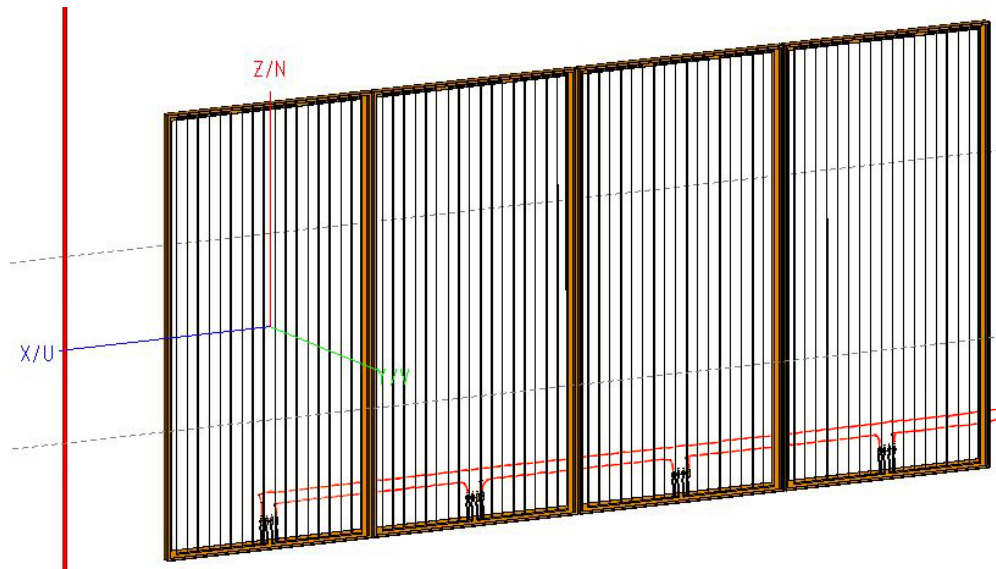


Figure 4.28: Simulation setup with multiple PV modules and better inter-module wiring.

In the above figures, the following labelling pattern was used - from left to right, Diodes 1-3 are the diodes in the first module, Diodes 4-6 are the diodes in the second module, Diodes 7-9 are the diodes in the third module, and Diodes 10-12 are the diodes in the fourth module. The polarity of the port used to measure the induced current for the inter-module wiring was of opposite polarity to the ports used to measure the currents through the bypass diodes (as was the case with simulations involving single short-circuited PV modules).

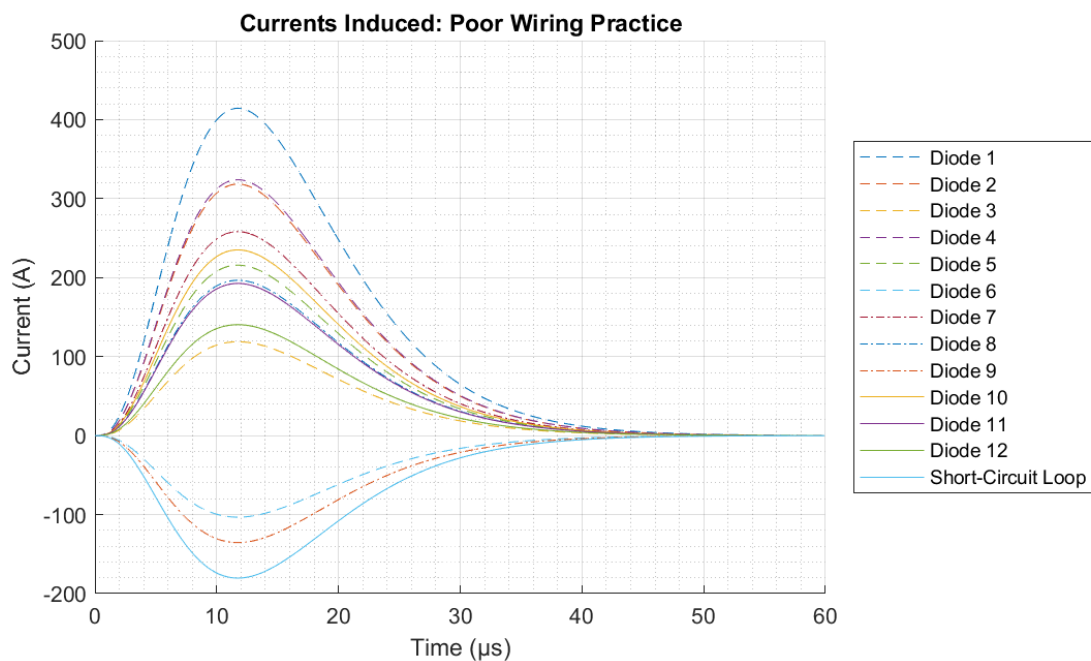


Figure 4.29: Induced currents in a PV installation where poor inter-module wiring practice was used.

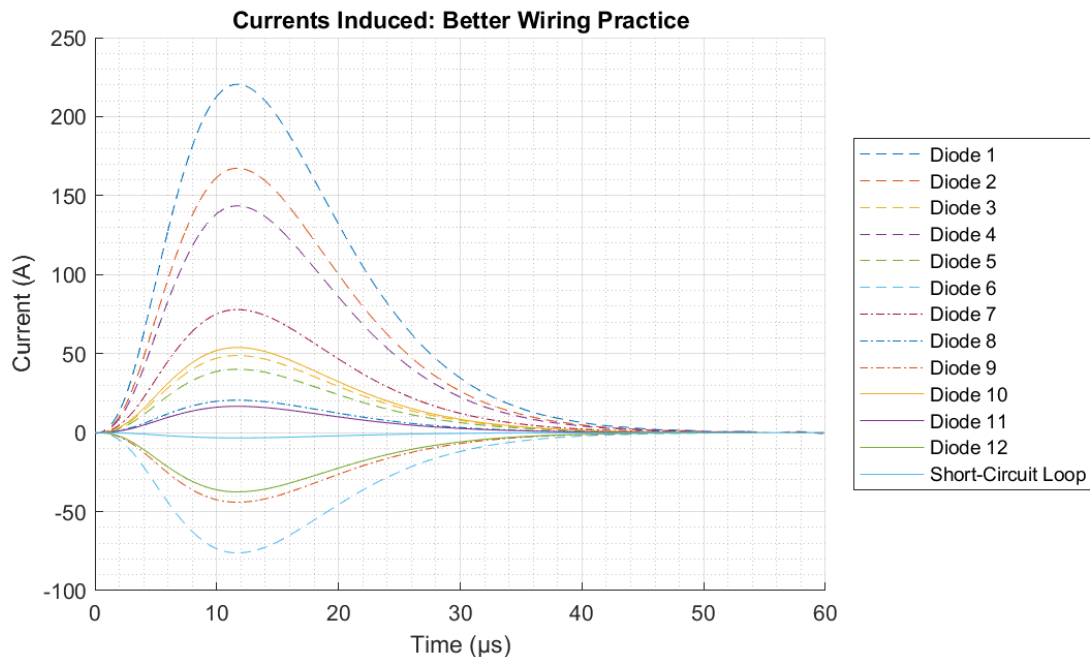


Figure 4.30: Induced currents in a PV installation where better inter-module wiring practice was used.

The general trend observed was that the magnitudes of the currents induced within the loops connected to the bypass diodes in the better installation were approximately half that of the induced currents in the poor installation. In the poor installation, the short-circuit loop representing the inter-module wiring had a peak current of 180 A, whilst in the better installation the peak current in this loop was reduced to 2 A (a significant reduction).

The influence of the magnetic fields created by the frames and the current flowing through the short-circuit loop resulted in a reversal of the polarity of the net magnetic flux passing through the loops connected to Diode 6 and Diode 9 (the outermost loops in the second and third modules, respectively) in the case with the poor installation. The same occurred for the loops connected to Diode 6 and Diode 9, as well as Diode 12, in the case with the better installation.

The simulation for the poor installation and the better installation were recomputed for the cases in which the frames of the modules were not present (the results of which are shown in Figure 4.31 and Figure 4.32, respectively). In the case with the poor installation without the presence of the module frames, the current induced within the short-circuit loop had a peak current of 330 A. In the case with the better installation without the presence of the module frames, the peak magnitude of the current induced within the short-circuit loop was -22 A - again, a significant reduction.

For the poor installation, the currents induced in the loops connected to Diode 6 and Diode 9 were once again of the opposite polarity as the currents induced within the other diodes. This polarity reversal was the similar as that observed in the case of the poor installation where the frames were present, although the peak magnitudes, however, were approximately eight times larger in the case where the frame was not present.

For the better installation, the currents induced in the loops connected to most bypass diodes were mostly of a positive polarity, as would be expected due to the low peak magnitude of the current in the short-circuit loop and the absence of the counter-acting magnetic flux typically seen in cases where the frame was present.

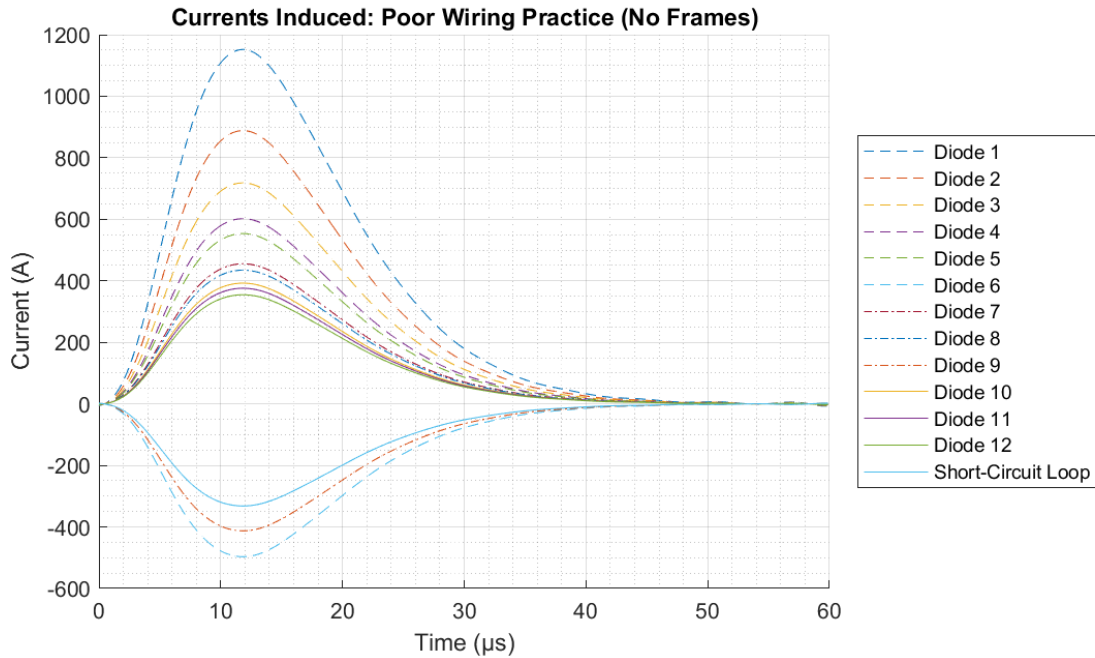


Figure 4.31: Induced currents in a PV installation where poor inter-module wiring practice was used (without frames).

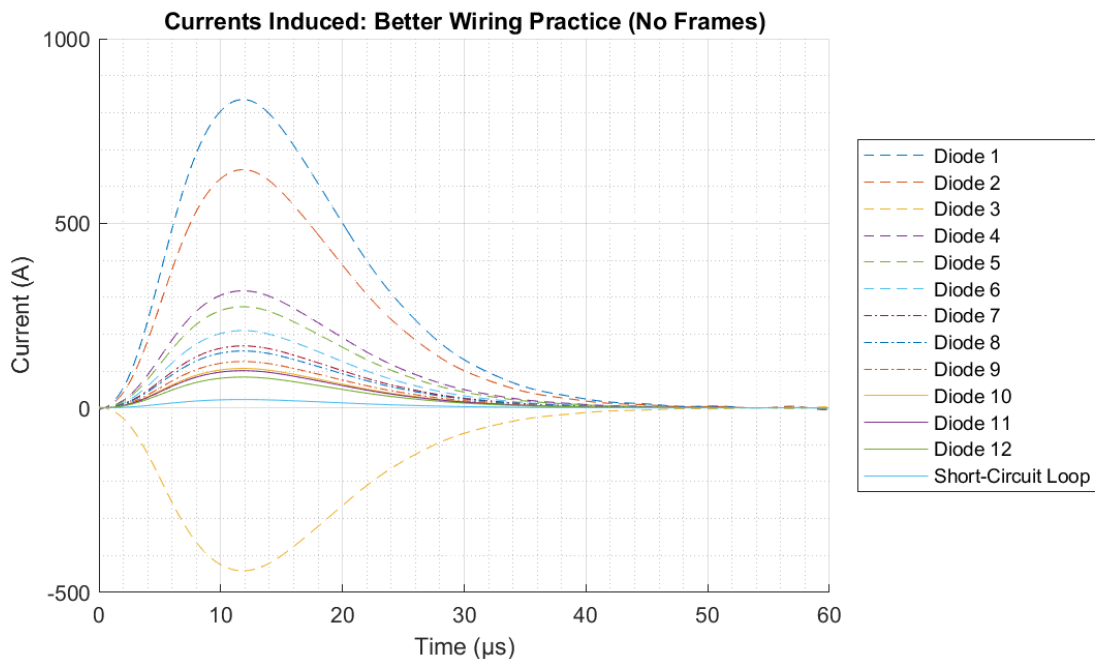


Figure 4.32: Induced currents in a PV installation where better inter-module wiring practice was used (without frames).

4.6 Challenges Encountered with Electromagnetic Modelling

The largest challenge encountered during the electromagnetic modelling process involved incorrect meshing of the CAD model. Errors relating to intersecting triangles were often reported, resulting in the termination of the solver processes by the FEKO kernel. Running the *Find Intersecting triangles* utility resulted in the finding of zero intersecting triangles. The challenge was finally overcome by setting the export accuracy of the .stp file in Autodesk Inventor Professional 2018 to 0.0001 mm, disabling the *Allow elongated triangles* option in the FEKO mesh settings.

Due to the large number of mesh triangles (anywhere from 9000 to 32000) involved in any one simulation, simulations usually took long to complete (anywhere from 180 CPU hours for the simplest cases to over 5000 CPU hours for more complex simulations). In order to speed up simulation progress, CPU parallelisation (the action of utilizing multiple CPU cores running multiple processes) and GPU acceleration were compared, with CPU parallelisation resulting in faster completion of simulation. Currently, CPU parallelisation cannot be used simultaneously with GPU acceleration in FEKO.

Larger simulations remained particularly resource-heavy, and therefore required the use of computing clusters in order to satisfy the RAM requirements (sometimes as much as 80 GB) to reduce real-world computation time. The smaller computing cluster had 24 cores and 250 GB of RAM, and the larger computing cluster had 48 cores and 750 GB of RAM.

4.7 Chapter Conclusion

The first conclusion drawn from the simulations performed in this chapter was that the presence of the frame of a PV module has a drastic influence on the magnitudes of the currents induced within the module. At a separation distance of 1 m, the peak magnitudes of the induced currents in the case where the frame was present were approximately 30-40% of the peak magnitudes in the case where the frame was not present. At a separation distance of 5 m, this margin decreased to 20-35%. At a separation distance of 10 m, this margin further decreased to 6.6-34% - this suggests that the presence of the frame results in a proportionally greater reduction in the magnitudes of the induced currents as the separation distance increases.

The second conclusion drawn was that the presence of a short-circuit loop between the output terminals of a PV module resulted in an additive contribution to the currents induced within the bypass diodes. Comparing the cases with the frame present, with and without the presence of the short-circuit loop, at a separation distance of 1 m, it can be seen that the peak magnitudes of the induced currents increased by 80-90%, indicating the potential influence of large loop areas within the inter-module wiring. The influence of the presence of the short-circuit loop was sufficient to reverse the polarity of the current induced in the loop connected to Diode 3.

Further simulations were performed in order to examine the influence of the frame and inter-module wiring in a multi-module installation. Better wiring practice was shown to

reduce the currents induced within the inter-module wiring by between 93 % and 98 % in the cases with and without the presence of the frames, respectively. This emphasized the importance of good wiring practice (the minimisation of any loop areas in the inter-module wiring) in order to minimise the susceptibility of an installation to EMI.

In the case of the multi-module installation with the poor wiring practice, the presence of the frames of the modules reduced the peak magnitude of the current induced within the inter-module wiring from approximately 300 A to approximately 180 A. There is an increasing trend towards the adoption of frameless PV modules, especially of the glass-on-glass variety (where the PV module is located between two layers of glass) for three main reasons - reduced potential induced degradation, improved aesthetics, and increased fire-safety [62]. As these PV modules are not encompassed by a conductive frame in which a current could be induced, lowering the net magnetic flux passing through the loop formed by the inter-module wiring, the magnitudes of the currents induced within the inter-module wiring would be larger - creating possible cause for concern for the susceptibility of these new module designs to the effects of nearby lightning strikes. The effect of the inclusion of a conductive loop, surrounding (but not connected to) the trace layouts within a PV module (mimicking the conductive loop formed by the frame), would be worth investigating for reducing the net magnetic flux passing through a frameless PV module.

The third research goal (investigate how the configuration of a PV installation, including the frame and internal layout of a PV module, as well as the inter-module wiring, may influence the magnitudes of the currents induced within the installation) was achieved in this chapter by simulating how the magnitudes of the currents induced within a PV installation are affected by separation distance, the presence of the frame, and the inter-module wiring.

A number of assumptions were made in the design of the model used in the electromagnetic modelling presented in this chapter. The following chapter recreates some of the simulation configurations used within this chapter in order to test these assumptions.

Chapter 5

High-Voltage Testing

5.1 Chapter Overview

Testing was performed in a high-voltage laboratory in order to gather real-world results pertaining to induced currents within a PV module resulting from the magnetic field radiating from a nearby lightning stroke (further satisfying the third research goal defined in Section 1.5). The focus of the study was to determine the extent to which currents may be induced within a PV module, and the extent to which external wiring connected to the module may influence the currents conducted through the bypass diodes in the module. Some of the results found challenge the assumptions made in the electromagnetic modelling presented in the previous chapter.

5.2 High-Voltage Impulse Generator

The available impulse generator was a Philips model 14030, designed in the 1940s. It is comprised of a Marx generator with spark-gap switches, and was charged and discharged through a network of resistors. The charging generator for the Marx generator was able to supply up to 200 kV. Eight 0.125 μF capacitors formed the eight stages of the Marx generator, which when configured to provide voltage impulses was able to supply up to 1.4 MV [63].

As this investigation required the generation of a large current impulse by the generator (in order to create a large magnetic field), the impulse generator was switched to the current commutation. This resulted in the generator both charging and discharging with the capacitors placed in parallel. The Marx generator would discharge through a spark-gap, whose gap size would determine the level at which the Marx generator would charge to.

5.3 Impulse Generator Simulation

As the 8/20 μs waveform had been used in the electromagnetic modelling in Chapter 4, this was the desired current impulse waveform for the testing in the high-voltage environment. This would allow for the comparison of the electromagnetic model with the real-world induced current measurements. The impulse generator produced a negative impulse, therefore all waveforms in this section are of a negative polarity.

An initial short-circuit current waveform from the impulse generator was recorded, as shown in Figure 5.1. This waveform had a front time τ_1 of 3.8 μs and a time to half-value τ_2 of 10.4 μs - shorter than the $\pm 20\%$ tolerance specified in [39] allowed for. The recorded undershoot of 11.3% was below the maximum tolerable level of 30%.

The impulse generator was simulated using Simulink in order to ascertain how the impulse generator should be reconfigured in order to obtain the desired timing parameters. The physical layout of the generator was observed, and the circuit shown in Figure 5.2 was developed. The charging generator was excluded from the simulation, as the current at which it was capable of charging the impulse generator was negligible in comparison with the magnitude of the current waveform provided by the impulse generator.

Initial simulated current waveforms were shorter in duration than the recorded waveform in Figure 5.1, therefore a series inductor was added to represent the self-inductance of the impulse generator. The series inductor and the initial capacitor voltages were adjusted until the waveform shown in Figure 5.4 (labelled "Without External Inductor") was obtained. This waveform had an output with a peak magnitude of -5.75 kA and front time τ_1 of 4.08 μs , similar to that shown in Figure 5.1. The simulated time to half-value τ_2 of 14.9 μs , however, was longer than that shown in Figure 5.1. No undershoot was present in this simulation. The capacitors in the simulation were set to an initial voltage of -125 kV , and the series inductor was set to 50 μH for this waveform.

An additional series inductor was added in order to further shape the short-circuit current waveform (as shown in Figure 5.3). This series inductor was adjusted to 50 μH , resulting in the short-circuit current waveform shown in Figure 5.4 (labelled "With External Inductor"). This waveform had a output with a peak magnitude of -4.9 kA , a front time τ_1 of 6.72 μs , and a time to half-value τ_2 of 21.77 μs . No undershoot was present in this simulation. The timing parameters τ_1 and τ_2 were within the allowable tolerances specified in [39]. Consulting the datasheet of the impulse generator found that an approximate inductance of 51 μH should be added for a 10/20 μs waveform [63], similar to the inductance of the necessary series inductor determined in simulation - a reinforcement that the simulation was of reasonable accuracy.

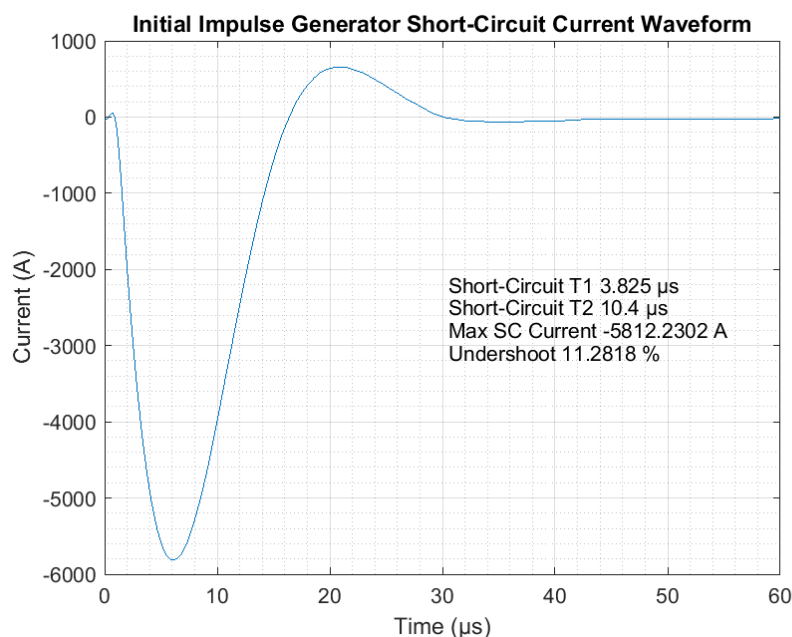


Figure 5.1: Initial short-circuit current waveform obtained from the HV impulse generator.

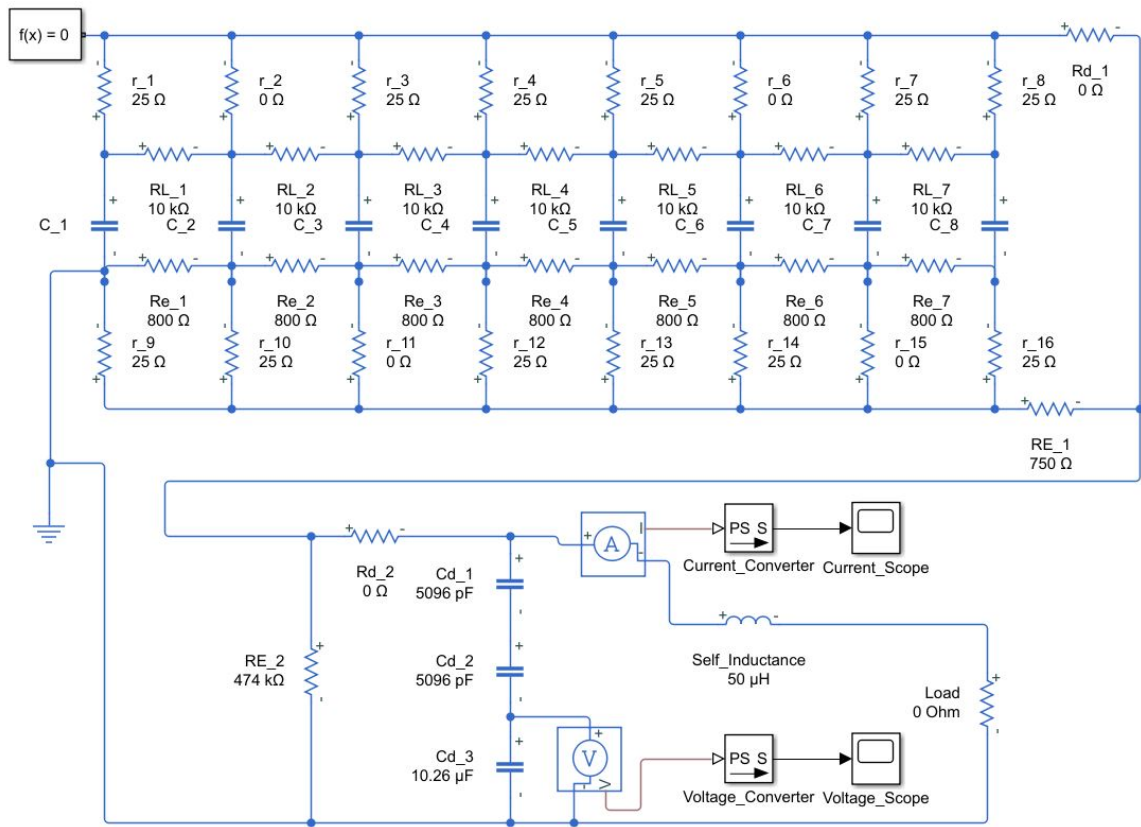


Figure 5.2: The circuit used for the simulation of the impulse generator.

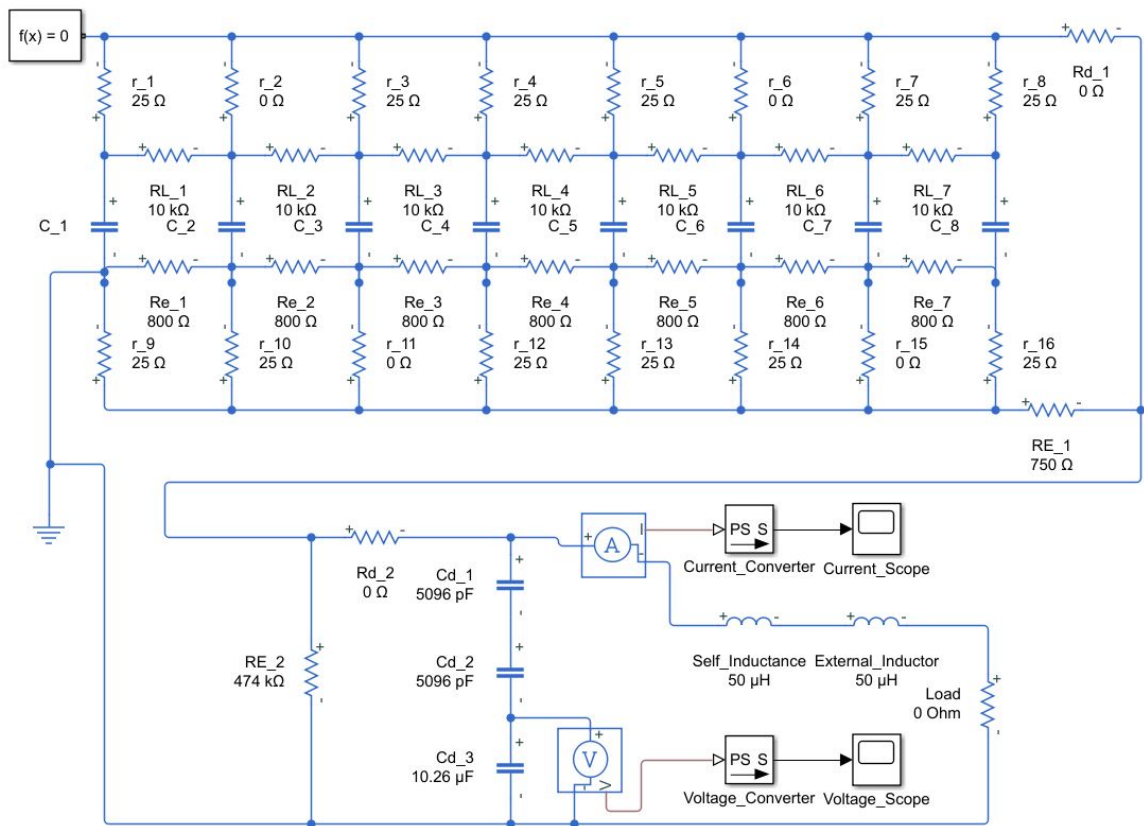


Figure 5.3: The circuit used for the simulation of the impulse generator (with external inductor).

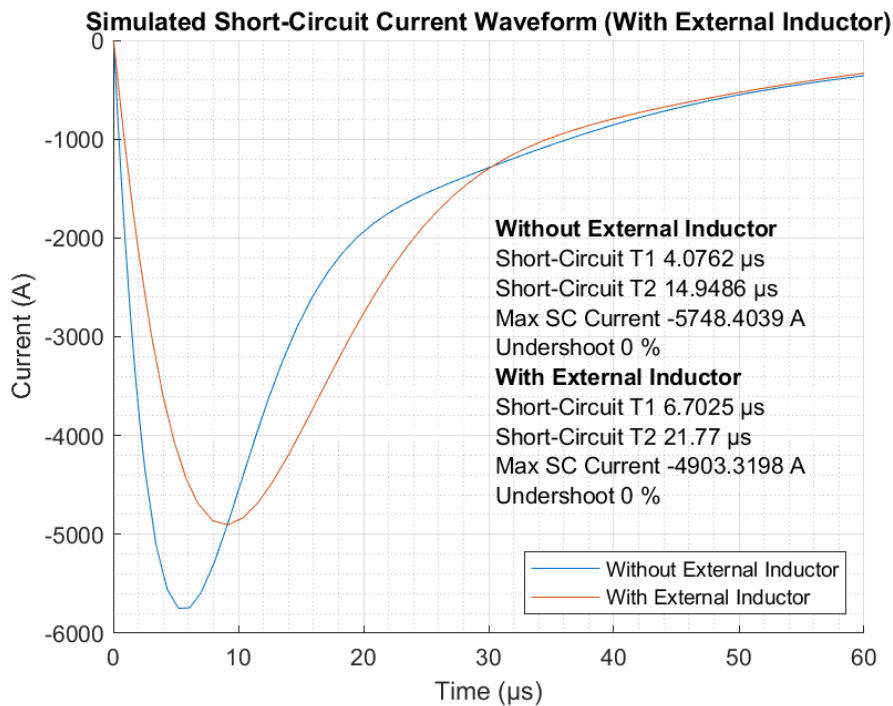


Figure 5.4: The short-circuit current waveforms obtained from simulation.

An air core inductor, made by coiling wire of thickness 10 mm, was added in series with the output of the impulse generator. This inductor had 9 turns, with a loop diameter of approximately 30 cm. According to Equation E.1, this should have resulted in an inductance of about 53.1 μH . The inductor was physically adjusted until the waveform shown in Figure 5.5 was obtained. This waveform had a peak magnitude of -4420 A, a front time τ_1 of 9.25 μs , and a time to half-value τ_2 of 21.7 μs . Both of the timing parameters were within the allowable $\pm 20\%$ tolerance specified in [39].

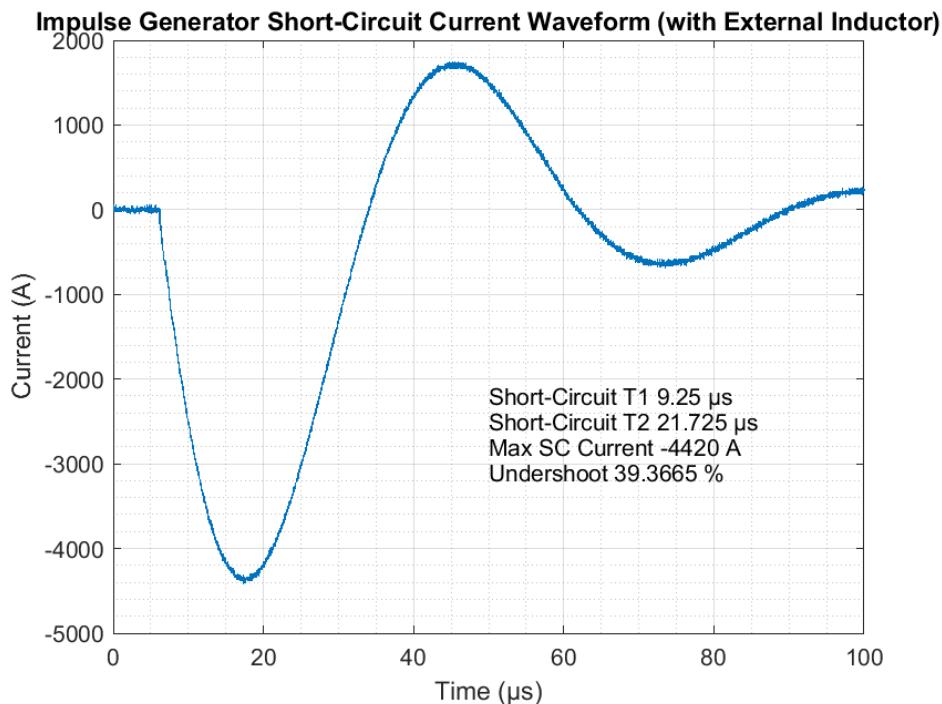


Figure 5.5: The short-circuit current waveform obtained from the HV impulse generator (with external inductor).

A resonance appeared to have occurred within the impulse generator, resulting in an underdamped short-circuit current waveform. The recorded undershoot was 39 %, greater than the 30 % tolerance specified in [39]. The timing parameters τ_1 and τ_2 were more critical than the undershoot of the waveform for the tests to be performed, therefore it was decided to make use of this waveform for all high-voltage induced current testing. The size of the spark gap was not changed during the testing.

5.4 Test Setup

The test setup used involved placing a vertical rod at the output of the impulse generator. The current impulse from the generator would discharge through this rod, creating a time-varying magnetic field. A PV module (or a model of a PV module) would be placed vertically at set distances from the vertically-flowing current impulse, perpendicular to the radiated magnetic field (maximising the loop area cut by the magnetic field, and therefore maximising the induced currents), as shown in Figure 5.6. Currents were measured using a wide band current measuring toroid, connected to a Yokogawa digital storage oscilloscope. The toroid was double-shielded for resilience to EMI, had a low frequency 3dB cut-off at 5 Hz, and a high-frequency 3 dB cut-off at 2 MHz, had an attenuation of 100x, and had a maximum peak current of 50 kA [64].

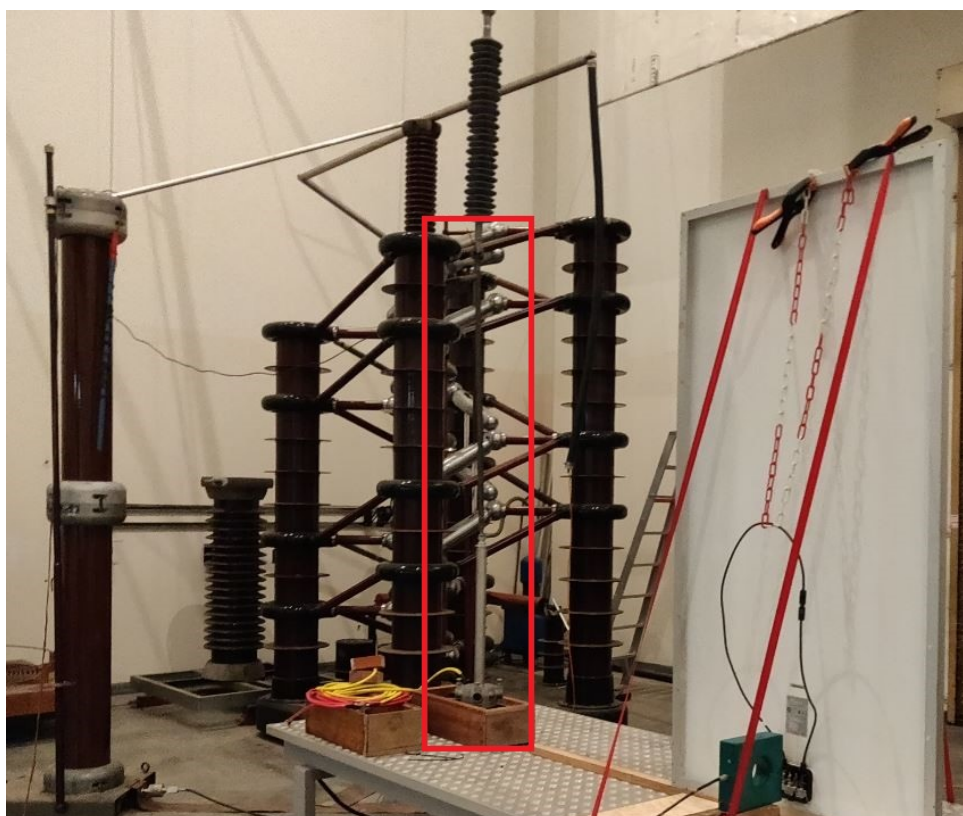


Figure 5.6: The complete high-voltage test setup.

A model of a PV module was constructed using insulated copper wiring (of diameter 2.5 mm) in the layout used in the electromagnetic modelling of a PV module, for the

purpose of comparing the simulation results with real-world results. This model is shown in Figure 5.7.

As with the CAD model, this model took into account that a string of PV cells typically has three conductive tracks, and not just a single track passing through the centre of gravity of each PV cell (as shown in Figure 5.8).

Four crocodile clips (shown in Figure 5.9), mimicked the connections in the junction box of a PV module, allowed for the installation of bypass diodes (either modelled as short-circuits, or actual bypass diodes), or a short-circuited external wiring loop to the model.

The model contained an outer, short-circuited loop (which was not connected to the wiring representing the cells of a PV module), in order to account for the counteracting magnetic fields created by the current flowing in the frame of a PV module.



Figure 5.7: The full-scale model of a PV module.



Figure 5.8: A close-up showing the three traces used to model each row of PV cells in the model of a PV module.



Figure 5.9: The junction box of the model of a PV module.

5.5 Results

Results were recorded with both the model of a PV module and an actual PV module (a BYD 310P6C-36, as shown previously in Figure 2.5), at separation distances of 1 m and 1.6 m, with the bypass diode connections short-circuited and with bypass diodes in place.

5.5.1 PV Module Model Results

5.5.1.1 Short-Circuited Bypass Diodes

The first tests performed were those which made use of the model of a PV module. Short-circuits were placed between the crocodile clips in order to mimic perfectly conducting bypass diodes. This was done in order to obtain the maximum possible induced currents. This configuration was similar to the simulation used in Section 4.5.1. Figure 5.10 shows the induced currents within the model at a separation distance of 1 m, and Figure 5.11 shows the induced currents within the model at a separation distance of 1.6 m.

The peak magnitude of the induced currents shown in Figure 5.10 are all larger than those shown in Figure 5.11. The currents induced in Diode 1 and Diode 2 with a 1 m separation distance are approximately double that of the currents induced in the same positions with a separation distance of 1.6 m - indicating that the induced currents are highly dependent on the separation distance. This is as would be expected, as the strength of the magnetic field resulting from the current impulse attenuates with $1/r$ where r is the distance from the current (as shown in Equation 2.7). A decrease in the peak magnitude of the induced current in Diode 3 did occur with the increase in separation distance, however it was not as drastic as the decrease observed in Diode 1 and Diode 2, likely due to the influence of a circulating current in the loop representing the frame of the PV module.

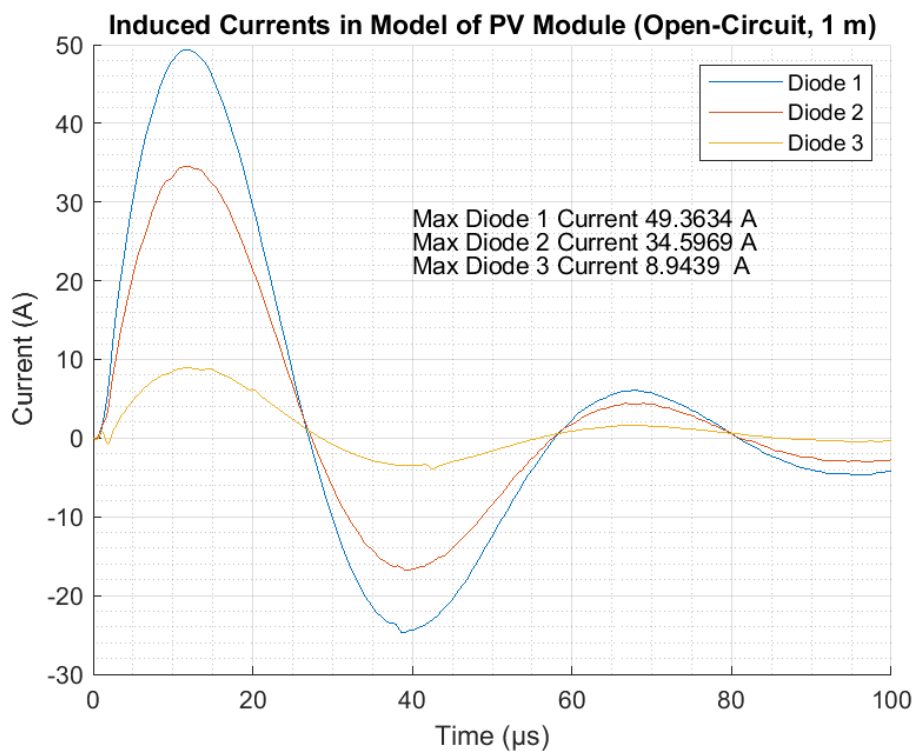


Figure 5.10: Induced currents within the model of a PV module at a separation distance of 1 m.

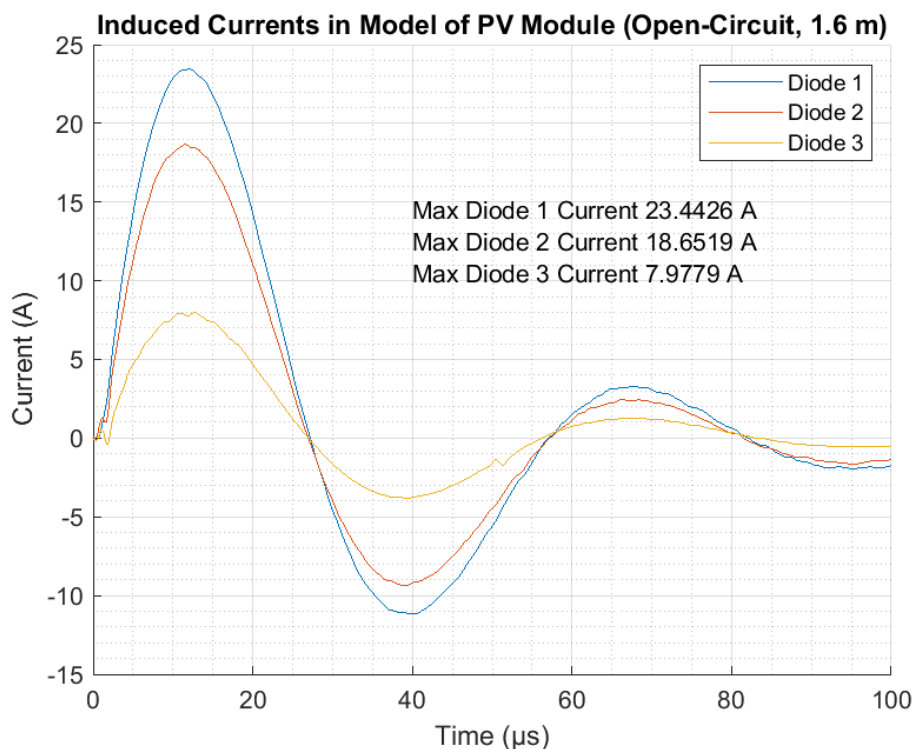


Figure 5.11: Induced currents within the model of a PV module at a separation distance of 1.6 m.

A short-circuit loop was then placed between the output terminals of the model, in order to mimic the simulation setup documented in Section 4.5.2. Figure 5.12 shows the induced currents within the model (with addition of the short-circuit loop) at a separation distance of 1 m, and Figure 5.13 shows the induced currents within the model (with the addition of the short-circuit loop) at a separation distance of 1.6 m.

As expected, the current through all diodes increased with the addition of the short-circuit loop. For the separation distance of 1 m, all diode currents increased by 16-19 A. The current in the short-circuit loop was 27 A, indicating that most of the current induced in the short-circuit loop had passed through the bypass diodes, leaving 8-11 A to flow through the conductive traces in the model. For the separation distance of 1.6 m, all diode currents increased by 12–18 A. The current in the short-circuit loop was 20 A, once again indicating that most of the current induced in the short-circuit loop had passed through the bypass diodes, leaving 2-8 A to pass through the conductive traces in the model.

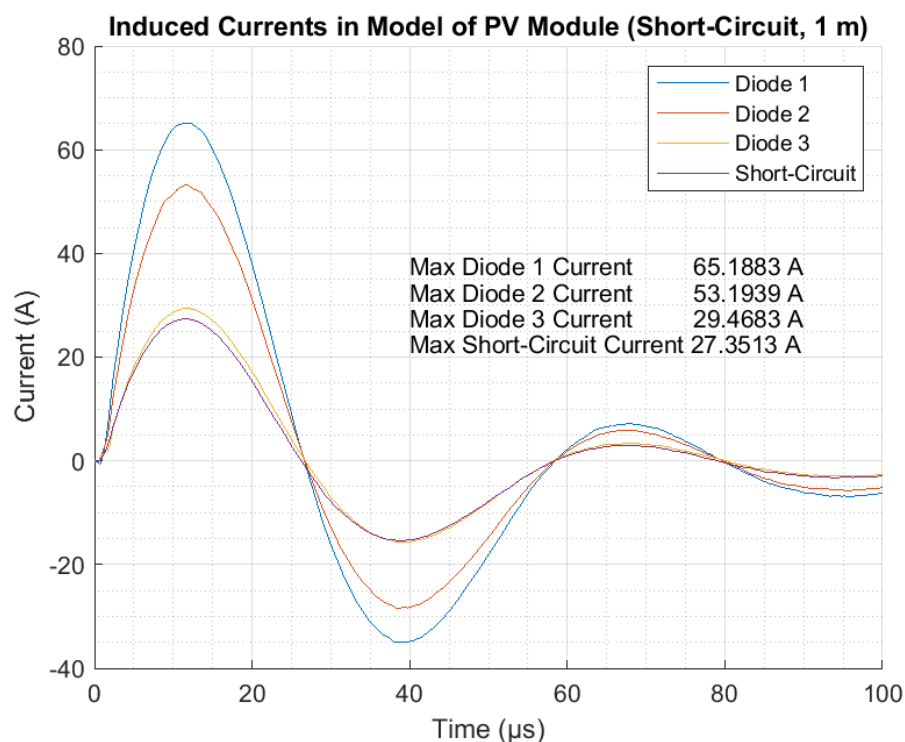


Figure 5.12: Induced currents within the model of a PV module (with an external short-circuit) at a separation distance of 1 m.

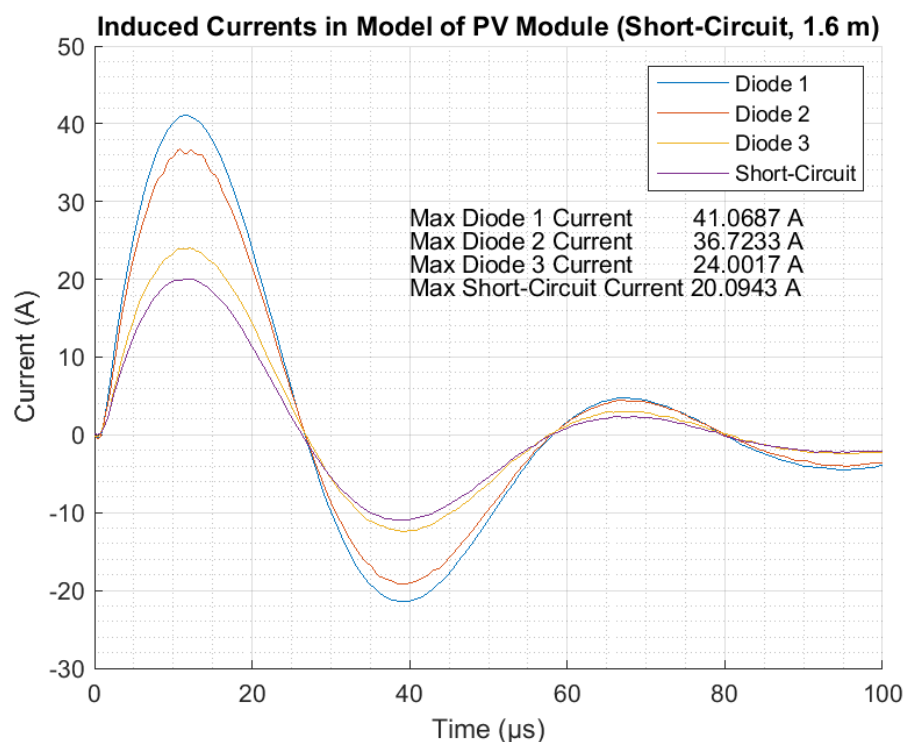


Figure 5.13: Induced currents within the model of a PV module (with an external short-circuit) a separation distance of 1.6 m.

5.5.1.2 Actual Bypass Diodes

The short-circuits between the crocodile clips in the model of a PV module were then replaced with HY 10SQ045 bypass diodes. The experiments from Section 5.5.1.1 were repeated, and the results recorded.

Figure 5.14 and Figure 5.15 show the results gathered for the cases without the short-circuit loop at separation distances of 1 m and 1.6 m, respectively.

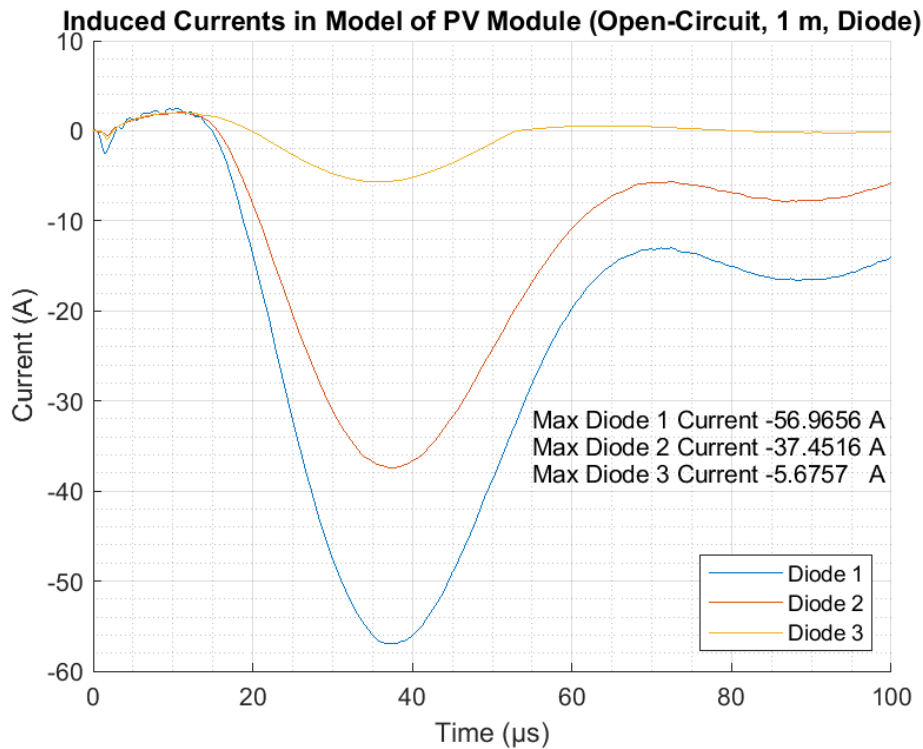


Figure 5.14: Induced currents within the model of a PV module (with bypass diodes) at a separation distance of 1 m.

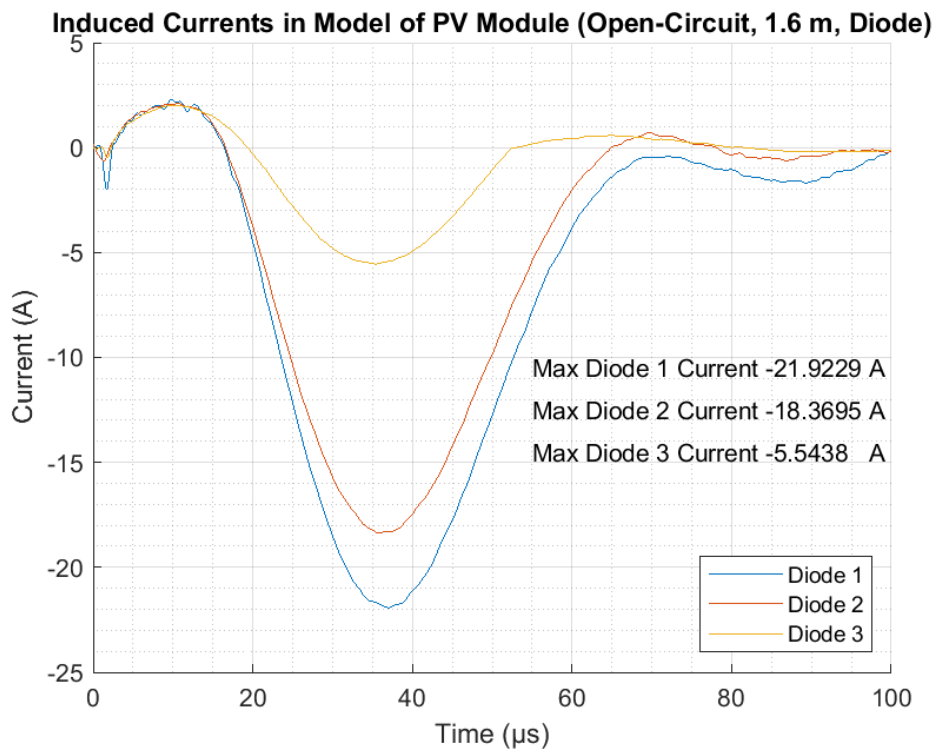


Figure 5.15: Induced currents within the model of a PV module (with bypass diodes) at a separation distance of 1.6 m.

Figure 5.16 and Figure 5.17 show the results gathered for the cases with the short-circuit loop at separation distances of 1 m and 1.6 m, respectively.

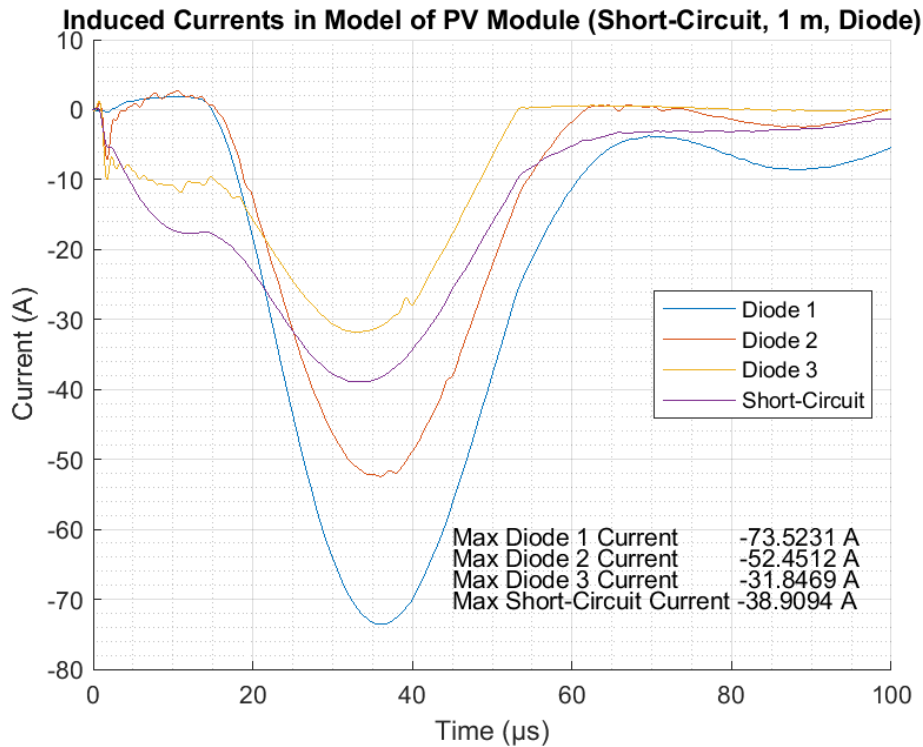


Figure 5.16: Induced currents within the model of a PV module (with bypass diodes and an external short-circuit) at a separation distance of 1 m.

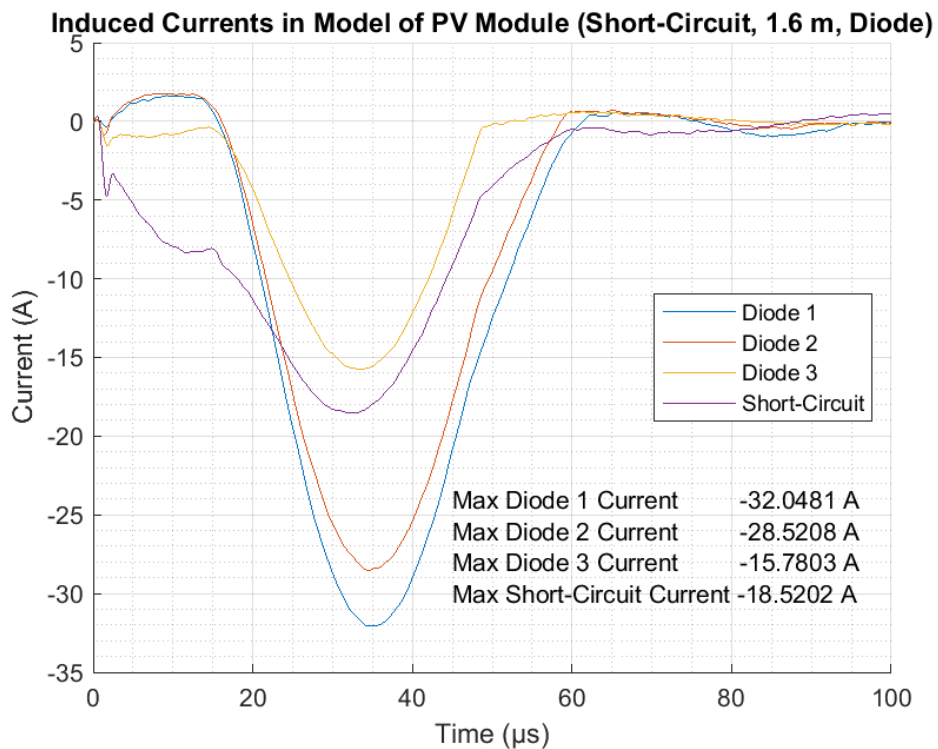


Figure 5.17: Induced currents within the model of a PV module (with bypass diodes and an external short-circuit) a separation distance of 1.6 m.

The diodes were not able to be reverse biased beyond approximately 2 A in any of the tests, at either separation distance, or with the addition of a short-circuit loop. Forward biasing of the diodes occurred during the undershoot of the lightning waveform.

The addition of a short-circuit loop increased the induced currents by 15-25 A at a separation distance of 1 m, and by 10-11 A at a separation distance of 1.6 m.

5.5.2 PV Module Results

5.5.2.1 Short-Circuited Bypass Diodes

A BYD 310P6C-36 PV module (an additive module, as described in Section 2.5.3) was positioned in the same manner as the model of a PV module. The bypass diodes of the PV module were replaced with short-circuits, and the tests from Section 5.5.1.1 were repeated.

Figure 5.18 and Figure 5.19 show the results recorded for separation distances of 1 m and 1.6 m, respectively. The waveforms of the induced currents through the three bypass diodes were similar to each other in each case, with the peak magnitudes of the induced currents being slightly higher (approximately 2.5 A) for the case with a separation distance of 1 m, than the peak magnitudes of the induced currents for the case with a separation distance of 1.6 m (approximately 2.25 A). Most importantly, what these waveforms showed was that it was possible to induce either a negative or positive polarity current within a polycrystalline PV module.

When comparing the waveforms of the induced currents recorded in the actual PV module (shown in Figure 5.18 and Figure 5.19) with the waveforms of the induced currents recorded in the model of a PV module (shown in Figure 5.10 and Figure 5.11), the first difference observed was that of magnitude. The magnitudes of the induced currents in the PV module were between 4 and 20 times lower than the magnitudes of the induced currents in the model of a PV module at a separation distance of 1 m. At a separation distance of 1.6 m, this margin lowered to between 3 and 10 times. This result indicates the presence of a series impedance within the internal loops of the module (as a result of the PV cells), challenging the short-circuit assumption made in the electromagnetic modelling process. As the purpose of the electromagnetic model was to simulate a worst-case scenario, it was intended that the actual induced currents would be lower.

Figure 5.20 and Figure 5.21 show the results recorded for the case with the short-circuit loop at separation distances of 1 m and 1.6 m, respectively. It can be seen that the addition of the short-circuit loop greatly increases the magnitude of the induced currents in both cases.

With a separation distance of 1 m, the currents through the bypass diodes increased from a peak current magnitude of around 2.5 A through each bypass diode to a peak current magnitude of around 19 A. The current through the short-circuit loop had a peak current magnitude of 22 A, leaving 3 A to flow through the cells of the PV module.

With a separation distance of 1.6 m, the currents through the bypass diodes increased from a peak current magnitude of around 2.25 A through each bypass diode to a peak

current magnitude of around 11 A. The current through the short-circuit loop had a peak current magnitude of 13 A, leaving 2 A to flow through the cells of the PV module.

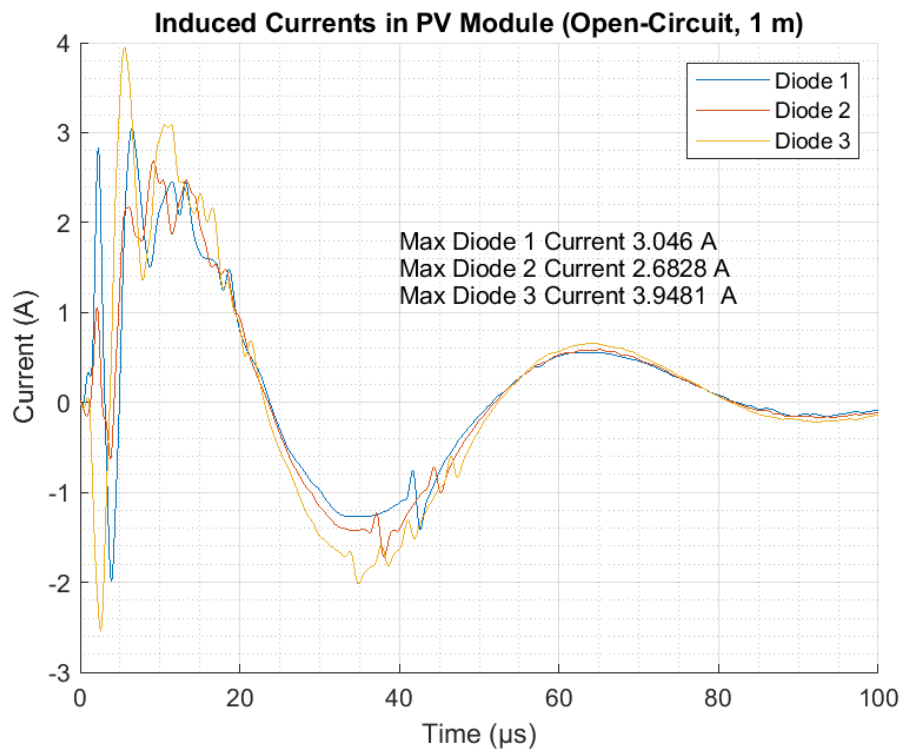


Figure 5.18: Induced currents within the PV module at a separation distance of 1 m.

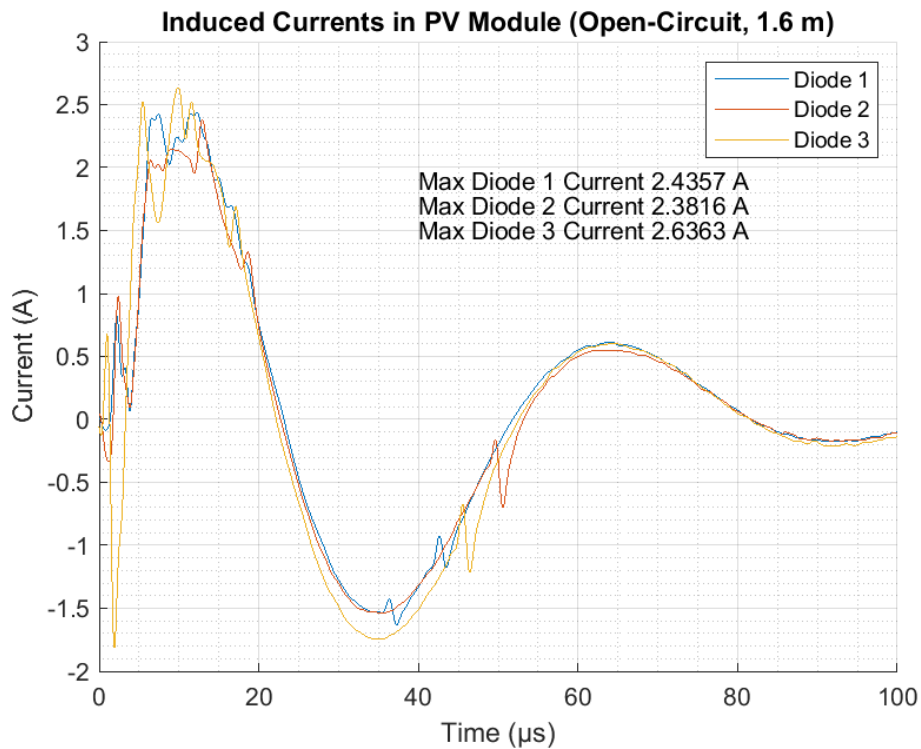


Figure 5.19: Induced currents within the PV module at a separation distance of 1.6 m.

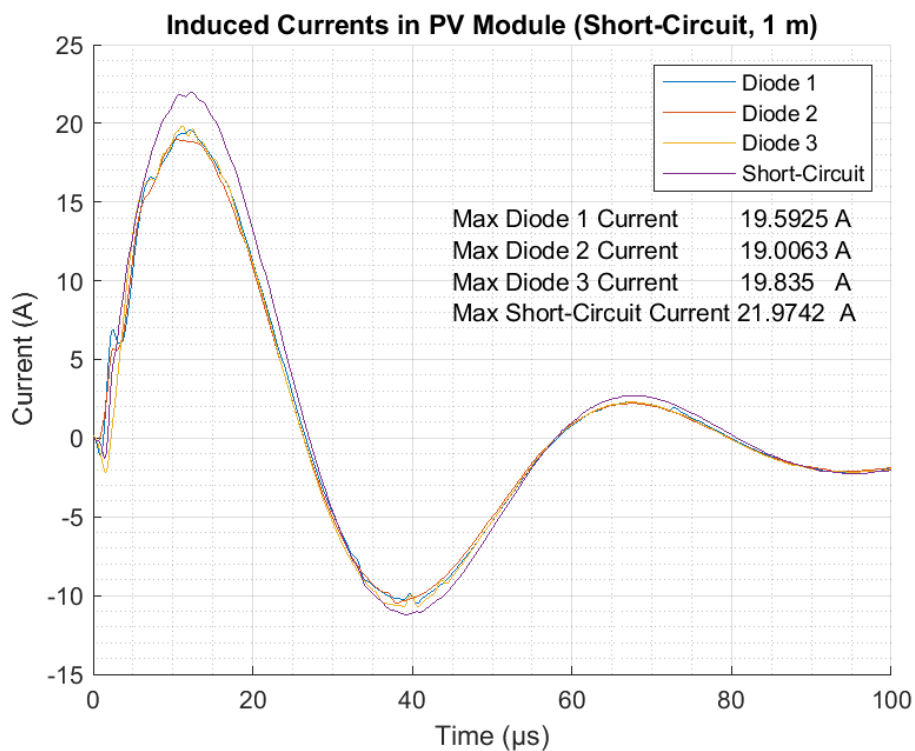


Figure 5.20: Induced currents within the PV module (with an external short-circuit) at a separation distance of 1 m.

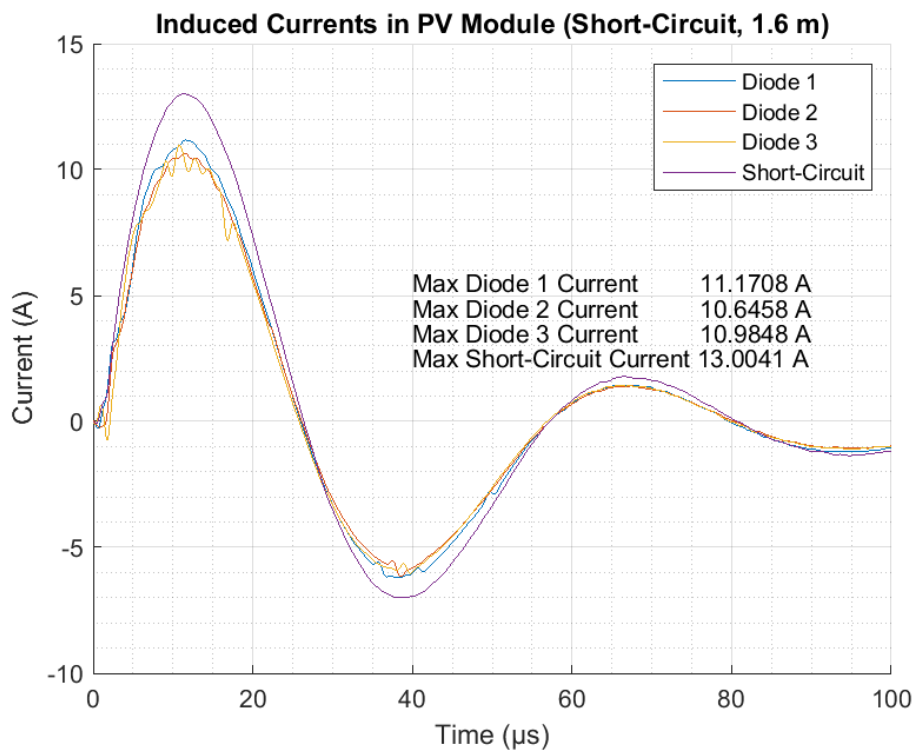


Figure 5.21: Induced currents within the PV module (with an external short-circuit) a separation distance of 1.6 m.

5.5.3 Actual Bypass Diodes

The short-circuits within the junction box of the PV module were then replaced with HY 10SQ045 bypass diodes. The experiments from Section 5.5.1.2 were repeated, and the results recorded.

Figure 5.22 and Figure 5.23 show the results gathered for the cases without the short-circuit loop at separation distances of 1 m and 1.6 m, respectively. Slightly lower induced currents were recorded in the actual bypass diodes of the module when compared with the module with the short-circuited bypass diodes shown in Figure 5.18. At a separation distance of 1.6 m, the induced currents in the actual bypass diodes were similar to those recorded in the module with the short-circuited bypass diodes shown in Figure 5.19.

Figure 5.24 and Figure 5.25 show the results gathered for the cases with the short-circuit loop at separation distances of 1 m and 1.6 m, respectively. As in previous cases, the induced reverse current through each bypass peaked at approximately 2 A.

At a separation distance of 1 m, the addition of the short-circuit loop drastically increased the magnitude of the forward bias currents through the bypass diodes from a peak magnitude of approximately 1.5 A (as shown in Figure 5.22) to an average of 11.5 A (as shown in Figure 5.24). The peak magnitude of the induced current through the short-circuit loop at this point was in the region of 16 A for this separation distance.

At a separation distance of 1.6 m, the addition of the short-circuit loop again increased the magnitude of the forward bias currents through the bypass diodes from a peak magnitude of approximately 1.5 A (as shown in Figure 5.23) to an average of 3.5 A (as shown in Figure 5.25). The peak magnitude of the induced current through the short-circuit loop at this point was in the region of 5.2 A for this separation distance.

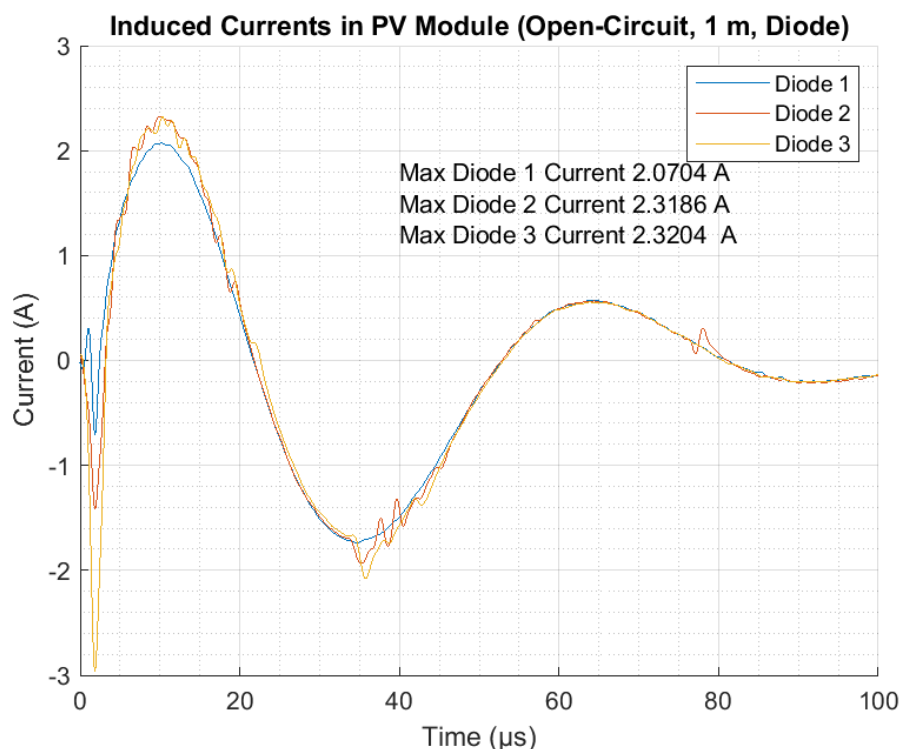


Figure 5.22: Induced currents within the PV module (with bypass diodes) at a separation distance of 1 m.

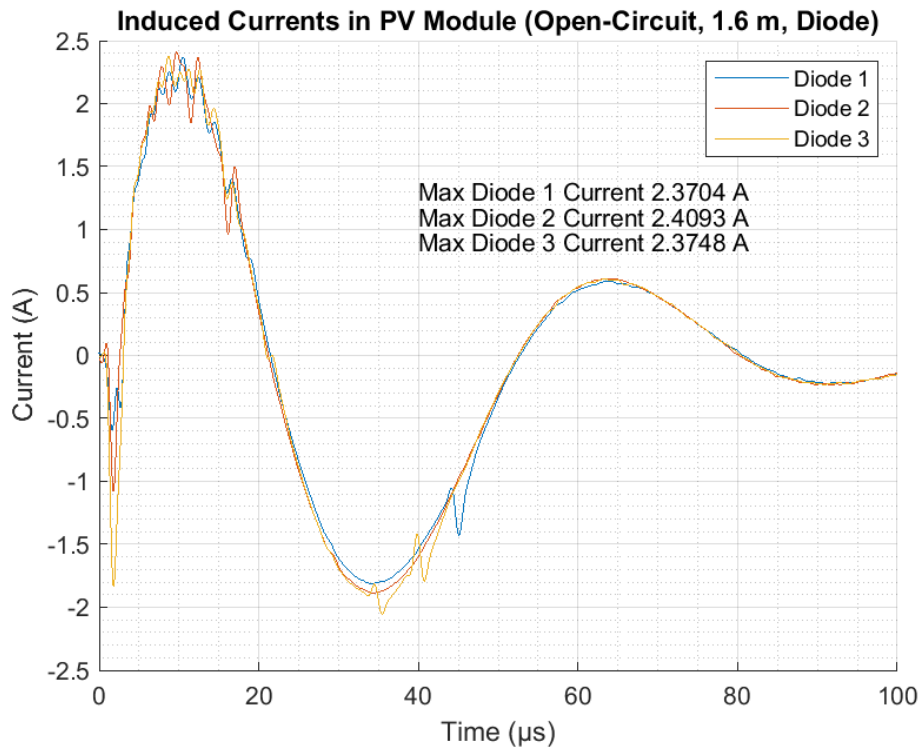


Figure 5.23: Induced currents within the PV module (with bypass diodes) at a separation distance of 1.6 m.

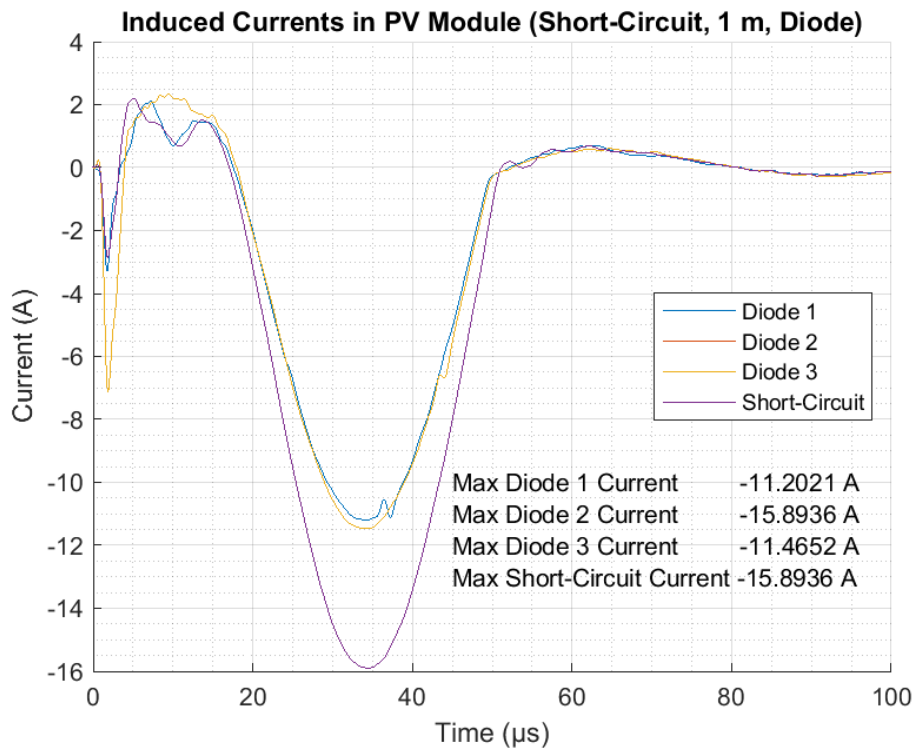


Figure 5.24: Induced currents within the PV module (with bypass diodes and an external short-circuit) at a separation distance of 1 m.

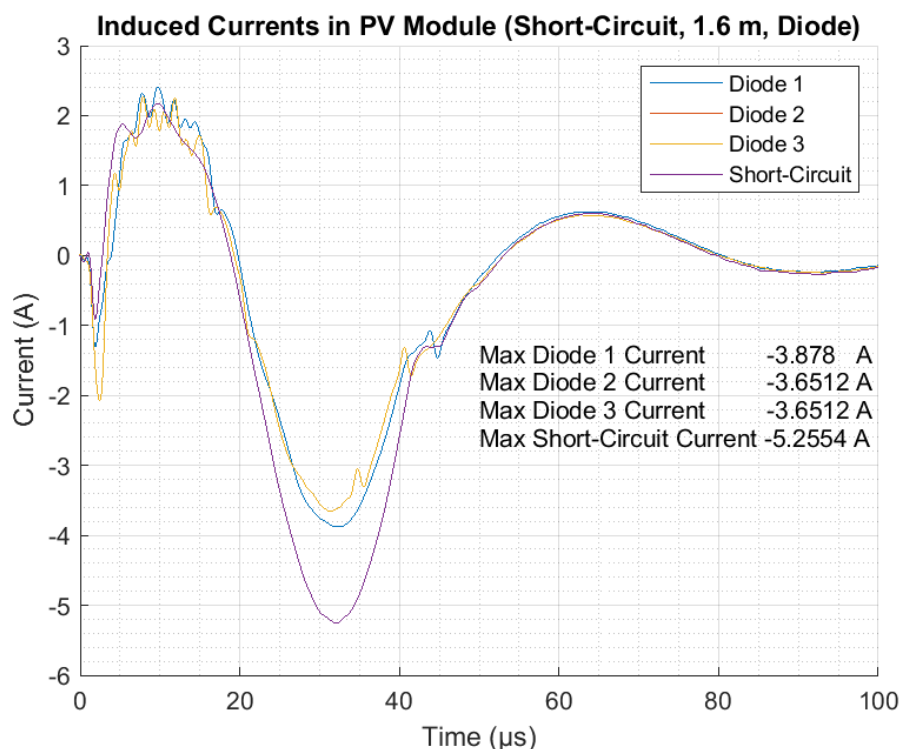


Figure 5.25: Induced currents within the PV module (with bypass diodes and an external short-circuit) a separation distance of 1.6 m.

5.5.3.1 Comparison with EM Simulations

The open-circuit EM simulation (with short-circuited bypass diodes) from Chapter 4 was adjusted for a negative $-4.4 \text{ kA } 8/20 \mu\text{s}$, at separation distances of 1 m and 1.6 m along the negative X-axis, the results of which are shown in Figure 5.26 and Figure 5.27, respectively, for the open-circuit case. Although results of similar peak magnitudes were computed when compared with the actual results of the open-circuited case, no reversal of the currents through Diode 3 was recorded. This indicated that the geometry of the frame itself, and not just the presence of the outer short-circuited loop which it created, had an influence on the induced currents.

The frame was replaced with a short-circuited loop (as shown in Figure 5.28, which would better represent the model of a PV module used in the high-voltage test setup. The results were recomputed for separation distances of 1 m and 1.6 m, as shown in Figure 5.29 and Figure 5.30, respectively. The polarities of the induced currents were now all positive (agreeing with the actual measured results), and of larger peak magnitudes, further validating the hypothesis that the geometry of the frame itself, and not just the presence of an outer short-circuited loop, had a noticeable impact on the magnitudes of the currents induced within the model. As in the case of Figure 5.10 and Figure 5.11, the currents were largest in the loop connected to Diode 1, and lowest in the loop connected to Diode 3. The currents through the diodes decreased and became more similar in magnitude with increasing separation distance. The peak current magnitudes observed in the simulation with the separation distance of 1 m were approximately double that of the peak current magnitudes observed in the actual case with a separation distance of 1 m (the same was true for the respective cases with a separation distance of 1.6 m). When comparing the simulated cases, it was found that the peak current magnitudes in the

case with a separation distance of 1 m was approximately double that of those computed for the separation distance of 1.6 m, which was analogous to the actual measurements recorded.

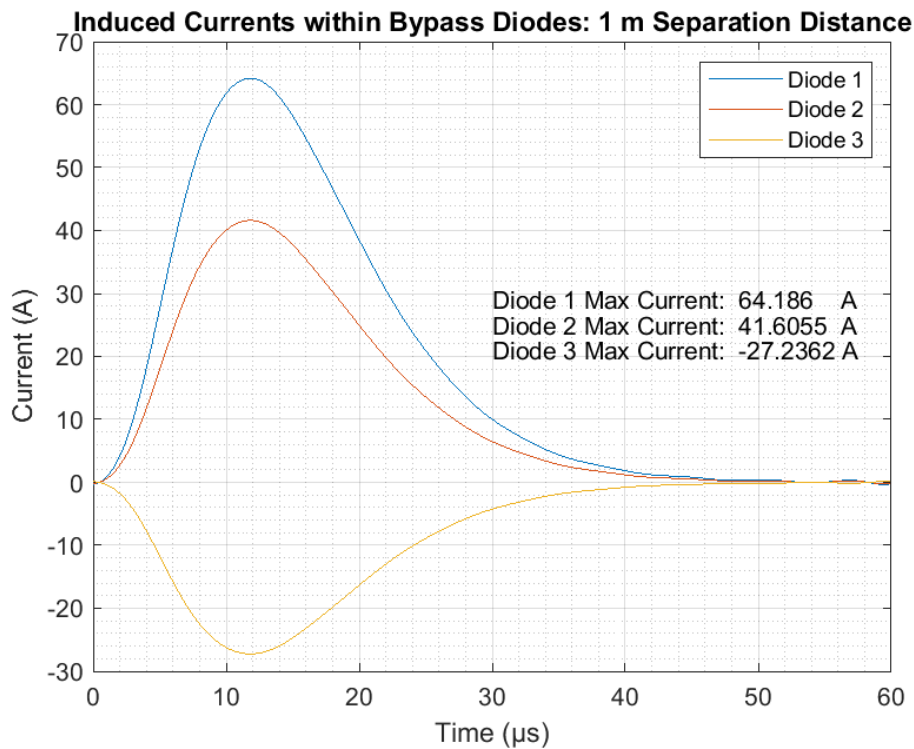


Figure 5.26: The simulated induced currents at a separation distance of 1 m with an $-4.4 \text{ kA } 8/20 \mu\text{s}$ current impulse.

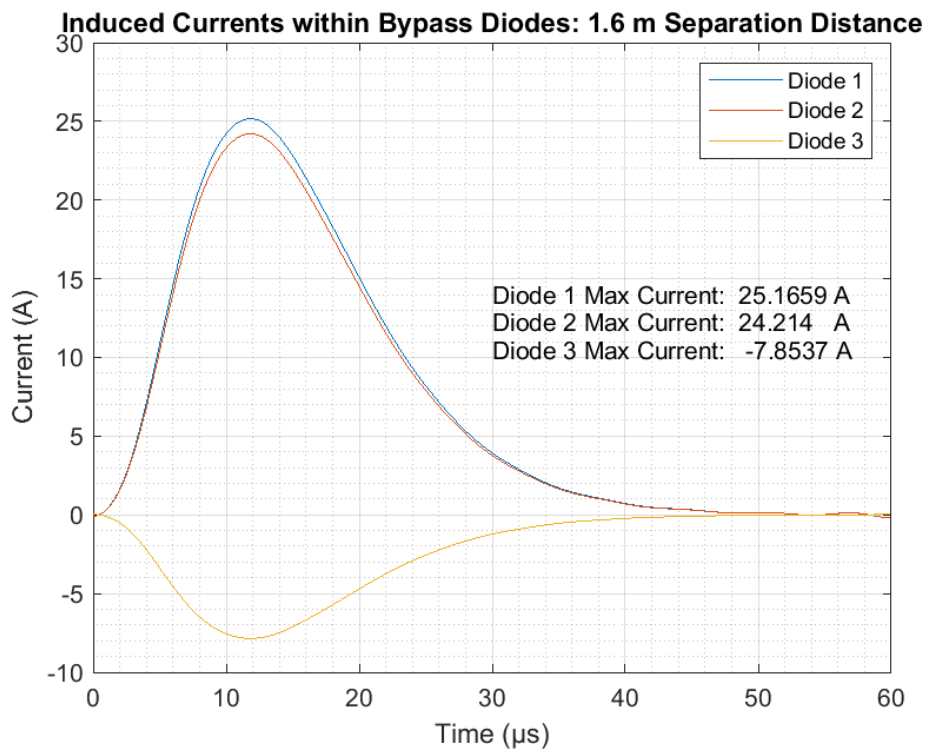


Figure 5.27: The simulated induced currents at a separation distance of 1 m with an $-4.4 \text{ kA } 8/20 \mu\text{s}$ current impulse.

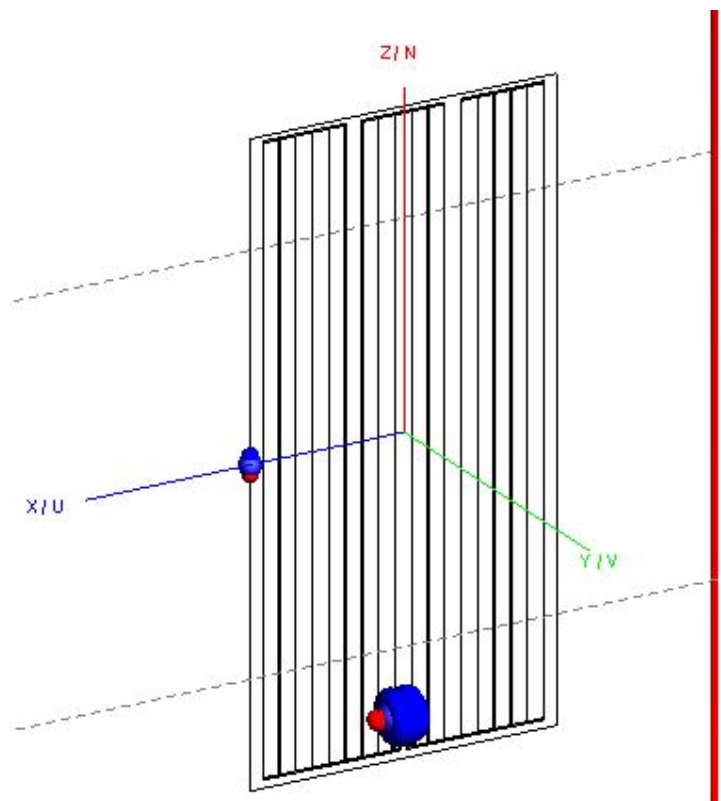


Figure 5.28: The adjusted simulation setup, with a thin-wire approximation of the frame of a PV module.

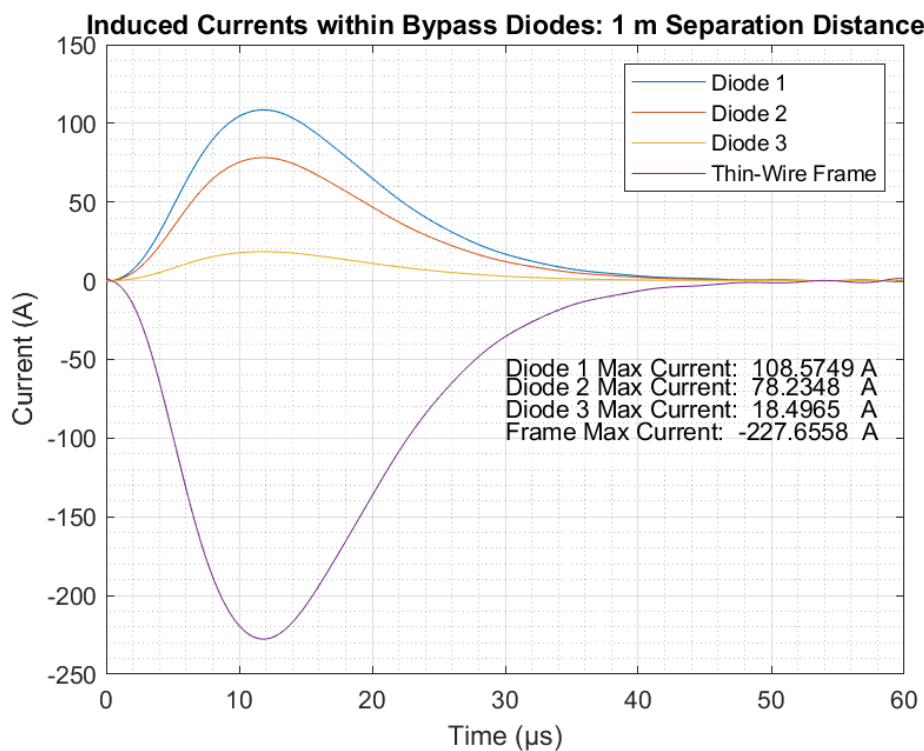


Figure 5.29: The simulated induced currents at a separation distance of 1.6 m with an -4.4 kA $8/20$ μ s current impulse (with thin-wire frame).

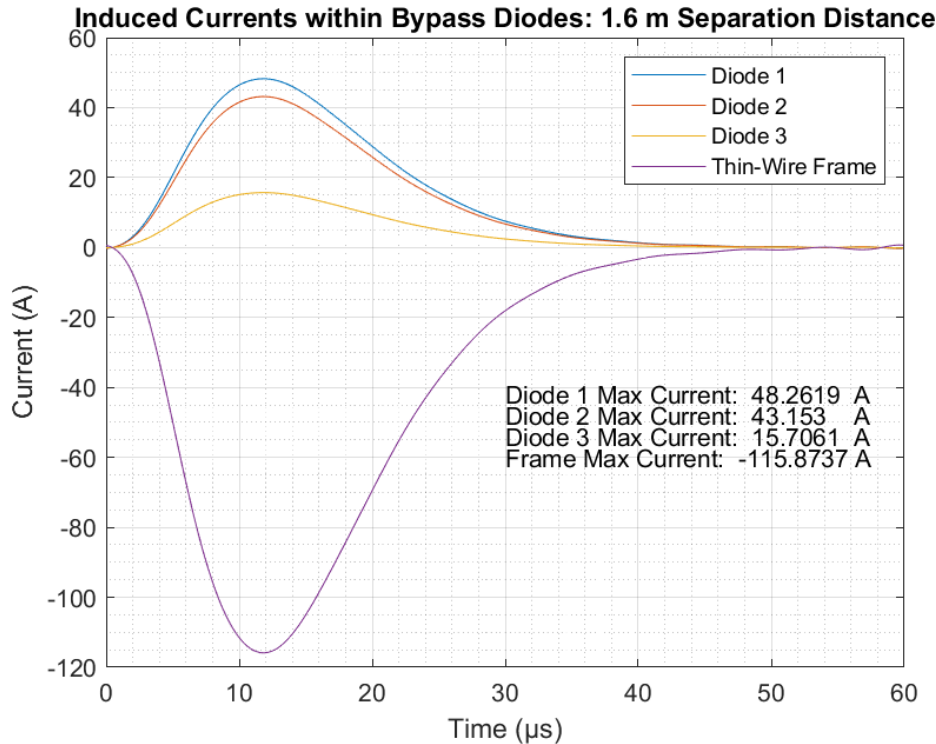


Figure 5.30: The simulated induced currents at a separation distance of 1.6 m with an -4.4 kA $8/20$ μ s current impulse (with thin-wire frame).

A short-circuit loop was then added between the output terminals of the model of a PV module and the results were recomputed. These results are shown in Figure 5.31 and Figure 5.32, for separation distances of 1 m and 1.6 m, respectively.

Comparing the results for a separation distance of 1 m, the case with the additional short-circuit loop (Figure 5.31) experienced an average increase of 63 A in the peak magnitudes of the currents through the bypass diodes when compared to the case without the short-circuit loop connected between the output terminals of the model of a PV module (Figure 5.29). The peak magnitudes of the currents through Diode 1 and Diode 2 increased by approximately 65 %, whilst the peak magnitude of the current through Diode 3 increased by approximately 170 %.

Comparing the results for a separation distance of 1.6 m, the case with the additional short-circuit loop (Figure 5.32) experienced an average increase of 35 A in the peak magnitudes of the currents through the bypass diodes when compared to the case without the short-circuit loop connected between the output terminals of the model of a PV module (Figure 5.30). The peak magnitudes of the currents through Diode 1 and Diode 2 increased by approximately 73 %, whilst the peak magnitude of the current through Diode 3 increased by approximately 250 %.

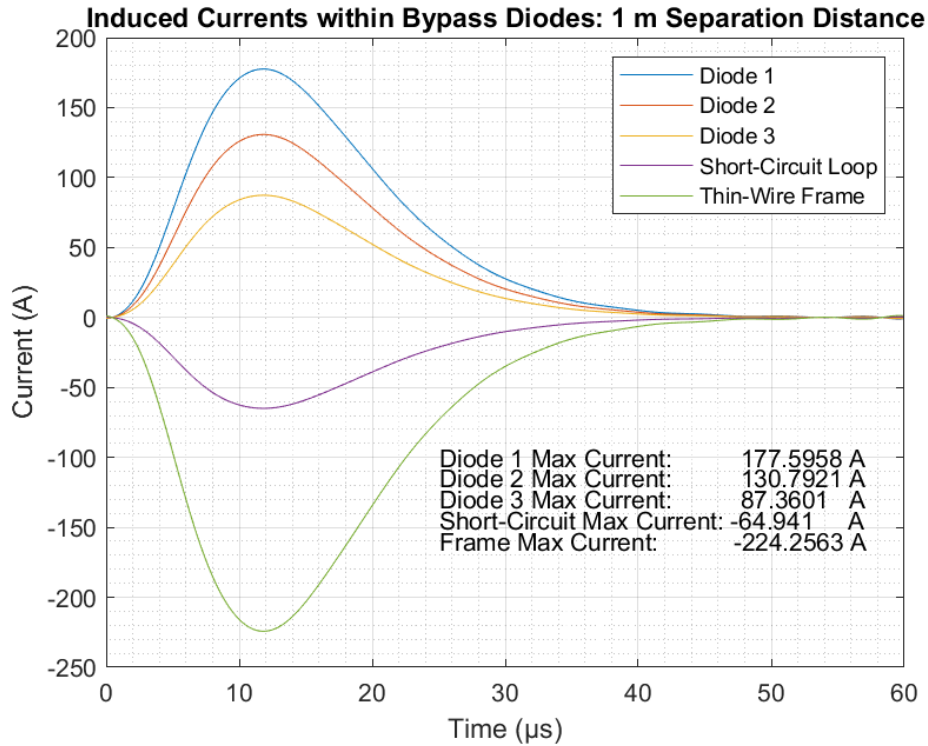


Figure 5.31: The simulated induced currents at a separation distance of 1.6 m with an $-4.4\text{ kA } 8/20\ \mu\text{s}$ current impulse (with thin-wire frame and short-circuit loop).

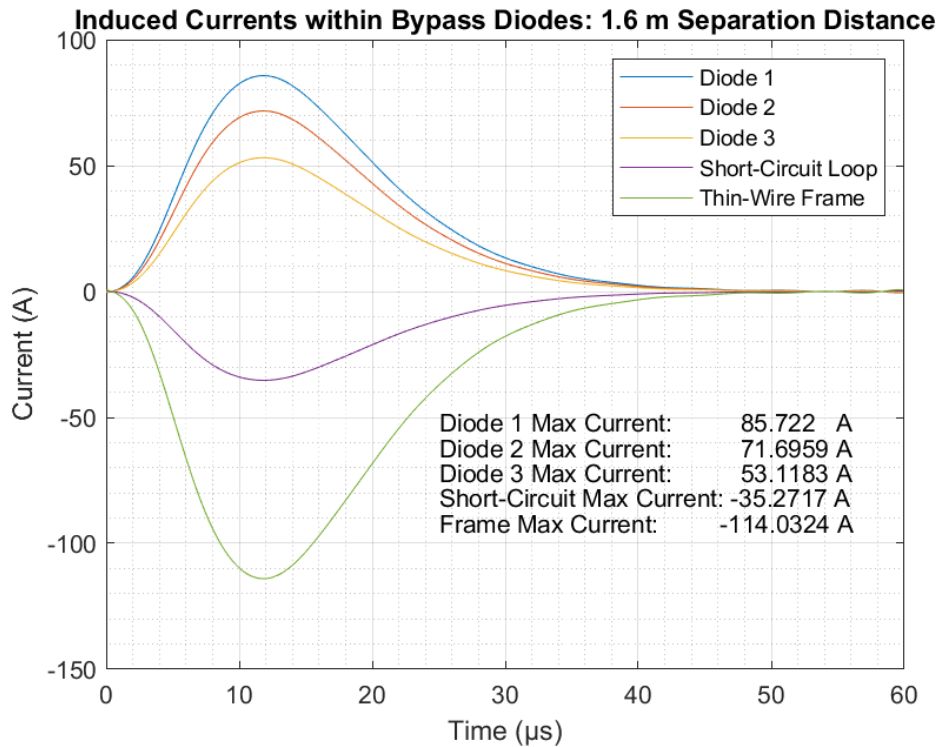


Figure 5.32: The simulated induced currents at a separation distance of 1.6 m with an $-4.4\text{ kA } 8/20\ \mu\text{s}$ current impulse (with thin-wire frame and short-circuit loop).

A comparison of the peak current magnitudes computed in simulation, and the peak current magnitudes recorded in the HV testing performed (for both the model of a PV module, and the actual PV module) are shown in Table 5.1 (for the cases with short-circuited bypass diodes).

Comparing the results for the case without the short-circuit loop between the output terminals, it can be seen that the currents induced within the model of a PV module were 51.4-54.7% lower than the results from simulation. The discrepancy between the peak simulated and measured magnitudes can be attributed to non-idealities in the model of a PV module, as the simulation had assumed that all materials were constructed of perfect electrical conductors, therefore negating the effects of the impedances in the model of a PV module. For the simulation, the peak current magnitude decreased by 55.8% when the separation distance was increased from 1 m to 1.6 m. For this same increase in separation distance, the peak current magnitude in the model of a PV module decreased by 52.6% - a similar amount, suggesting the presence of a linear scaling between the simulated results and the recorded results from the model of a PV module.

The magnitudes of the currents induced within the actual PV module were far lower than those induced in either the simulation or the model of a PV module (for the case without the short-circuit loop between the output terminals). The decrease in induced currents in the PV module was 13%. Proportionally, this was a much lower decrease than that observed in either the simulation or the model of a PV module. This was expected, as the cells within a PV module are non-linear components.

For the cases which included the short-circuit loop between the output terminals, the currents induced within the model of a PV module were 52.0-63.4% lower than the results from simulation, which can again be attributed to the non-idealities in the model of a PV module mentioned earlier. Of particular interest was that, with the addition of the short-circuit loop between the output terminals, the currents induced within the model of a PV module and the actual PV module increased by similar amounts (15.8 A and 16.8 A, respectively) at a separation distance of 1 m. Increasing the separation distance to 1.6 m saw an increase of 8.64 A in the induced currents within the actual PV module with the addition of the short-circuit loop between the output terminals - a reduction of 48.6% when compared to the current increase at a separation distance of 1 m. Theoretically, the magnetic flux should have reduced by 37.5%, however a slight decrease in the area of the short-circuited loop may have occurred during the increasing of the separation distance in the test setup, resulting in a larger than estimated reduction.

Table 5.1: A comparison of the peak current magnitudes from simulation, with the model of a PV module, and an actual PV module (with short-circuited bypass diodes).

Separation Distance [m]	Simulation [A]	Model of PV Module [A]	PV Module [A]	Short-Circuit Loop Between Output Terminals
1 m	109	49.4	3.05	No
1 m	178	65.2	19.8	Yes
1.6 m	48.2	23.4	2.64	No
1.6 m	85.7	41.1	11.2	Yes

The following section presents practical methods for reducing PV plant susceptibility to EMI, based on the results gathered in this section.

5.6 Wiring Guidelines for Decreased EMI Susceptibility

Traditionally, a PV module in a series-connected string would be electrically connected to the adjacent modules (known as the "daisy-chain" method). A long wire would be added to the furthest module in the string in order to return the final connection at this module to the combiner box (as shown in Figure 5.34). As each module would be supplied with a standard length of wire (approximately 1 m, attached to both the positive and negative terminals [2]), and the distance between adjacent junction boxes would be shorter than this length, excess wiring between PV modules would often be present. This excess wiring is usually coiled and fastened together, as shown in Figure 5.33. In terms of EMI susceptibility prevention, this is seen as bad practice as the coils form loops for which magnetic flux can pass through, resulting in induced currents and voltages within the installation.

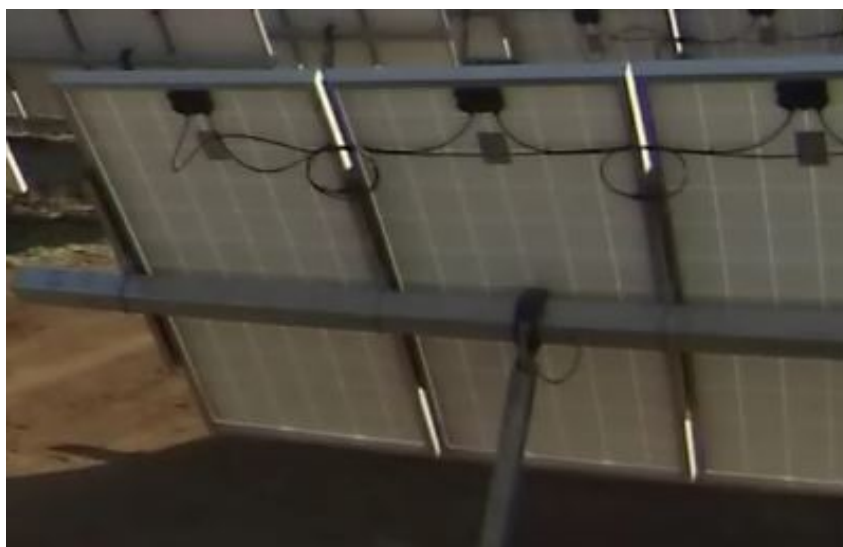


Figure 5.33: Looping of excess inter-module wiring at a solar plant.

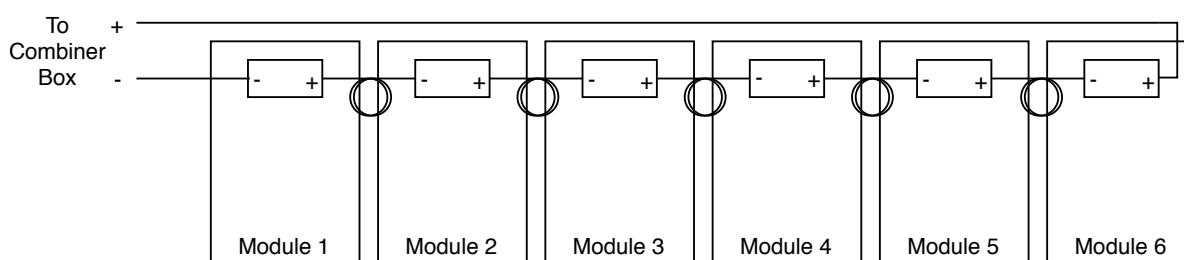


Figure 5.34: A string of 6 series-connected PV modules with looping of excess inter-module wiring.

An alternative to coiling the inter-module wiring would be to fasten it in a figure-of-eight pattern, as shown in Figure 5.35. Forming a figure-of-eight results in the induction of EMFs of opposing polarity in the left and right-hand lobes of the figure-of-eight. This results in the net cancellation of the induced EMFs (so long as the figure-of-eight has an equal number of lobe loops on each side).

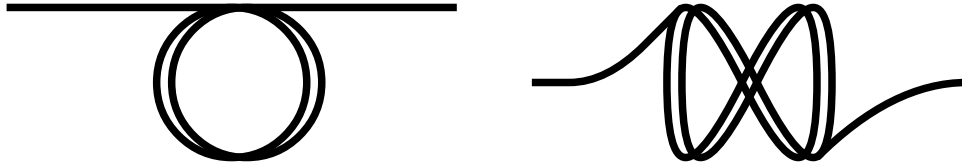


Figure 5.35: Methods of neatening excess wiring: A loop (left) versus a figure-of-eight (right).

A double-stacked installation (such as in Figure 1.2) may have a wiring layout as shown in Figure 5.36. In addition to the loops resulting from the excess inter-module wiring, a larger loop is formed by the overall layout of the wiring. Due to the area of this larger loop, this installation may be particularly susceptible to induced currents and voltages. One benefit of the double-stacked installation is the lack of the need for a long return wire as in the case of Figure 5.34, resulting in cost savings.

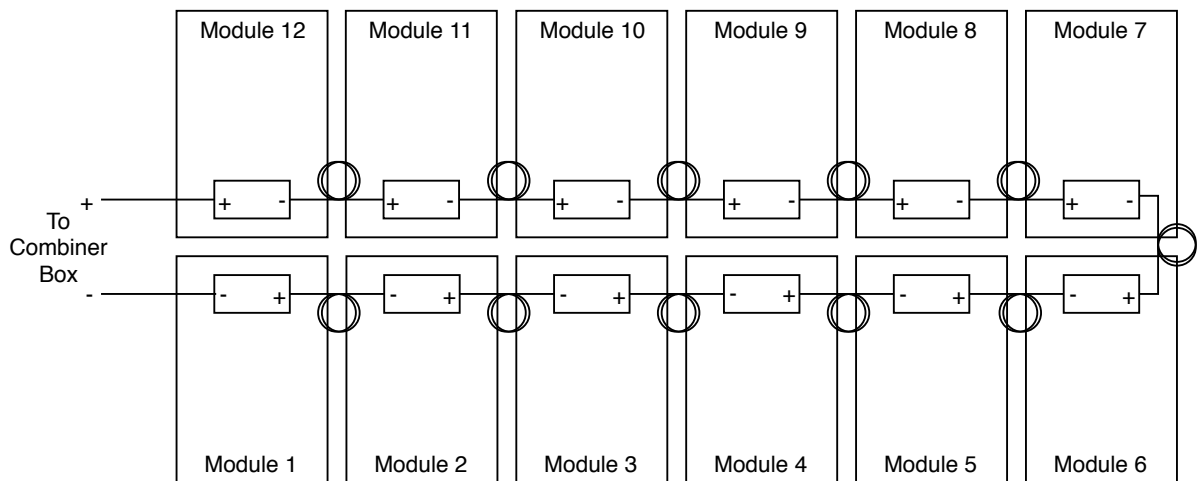


Figure 5.36: A string of 12 PV modules with looping of excess inter-module wiring.

Excess wiring, instead of being coiled, could be used to lessen the area of this loop (as shown in Figure 5.37)

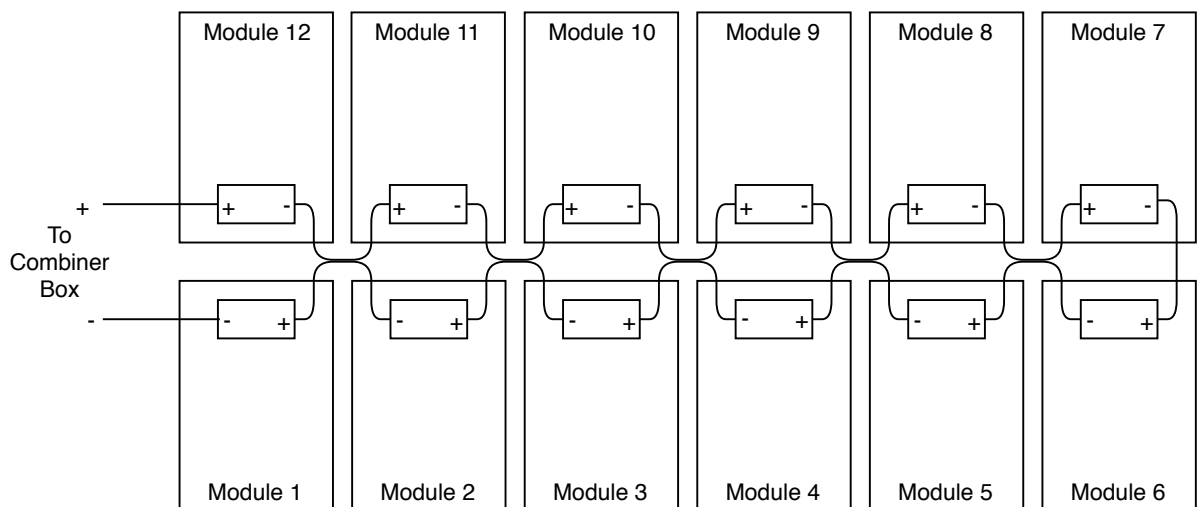


Figure 5.37: A string of 12 PV modules without looping of excess inter-module wiring.

A more recent practice adopted by PV system installers is the cost-saving (or "leapfrog") wire routing method. Using this method, a module is not connected to the modules immediately adjacent to it (as in the daisy-chain method), but rather connected to the module adjacent to the immediately adjacent modules (as shown in Figure 5.38). This configuration negates the need for the long return wire from the furthest module in the string to the combiner box (shown in Figure 5.34). These connections are accomplished without the need for any additional wires, as they make use of only the wiring supplied with the PV module from the factory, resulting in cost savings. It is suggested in [65] that the cost of a 5 MW installation which makes use of 72-cell PV modules can be reduced by as much as \$20k (USD). Since a 72-cell PV module is approximately 1 m wide, and the length of wire supplied by the manufacturer is usually 1 m, the 2 m distance between the junction boxes of series-connected modules is often spanned sufficiently without any excess wiring (which may otherwise have been coiled), therefore making the cost-saving wire routing method a good option from an EMI susceptibility perspective. The wires should be fastened together in order to minimise the formation of any loop area between the positive and negative wiring - they are spread apart in the Figure below to illustrate the wiring concept.

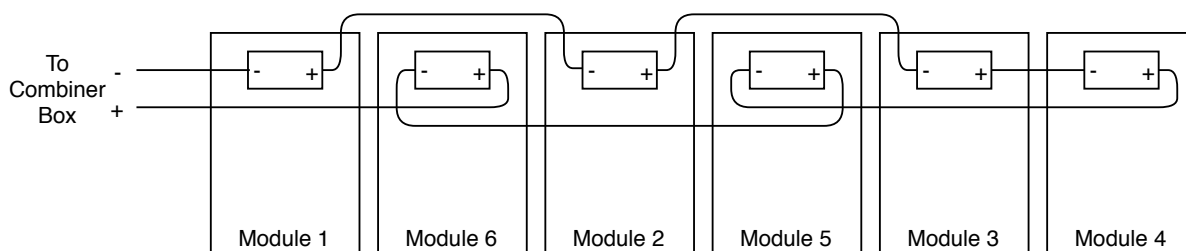


Figure 5.38: A string of 6 series-connected PV modules with the "leapfrog" wiring method.

The cost-saving wire routing method could also be applied in a double-stacked installation, as shown in Figure 5.39. The upper and lower rows of modules could be independently wired using this method, and then joined together at the end nearest the combiner box (see Module 6 and Module 7). If the inter-module wiring is fastened together properly, this method will result in no excess wiring (which could potentially be coiled by an installer), and no formation of a larger outer loop (as shown in Figure 5.36).

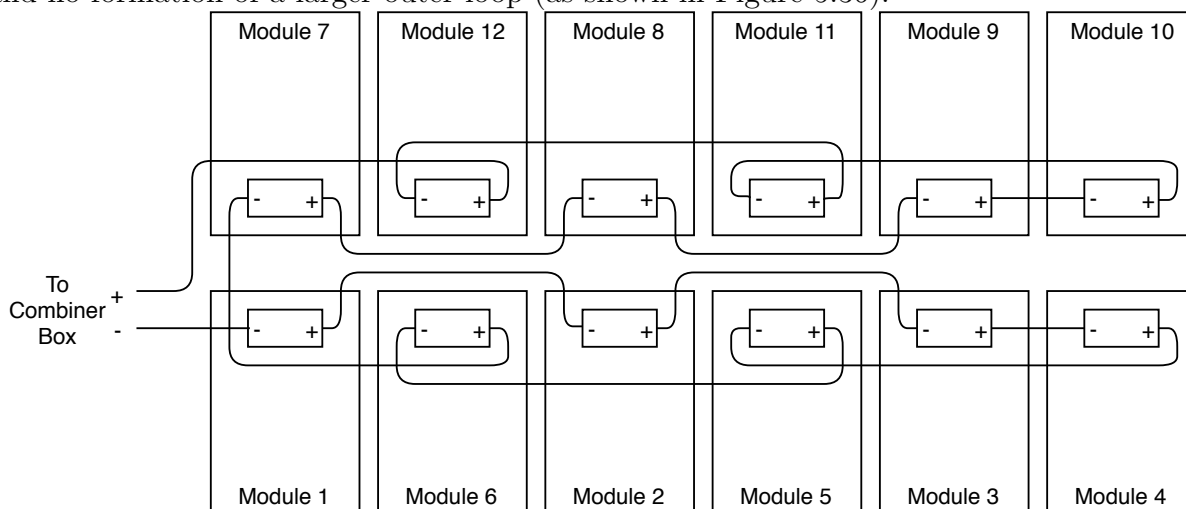


Figure 5.39: A string of 12 series-connected PV modules with the 'leapfrog' wiring method.

Furthermore, when external lightning protection systems are installed, down-conductors should be installed in such a way as to minimise the amount of magnetic flux (radiated during the conduction of a lightning current) which passes through any loop areas in a PV installation.

5.7 Challenges Encountered with High-Voltage Testing

The first challenge encountered was the generation of the necessary waveform. Obtaining timing parameters τ_1 and τ_2 within the tolerances set out in [39] required much trial and error, with many simulation adjustments. The second challenge was the production of undesirable EMI by the generator during the execution of the current impulse. Broad-band EMI noise would be produced, as well as a resonance at approximately 1 MHz. As the influence of this noise was beyond the scope of the lightning waveforms under consideration, it was determined that this noise should be filtered out in order to examine the effects of the desired waveforms. This resulted in the use of the MATLAB digital low-pass filter (LPF) with a cut-off frequency of 600 kHz, a steepness of 0.99, and a stop-band attenuation of 120 dB for the waveforms presented in this chapter. This filtering sufficiently attenuated the noise, whilst keeping the desired signal intact, as shown in Figure 5.40.

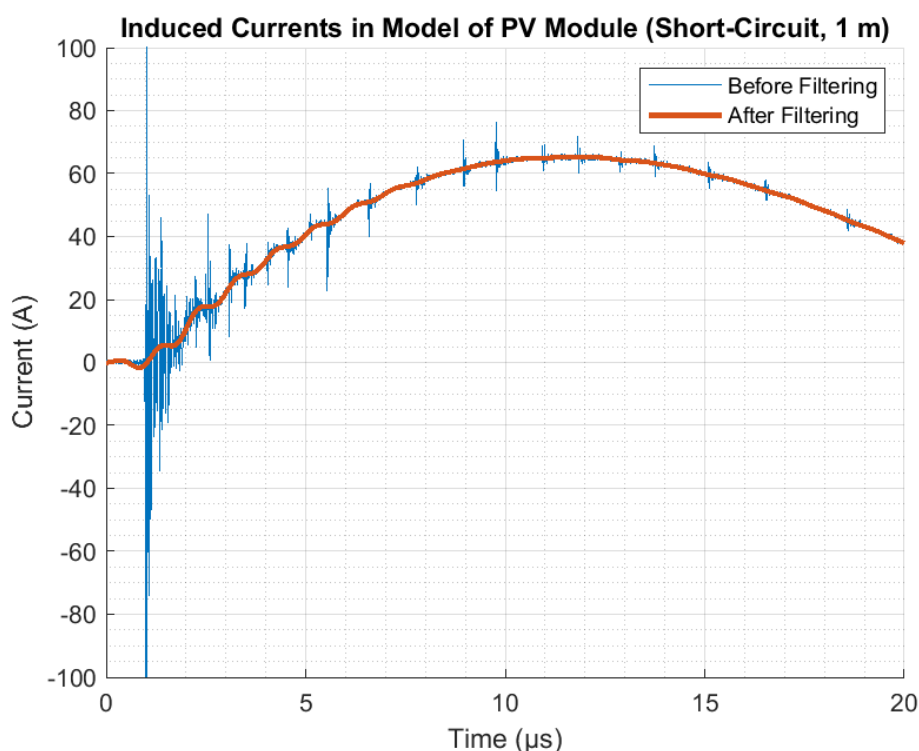


Figure 5.40: A recorded current waveform, before and after low-pass filtering.

5.8 Chapter Conclusion

This chapter compared the induced currents within a PV module with the currents induced within a thin-wire approximation of a PV module (constructed using dimensions from the actual PV module), with short-circuited bypass diodes and with actual bypass diodes in place.

For the thin-wire approximation, the magnitudes of the induced currents were found to rapidly attenuate with increasing separation distance from the current impulse. For the case with the short-circuited bypass diodes, the currents induced were larger in the conductive loops located closer to the current impulse than in the conductive loops located further away, as would be expected. The addition of a short-circuit loop between the output terminals of the model increased the induced currents by 16-19 A for the separation distance of 1 m and by 8-11 A for the separation distance of 1.6 m.

When the short-circuited bypass diodes were replaced with actual bypass diodes, low negative reverse currents (of approximately 2 A) were induced within the bypass diodes, resulting in no failures. This was due to the relatively low peak current magnitude provided by the high-voltage impulse generator (when compared with the currents involved in an actual lightning flash, or in the impulse generators used in the literature reviewed in Section 2.5). Forward biasing of the bypass diodes did occur during the undershoot of the lightning waveform, resulting in the largest peak magnitudes being induced within the bypass diodes connected to the loops closest to the current impulse, and the lowest currents being induced within the bypass diodes connected to the loops furthest from the current impulse. The forward bias currents induced in the case with a separation distance of 1 m were approximately double that of the currents induced with a separation distance of 1.6 m. The addition of a short-circuit loop between the output terminals of the model increased the induced currents by 15-25 A at a separation distance of 1 m and by 10-11 A at a separation distance of 1.6 m - similar to the case with the short-circuited bypass diodes.

For the actual PV module, the magnitudes of the induced currents were far lower than in the case with the thin-wire approximation, or in the simulations. Little difference was observed between the cases with the short-circuited bypass diodes and the cases with the actual bypass diodes, for either separation distance. The presence of a short-circuit loop between the output terminals of the PV module, however, resulted in a noticeable increase in the peak magnitudes of the induced currents. For the cases with the short-circuited bypass diodes, currents of up to 19 A were observed in the case with a separation distance of 1 m, and currents with peak magnitudes of up to 11 A were observed in the case with a separation distance of 1.6 m.

As in the case of the thin-wire approximation, only low negative reverse currents (approximately 2 A) were induced within the bypass diodes of the PV module, with or without the presence of the short-circuit. The presence of the short-circuit did, however, also result in the forward biasing of the bypass diodes during the undershoot of the current impulse. Currents of up to 11 A were observed in the case with a separation distance of 1 m, and currents with peak magnitudes of up to 3.8 A were observed in the case with a separation distance of 1.6 m.

It is extrapolated that (for a separation distance of 1 m) if the magnitude of the impulse current were to be increased by a factor of 30 (a current of 132 kA), a reverse current of 60 A may flow through the bypass diodes. This is the critical reverse current above which a bypass diode is likely to fail (as determined in Section 3.11.2). From the lightning data surrounding the three plants considered in Section 1.2, a current of 132 kA occurred 0.07% of the time. Between 46 to 64 occurrences of currents of this magnitude or larger had been recorded in the areas surrounding each plant between 2006 and 2016.

The resulting overall conclusion from this chapter is that a current is far more likely to be induced within a PV installation as a result of large loop areas being formed by wiring connected to the PV modules, and not by the PV modules themselves. This is positive news for PV power plants experiencing issues with the indirect effects of nearby lightning strikes, as it is far easier and more cost effective to alter the wiring in an installation than adjust the internal layout of the PV modules to be less susceptible to the effects of induced currents resulting from large magnetic fields. This chapter further satisfied the third research goal defined in Section 1.5, as it established the extent to which current may be induced within both the internal layout of a PV module, as well as within external wiring connected to the module.

Chapter 6

Conclusions and Recommendations

The work presented in this thesis is on investigations relating to PV module failure mechanisms caused by indirect lightning strikes. These investigations were formulated after the examination of repair log data from three utility-scale PV power plants revealed multiple cases of bypass diode failures. Multiple cases of bypass diode failures were recorded, prompting an investigation into how a bypass diode may fail. A short-circuit bypass diode failure would prevent the internal string of PV cells within a module from producing any useful output power, as the power would simply circulate through the short-circuited bypass diode. Once the conditions under which a bypass diode may fail were established, investigations into the possible causes of these conditions were performed.

6.1 Impulse Generator

An impulse generator was designed and constructed in order to test the failure modes of Schottky barrier diodes, which are commonly implemented as bypass diodes in PV modules. Forward bias testing of the diodes resulted in zero failures at any of the impulse magnitudes considered, whilst reverse bias testing resulted in the establishment of a critical reverse current - above which a diode would certainly fail in the short-circuit position. Further testing was performed in order to ascertain whether a degradation of the electrical characteristics of the diodes would occur from the application of successive impulses (in either the forward or the reverse bias) - no degrading effect was found. Two alternative models of Schottky barrier diodes of similar specifications from different brands were tested, and similar results were observed. A initial degradation of the one alternative model of diode was observed, indicating poor resilience of that particular alternative diode to impulses applied in the reverse bias. This section therefore directly achieved the first research goal set out in Section 1.5.

MOVs were tested as a potential bypass diode protection measure. A MOV placed in parallel with a bypass diode would begin conducting before the bypass diode, providing an alternative path for the current impulse to be routed through, protecting the diode. Multiple MOVs can be placed in parallel in order to increase the resilience to impulses. MOVs were found to be a cost-effective measure of increasing the resilience of a PV module to bypass diode failure. This section therefore directly achieved the second research goal set out in Section 1.5.

6.2 Electromagnetic Modelling

Electromagnetic modelling of a CAD model of a PV module was performed in order to establish the influence of the geometry of a PV module on the currents induced within it. A current would flow in the continuously conductive frame of the PV module, creating an opposing magnetic field to the magnetic field created by the lightning stroke, reducing the net magnetic flux passing through the PV module - thereby resulting in reduced magnitudes of the induced currents (when compared to a PV module without the frame). The addition of a short-circuit loop between the output terminals of the PV module resulted in an additive contribution to the magnitudes of the induced currents within the bypass diodes. Further simulations were performed with four series-connected PV modules in order to examine the combined effects of both poor and better inter-module wiring practices, with and without the frames of the modules present. Although the magnitudes of the currents induced within the inter-module wiring did reduce with the frames of the modules present, the largest reduction in the induced currents within the inter-module wiring was observed by reducing the loop area of the inter-module wiring. This chapter therefore achieved the third research goal set out in Section 1.5.

6.3 High-Voltage Testing

As certain assumptions had been made in the electromagnetic modelling process, real-world testing was performed in a high-voltage laboratory in order to determine the extent to which currents may be induced within an actual PV-module. Larger currents were found to be induced within a short-circuited loop connected to the output terminals of the module than within the loops formed by the traces internal to the module. The magnitudes of the induced currents were highly sensitive to the separation distance between the PV module and the current impulse.

Chapter 4 and Chapter 5 both demonstrated that the presence of a low-impedance loop connected to the output terminals of a PV module (or string of modules) provides the potential for large currents to be induced within the installation through the inter-module wiring. This same conclusion was reached in both the simulation work and the real-world testing. This study further achieved the third research goal set out in Section 1.5.

6.4 Recommendations

The findings from the experiments conducted in Chapter 3, Chapter 4, and Chapter 5 were combined to produce the following two recommendations:

- MOVs should be implemented in parallel with the bypass diodes of PV modules in regions of high lightning activity in order to increase the resilience of bypass diodes to induced impulses.
- Good inter-module wiring practice (suggestions for which are covered in Section 5.6) should be applied to PV installations in order to minimize the magnitudes of the induced impulses.

A decreased susceptibility to EMI is always preferable to an increased resilience provided by a third-party protection measure, however, the combination of the suggested protection measure with the suggestions for the decreased susceptibility would result in the lowest possible probability of the failure of the bypass diodes within a PV module.

Bibliography

- [1] International Energy Agency, “Renewables 2017 - Analysis and Forecasts to 2022,” 2017. [Online]. Available: <https://www.iea.org/Textbase/npsum/renew2017MRSsum.pdf>
- [2] BYD Company, *BYD P6C-36 Series-3BB*, BYD, Shenzhen, 2013. [Online]. Available: [http://www.byd.com/br/pv/download/Spec/en/tuv/p6c-36/BYD_3BB_PV_Module_TUV_40mm_\(P6C-36-Black\)_Oct.2013.pdf](http://www.byd.com/br/pv/download/Spec/en/tuv/p6c-36/BYD_3BB_PV_Module_TUV_40mm_(P6C-36-Black)_Oct.2013.pdf)
- [3] T. Gill, “Initial Steps in the Development of a Comprehensive Lightning Climatology of South Africa,” Master’s thesis, School of Geography, Archaeology and Environmental Studies: Climatology Research Group, 2009. [Online]. Available: <https://core.ac.uk/download/pdf/39666083.pdf>
- [4] Arup. (2014) A 75MW photovoltaic power plant including over 300,000 PV modules. Arup. [Online]. Available: <https://www.arup.com/projects/kalkbult-pv>
- [5] D. M. Romps, J. T. Seeley, D. Volaro, and J. Molinari, “Projected increase in lightning strikes in the united states due to global warming,” *Science*, vol. 346, no. 6211, pp. 851–854, 2014. [Online]. Available: <http://science.sciencemag.org/content/346/6211/851>
- [6] N. Reeve and R. Toumi, “Lightning activity as an indicator of climate change,” *Quarterly Journal of the Royal Meteorological Society*, vol. 125, no. 555, pp. 893–903, 2006. [Online]. Available: <https://rmets.onlinelibrary.wiley.com/doi/abs/10.1002/qj.49712555507>
- [7] H. Volland, *Handbook of atmospheric electrodynamics*. Boca Ratona: CRC Press, 1995.
- [8] C. Price and D. Rind, “A simple lightning parameterization for calculating global lightning distributions,” *Journal of Geophysical Research: Atmospheres*, vol. 97, no. D9, pp. 9919–9933, 1992. [Online]. Available: <https://agupubs.onlinelibrary.wiley.com/doi/abs/10.1029/92JD00719>
- [9] K. M. Coetzer, A. J. Rix, and P. G. Wiid, “Impulse generator design to investigate indirect lightning strike effects on utility-scale photovoltaic installations,” in *Proc. 26th South African Universities Power and Engineering Conference*, Johannesburg, 2018, pp. 181–185.
- [10] Y. Tu, C. Zhang, J. Hu, S. Wang, W. Sun, and H. Li, “Research on lightning overvoltages of solar arrays in a rooftop photovoltaic power system,” *Electric Power Systems Research*, vol. 94, pp. 10 – 15, 2013, lightning Protection of Advanced Energy Systems. [Online]. Available: <http://www.sciencedirect.com/science/article/pii/S0378779612001976>
- [11] G. M. Masters, *Renewable and Efficient Electric Power Systems*, 2nd ed. Hoboken: Wiley-Interscience, 2004.

-
- [12] W. Smith, “Effect of light on selenium during the passage of an electric current,” *International Journal of Science*, vol. 7, p. 303, 1873. [Online]. Available: <http://dx.doi.org/10.1038/007303e0>
- [13] “Discovery of the photovoltaic (pv) effect,” 2018. [Online]. Available: http://solarcellcentral.com/history_page.html
- [14] ST Microelectronics, *How to choose a bypass diode for a silicon panel junction box*, Geneva, 2011. [Online]. Available: https://www.st.com/content/ccc/resource/technical/document/application_note/cc/6a/fe/6d/f6/17/40/3c/DM00034029.pdf/files/DM00034029.pdf/jcr:content/translations/en.DM00034029.pdf
- [15] A. I. Watson, R. E. López, and R. L. Holle, “Diurnal Cloud-to-Ground Lightning Patterns in Arizona during the Southwest Monsoon,” *Monthly Weather Review*, vol. 122, no. 8, pp. 1716–1725, 1994. [Online]. Available: <https://journals.ametsoc.org/doi/abs/10.1175/1520-0493%281994%29122%3C1716%3ADCTGLP%3E2.0.CO%3B2>
- [16] V. A. Rakov and M. A. Uman, *Lightning: Physics and Effects*. Cambridge University Press, 2006. [Online]. Available: <https://books.google.co.za/books?id=TuMa5lAa3RAC>
- [17] D. J. Malan, “Physics of lightning,” *Quarterly Journal of the Royal Meteorological Society*, vol. 90, no. 384, p. 221, 1964. [Online]. Available: <https://rmets.onlinelibrary.wiley.com/doi/abs/10.1002/j.1477-8696.1964.tb02110.x>
- [18] S. E. Reynolds, M. Brook, and M. F. Gourley, “Thunderstorm charge separation,” *Journal of Meteorology*, vol. 14, no. 5, pp. 426–436, 1957. [Online]. Available: [https://doi.org/10.1175/1520-0469\(1957\)014\(0426:TCS\)2.0.CO;2](https://doi.org/10.1175/1520-0469(1957)014(0426:TCS)2.0.CO;2)
- [19] T. Takahashi, “Riming electrification as a charge generation mechanism in thunderstorms,” *Journal of the Atmospheric Sciences*, vol. 35, no. 8, pp. 1536–1548, 1978. [Online]. Available: [https://doi.org/10.1175/1520-0469\(1978\)035<1536:REAACG>2.0.CO;2](https://doi.org/10.1175/1520-0469(1978)035<1536:REAACG>2.0.CO;2)
- [20] E. R. Jayaratne and C. P. R. Saunders, “Thunderstorm electrification: The effect of cloud droplets,” *Journal of Geophysical Research: Atmospheres*, vol. 90, no. D7, pp. 13 063–13 066, 1985. [Online]. Available: <https://agupubs.onlinelibrary.wiley.com/doi/abs/10.1029/JD090iD07p13063>
- [21] C. P. R. Saunders, H. Bax-norman, C. Emersic, E. E. Avila, and N. E. Castellano, “Laboratory studies of the effect of cloud conditions on graupel/crystal charge transfer in thunderstorm electrification,” *Quarterly Journal of the Royal Meteorological Society*, vol. 132, no. 621, pp. 2653–2673, 2007. [Online]. Available: <https://rmets.onlinelibrary.wiley.com/doi/abs/10.1256/qj.05.218>
- [22] S. C. Sherwood, V. T. J. Phillips, and J. S. Wettlaufer, “Small ice crystals and the climatology of lightning,” *Geophysical Research Letters*, vol. 33, no. 5, 2006. [Online]. Available: <https://agupubs.onlinelibrary.wiley.com/doi/abs/10.1029/2005GL025242>
- [23] D. E. Proctor, “Regions where lightning flashes began,” *Journal of Geophysical Research*, vol. 96, no. D3, p. 5099, 1991. [Online]. Available: <https://agupubs.onlinelibrary.wiley.com/doi/epdf/10.1029/90JD02120>
-

-
- [24] V. Cooray, "Energy dissipation in lightning flashes," *Journal of Geophysical Research: Atmospheres*, vol. 102, no. D17, pp. 21 401–21 410, 1997. [Online]. Available: <https://agupubs.onlinelibrary.wiley.com/doi/abs/10.1029/96JD01917>
- [25] N. Kitagawa, M. Brook, and E. J. Workman, "Continuing currents in cloud-to-ground lightning discharges," *Journal of Geophysical Research*, vol. 67, no. 2, pp. 637–647, 1962. [Online]. Available: <https://agupubs.onlinelibrary.wiley.com/doi/abs/10.1029/JZ067i002p00637>
- [26] B. A. Zajac and S. A. Rutledge, "Cloud-to-ground lightning activity in the contiguous united states from 1995 to 1999," *Monthly Weather Review*, vol. 129, no. 5, pp. 999–1019, 2001. [Online]. Available: [https://doi.org/10.1175/1520-0493\(2001\)129<0999:CTGLAI>2.0.CO;2](https://doi.org/10.1175/1520-0493(2001)129<0999:CTGLAI>2.0.CO;2)
- [27] South African National Standards, "Crystalline silicon terrestrial photovoltaic (PV) modules - Design qualification and type approval," *SANS 61215:2015, Edition 1*, pp. 1–51, 2015.
- [28] South African National Standards, "Protection against lightning Part 1: General principles," *SANS 62305-1:2010, Edition 2*, pp. 1–71, 2011.
- [29] South African National Standards, "Low-voltage surge protective devices Part 12: Surge protective devices connected to low-voltage power distribution systems - Selection and application principles," *SANS 61643-12:2009, Edition 2*, p. 13, 2009.
- [30] South African National Standards, "Protection against lightning Part 2: Risk management," *SANS 62305-2:2010, Edition 2*, pp. 1–87, 2011.
- [31] South African National Standards, "Protection against lightning Part 3: Physical damage to structures and life hazard," *SANS 62305-3:2010, Edition 2*, pp. 1–159, 2011.
- [32] South African National Standards, "Protection against lightning Part 4: Electrical and electronic systems within structures," *SANS 62305-4:2010, Edition 2*, pp. 1–91, 2011.
- [33] South African National Standards, "Electrical installations of buildings Part 7-712: Requirements for special installations or locations - Solar photovoltaic (PV) power supply systems," *SANS60364-7-712:2016, Edition 1*, pp. 1–17, 2016.
- [34] 2018. [Online]. Available: <https://www.dehn-africa.com/en-za/2199/31519/Familie-html/31519/DEHNguardmodular%28Y%29PVSCI....html>
- [35] H. Haeberlin and R. Minkner, "Tests of lightning withstand capability and measurements of induced voltages at a model of a pv-system with zno-surge-arresters," in *Proc. 11th European Photovoltaic Solar Energy Conference*, Montreux, 1992.
- [36] H. Haeberlin and R. Minkner, "A simple method for lightning protection of PV-systems," in *Proc. 12th European Solar Energy Conference and Exhibition*, Amsterdam, 1994.
- [37] H. Haeberlin, "Interference voltages induced by magnetic fields of simulated lightning currents in photovoltaic modules and arrays," in *Proc. 17th European Photovoltaic Solar Energy Conference*, Munich, 2001.
-

-
- [38] South African National Standards, “High-Voltage test techniques Part 1: General Definitions and test requirements,” *SANS 60060-1:2011, Edition 2*, pp. 26–36, 2011.
- [39] South African National Standards, “Electromagnetic compatibility (EMC) Part 4-5: Testing and measurement techniques - Surge immunity test,” *SANS 61000-4-5:2006, Edition 2*, pp. 13–35, 2006.
- [40] R. B. Standler, “Equations for some transient overvoltage test waveforms,” *IEEE Transactions on Electromagnetic Compatibility*, vol. 30, no. 1, pp. 69–71, Feb 1988. [Online]. Available: <https://ieeexplore.ieee.org/stamp/stamp.jsp?arnumber=19891>
- [41] E. O. Marx, “Versuche über die prüfung von isolatoren mit spannungsstößen,” *Elektrotechnische Zeitschrift*, vol. 45, pp. 652–654, 1924.
- [42] I. Ahrens, “Marx, Erwin,” *Neue Deutsche Biographie 16*, pp. 324–326, 1990. [Online]. Available: <https://www.deutsche-biographie.de/pnd119091275.html#ndbcontent>
- [43] W. J. Carey and J. R. Mayes, “Marx generator design and performance,” in *Conference Record of the Twenty-Fifth International Power Modulator Symposium, 2002 and 2002 High-Voltage Workshop.*, June 2002, pp. 625–628. [Online]. Available: <https://ieeexplore.ieee.org/document/1189556>
- [44] Sandia National Laboratories, “Z pulsed power facility,” 2018. [Online]. Available: <https://www.sandia.gov/z-machine/>
- [45] J. R. Mayes, E. Eubank, M. Lara, M. G. Mayes, and J. Tatoian, “A moderate energy, high repetition rate marx generator system for pulse charging wide band antenna structures,” in *Conference Record of the 2006 Twenty-Seventh International Power Modulator Symposium*, May 2006, pp. 548–551. [Online]. Available: <https://ieeexplore.ieee.org/stamp/stamp.jsp?arnumber=19891>
- [46] Toshiba Corporation, *GT40WR21 Silicon N-Channel IGBT*, Toshiba Corporation, Minato, 2018. [Online]. Available: <https://toshiba.semicon-storage.com/info/docget.jsp?did=13219&prodName=GT40WR21>
- [47] International Rectifier, *IR2104(S) and (PbF) Half-Bridge Driver*, International Rectifier, El-Segundo, 2004. [Online]. Available: <https://docs-emea.rs-online.com/webdocs/0791/0900766b80791096.pdf>
- [48] Panasonic Corporation, *Metallized Polypropylene Film Capacitor*, Panasonic Corporation, Kadoma, 2016. [Online]. Available: <https://industrial.panasonic.com/cdbs/www-data/pdf/RDL0000/ABD0000C200.pdf>
- [49] TDK Corporation, *Aluminium electrolytic capacitors*, Tokyo, 2016. [Online]. Available: <https://www.mouser.com/ds/2/400/B43541-1220071.pdf>
- [50] ON Semiconductor, *RHRP30120 30 A, 1200 V, Hyperfast Diode*, ON Semiconductor, Aurora, 2013. [Online]. Available: <https://docs-emea.rs-online.com/webdocs/14f5/0900766b814f523b.pdf>
- [51] XP Power, *ITV Series DC-DC Converter*, XP Power, Sunnyvale, 2014. [Online]. Available: <https://docs-emea.rs-online.com/webdocs/1526/0900766b8152608b.pdf>
-

-
- [52] Cosmo Electronics Corporation, *K1010 Series 4 Pin Phototransistor Photocoupler*, Cosmo Electronics Corporation, Taipei. [Online]. Available: pribor-systems.ru/fromoremax/PDF/Cosmo/K1010.pdf
- [53] Microchip Technology, *Atmel ATmega640/V-1280/V-1281/V-2560/V-2561/V*, Microchip Technology, San Jose, 2014. [Online]. Available: http://ww1.microchip.com/downloads/en/devicedoc/atmel-2549-8-bit-avr-microcontroller-atmega640-1280-1281-2560-2561_datasheet.pdf
- [54] K. M. Coetzer, P. G. Wiid, and A. J. Rix, “An investigation into the failure mechanisms of schottky barrier diodes, as commonly implemented as bypass diodes in photovoltaic modules,” in *Proc. 5th South African Solar Energy Conference*, Durban, 2018. [Online]. Available: https://www.sasec.org.za/full_papers/34.pdf
- [55] DC Components Co., Ltd., *15SQ030 thru 15SQ100*, Taichung, 2013. [Online]. Available: <http://www.mantech.co.za/Datasheets/Products/15SQ-DC-19X.pdf>
- [56] Vishay Intertechnology, Inc., *VSB2045-M3*, Malvern, 2013. [Online]. Available: <https://docs-emea.rs-online.com/webdocs/100a/0900766b8100a45b.pdf>
- [57] W. A. Schilloff, “Metal oxide varistor,” United States of America Patent US 20 080 024 264A1, 01, 2008. [Online]. Available: <https://patentimages.storage.googleapis.com/dc/ce/c1/3b5cb5b8a2752b/US20080024264A1.pdf>
- [58] TDK Corporation, *SIOV metal oxide varistors*, Tokyo, 2011. [Online]. Available: <https://docs-emea.rs-online.com/webdocs/13c2/0900766b813c267f.pdf>
- [59] 2018. [Online]. Available: <https://altairhyperworks.com/feko/>
- [60] “Numerical Methods in FEKO,” 2016. [Online]. Available: <https://www.altair.com/RelatedCaseStudy.aspx?id=7172>
- [61] EM Software and Systems SA (Pty) Ltd, *FEKO 7.0 User Manual*, Stellenbosch, 2014. [Online]. Available: www.altairuniversity.com/wp-content/uploads/2015/03/UserManual.pdf
- [62] K. Pickerel, “The 411 on frameless solar modules,” 2015. [Online]. Available: <https://www.solarpowerworldonline.com/2015/01/411-frameless-solar-modules/>
- [63] Philips Service, *Impulse Voltage Generator Type 1430-14031-14032*, Amsterdam, 1948.
- [64] Pearson Electronics, Inc, *Impulse Voltage Generator Type 1430-14031-14032*, Palo Alto, 1999. [Online]. Available: pearsonelectronics.com/pdf/301X.pdf
- [65] C. Colp, “Cost-saving pv source-circuit wiring method,” 2018. [Online]. Available: <https://solarprofessional.com/articles/design-installation/cost-saving-pv-source-circuit-wiring-method#.XAQNUbhx2Uk>
- [66] B. Hesterman and D. E. Powell, “Introduction to voltage surge immunity testing,” in *Proc. IEEE Power Electronics Society Denver Chapter Meeting*, Denver, 2007. [Online]. Available: http://www.denverpels.org/Downloads/Denver_PELS_20070918_Hesterman_Voltage_Surge_Immunity.pdf
-

- [67] “Coil inductance calculator,” 2018. [Online]. Available: <https://www.allaboutcircuits.com/tools/coil-inductance-calculator/>

Appendix A

Derivation of Pulse-Shaping Network Equations

Figure 3.5 is adapted for the derivation of the open-circuit voltage and short-circuit current equations which govern the dynamics of the pulse-shaping network. The Marx generator detailed in Chapter 3.4 is approximated as a capacitor C_1 and a switch S_1 . It should be mentioned that the procedure followed was similar to that demonstrated in [66], however the authors of [66] did not include resistor R_4 (seen in Figure A.1), which allowed the authors of [66] to make simplifications to their equations which could not be made when R_4 was taken into account.

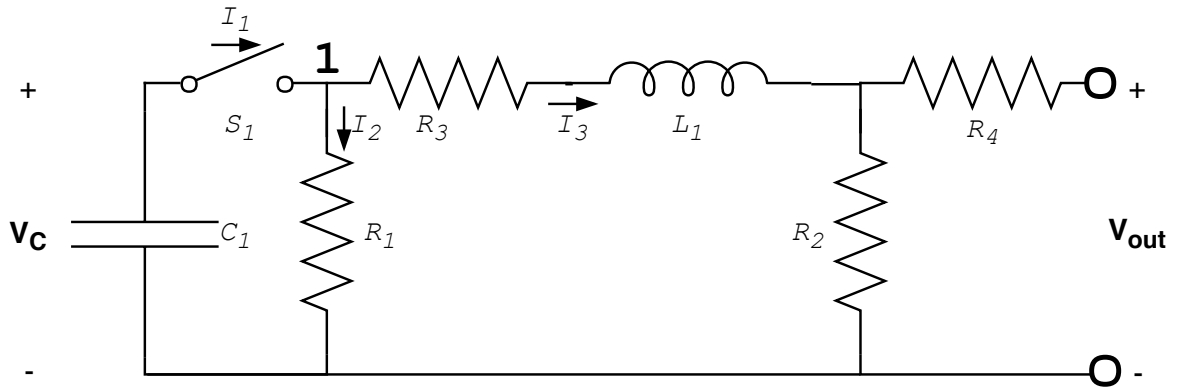


Figure A.1: The labelled diagram of the chosen pulse-shaping network topology for use in deriving suitable component values.

In order to derive the open-circuit voltage equation of the pulse-shaping network, the output of the pulse-shaping network is initially placed in the open-circuit position. Applying Kirchhoff's Current Law to node 1 in Figure A.1, it can be stated that

$$i_1(t) = i_2(t) + i_3(t) \quad (\text{A.1})$$

Applying the Laplace transform to Equation A.1 gives Equation A.2.

$$I_1(s) = I_2(s) + I_3(s) \quad (\text{A.2})$$

Equations are derived for I_1 , I_2 , and I_3 .

The time-domain equation for the current through capacitor C_1 is shown in Equation A.3.

$$i_{C_1}(t) = C \frac{dv_{C_1}(t)}{dt} \quad (\text{A.3})$$

where $i_{C_1}(t)$ is defined as the current entering capacitor C_1 , C is defined as the capacitance of capacitor C_1 , and $\frac{dv_{C_1}(t)}{dt}$ is defined as the rate of change of voltage across capacitor C_1 . The Laplace transform is applied to Equation A.3, giving Equation A.4.

$$I_{C_1}(s) = sCV_{C_1}(s) - CV_{C_0} = C(sV_{C_1}(s) - V_{C_0}) \quad (\text{A.4})$$

where $V_{C_1}(s)$ is defined as the voltage over capacitor C_1 , V_{C_0} is defined as the initial voltage over capacitor C_1 , C is defined as the capacitance of capacitor C_1 , and $I_C(s)$ is defined as the current entering capacitor C_1 .

The relationship between the current entering capacitor C_1 and current I_1 is given by Equation A.5.

$$I_{C_1}(s) = -I_1(s) \quad (\text{A.5})$$

Substituting Equation A.5 into Equation A.4 gives Equation A.6.

$$I_1(s) = -C(sV_{C_1}(s) - V_{C_0}) \quad (\text{A.6})$$

I_2 is simply derived in Equation A.7 using Ohm's Law.

$$I_2(s) = \frac{V_{C_1}(s)}{R_1} \quad (\text{A.7})$$

The time-domain equation for the voltage over inductor L_1 is shown in Equation A.8.

$$V_{L_1}(t) = L \frac{di_{L_1}(t)}{dt} \quad (\text{A.8})$$

where $i_{L_1}(t)$ is defined as the current entering inductor L_1 , L is defined as the inductance of inductor L_1 , and $\frac{di_{L_1}(t)}{dt}$ is defined as the rate of change of current entering inductor L_1 . The Laplace transform is then applied to Equation A.8, giving Equation A.9.

$$V_{L_1}(s) = L(sI_{L_1}(s) - I_{L_0}) \quad (\text{A.9})$$

where $V_{L_1}(s)$ is defined as the voltage over inductor L_1 , I_{L_0} is defined as the initial current entering inductor L_1 , L is defined as the inductance of inductor L_1 , and $I_L(s)$ is defined as the current entering L_1 . Once the initial current through the inductor is set to zero, the relationship between I_3 and I_{L_1} is stated in Equation A.10.

$$V_{L_1}(s) = sLI_{L_1}(s) = V_{C_1}(s) - I_3(s)(R_2 + R_3) \quad (\text{A.10})$$

Equation A.10 is then rearranged to make $I_3(s)$ the subject of the formula, as shown in Equation A.11

$$I_3(s) = \frac{V_{C_1}(s) - sLI_{L_1}(s)}{R_2 + R_3} \quad (\text{A.11})$$

Due to the series configuration of L_1 , R_2 and R_3 , the relationship shown in Equation A.12 holds.

$$I_3(s) = I_{L_1}(s) \quad (\text{A.12})$$

Substituting Equation A.12 into Equation A.11 yields Equation A.13.

$$I_3(s) = \frac{V_{C_1}(s) - sLI_3(s)}{R_2 + R_3} \quad (\text{A.13})$$

Equation A.13 is then rearranged to make $I_3(s)$ the subject of the formula, as shown in Equation A.14.

$$I_3(s) = \frac{V_{C_1}(s)}{R_2 + R_3 + sL} \quad (\text{A.14})$$

Substituting Equations A.6, A.7, and A.14 into Equation A.2 yields Equation A.15.

$$-C(sV_{C_1}(s) - V_{C_0}) = \frac{V_{C_1}(s)}{R_1} + \frac{V_{C_1}(s)}{R_2 + R_3 + sL} \quad (\text{A.15})$$

Equation A.15 is then rearranged to make $V_{C_1}(s)$ the subject of the formula, giving Equation A.16.

$$V_{C_1}(s) = \frac{V_{C_0}CR_1(R_2 + R_3 + sL)}{s^2(CL R_1) + s(L + CR_1(R_2 + R_3)) + (R_1 + R_2 + R_3)} \quad (\text{A.16})$$

The output voltage $V_{oc}(s)$ can be written as a function of the current through resistor R_2 .

$$V_{oc}(s) = I_3(s)R_2 \quad (\text{A.17})$$

Substituting Equation A.14 into A.17 yields Equation A.18, which is the s-domain open-circuit output voltage $V_{out}(s)$ as a function of the s-domain capacitor voltage $V_{C_1}(s)$.

$$V_{oc}(s) = \frac{V_{C_1}(s)R_2}{R_2 + R_3 + sL} \quad (\text{A.18})$$

Equation A.16 can then be substituted into Equation A.18 in order to obtain Equation A.19, which is the s-domain open-circuit output voltage, which is not a function of any other s-domain functions.

$$V_{oc}(s) = \frac{V_{C_0} C R_1 R_2 (R_2 + R_3 + sL)}{(s^2(CLR_1) + s(L + CR_1(R_2 + R_3)) + (R_1 + R_2 + R_3))(R_2 + R_3 + sL)} \quad (\text{A.19})$$

The inverse Laplace transform function was then used to find the time-domain equivalent of Equation A.19. The code is shown below.

```

syms s R1 R2 R3 Vc0 L C
Voc = Vc0·C·R1·R2·(R2+R3+s·L)/
      ((R2+R3+s·L)·
      ((s·s·(C·L·R1)+s·(L+C·R1·(R2+R3)))+(R1+R2+R3))))
voc = ilaplace(Voc)

```

The returned function was then simplified, giving Equation A.20.

$$v_{oc}(t) = \frac{2CR_1R_2V_{C_0} \sinh\left(\frac{\sqrt{C^2R_1^2(R_2+R_3)^2 - CL(4R_1^2 + 2R_1(R_2+R_3)) + L^2}}{2CLR_1}t\right)}{\left(\sqrt{C^2R_1^2(R_2+R_3)^2 - CL(4R_1^2 + 2R_1(R_2+R_3)) + L^2}\right) \left(e^{\frac{L+CR_1(R_2+R_3)}{2CLR_1}t}\right)} \quad (\text{A.20})$$

The hyperbolic sine function in Equation A.20 was then expanded using Equation A.21, giving Equation A.22.

$$\sinh(x) = \frac{e^x - e^{-x}}{2} = \frac{1 - e^{-2x}}{2e^{-x}} \quad (\text{A.21})$$

$$v_{oc}(t) = V_{C_0} \frac{R_2}{L} \tau_1 e^{\frac{-t}{\tau_2}} (1 - e^{\frac{-t}{\tau_1}}) \quad (\text{A.22})$$

where

$$\tau_1 = \frac{CLR_1}{\sqrt{C^2R_1^2(R_2+R_3)^2 - CL(4R_1^2 + 2R_1(R_2+R_3)) + L^2}} \quad (\text{A.23})$$

$$\tau_2 = \frac{2CLR_1}{CR_1(R_2+R_3) + L - \sqrt{C^2R_1^2(R_2+R_3)^2 - CL(4R_1^2 + 2R_1(R_2+R_3)) + L^2}} \quad (\text{A.24})$$

The location of the peak open-circuit voltage can be determined by taking the time derivative of Equation A.22, and setting the result to zero. Equation A.25 is the derived result for the time at which the peak open-circuit voltage occurs.

$$\begin{aligned}
\frac{d}{dt} \left(V_{C_0} \frac{R_2}{L} \tau_1 e^{\frac{-t}{\tau_2}} (1 - e^{\frac{-t}{\tau_1}}) \right) &= V_{C_0} \frac{R_2}{L} \tau_1 \frac{d}{dt} \left(e^{\frac{-t}{\tau_2}} (1 - e^{\frac{-t}{\tau_1}}) \right) = 0 \\
\therefore V_{C_0} \frac{R_2}{L} \tau_1 \frac{d}{dt} \left(e^{\frac{-t}{\tau_2}} (1 - e^{\frac{-t}{\tau_1}}) \right) &= V_{C_0} \frac{R_2}{L} \tau_1 \left[e^{\frac{-t}{\tau_2}} \left(\frac{-1}{\tau_2} \right) (1 - e^{\frac{-t}{\tau_1}}) + (e^{\frac{-t}{\tau_2}}) \left(\frac{-1}{\tau_1} \right) (-e^{\frac{-t}{\tau_1}}) \right] = 0 \\
\therefore V_{C_0} \frac{R_2}{L} \left[e^{\frac{-t}{\tau_2}} e^{\frac{-t}{\tau_1}} - \frac{\tau_1}{\tau_2} e^{\frac{-t}{\tau_2}} (1 - e^{\frac{-t}{\tau_1}}) \right] &= V_{C_0} \frac{R_2}{L} \left[e^{\frac{-t}{\tau_2}} e^{\frac{-t}{\tau_1}} - \frac{\tau_1}{\tau_2} e^{\frac{-t}{\tau_2}} + \frac{\tau_1}{\tau_2} e^{\frac{-t}{\tau_2}} e^{\frac{-t}{\tau_1}} \right] = 0 \\
\therefore V_{C_0} \frac{R_2}{L} \left[\left(1 + \frac{\tau_1}{\tau_2} \right) e^{\frac{-t}{\tau_2}} e^{\frac{-t}{\tau_1}} - \frac{\tau_1}{\tau_2} e^{\frac{-t}{\tau_2}} \right] &= 0 \\
\therefore \left(1 + \frac{\tau_1}{\tau_2} \right) e^{\frac{-t}{\tau_1}} &= \frac{\tau_1}{\tau_2} \\
\therefore (\tau_1 + \tau_2) e^{\frac{-t}{\tau_1}} &= \tau_1 \\
\therefore e^{\frac{-t}{\tau_1}} &= \frac{\tau_1}{\tau_1 + \tau_2} \\
\therefore \ln[e^{\frac{-t}{\tau_1}}] &= \ln \left[\frac{\tau_1}{\tau_1 + \tau_2} \right] \\
\therefore \frac{-t}{\tau_1} &= \ln \left[\frac{\tau_1}{\tau_1 + \tau_2} \right] \\
\therefore t &= -\tau_1 \ln \left[\frac{\tau_1}{\tau_1 + \tau_2} \right] \\
t_{\text{ocpeak}} &= \tau_1 \ln \left[\frac{\tau_1 + \tau_2}{\tau_1} \right] \tag{A.25}
\end{aligned}$$

Equation A.25 is then substituted into Equation A.22 in order to determine the expression for the value of the peak open-circuit output voltage, as shown in Equation A.26.

$$\begin{aligned}
v_{\text{oc}}(t_{\text{ocpeak}}) &= V_{C_0} \frac{R_2}{L} \tau_1 e^{\frac{-t_{\text{ocpeak}}}{\tau_2}} (1 - e^{\frac{-t_{\text{ocpeak}}}{\tau_1}}) \\
&= V_{C_0} \frac{R_2}{L} \tau_1 e^{\frac{-\tau_1 \ln \left(\frac{\tau_1 + \tau_2}{\tau_1} \right)}{\tau_2}} \left(1 - e^{\frac{-\tau_1 \ln \left(\frac{\tau_1 + \tau_2}{\tau_1} \right)}{\tau_1}} \right) \\
&= V_{C_0} \frac{R_2}{L} \tau_1 \left(\frac{\tau_1}{\tau_1 + \tau_2} \right)^{\frac{\tau_1}{\tau_2}} \left(1 - \frac{\tau_1}{\tau_1 + \tau_2} \right) \\
&= V_{C_0} \frac{R_2}{L} \tau_1 \left(\frac{\tau_1}{\tau_1 + \tau_2} \right)^{\frac{\tau_1}{\tau_2}} \left(\frac{\tau_1 + \tau_2}{\tau_1 + \tau_2} - \frac{\tau_1}{\tau_1 + \tau_2} \right) \\
&= V_{C_0} \frac{R_2}{L} \tau_1 \left(\frac{\tau_1}{\tau_1 + \tau_2} \right)^{\frac{\tau_1}{\tau_2}} \left(\frac{\tau_2}{\tau_1 + \tau_2} \right) \\
&= V_{C_0} \frac{R_2}{L} \tau_2 \left(\frac{\tau_1}{\tau_1 + \tau_2} \right)^{\frac{\tau_1}{\tau_2}} \left(\frac{\tau_1}{\tau_1 + \tau_2} \right) \\
&= V_{C_0} \frac{R_2}{L} \tau_2 \left(\frac{\tau_1}{\tau_1 + \tau_2} \right)^{\frac{\tau_1}{\tau_2} + 1} \\
&= V_{C_0} \frac{R_2}{L} \tau_2 \left(\frac{\tau_1}{\tau_1 + \tau_2} \right)^{\frac{\tau_1 + \tau_2}{\tau_2}} = v_{\text{ocpeak}} \tag{A.26}
\end{aligned}$$

An equation for the short-circuit current can now be derived. When in the short-circuit position R_2 and R_4 are in parallel, therefore one can combine R_2 and R_4 into a single equivalent resistance R_{eq} , as shown in Equation A.27.

$$R_{eq} = R_2 || R_4 = \frac{R_2 R_4}{R_2 + R_4} \quad (\text{A.27})$$

Equations A.14 and A.16 are then combined, while substituting any R_2 with R_{eq} . This gives an s-domain equation for the short-circuit current $I_3(s)$, as shown in Equation A.28.

$$\begin{aligned} I_3(s) &= \frac{V_{C_1}(s)}{R_{eq} + R_3 + sL} \\ &= \frac{V_{C_0} C R_1}{s^2 (C L R_1) + s(L + C R_1 (R_{eq} + R_3)) + (R_1 + R_{eq} + R_3)} \end{aligned} \quad (\text{A.28})$$

The inverse Laplace transform function was then used to find the time-domain equivalent of Equation A.28. The code is shown below.

```
syms s R1 Req R3 Vc0 L C
I3 = (Vc0*C*R1)/
      (s*s*(C*L*R1)+s*(L+C*R1*(Req+R3))+(R1+Req+R3))
i3 = ilaplace(I3)
```

The returned function was then simplified, giving Equation A.29.

$$i_3(t) = \frac{V_{C_0} e^{-\frac{t}{\tau_{sc}}} \sinh(\omega_{sc} t)}{\omega_{sc} L} \quad (\text{A.29})$$

where

$$\omega_{sc} = \frac{\sqrt{R_1^2 C^2 (R_3^2 + 2R_3 R_{eq} + R_{eq}^2) - 2R_1 C L (2R_1 + R_3 + R_{eq}) + L^2}}{2C L R_1} \quad (\text{A.30})$$

$$\tau_{sc} = \frac{2C L R_1}{L + C R_1 R_3 + C R_1 R_{eq}} \quad (\text{A.31})$$

As resistors R_2 and R_4 are in parallel, current division of i_3 will occur. This allows for the derivation of an equation for the time-domain short-circuit current $i_{sc}(t)$ using Equation A.29, as shown in Equation A.32.

$$\begin{aligned} i_{sc}(t) &= \frac{i_3(t) R_{eq}}{R_4} = \frac{i_3(t) \left(\frac{R_2 R_4}{R_2 + R_4} \right)}{R_4} = i_3(t) \left(\frac{R_2}{R_2 + R_4} \right) \\ &= \frac{V_{C_0} \left(\frac{R_2}{R_2 + R_4} \right) e^{-\frac{t}{\tau_{sc}}} \sinh(\omega_{sc} t)}{\omega_{sc} L} \end{aligned} \quad (\text{A.32})$$

The location of the peak open-circuit voltage can be determined by taking the time derivative of Equation A.22, and setting the result to zero.

$$\begin{aligned}
\frac{d}{dt} \left(\frac{V_{C_0} \left(\frac{R_2}{R_2+R_4} \right) e^{\frac{-t}{\tau_{sc}}} \sinh(\omega_{sc} t)}{\omega_{sc} L} \right) &= \frac{V_{C_0} \left(\frac{R_2}{R_2+R_4} \right)}{\omega_{sc} L} \frac{d}{dt} \left(e^{\frac{-t}{\tau_{sc}}} \sinh(\omega_{sc} t) \right) = 0 \\
&= \frac{V_{C_0} \left(\frac{R_2}{R_2+R_4} \right)}{\omega_{sc} L} \left[\left(-\frac{1}{\tau_{sc}} \right) \left(e^{\frac{-t}{\tau_{sc}}} \right) \sinh(\omega_{sc} t) + (\omega_{sc}) \left(e^{\frac{-t}{\tau_{sc}}} \right) \cosh(\omega_{sc} t) \right] \\
\therefore (\omega_{sc}) \cosh(\omega_{sc} t) &= \left(\frac{1}{\tau_{sc}} \right) \sinh(\omega_{sc} t) \\
\therefore \tau_{sc} \omega_{sc} &= \frac{\sinh(\omega_{sc} t)}{\cosh(\omega_{sc} t)} = \tanh(\omega_{sc} t) \\
\therefore \tanh^{-1}(\tau_{sc} \omega_{sc}) &= \omega_{sc} t \\
\therefore t_{sc\text{peak}} &= \frac{\tanh^{-1}(\tau_{sc} \omega_{sc})}{\omega_{sc}} \tag{A.33}
\end{aligned}$$

Equation A.33 is then substituted into Equation A.32 in order to determine the expression for the value of the peak short-circuit output current, as shown in Equation A.34.

$$\begin{aligned}
i_{sc}(t_{sc\text{peak}}) &= \frac{V_{C_0} \left(\frac{R_2}{R_2+R_4} \right) e^{-\frac{\tanh^{-1}(\tau_{sc} \omega_{sc})}{\tau_{sc}}} \sinh \left(\omega_{sc} \frac{\tanh^{-1}(\tau_{sc} \omega_{sc})}{\omega_{sc}} \right)}{\omega_{sc} L} \\
&= \frac{V_{C_0} \left(\frac{R_2}{R_2+R_4} \right) e^{-\frac{\tanh^{-1}(\tau_{sc} \omega_{sc})}{\tau_{sc} \omega_{sc}}} \sinh \left(\tanh^{-1}(\tau_{sc} \omega_{sc}) \right)}{\omega_{sc} L} \tag{A.34}
\end{aligned}$$

Equation A.34 is then simplified using Equation A.21 and Equation A.35, giving Equation A.36.

$$\tanh^{-1}(x) = \frac{1}{2} \ln(x+1) - \frac{1}{2} \ln(1-x) \quad |x| < 1 \tag{A.35}$$

$$\begin{aligned}
i_{sc}(t_{sc_{peak}}) &= \frac{V_{C_0} \left(\frac{R_2}{R_2+R_4} \right) e^{-\frac{\tanh^{-1}(\tau_{sc}\omega_{sc})}{\tau_{sc}\omega_{sc}}} \sinh \left(\tanh^{-1}(\tau_{sc}\omega_{sc}) \right)}{\omega_{sc}L} \\
&= \frac{V_{C_0} \left(\frac{R_2}{R_2+R_4} \right) e^{-\frac{\tanh^{-1}(\tau_{sc}\omega_{sc})}{\tau_{sc}\omega_{sc}}} \sinh \left(\frac{1}{2} \ln(\tau_{sc}\omega_{sc} + 1) - \frac{1}{2} \ln(1 - \tau_{sc}\omega_{sc}) \right)}{\omega_{sc}L} \\
&= \frac{V_{C_0} \left(\frac{R_2}{R_2+R_4} \right) e^{-\frac{\tanh^{-1}(\tau_{sc}\omega_{sc})}{\tau_{sc}\omega_{sc}}}}{\omega_{sc}L} \left[\frac{1 - e^{-2[\frac{1}{2} \ln(\tau_{sc}\omega_{sc}+1) + \frac{1}{2} \ln(1-\tau_{sc}\omega_{sc})]}}{2e^{-[\frac{1}{2} \ln(\tau_{sc}\omega_{sc}+1) - \frac{1}{2} \ln(1-\tau_{sc}\omega_{sc})]}} \right] \\
&= \frac{V_{C_0} \left(\frac{R_2}{R_2+R_4} \right) e^{-\frac{\tanh^{-1}(\tau_{sc}\omega_{sc})}{\tau_{sc}\omega_{sc}}}}{\omega_{sc}L} \left[\frac{1 - e^{-[\ln(\frac{\tau_{sc}\omega_{sc}+1}{1-\tau_{sc}\omega_{sc}})]}}{2e^{\frac{1}{2} \ln(\frac{1-\tau_{sc}\omega_{sc}}{\tau_{sc}\omega_{sc}+1})}} \right] \\
&= \frac{V_{C_0} \left(\frac{R_2}{R_2+R_4} \right) e^{-\frac{\tanh^{-1}(\tau_{sc}\omega_{sc})}{\tau_{sc}\omega_{sc}}}}{\omega_{sc}L} \left[\frac{1 - \frac{1-\tau_{sc}\omega_{sc}}{\tau_{sc}\omega_{sc}+1}}{2\sqrt{\frac{1-\tau_{sc}\omega_{sc}}{\tau_{sc}\omega_{sc}+1}}} \right] \\
&= \frac{V_{C_0} \left(\frac{R_2}{R_2+R_4} \right) e^{-\frac{\tanh^{-1}(\tau_{sc}\omega_{sc})}{\tau_{sc}\omega_{sc}}}}{\omega_{sc}L} \left[\frac{\frac{\tau_{sc}\omega_{sc}+1}{\tau_{sc}\omega_{sc}+1} - \frac{1-\tau_{sc}\omega_{sc}}{\tau_{sc}\omega_{sc}+1}}{2\sqrt{\frac{1-\tau_{sc}\omega_{sc}}{\tau_{sc}\omega_{sc}+1}}} \right] \\
&= \frac{V_{C_0} \left(\frac{R_2}{R_2+R_4} \right) e^{-\frac{\tanh^{-1}(\tau_{sc}\omega_{sc})}{\tau_{sc}\omega_{sc}}}}{\omega_{sc}L} \left[\frac{\frac{2\tau_{sc}\omega_{sc}}{\tau_{sc}\omega_{sc}+1}}{2\sqrt{\frac{(1-\tau_{sc}\omega_{sc})(\tau_{sc}\omega_{sc}+1)}{(\tau_{sc}\omega_{sc}+1)^2}}} \right] \\
&= \frac{V_{C_0} \left(\frac{R_2}{R_2+R_4} \right) e^{-\frac{\tanh^{-1}(\tau_{sc}\omega_{sc})}{\tau_{sc}\omega_{sc}}}}{\omega_{sc}L} \left[\frac{\frac{2\tau_{sc}\omega_{sc}}{\tau_{sc}\omega_{sc}+1}}{\frac{2}{\tau_{sc}\omega_{sc}+1} \sqrt{(1-\tau_{sc}\omega_{sc})(\tau_{sc}\omega_{sc}+1)}} \right] \\
&= \frac{V_{C_0} \left(\frac{R_2}{R_2+R_4} \right) e^{-\frac{\tanh^{-1}(\tau_{sc}\omega_{sc})}{\tau_{sc}\omega_{sc}}}}{\omega_{sc}L} \left[\frac{\tau_{sc}\omega_{sc}}{\sqrt{(1-\tau_{sc}\omega_{sc})(\tau_{sc}\omega_{sc}+1)}} \right] \\
&= \frac{V_{C_0} \left(\frac{R_2}{R_2+R_4} \right) e^{-\frac{\tanh^{-1}(\tau_{sc}\omega_{sc})}{\tau_{sc}\omega_{sc}}}}{\omega_{sc}L} \left[\frac{\tau_{sc}\omega_{sc}}{\sqrt{1 - (\tau_{sc}\omega_{sc})^2}} \right] \\
&= \frac{V_{C_0} \tau_{sc} \left(\frac{R_2}{R_2+R_4} \right) e^{-\frac{\tanh^{-1}(\tau_{sc}\omega_{sc})}{\tau_{sc}\omega_{sc}}}}{L\sqrt{1 - (\tau_{sc}\omega_{sc})^2}} \tag{A.36}
\end{aligned}$$

Thus far, the equations for the time-domain short-circuit current have included a hyperbolic term. It is sometimes useful to make use of ordinary trigonometric terms instead of hyperbolic terms. One such example is when finding the equation for the location of the first negative peak of the short-circuit current, as it would be located π radians after the first positive peak. In order to accomplish this, ω_{sc} is rewritten as shown in Equation A.37.

$$\begin{aligned}
\omega_{sc} &= \frac{\sqrt{R_1^2 C^2 (R_3^2 + 2R_3 R_{eq} + R_{eq}^2) - 2R_1 CL(2R_1 + R_3 + R_{eq}) + L^2}}{2CLR_1} \\
&= \frac{\sqrt{(-1)(-R_1^2 C^2 (R_3^2 + 2R_3 R_{eq} + R_{eq}^2) + 2R_1 CL(2R_1 + R_3 + R_{eq}) - L^2)}}{2CLR_1} \\
&= i \frac{\sqrt{-R_1^2 C^2 (R_3^2 + 2R_3 R_{eq} + R_{eq}^2) + 2R_1 CL(2R_1 + R_3 + R_{eq}) - L^2}}{2CLR_1} \\
&= i(\omega'_{sc}) \\
\therefore \omega'_{sc} &= \frac{\omega_{sc}}{i} = -i\omega_{sc}
\end{aligned} \tag{A.37}$$

Substituting Equation A.37 into Equation A.32 allows for the trigonometric identity seen in Equation A.38 to be used, giving Equation A.39, which is an expression for the time-domain short-circuit current i_{sc} which does not include any hyperbolic terms.

$$\begin{aligned}
\sinh(x) &= -i \sin(ix) \\
\therefore \sinh(ix) &= i \sin(x) \\
\therefore -i \sinh(ix) &= \sin(x)
\end{aligned} \tag{A.38}$$

$$\begin{aligned}
i_{sc}(t) &= \frac{V_{C_0} \left(\frac{R_2}{R_2 + R_4} \right) e^{\frac{-t}{\tau_{sc}}} \sinh(\omega_{sc} t)}{\omega_{sc} L} \\
&= \frac{V_{C_0} \left(\frac{R_2}{R_2 + R_4} \right) e^{\frac{-t}{\tau_{sc}}} \sinh(i(\omega'_{sc}) t)}{i\omega'_{sc} L} \\
&= \frac{-i V_{C_0} \left(\frac{R_2}{R_2 + R_4} \right) e^{\frac{-t}{\tau_{sc}}} \sin(i(\omega'_{sc}) t)}{\omega'_{sc} L} \\
&= \frac{V_{C_0} \left(\frac{R_2}{R_2 + R_4} \right) e^{\frac{-t}{\tau_{sc}}} \sin(\omega'_{sc} t)}{\omega'_{sc} L}
\end{aligned} \tag{A.39}$$

Similarly to in Equation A.39, substituting Equation A.37 into Equation A.36 allows for the trigonometric identity seen in Equation A.38 to be used, giving Equation A.41, which is an expression for the time-domain short-circuit current $i_{sc_{peak}}$ which does not include any hyperbolic terms.

$$\begin{aligned}
\tan^{-1}(ix) &= i \tanh^{-1}(x) \\
\therefore \tan^{-1}(-x) &= i \tanh^{-1}(ix) \\
\therefore -\tan^{-1}(x) &= i \tanh^{-1}(ix)
\end{aligned} \tag{A.40}$$

$$\begin{aligned}
 i_{sc}(t_{sc\text{peak}}) &= \frac{V_{C_0} \tau_{sc} \left(\frac{R_2}{R_2+R_4} \right) e^{-\frac{\tanh^{-1}(\tau_{sc}\omega_{sc})}{\tau_{sc}\omega_{sc}}}}{L \sqrt{1 - (\tau_{sc}\omega_{sc})^2}} \\
 &= \frac{V_{C_0} \tau_{sc} \left(\frac{R_2}{R_2+R_4} \right) e^{-\frac{\tanh^{-1}(i\tau_{sc}\omega'_{sc})}{i\tau_{sc}\omega'_{sc}}}}{L \sqrt{1 - (i\tau_{sc}\omega'_{sc})^2}} \\
 &= \frac{V_{C_0} \tau_{sc} \left(\frac{R_2}{R_2+R_4} \right) e^{-\frac{\tanh^{-1}(i\tau_{sc}\omega'_{sc})}{i\tau_{sc}\omega'_{sc}}}}{L \sqrt{1 + (\tau_{sc}\omega'_{sc})^2}} \\
 &= \frac{V_{C_0} \tau_{sc} \left(\frac{R_2}{R_2+R_4} \right) e^{\frac{i \tanh^{-1}(i\tau_{sc}\omega'_{sc})}{\tau_{sc}\omega'_{sc}}}}{L \sqrt{1 + (\tau_{sc}\omega'_{sc})^2}} \\
 &= \frac{V_{C_0} \tau_{sc} \left(\frac{R_2}{R_2+R_4} \right) e^{-\frac{\tan^{-1}(\tau_{sc}\omega'_{sc})}{\tau_{sc}\omega'_{sc}}}}{L \sqrt{1 + (\tau_{sc}\omega'_{sc})^2}} = i_{sc\text{peak}} \tag{A.41}
 \end{aligned}$$

Equation A.40 is then applied to Equation A.33, giving Equation A.42, which is an expression for the time at which the time-domain short-circuit current $i_{sc\text{peak}}$ occurs.

$$\begin{aligned}
 t_{sc\text{peak}} &= \frac{\tanh^{-1}(\tau_{sc}\omega_{sc})}{\omega_{sc}} \\
 &= \frac{\tanh^{-1}(i\tau_{sc}\omega'_{sc})}{i\omega'_{sc}} \\
 &= \frac{-i \tanh^{-1}(i\tau_{sc}\omega'_{sc})}{\omega'_{sc}} \\
 &= \frac{\tan^{-1}(\tau_{sc}\omega'_{sc})}{\omega'_{sc}} \tag{A.42}
 \end{aligned}$$

As previously mentioned, the location of the first negative peak of the short-circuit current appears π radians after the first positive peak. This is due to the sin term in the equation for the time-domain short-circuit current, Equation A.39. The time at which the first negative peak occurs $t_{sc\text{min}}$ can be expressed as shown in Equation A.43.

$$t_{sc\text{min}} = \frac{\tan^{-1}(\tau_{sc}\omega'_{sc}) + \pi}{\omega'_{sc}} \tag{A.43}$$

Equation A.43 is then substituted into Equation A.39, yielding Equation A.44, which is the value of the first negative peak of the short-circuit current.

$$\begin{aligned}
i_{sc}(t_{sc_{\min}}) &= \frac{V_{C_0} \left(\frac{R_2}{R_2+R_4} \right) e^{-\frac{t_{sc_{\min}}}{\tau_{sc}}} \sin \left(\omega'_{sc} t_{sc_{\min}} \right)}{\omega'_{sc} L} \\
&= \frac{V_{C_0} \left(\frac{R_2}{R_2+R_4} \right) e^{-\frac{\tan^{-1}(\tau_{sc}\omega'_{sc})+\pi}{\tau_{sc}\omega'_{sc}}} \sin \left(\omega'_{sc} \frac{\tan^{-1}(\tau_{sc}\omega'_{sc})+\pi}{\omega'_{sc}} \right)}{\omega'_{sc} L} \\
&= \frac{V_{C_0} \left(\frac{R_2}{R_2+R_4} \right) e^{-\frac{\tan^{-1}(\tau_{sc}\omega'_{sc})+\pi}{\tau_{sc}\omega'_{sc}}} \sin \left(\tan^{-1}(\tau_{sc}\omega'_{sc}) + \pi \right)}{\omega'_{sc} L} \\
&= \frac{V_{C_0} \left(\frac{R_2}{R_2+R_4} \right) e^{-\frac{\tan^{-1}(\tau_{sc}\omega'_{sc})+\pi}{\tau_{sc}\omega'_{sc}}} \left[\sin \left(\tan^{-1}(\tau_{sc}\omega'_{sc}) \right) \cos(\pi) + \cos \left(\tan^{-1}(\tau_{sc}\omega'_{sc}) \right) \sin(\pi) \right]}{\omega'_{sc} L} \\
&= \frac{V_{C_0} \left(\frac{R_2}{R_2+R_4} \right) e^{-\frac{\tan^{-1}(\tau_{sc}\omega'_{sc})+\pi}{\tau_{sc}\omega'_{sc}}} \left[-\sin \left(\tan^{-1}(\tau_{sc}\omega'_{sc}) \right) \right]}{\omega'_{sc} L} \\
&= \frac{-V_{C_0} \left(\frac{R_2}{R_2+R_4} \right) e^{-\frac{\tan^{-1}(\tau_{sc}\omega'_{sc})+\pi}{\tau_{sc}\omega'_{sc}}} (\tau_{sc}\omega'_{sc})}{\omega'_{sc} L \sqrt{1 + \tau_{sc}\omega'_{sc}{}^2}} \\
&= \frac{-V_{C_0} \tau_{sc} \left(\frac{R_2}{R_2+R_4} \right) e^{-\frac{\tan^{-1}(\tau_{sc}\omega'_{sc})+\pi}{\tau_{sc}\omega'_{sc}}}}{L \sqrt{1 + (\tau_{sc}\omega'_{sc})^2}} = i_{sc_{\min}} \tag{A.44}
\end{aligned}$$

Appendix B

Justification of Chosen Electromagnetic Simulation Frequencies

In order to determine whether 30 discrete simulation frequencies between 10 kHz and 600 kHz would be sufficient for the electromagnetic simulations performed, simulations were performed for an open-circuited PV module with short-circuited bypass diodes for 30, 60, and 120 frequencies in this range. The module was centrally positioned in the XZ-plane, with an impressed current at a distance of 1 m along the positive X-axis (as shown in Figure 4.8).

The results of these simulations are shown in Figure B.1, Figure B.2, and Figure B.3. In each case, a current of around 292 A was induced in the loop connected to Diode 1, 189 A was induced in the loop connected to Diode 2, and 124 A was induced in the loop connected to Diode 3. No resonances appeared to have occurred within the model for the chosen frequency range, therefore no further investigation was required around any particular group of frequencies. This served as justification that 30 discrete frequency steps were adequate for the considered frequency range.

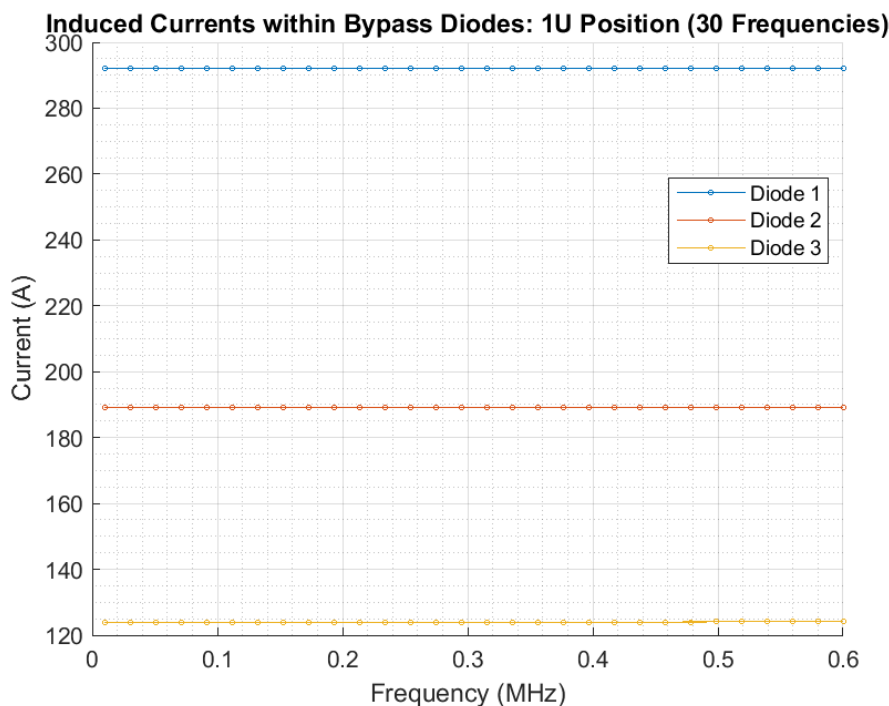


Figure B.1: Induced currents per frequency for 30 discrete frequency steps.

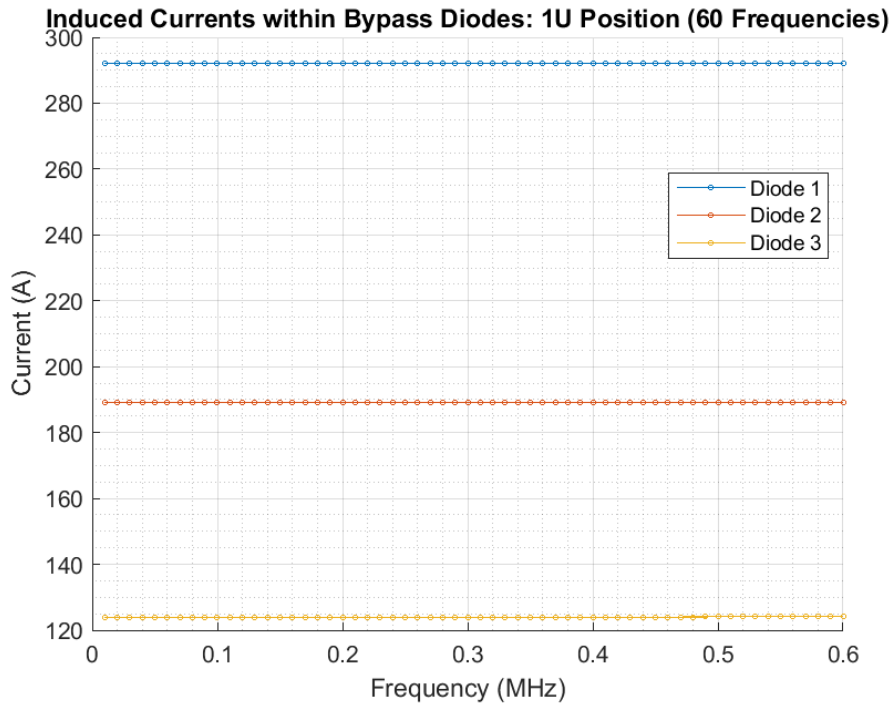


Figure B.2: Induced currents per frequency for 60 discrete frequency steps.

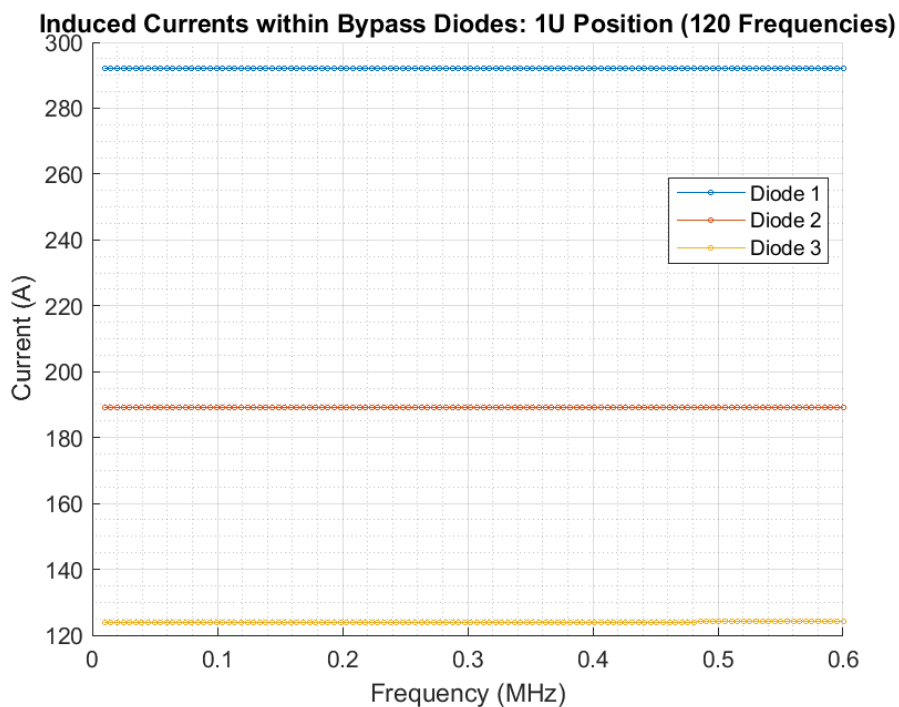


Figure B.3: Induced currents per frequency for 120 discrete frequency steps.

As an additional check, the calculated frequency domain results were used to calculate time domain results for the induced currents through the short-circuited bypass diodes. These time domain results were plotted for 30, 60, and 120 discrete frequency steps - as shown in Figure B.4, Figure B.5, and Figure B.6. The source waveform was an $8/20 \mu\text{s}$

impulse. The resulting waveforms from the time domain analysis all agreed for 30, 60, and 120 frequency steps.

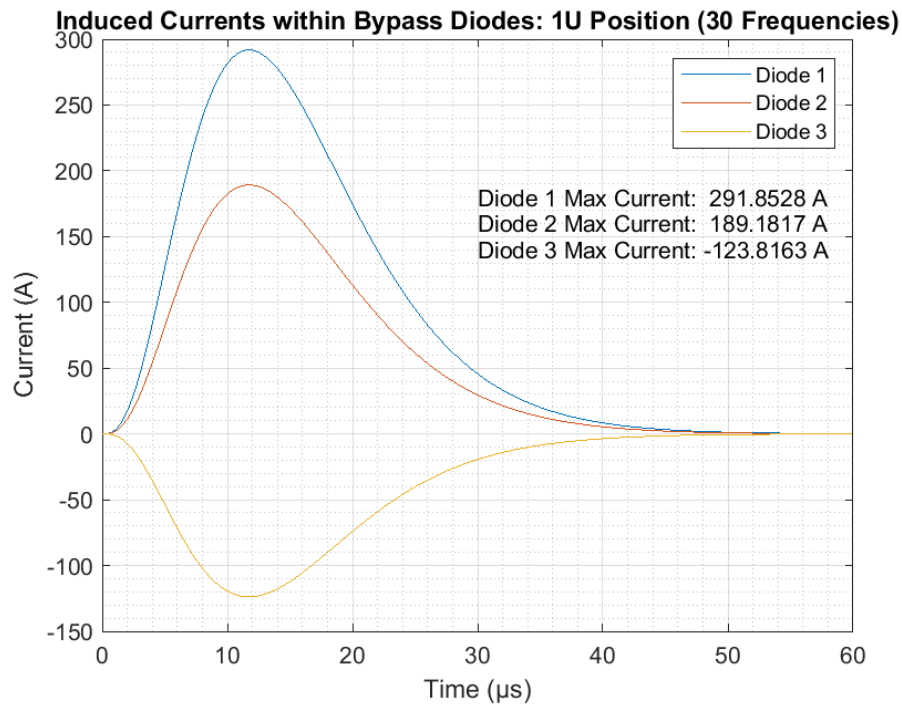


Figure B.4: Time domain induced currents for 30 discrete frequency steps.

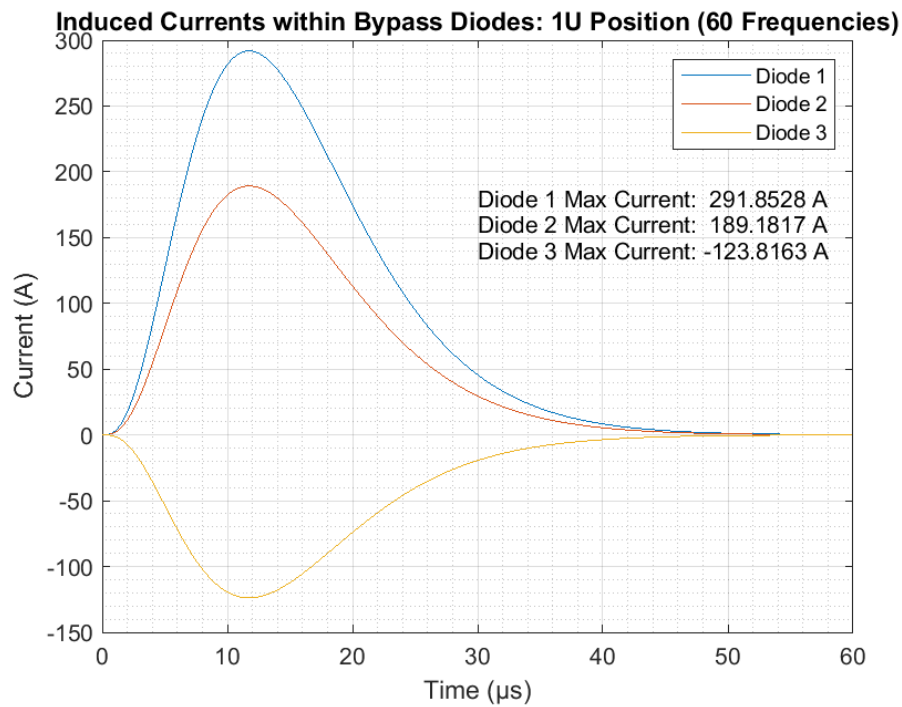


Figure B.5: Time domain induced currents for 60 discrete frequency steps.

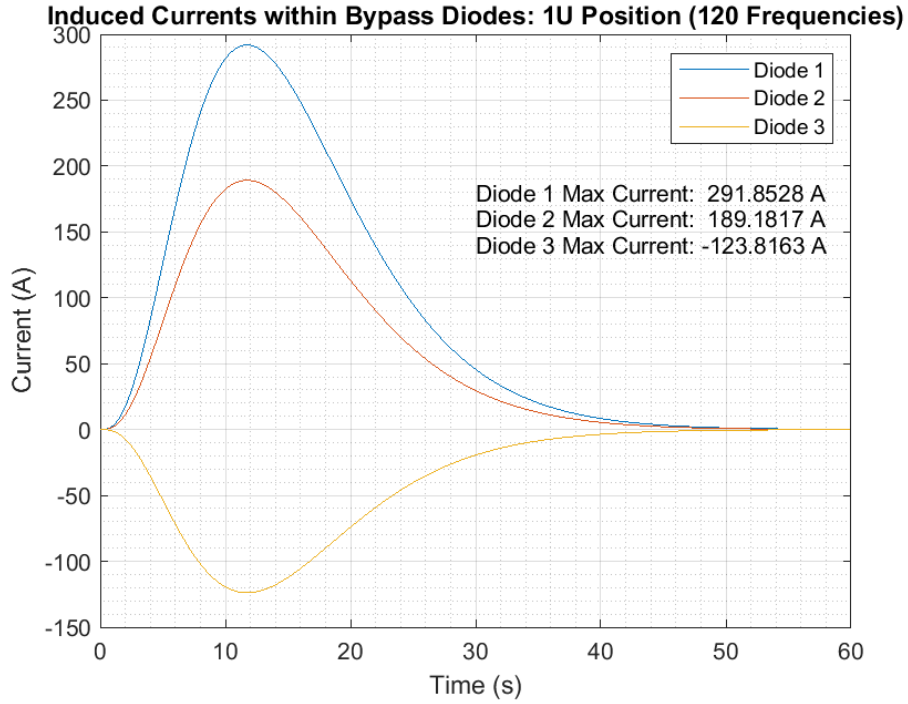


Figure B.6: Time domain induced currents for 120 discrete frequency steps.

Solutions for a continuous (interpolated) frequency range between 1 kHz and 600 kHz were also computed. The sampling algorithm used by this type of frequency uses finer sampling where results are found to change rapidly, specifically in order to take resonance effects into account [61]. The time domain result from this computation is shown in Figure B.7, and the frequency domain result is shown in Figure B.8.

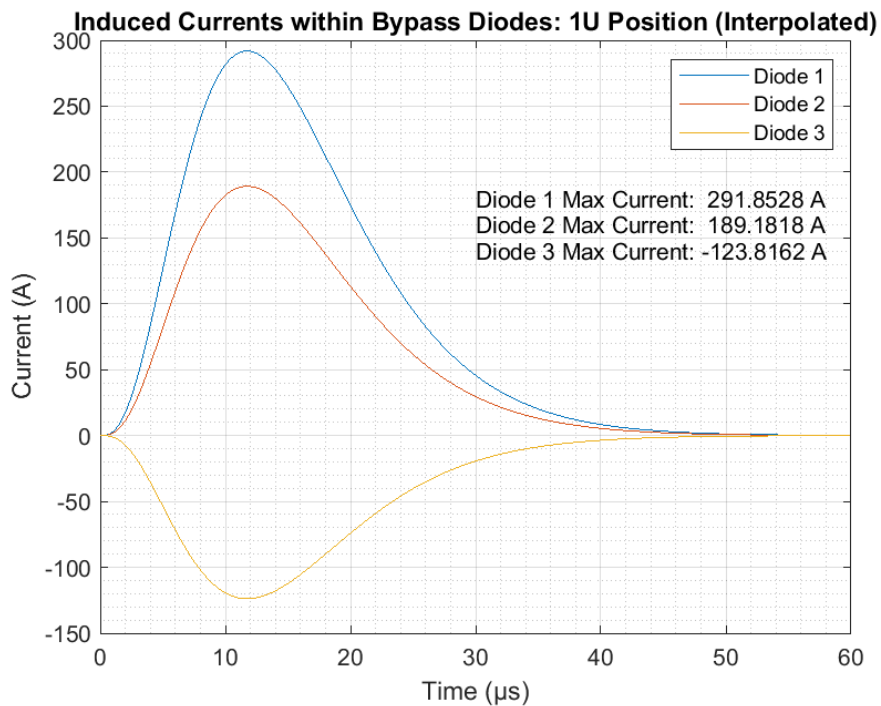


Figure B.7: Time domain induced currents for an interpolated range of frequencies.

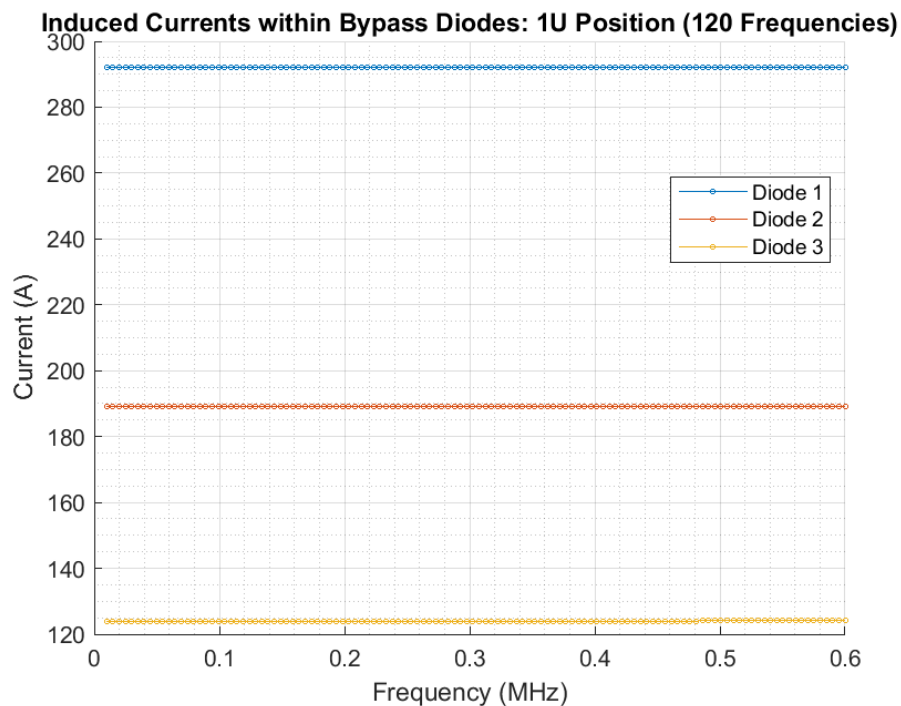


Figure B.8: Induced currents per frequency for interpolated frequency range.

These results do not differ from those computed with 30, 60, and 120 linearly spaced frequencies, therefore the choice of 30 linearly spaced frequencies was seen as a suitable one for all simulations computed.

As a final fail-safe, FEKO would produce a warning if insufficient frequencies were computed for the proper time-domain analysis of the intended signal (for any frequency range setting).

Appendix C

Justification of Lightning Polarity in Electromagnetic Simulations

Simulations were performed with both a positive and a negative polarity 20 kA, 8/20 μ s impressed current waveform, the results of which are shown in Figure C.1 and Figure C.2, respectively.

By examining the figures, it is seen that the polarities of the induced currents are reversed (as would be expected as a result of reversing the polarity of the impressed current). When comparing the respective magnitudes of the induced currents through Diode 1, Diode 2, and Diode 3 with each other (for each polarity), it is observed that a difference only occurs after the 2nd decimal place. This leads to the conclusion that the influence of the front-back asymmetry of the CAD model has little impact on the magnitudes of the induced currents. A positive, or negative, polarity impressed current could therefore be used during the simulations. A positive impressed current was chosen for simplicity.

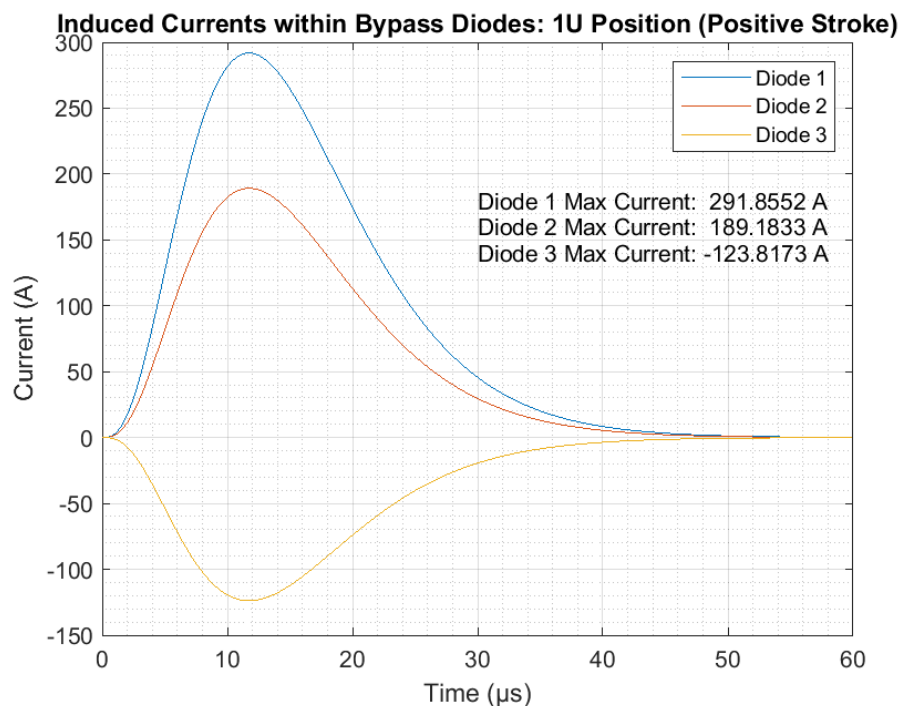


Figure C.1: Induced currents through bypass diodes at a distance of 1 m from the positive polarity lightning stroke (with frame).

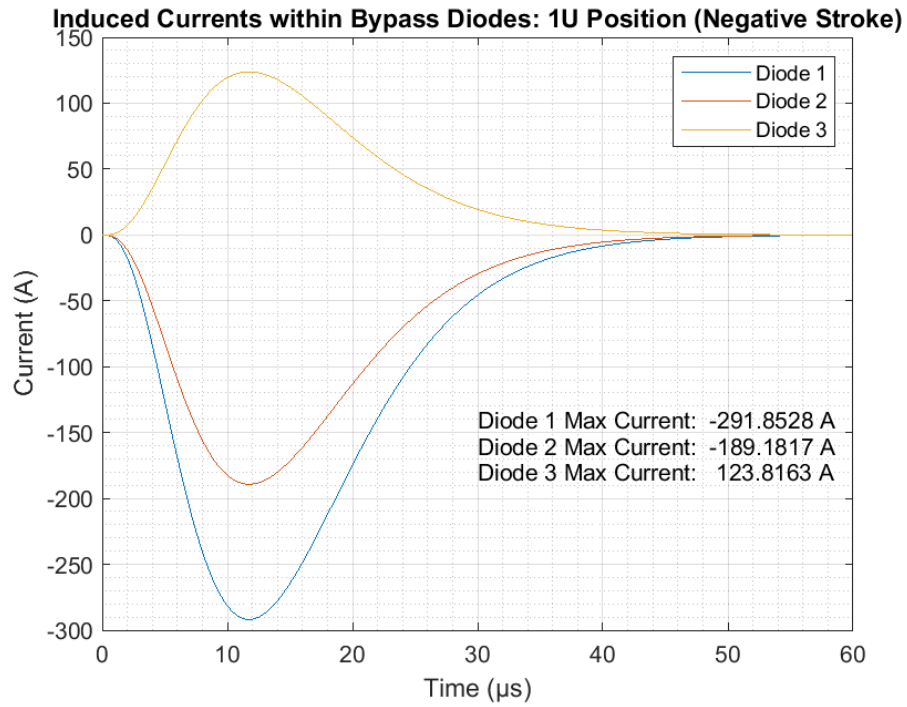


Figure C.2: Induced currents through bypass diodes at a distance of 1 m from the negative polarity lightning stroke (with frame).

Appendix D

PCB Schematics

The PCB schematics for a single impulse generator module, the distribution board, and the charge-controlling module are presented in this appendix. They are shown in Figure D.1, Figure D.2, and Figure D.3, respectively.

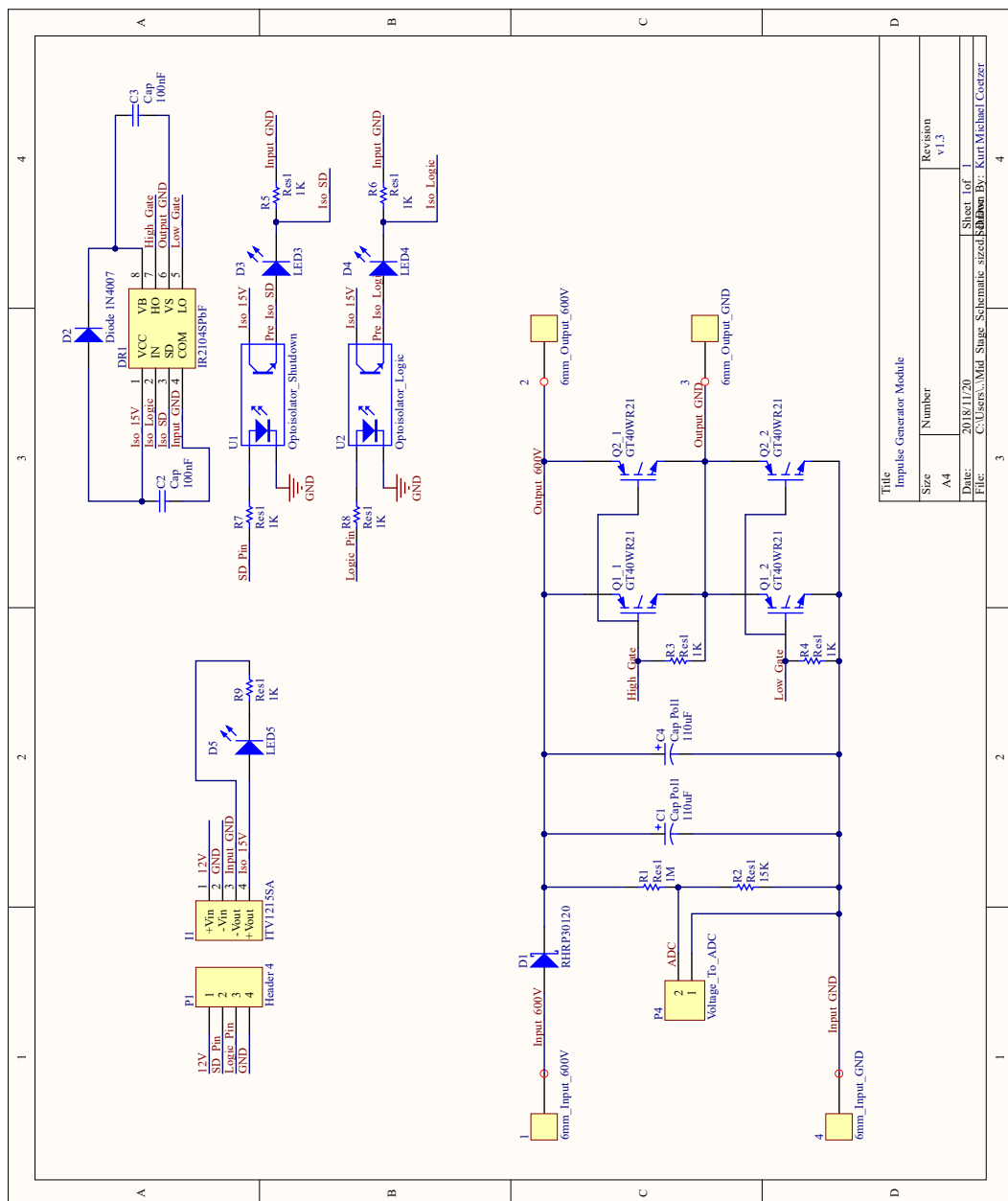


Figure D.1: The PCB schematic for a single impulse generator module.

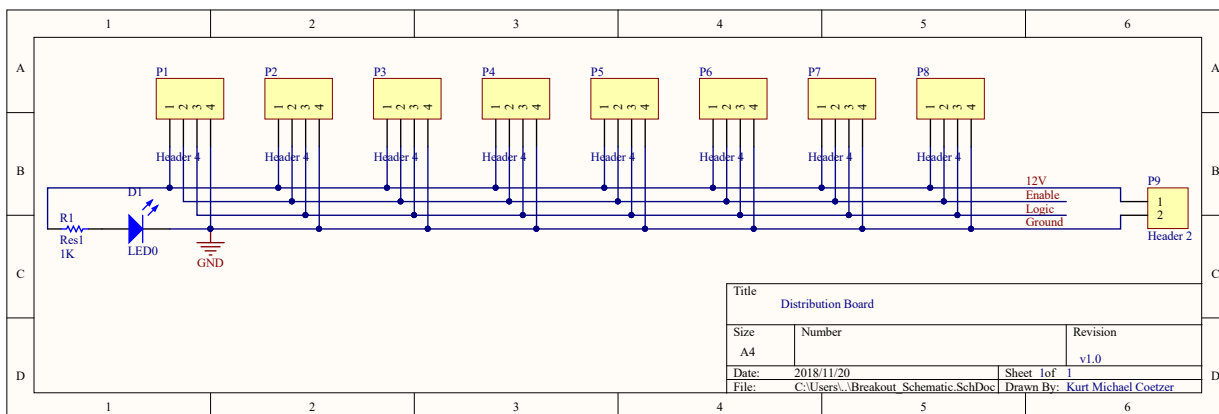


Figure D.2: The PCB schematic for the distribution board.

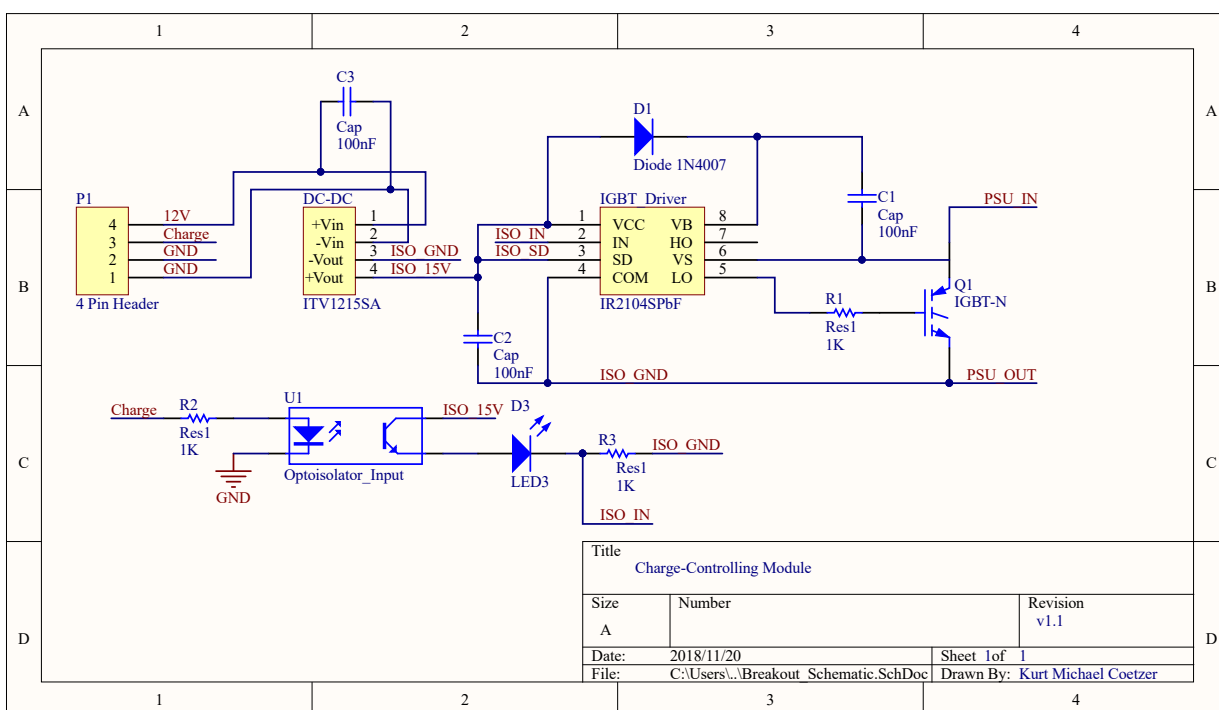


Figure D.3: The PCB schematic for the charge-controlling module.

Appendix E

Construction of Impulse Generator

Each of the six Marx generator modules was constructed on a separate PCB. These modules were designed to stack together in a tower configuration in order to decrease the footprint of the device. Connections between stages were made using 50 A Anderson connectors (with crimped terminals) with 16 mm² copper wiring. The Anderson connectors allow for stages to be easily added or removed from the Marx generator. The constructed Marx generator is shown in Figure E.1. Each Marx generator module had three LEDs to signify if they were powered on (red), and if the Enable or Charge/Discharge signals were a logical high (blue and green, respectively), as shown in Figure E.2. The schematic for the Marx generator module PCB can be seen in Figure D.1 in Appendix D. Each module was designed with sufficient space and mounting holes for an additional capacitor (in parallel with the original capacitor) and additional set of IGBTs (in parallel with the original IGBTs), should the Marx generator need to be upgraded for future testing (shown in Figure E.3).

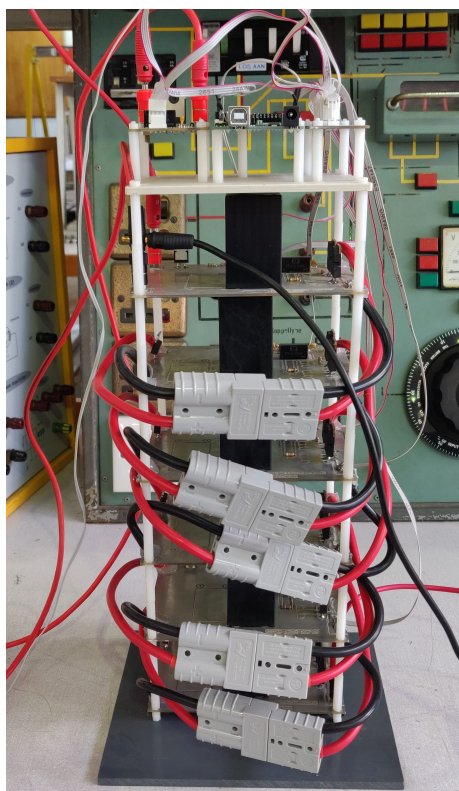


Figure E.1: The constructed six stage Marx generator.

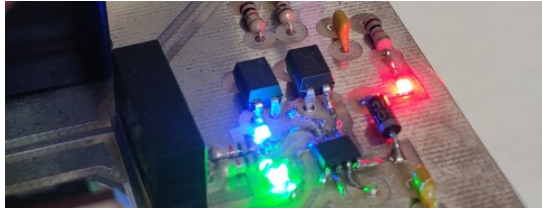


Figure E.2: The LEDs within the Marx generator module.

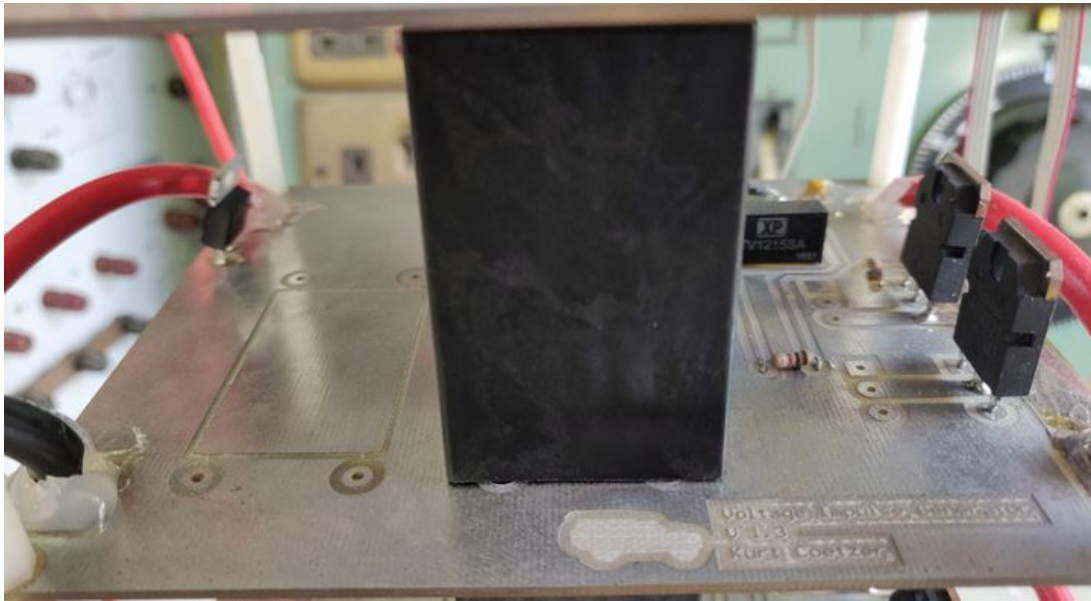


Figure E.3: A photograph of the Marx generator module.

A 3D printed platform was used to provide a mounting for the charge-controlling module, the microcontroller, and the distribution board. This platform was mounted on top of the Marx generator, making the "power on" LED of the distribution board and the "high-voltage DC power supply disconnected" LED of the charge-controlling module visible to the user.

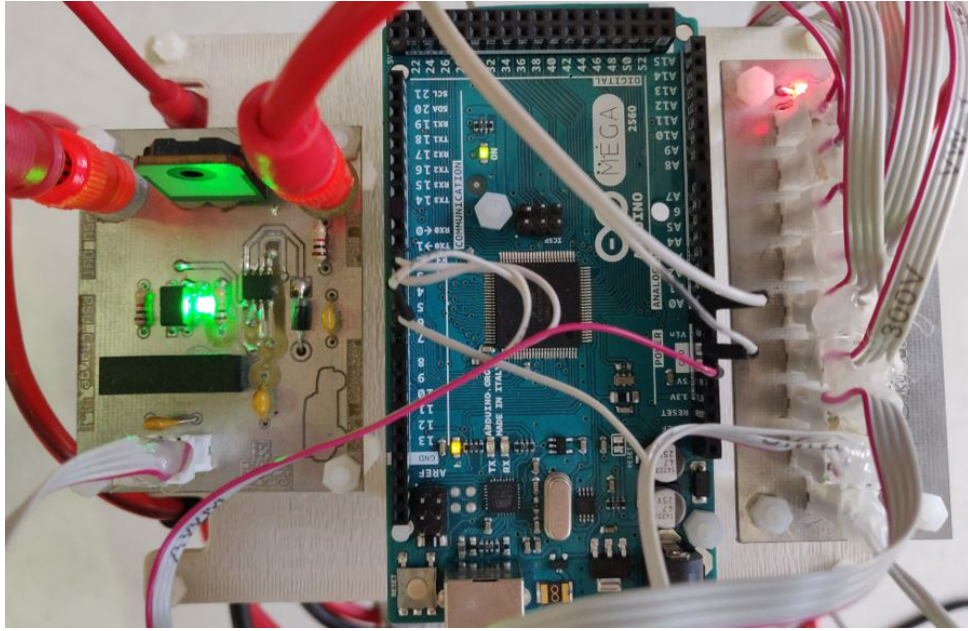


Figure E.4: From left to right, the charge-controlling module, the microcontroller, and the distribution board.

The pulse-shaping network (shown in Figure E.5) was constructed using two parallel-connected $8\ \Omega$ power resistors for resistor R_1 , and two series-connected $8\ \Omega$ power resistors for resistor R_3 . Resistor R_4 (not pictured) was realised using a rheostat with a maximum resistance of $5\ \Omega$ in order to allow for the output impedance of the impulse generator to be adjusted. Resistor R_3 was omitted, as all design work had indicated that its value should be as low as possible. A hand-wound air core inductor was used for inductor L_1 . Inductor L_1 was designed as follows.

Equation E.1 provides an estimate of the inductance of a coil [67].

$$L_{\text{coil}} \approx N^2 \mu_0 \mu_r \frac{D}{2} \left[\ln\left(\frac{8D}{d}\right) - 2 \right] \quad (\text{E.1})$$

- N represents the number of turns.
- μ_0 represents the permeability of free space ($4\pi \times 10^{-7}$ H/m).
- μ_r represents the relative permeability of the core material (which is 1 for an air core inductor).
- D represents the diameter of the coil.
- d represents the diameter of the wire.

Equation E.1 was used to calculate that an air core inductor with 17 turns, with a coil diameter 25 mm, with a wire diameter of 2.5 mm would produce an inductor of approximately $10.4\ \mu\text{H}$. This was larger than the $7.1\ \mu\text{H}$ calculated in Section 3.3.1.2, however it was chosen to construct an inductor with a larger inductance than necessary, with the idea that turns could easily be removed to lower the inductance if the open-circuit voltage and short-circuit current waveforms required it. Note that for the circuit

shown in Figure E.5, the inductor's turns had been separated slightly in order to modulate the inductance.

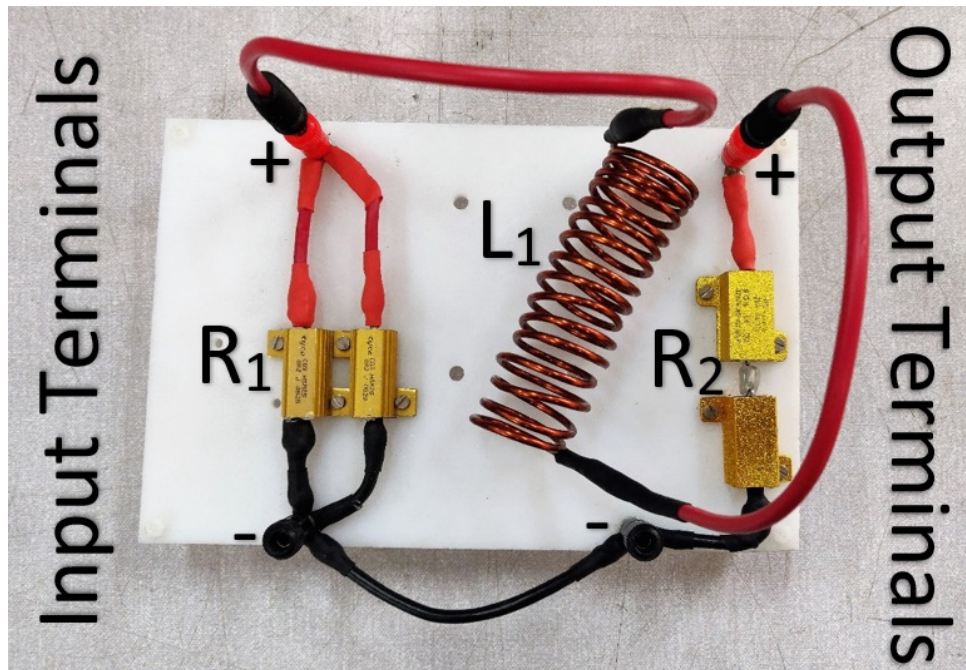


Figure E.5: The constructed pulse-shaping network.